Andreas Kautsch

Photoinduced Dynamics of Transition Metal Atoms and Clusters in Helium Nanodroplets

DOCTORAL THESIS

For obtaining the academic degree of

Doktor der technischen Wissenschaften

Doctoral Programme of Technical Sciences
Technical Physics

Graz University of Technology

Supervisor:

Univ.-Prof. Dipl.-Phys. Dr.rer.nat. Wolfgang E. Ernst

Co-Supervisor:

Ass.Prof. Dipl.-Ing. Dr.techn. Markus Koch

Institute of Experimental Physics

Graz, July 2014

Abstract

Photoinduced Dynamics of Transition Metal Atoms and Clusters in Helium Nanodroplets

Superfluid helium nanodroplets (He_N) serve as ideal matrix to isolate and analyze single atoms, molecules, and clusters. To study the influence of this cold, chemically inert environment on the dynamics of transition metal atoms and clusters upon photoexcitation, He_N are doped with chromium (Cr) and copper (Cu) by passing through a pick-up region where the desired species is present as vapor. Besides the doping with single atoms, dimers and clusters form inside the He_N after the pick-up of two or several atoms, respectively. After the dopants are cooled to the droplet temperature of 0.4 K, they are examined with laser excitation, laser induced fluorescence (LIF), and resonance ionization mass spectrometry (RIMS). For the first time, detailed information about the perturbation upon electronic excitation and relaxation of Cr and Cu in He_N, as well as the dopant's position on the droplet, was experimentally obtained and interpreted.
Deduced from the shifted and broadened ground state transitions, Cr and Cu atoms were found to be solvated inside the droplet. After laser excitation, relaxation into energetically lower states of different multiplicities, simultaneously to the ejection from the droplet, is observed. The relaxation process is strongly influenced by the matrix so that interesting sublevel population distributions are found. From these intermediate states, either fluorescence is recorded, or transitions to autoionizing states are excited with a further photon. Fano type resonances are found in the autoionization transition lines that are a result of the interfering discrete autoionizing states with the continuum states above the ionization potential.
Besides the ejection of bare atoms, also Cr and Cu atoms with a few He attached were formed after the excitation with a 308 nm laser photon. These showed wings to the blue side of the bare atom transition lines, which were compared to calculations from literature.
After the ground state excitation of Cr_2 into a predissociating state, the dopants remain on the droplet so that a whole cycle of photoinduced molecular dissociation, stable spatial separation of the fragments, and finally, photoinduced recombination is observed. This very unique process is also observed for small Cr clusters, and is attributed to a strong dimerization effect.

Kurzfassung

Photoinduzierte Dynamik von Übergangsmetallatomen und -clustern in Helium Nanotröpfchen

Suprafluide Helium Nanotröpchen (He_N) bilden eine ideale Matrix für die Untersuchung von isolierten Atomen, Molekülen, und Clustern. Es wurde der Einfluss dieser kalten und chemisch inerten Umgebung auf Übergangsmetallatome und -cluster nach einer Photoanregung untersucht. Dafür wurden die He_N auf dem Flug durch Regionen von erhöhtem Dampfdruck mit Chrom (Cr) und Kupfer (Cu) Atomen dotiert, wobei, je nach Anzahl der pro Tröpfchen adsorbierten Atome, sich auch Dimere und Cluster bilden. Die Dopanden kühlen auf die Tröpchentemperatur von 0.4 K und wurden im Anschluss mit Laseranregung, Laser induzierter Fluoreszenz, und Resonanzionisations-Massenspektrometrie analysiert. In dieser Arbeit wurden zum ersten Mal detaillierte Informationen über den Einfluss des Tröpfchens auf die elektronischen Anregungen und Relaxationsmechanismen von Cr und Cu, sowie deren Position im Tröpfchen experimentell gewonnen und interpretiert.

Aus den energetisch verschobenen und verbreiterten Anregungsspektren ist der Aufenthalt im Inneren des Tröpfchens herauszulesen. Nach der Laseranregung relaxieren die Atome in energetisch niedrigere Zustände verschiedener Multiplizitäten, während sie gleichzeitig aus dem Tröpfchen katapultiert werden und folglich als freie Atome in verschiedenen elektronischen Zuständen vorliegen. Der Relaxationsprozess ist stark durch die Matrix geprägt, was in einer Ungleichbesetzung der Subniveaus resultiert. Von den besetzten Zuständen wurde Fluoreszenz beobachtet, sowie der Übergang auf Autoionisationszustände durch ein weiteres Photon angeregt. In den Autoionisationslinien wurden Fano Resonanzen beobachtet und ausgewertet, die aus der Interferenz zwischen dem diskreten Autoionisationszuständen und den Kontinuumzuständen über dem Ionisationspotential resultieren.

Im Vergleich dazu werden nach der Anregung mit einem 308 nm Photon auch Cr und Cu Atome beobachtet, an die einige He Atome gebunden sind. Diese manifestieren sich in Flanken auf der energetisch höheren Seite der freien Atomübergänge, welche auch mit theoretischen Berechnungen verglichen wurden.

Nach der Anregung von Cr_2 im Tröpfchen in einen prädissoziierenden Zustand verweilen die Cr Fragmente, im Gegensatz zum Fall der einzelnen Cr Atomanregung, am Tröpfchen. Dabei konnte ein gesamter Zyklus von photoinduzierter molekularer Dissoziation, örtlicher Separation der beiden Fragmente, und anschließender Rekombination beobachtet werden. Dieser einzigartige Mechanismus scheint auch für kleine Cr Cluster zuzutreffen, was auf den Aufbau dieser unter dem Einfluss eines starken Dimerisationseffekts zurückzuführen ist.

Articles related to this work

1. Fano Resonances in Chromium Photoionization Spectra after Photoinduced Ejection from a Superfluid Helium Nanodroplet.
   Andreas Kautsch, Matthias Hasewend, Markus Koch, and Wolfgang E. Ernst.
   Physical Review A: Atomic, Molecular, and Optical Physics **86** (2012) 033428-1 – 033428-4.
   DOI: 10.1103/PhysRevA.86.033428

2. Electronic Relaxation after Resonant Laser Excitation of Cr in Superfluid Helium Nanodroplets.
   Andreas Kautsch, Markus Koch, and Wolfgang E. Ernst.
   The Journal of Physical Chemistry A **117** (2013) 9621 – 9625.
   DOI: 10.1021/jp312336m

3. Laser Ionization and Spectroscopy of Cu in Superfluid Helium Nanodroplets.
   Friedrich Lindebner, Andreas Kautsch, Markus Koch, and Wolfgang E. Ernst.
   International Journal of Mass Spectrometry **365 − 366** (2014) 255 – 259.
   DOI: 10.1016/j.ijms.2013.12.022

4. One- and Two-Color Resonant Photoionization Spectroscopy of Chromium-doped Helium Nanodroplets.
   Markus Koch, Andreas Kautsch, Florian Lackner, and Wolfgang E. Ernst.
   The Journal of Physical Chemistry A (2014) in press.
   DOI: 10.1021/jp501285r

5. Photoinduced Molecular Dissociation and Photoinduced Recombination Mediated by Superfluid Helium Nanodroplets.
   Andreas Kautsch, Markus Koch, and Wolfgang E. Ernst.
   (2014) submitted.

Danksagung

An dieser Stelle möchte ich all jenen Personen danken, die mich im Laufe der letzten drei Jahre bei meiner Dissertation begleiteten und deren umfangreiche Unterstützung ich hier nur exemplarisch darbieten kann.

Allem voran gilt mein Dank Herrn Prof. Wolfgang E. Ernst. Er hat mir das Erreichen meiner Ziele ermöglicht, durch seinen umfassenden Überblick stetige Unterstützung geboten und bewies immer ein offenes Ohr für Anliegen aller Art. Darüber hinaus verhalf er mir zur Teilnahme an verschiedenen internationalen und nationalen Tagungen um die neuesten Ergebnisse zu präsentieren sowie interessante Anregungen zu finden.
Speziell bedanken möchte ich mich bei Markus Koch. Von ihm konnte ich viel lernen, er kümmerte sich immer hingebungsvoll auch um die auch noch so kleinen Angelegenheiten, und ließ mit seiner persönlichen Art gar kein anderes als ein freundschaftliches Verhältnis zu. Beachtenswert ist wohl seine Fähigkeit, sich sowohl experimentell selbstlos hineinzusteigern als auch beim Diskutieren und Publizieren der Erkenntnisse umfassende Geduld zu beweisen und nie die Freude an der Sache zu verlieren. Ihm gilt auch der Dank für das Korrekturlesen dieser Arbeit.
Während meiner Zeit hatte ich auch die ausgiebige Gelegenheit Matthias Hasewend und Friedrich Lindebner in allen Lebenslagen des Experimentierens an einer Helium Nanotröpchen Anlage kennen zu lernen und möchte die vielen gemeinsam verbrachten Stunden nicht missen. Mein Dank gilt insbesondere der tatkräftigen Mitarbeit und ihrer Loyalität bei den noch so schwierigen Herausforderungen. Ohne sie wäre vieles so sicher nicht möglich gewesen.
Umfangreicher Dank geht an meinen Arbeitsgruppenkollegen Martin Ratschek und Johann Pototschnig für die fachlichen Diskussionen und unterstützenden theoretischen Berechnungen, Florian Lackner für die geduldige Hilfe im Umgang mit den Geräten aus dem CLI, sowie meinen Kollegen aus den anderen Cluster-Laboren Alexander Volk, Günter Krois und Phillip Thaler, für viele praktische Hilfestellungen und Ideen. Außerdem gilt mein Dank Herrn Prof. Windholz für hilfreiche Ratschläge und das Borgen so manchen Equipments, Herrn Prof. Neger für die Beratung in Sachen Optik, Peter Reiter für die Ratschläge im Umgang mit Optik Simulationsprogrammen, Christian Gössweiner für die Konstruktion des Beam Profilers und Reinhold Hetzl für das Kalibrieren unserer Hg-Lampe.
Die Ergebnisse wären aber sicher nicht so erfolgreich ausgefallen ohne die praktische Unterstützung aller Mitarbeiter des Instituts für Experimentalphysik. Dazu zählen insbe-

sondere Rupert Maierhofer, Werner Luttenberger und Uwe Seidl aus dem Werkstattteam, unsere Elektroniker Reinhard Dämon und Josef Friedrich, unser Computeradministrator Josef Pichler, sowie das Sekretariatsteam Bettina Gsöls-Bedenik, Sandra Brunner und Elisabeth Weiß.

Ein außerordentlicher Dank gilt meiner Familie, welche mir mein Fortschreiten bis dato erst ermöglicht hat. Karin möchte ich für all ihre Unterstützung und Verständnis bei all dem, was ich gerne mache, danken.

EIDESSTATTLICHE ERKLÄRUNG

AFFIDAVIT

Ich erkläre an Eides statt, dass ich die vorliegende Arbeit selbstständig verfasst, andere als die angegebenen Quellen/Hilfsmittel nicht benutzt, und die den benutzten Quellen wörtlich und inhaltlich entnommenen Stellen als solche kenntlich gemacht habe. Das in TUGRAZonline hochgeladene Textdokument ist mit der vorliegenden Dissertation identisch.

I declare that I have authored this thesis independently, that I have not used other than the declared sources/resources, and that I have explicitly indicated all material which has been quoted either literally or by content from the sources used. The text document uploaded to TUGRAZonline is identical to the present doctoral dissertation.

Datum / Date

Unterschrift / Signature

Contents

Abbreviations

1CR2PI one-color resonant two-photon ionization

2CR2PI two-color resonant two-photon ionization

AI autoionization

arb. units arbitrary units

ASE amplified spontaneous emission

BD beam depletion

CLI Cluster Laboratory I

CLII Cluster Laboratory II

cw continuous wave

DPSS diode pumped solid state

ESR electron spin resonance

fwhm full width at half maximum

HENDI helium nanodroplet isolation

He$_N$ Helium Nanodroplets

IP ionization potential

IR infrared

LIF laser induced fluorescence

MC measurement chamber

MCD magnetic circular dichroism

MRI magnetic resonance imaging

NIST National Institute of Standards and Technology

PC pick-up chamber

PES potential energy surface

PI photoionization

PID proportional-integral-derivative

PMT photomultiplier tube

QMS quadrupole mass spectrometer

REMPI resonance-enhanced multiphoton ionization

RIMS resonance ionization mass spectrometry

SC source chamber

SEM secondary electrons muliplier

TTL transistor-transistor logic

UV ultraviolet

1 Introduction and General Principles

This thesis is organized in three main chapters. First, the interest in transition metal doped helium nanodroplets (He_N) is motivated and fundamental principles are explained. The second chapter treats the experimental techniques and some practical advice for the experimental setup is given. The results chapter contains all major results that were either published [1–4] or submitted [5] to peer reviewed journals, as well as some additional results.
Attached to the thesis, technical drawings and further information for the experimental setup can be found. The enclosed DVD contains some useful files for the future operation of the setup.

1.1 Photoinduced Dynamics of Transition Metal Atoms and Clusters in Helium Nanodroplets - Motivation

Helium nanodroplet isolation (HENDI) combines two well established techniques - matrix isolation and seeded supersonic beams - in an innovative way to establish a tool that overcomes limitations connected with both methods. Matrix isolation refers to the trapping of guest species in a rigid host that segregates the dopants and prevents them from undergoing diffusion. Usually, a substrate is mixed with a large amount of a chemically inert host gas, and condensed on a cooled surface that ensures rapid condensation [6]. Seeded supersonic beams are obtained by collimating a jet, formed upon supersonic expansion of seed molecules with a carrier gas from moderately high pressure (0.7 - 100 bar) into vacuum through an orifice. The seed gas internal degrees of freedom are substantially cooled by this process, which enables the formation of weakly bound van der Waals complexes after collisions in the region of high density [7, 8].
He_N are free, confined, superfluid, and cold (0.37 K) matrices made up of agglomerated He atoms. They are produced by a supersonic expansion of helium gas through a cooled nozzle into vacuum (see Fig. 1.1), where the droplet sizes are determined by the nozzle temperature, the He pressure, and the orifice diameter. Besides the study of He_N themselves, they serve as containers to examine isolated species in a cold matrix [9, 10]. The transparency over a wide wavelength range makes He_N ideal for the spectroscopic

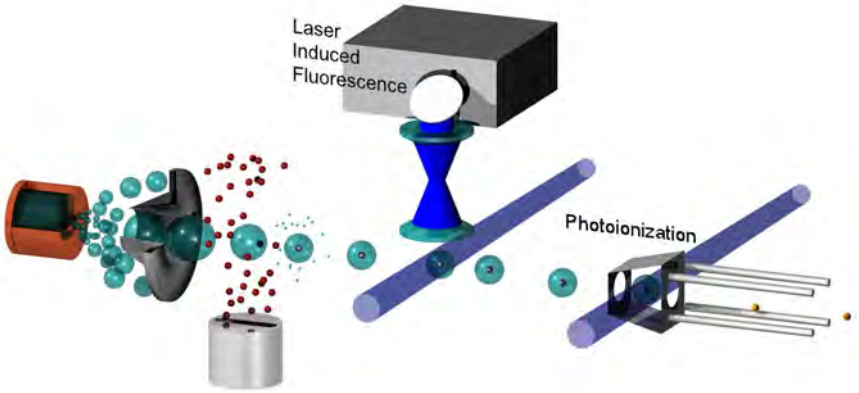

Figure 1.1: Schematic setup for dispersed laser induced fluorescence and photoionization experiments on He_N doped with transition metal atoms.

investigation of isolated atoms, molecules, and clusters. A controlled pick-up of foreign species from regions of higher partial pressure confines them to the droplet volume. Tailor made clusters can aggregate after the multiple pickup of atoms or molecules by one droplet. The dopants are efficiently cooled to the droplet temperature of 0.37 K [9] due to the high thermal conductivity. Hence, a "*collection of dopants inside individual droplets represents a micro-canonical ensemble, and as such each droplet may be considered an isolated cryo-reactor.*"[11] Overall, He_N provide the benefits of matrix spectroscopy, e.g., the caging effect for radicals which limits their reactivity, with the advantage of in many cases high spectral resolution, e.g., for rotationally resolved vibrational spectra [12].

A great variety of atoms and molecules have been doped to He_N [9]. Nevertheless, transition metal atoms, except for coinage metals, have been rarely studied in He_N. 3d metals and metal alloys are of practical importance e.g., in magnetism, metallurgy, and solid state lasers [13], and their chemical properties makes them widely applicable in chemistry, e.g., for catalysts [14]. Molecules containing transition metal atoms are also of great interest "*to model catalytic and chemisorption processes.*"[15] Furthermore, 3d transition metals belong to the more abundant elements in the universe, hence, a detailed knowledge about their properties is also of fundamental interest for astrophysics [13].
Chromium is unique among the 3d transition metals with only one electron in the 4s orbital. In combination with the half-filled 3d shell, it has six unpaired electrons that lead to a very high magnetic moment of 6 μ_B (Bohr magneton, $\mu_B = \frac{e\hbar}{2m_e}$) and a strong dimer binding character. *"Among the dimers of the first transition series, Cr_2 potentially provides the most extreme example of multiple metal-metal bonding.*"[16]. It exhibits an unusually short bond length of 1.68 Å for the strongly bound $^1\Sigma_g^+$ ground

state [17], and a dense manifold of high multiplicity excited states. Also, phenomena like predissociation [15, 18] or weakly bound metastable states [19], which are known to be promoted by the He_N [20, 21], were reported for Cr_2. Furthermore, the growth of small Cr_n clusters (n <12) was found to be governed by a strong dimerization effect [22, 23]. Driven by the high magnetic moment of Cr atoms, the nature of bonding and electronic structure in small chromium clusters has received considerable experimental and theoretical attention since these also affect the magnetic properties [24].

In contrast to chromium, copper has a fully filled 3d shell and only one electron in the 4s orbital. The electron shell is therefore similar to those of the other important group 11 elements Au and Ag, as well as it results in a more alkali metal like electron structure. Therefore it is also a very promising candidate to gain better knowledge about the behavior of transition metal atoms inside He_N, with the advantage of a simpler theoretical treatment.

To investigate dopants of different kind and physical or chemical properties in He_N, laser spectroscopy is a well suited method [9]. It describes the study of the interaction of light with matter and includes a variety of powerful methods for analysis. Many of the tools that have been developed for molecular beam studies are in principle applicable in combination with He_N [9, 25]. To study the spectroscopic properties of Cr in different environments is of practical importance. In the solar spectrum, Moore, Minneaert, and Houtgast [26] found 809 unblended Cr I lines between $\lambda = 293.5$ nm and $\lambda = 887$ nm. These lines are suitable to investigate stellar atmospheres, including microturbulence parameters or as an aid to test model solar atmospheres. Also, they can be used to study microturbulences on cold stars, when the commonly used Fe I lines are too strong [27]. In biology and medicine, human standard urine samples (NIST) contain a chromium concentration of 0.085 μg/ml. Using resonance ionization mass spectrometry (RIMS), these can be accurately measured showing the utility for the "*analysis of biological samples of complex matrix* [...]"[28]. Spectroscopic investigation of Cr autoinization states is of interest in plasma physics. For instance, due to the evaporation of Cr from JET tokamak antenna screens under strong heating, impurities increase that can be monitored with the knowledge about the ionization processes [29, 30].

From the many interesting facts sketched above, the key motivation for this thesis was the little knowledge about Cr and Cu atoms and clusters doped to He_N. With their physical and chemical properties, they have good prospects regarding magnetism and chemical reactions in a cold environment. New possibilities for further studies might be established with the obtained results that possibly apply for most of the transition metal atoms and clusters in He_N.

This work was supported by the *European Union and Styrian Government* (Seventh Framework Programme, FP7) and the *Fonds zur Förderung der wissenschaftlichen Forschung* (FWF, Grant: 22962-N20).

1.2 Helium

1.2.1 The Exploration of an Element

First evidence for helium was found in 1868 by the French astronomer Pierre J. C. Janssen. It was during a total solar eclipse on August 18^{th} in India when he observed a bright yellow line ($\lambda = 587$ nm, ^{3}D (1s3d) $\rightarrow$ ^{3}P$^\circ$ (1s2p)) in the spectrum of the Sun's chromosphere[1] [32]. Because of the spectral vicinity to the Na-D lines it was initially assumed to be a sodium line. In the same year, the English astronomer Norman Lockyer observed the same line in the solar spectrum and, together with the chemist Edward Frankland, named it "$\acute{\eta}\lambda\iota o\varsigma$" (helios) from the Greek name for Sun. So it is written in Ref. [33]

> "*Frankland and Lockyer find the yellow prominences to give a very decided bright line not far from D, but hitherto not identified with any terrestrial flame. It seems to indicate a new substance, which they propose to call helium.*"[33]

On earth, helium was spectroscopically detected by Luigi Palmieri when he analyzed the lava of Mount Vesuvius in 1882. The Scottish chemist Sir William Ramsay (1852 - 1916, Nobel prize 1904 for the discovery of noble gases) was the first to describe the isolation of He by treating the mineral cleveite (an impure radioactive variety of uraninite[2] containing uranium) with sulfuric acid in 1895. Almost simultaneously, the same observation was made by the British physicist W. Crookes and the Swedish chemists P. T. Cleve and N. Langlet [34]. Prior to Ramsay's discovery, the American geochemist William Francis Hillebrand was the first to isolate He while testing a sample of uraninite, but unfortunately thought it was nitrogen. The possibility to extract He with high quantity from natural gas in Dexter, Kansas, was found by H. Cady and D. McFarland in 1907, the same year when Ernest Rutherford and Thomas Royds discovered that alpha particles are He cores [34].
Many findings in the following years are related to the very special physical properties of He at low temperatures. Helium was first liquefied by the Dutch physicist H. Kamerlingh Onnes in 1908 (1853-1926, Nobel prize 1913) while cooling He gas to less than one Kelvin [35, 36]. This finding came hand in hand with the first observation of helium drops. H. Kamerlingh Onnes determined the boiling point of helium to $\sim$4 K and tried to solidify it upon further cooling, but failed due to the absence of a triple point for helium (see Fig. 1.2). 18 years later, Onnes' student W. H. Keesom was eventually able

[1] The chromosphere is the second of three main layers of the Sun's atmosphere. Because its density is significantly lower than the density of the photosphere below, it is invisible without special equipment under normal conditions [31].

[2] Uraninite, also known as pitchblende, is a radioactive, uranium-rich mineral and ore that mainly consist of UO_2.

to solidify He by applying additional external pressure of 25 MPa [34].
The superfluidity of ^{4}He was discovered[3] by the Russian physicist P. L. Kapitsa (1894 - 1984, Nobel prize 1978) in 1938 [37], 30 years after the first liquefaction. He found that the viscosity of He II is at least 1500 times smaller than that of He I. The striking problem was measuring the upper limit of the He II viscosity. The viscosity reached a level 10^4 times smaller than that of hydrogen gas, which was previously believed to be the fluid of least viscosity [34, 37]. Another 34 years later, the superfluidity of ^{3}He was observed by the American physicists D. D. Osheroff, R. C. Richardson, and D. M. Lee (all three were awarded the Nobel prize in 1996) at a temperature of 2.6 mK [38].

1.2.2 Physical and Chemical Properties

With the unique physical and chemical properties, e.g., it is one of the least reactive of all elements together with neon [39], helium is well suited as cold matrix for matrix isolation spectroscopy (c.f. Section 1.5). Of the eight known isotopes (^{3}He-^{10}He), only ^{3}He and ^{4}He are stable. After hydrogen, helium is the lightest element and has the highest thermal conductivity and, among all elements, it has the lowest melting- and boiling point [34]. In contrast to He I, boiling of He II is not possible due to the high thermal conductivity (approximately a hundred times that of copper) causing the evaporation of atoms from the surface. A rather important fact for the production of He_N is the negative Joule-Thomson-Coefficient of He at standard conditions, that would results in a temperature increase upon expansion [34].
Molecular orbital theory predicts that He_2 molecules don't exist [40]. Upon combination of two He atoms, the bonding and antibonding molecular orbital are occupied by the four 1s electrons and no molecular binding can be established since these cancel each other [34]. Nevertheless, because of van-der-Waals forces between all atoms the formation of a He-He Dimer is possible with a very low binding energy of 1.1 mK ($9.5{\cdot}10^{-26}$ J) and a large equilibrium distance of 5.2 nm [41].

1.2.3 Abundance, Synthesis, and Applications

Although it is the second most abundant element in the universe, only 5.2 ppm of the earth's atmosphere are helium because it vanishes into space due to several processes [42]. While the vast majority of He in the universe was formed shortly after the Big Bang, most He on earth is the result of radiactive decay in the earth's core. ^{4}He is the decay product of heavy elements like Uranium or Thorium, where α-particles are emitted that subsequently catch an electron. When rising toward the surface, the He is trapped under conditions that also trap natural gas. This is responsible for the relatively high

[3] An abnormal high heat conductivity was already observed by W. H. Keesom, but was not linked to superfluidity.

occurrence of He in natural gas [34].
Today, helium is extracted by low-temperature fractional distillation from natural gas, which can contain up to 7 % He [34]. Natural gas is treated under low temperature and high pressure so nearly all the other gases, except He (due to its low boiling point), are liquefied and can be extracted. Further purification is achieved by lowering the temperature, purifying with activated charcoal (99.995 % Grade-A), and final liquefying of the He [43].

The largest use of He is in cryogenic applications where the unique properties are required. For instance, in medicine the superconducting coils for magnetic resonance imaging (MRI)[4] are cooled with liquefied He. Further applications are in deep-sea breathing systems, as protection gas for welding, maintenance of controlled atmospheres, and leak detection. Filling He-balloons and inhalation to speak with a Mickey-Mouse voice[5], which are probably best known to most people, are only of minor significance [34].

1.3 Helium Nanodroplets

Large He_N clusters with $N \geq 10^3$ are referred to as Helium Nanodroplets [44]. Macroscopic helium droplets were first observed about 100 years ago in 1908, in the form of a mist above liquefied ^{4}He upon rapid Joule-Thomson expansion [35]. In the early days of He_N, they were mainly studied theoretically by nuclear physicists as a model for finite-size many body quantum systems [44]. Today, He_N can be formed in a supersonic expansion of helium gas through a cooled nozzle into vacuum, referred to as supersonic free jet expansion. This technique was first demonstrated by Becker et al. in 1961 [45]. The common case for the spectroscopic investigation of atoms and small clusters in He_N is a "subcritical" expansion. Inside the nozzle, the state of the He is well within the gaseous region of the He phase diagram (c.f. Fig. 1.2). With expansion, the He cools adiabatically following the isentropes in the phase diagram to conditions well beyond the vapor-liquid phase transition. In vicinity of the nozzle, the He atoms collide and condense due to their low temperature, which forms the droplets. Atoms from the surface of the formed cluster evaporate, and carry away energy to further cool the droplet (E_b = 7.2 K per ^{4}He atom, initially with a very high cooling rate of $\sim 10^{10}$ K/s). The cooling rate decreases exponentially until a temperature of 0.37 K for ^4He_N (0.14 K for ^3He_N) is reached after about 0.1 ms [44]. Because of this effect, He_N possess a very high effective heat capacity providing an almost ideal cryogenic container. The nature of ^{4}He at such low temperatures causes the superfluidity of the He_N with a vanishing

[4] Also called: nuclear magnetic resonance imaging (NMRI), or magnetic resonance tomography (MRT)
[5] Because of the low density and high velocity of sound, the vocal chords evolve higher resonance frequencies than in air that cause a squeaky voice.

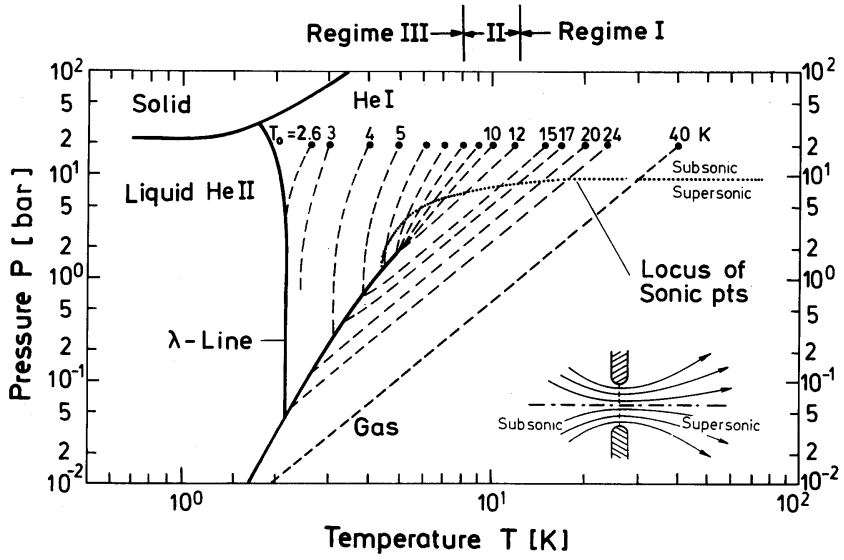

Figure 1.2: Phase diagram for the expansion of ^{4}He through a nozzle (T_0 ... nozzle temperature). Superfluidity is a property of the liquid He II phase. Reprinted with permission from Ref. [46]. Copyright 1990, AIP Publishing LLC.

small viscosity.
The nozzle has a diameter of several microns (d_{nozzle} = 2 - 20 μm) and is operated at low temperatures and high helium gas pressures (typically T_0 = 5 - 20 K, p_0 = 20 - 100 bar) [44]. The nozzle temperature influences the statistical formation process, which governs the droplet sizes (see Table 1.1) as well as the droplet flight velocity. The latter lies between 200 and 400 m/s and has an influence on e.g., the timing gate of the beam depletion measurements (see Section 2.3). Continuous and pulsed beam sources were established, where the latter ones produce 30-50 microsecond long pulses with 1000-times larger peak droplet intensities [44]. For continuous sources, flux rates in the order of 10^{14} He_N $sr^{-1}s^{-1}$ were estimated in the subcritical regime [44], but as droplet size increases, the absolute droplet flux rate decreases. In the experiments (Chapter 2), a continuous source was used that produces a constant flow of He_N.

He_N size distributions were measured in electrostatic field deflection experiments or stopping of droplet ions in electric fields [47]. In the subcritical regime, droplet sizes follow a log-normal distribution according to [48, 49]

$$P_{\mathrm{N}}^{ln}(N) = \frac{1}{\sqrt{2\pi}N\sigma} e^{-\frac{(ln(N)-\mu)^2}{2\sigma^2}} \tag{1.1}$$

with N, the number of He atoms in one droplet, the width of the distribution σ, and

Table 1.1: Typical nozzle temperatures (T_0) with average droplet sizes ($\bar{N}$), droplet size distribution maxima ($\hat{N}$), and corresonding droplet radius ($\hat{r}$).

T_0 [K]	$\bar{N}$ [1]	$\hat{N}$ [1]	$\hat{r}$ [nm]	T_0 [K]	$\bar{N}$ [1]	$\hat{N}$ [1]	$\hat{r}$ [nm]
13.0	21 200	7 200	4.30	20.0	4 000	1 400	2.46
13.5	18 300	6 800	4.20	20.5	3 600	1 100	2.32
14.0	15 900	6 300	4.10	21.0	3 300	1 000	2.19
14.5	13 900	5 800	3.98	21.5	3 000	800	2.07
15.0	12 200	5 200	3.85	22.0	2 750	680	1.95
15.5	10 700	4 700	3.72	22.5	2 520	560	1.83
16.0	9 500	4 200	3.59	23.0	2 310	470	1.72
16.5	8 400	3 700	3.45	23.5	2 130	380	1.61
17.0	7 500	3 300	3.30	24.0	1 960	320	1.51
17.5	6 700	2 900	3.16	24.5	1 810	260	1.42
18.0	6 000	2 500	3.02	25.0	1 670	210	1.32
18.5	5 400	2 200	2.87	25.5	1 550	170	1.24
19.0	4 900	1 900	2.73	26.0	1 440	140	1.15
19.5	4 400	1 600	2.59				

the distribution maximum μ. The mean droplet size of this distribution is

$$\bar{N} = e^{\mu+\sigma^2/2} \tag{1.2}$$

whereas the maximum of the droplet size distribution is given by

$$\hat{N} = e^{\mu-\sigma^2}. \tag{1.3}$$

The majority of spectroscopic signal has to be assigned to the droplet sizes represented by the maximum of the log-normal size distribution rather than the mean droplet sizes [50]. Therefore, in this thesis the distribution maxima are primarily provided. To obtain $\hat{N}$, both parameters μ and σ have to be known where only one source is available in literature (Ref. [49]). The values in Ref. [49] are given for other stagnation pressures than used here, so fitting models need to be applied which are described in detail in Refs. [51, 52]. Some typical values for $\bar{N}$ and $\hat{N}$ are given in Table 1.1, where the *Power Model* was used (see Ref. [51]) to fit μ and σ.

Various interesting He_N properties were found and are reviewed in Refs. [9, 12, 25, 44, 53, 54]. In addition to the smaller droplets used here, larger He_N show fascinating properties regarding the formation of vortices [55]. Large droplets can be formed by a supercritical expansion that leads to the break up of a jet of liquid He passing through the nozzle. For this supercritical regime the flux rate is orders of magnitude

lower compared to the subcritical regime [56]. Also, in contrast to the log-normal size distribution for the subcritical expansion (see Eq. (1.1)), the size distribution for a supercritical expansion is given by the linear-exponential function [47]

$$P_{\mathrm{N}}^{le}(N) = \frac{1}{\bar{N}} \mathrm{e}^{-\frac{N}{\bar{N}}}. \tag{1.4}$$

In principle, droplets can be formed from ^{4}He as well as ^{3}He. Forming $\mathrm{He_N}$ from the isotopes leads to differences in the final equilibrium temperature (^{4}He: 0.37 K, ^{3}He: 0.15 K) and the superfluid properties (^{4}He: superfluid, ^{3}He: normal fluid)[9]. Some experiments were carried out using ^{3}He [9, 44], but are not of relevance here.

1.4 Doping Helium Nanodroplets

$\mathrm{He_N}$ are doped by an in-flight pick-up process of foreign atoms or molecules. Nearly all species that are isolable substance and volatilizable without decomposition[6] can be attached to $\mathrm{He_N}$. A systematic overview of the dopants used in different groups can be found in Ref. [9].
Initially, it was not clear if foreign atoms can be attached to $\mathrm{He_N}$ because of their superfluid state. Experiments in the group of Gspann [57] were interpreted as indication for the transparency of He droplets for species such as Xe and Cs atoms. Later, mass spectroscopic experiments showed that $\mathrm{He_N}$ have the ability to pick-up species on their flight [58]. The atoms or molecules originate from the residual gas in the vacuum chamber or from areas of increased partial pressure ($>10^{-4}$ mbar [9]) along the $\mathrm{He_N}$ beam. In the latter case, evaporation sources or gas cells are preferably used to establish defined doping conditions. In the simplest case, the droplets penetrate a pick-up cell filled with the vapor of the desired species. Alternatively, in a crossed pick-up geometry, the $\mathrm{He_N}$ pass close to an evaporation cell that emits dopant atoms or molecules perpendicular to the $\mathrm{He_N}$ beam direction. When assuming a unity sticking coefficient to the droplet, the pick-up cross section of dopants is the geometrical cross section [9, 44] and the number of dopant particles attached to the droplets is given by a Poisson distribution [59]

$$P_{\mathrm{n}} = \frac{(N\sigma l)^n}{n!} \mathrm{e}^{-N\sigma l} \tag{1.5}$$

with the number of picked-up atoms n, the number density of dopant atoms in the interaction volume crossed by the droplet beam N, the cross section for the pickup of a dopant by a droplet σ, and the interaction path length l.

[6] This excludes some interesting compounds of biological relevance, at least in their native forms [6].

The subsequent pickup of dopants by He_N enables the production of tailor-made[7] clusters consisting out of a homogenous or different components [56, 60]. In gas phase, three body collisions are a prerequisite for the formation of clusters due to the conservation of momentum and energy. Only if a third particle, mostly an inert gas atom, carries away the excess energy, the other two particles can bind [61]. This process is simpler inside He_N, where the matrix can absorb the excess energy and momentum which leads to the bonding of the collision partners. The total, energy introduced during the pickup process consists of the collision energy, the solvation energy, and, if more than one dopant is picked up by the droplet, the binding energy between the dopants [9].
If the dimer and cluster formation out of single atoms would not be promoted by the droplet, the observation of this species would be very unlikely. E.g., by heating bulk Cr, also Cr_2 molecules are evaporated and the Cr_2 vapor pressure in a Knudsen cell was determined to be (valid in the temperature range of 1542 - 1819 K)[62]

$$ln(p[Pa]) = -7.337\frac{10^4}{T[K]} + 31.831 \tag{1.6}$$

Compared to the partial pressure of Cr atoms (valid in the temperature range of 1283 - 1561 K)[63]

$$log(p[atm]) = -20\,473\frac{1}{T[K]} + 7.467 \tag{1.7}$$

the Cr_2 partial pressure (Eq. (1.6)) is approximately six orders of magnitude lower which would not yield a sufficient doping probability. A MATLAB® script can be found on the enclosed DVD ('Cr_Cr2_VaporPressure.m') that compares both partial pressures.

Pick-up cells are built in a variety of layouts and working principles, depending mainly on the evaporation properties of the dopant species or restrictions like stray magnetic fields or pulsed He_N beams. Doping with gas atoms is quite simple by controlling the gas flow into the vacuum chamber or pickup volume. Low temperature pick-up cells are used for the evaporation of organic molecules, alkali-, and alkaline earth metals [44]. These species have a high partial pressure already at low temperatures. To dope He_N with high melting metals, heated ovens or laser ablation from a target can be used. Nevertheless, various problems are linked to the latter method. One of them is the simultaneous excitation and ionization of laser ablated atoms which causes the need of a time delay between ablation and experiment (see e.g., Ref. [64]). Therefore, high temperature evaporation sources based on electron bombardment [65] and resistive heating were used to produce vaporized Cr and Cu atoms, respectively.

To predict the location of a dopant on the droplet, a dimensionless parameter λ_A was introduced by Ancilotto et al. [66]. It builds on the estimate that for $\lambda_A > 1.9$ the dopants are solvated, whereas for $\lambda_A < 1.9$ the dopants reside in a surface position [66]. The

[7] *Tailor-made* means to have something specifically made just to fit. The professions who manufacture this are the tailors.

parameter is calculated on basis of the dopant-helium diatomic potential and compares the energy required to deform the droplet and form an additional surface with the energy gained by the dopant-helium interaction. Counterplayers are therefore the solvation energy (long-range, attractive van der Waals forces) and steric hindrance (short-range, repulsive Pauli forces)[9]. The equation for calculating the Ancilotto parameter is [66]

$$\lambda_A = 2^{-1/6} \frac{\rho \varepsilon r_e}{\sigma} \tag{1.8}$$

with the well depth of the dopant-helium pair potential ε (in cm^{-1}), the surface tension σ (0.179 cm^{-1} $Å^{-2}$ [67]), the He density ρ (0.022 $Å^{-3}$ [44, and references therein]), and the equilibrium bond length for the dopant-helium pair potential r_e [68]. So the dopant is preferably solvated inside the He_N for deep dopant-helium potential wells and large equilibrium distances.
$\lambda_A \approx 2.7$ [69] and $\lambda_A \approx 2.9$ [70] were determined for Cr and Cu, respectively, indicating the solvation of both. In contrast, a surface position of the dopant can be energetically favored if only long-range attractive dopant-helium forces play a role (e.g., for most earth-/ alkali metal atoms $\lambda_A \approx 0.7$ [71]). Then, the dopant resides in a "dimple" on the droplets's surface caused by the balance between the long-range attractive and short-range repulsive forces [72].

1.5 Matrix Isolation Spectroscopy

Matrix isolation is a well-established technique that allows to immobilize and isolate substrate atoms, molecules, or clusters in a matrix [10, 73]. Ideally, each dopant is trapped in a cavity to be probed by laser spectroscopy [74–77] or characterized by electron spin resonance (ESR) [78–80]. The matrix is formed by mixing the substrate with a large excess of the host gas and condensing the mixture on a cold surface that ensures rapid solidification. In the original sense, inert gas atoms are mostly chosen as unreactive matrix because of the weak influence on the behavior of the dopant. Nowadays, the term matrix isolation is used in a more general sense that also includes trapping in rigid host materials, e.g., crystals, clays, and polymers [6].
Matrix isolation allows the observation of species that are only of fleeting existence under ambient conditions with conventional spectroscopic tools. The stable condition of isolated dopants in the matrix allows a detailed investigation concerning e.g., the electronic and molecular structure of reactive intermediates. Furthermore, the low temperature required to solidify the host gases, enables to study species under low temperatures that suppresses thermally activated processes. An embracing disadvantage of all matrix isolation is the transfer of the examined species into a perturbing environment. Hence, no unambiguous conclusions on the performance of the species in their natural environment

(e.g., in gas phase) can be drawn [6]. One example is the so-called *cage effect*, that can hinder the formation of reactive intermediates when fragments are confined to the same cavity and may therefore undergo recombination [81]. Further disadvantages are the opaqueness of some matrices throughout wide regions of the infrared (IR) and part of the ultraviolet (UV) spectral range or the poor heat sink characteristics of noble gas matrices when only very low energy lattice phonons are available to accept molecular vibrational quanta [6].
When using He_N spectroscopy, some of these disadvantages are eliminated. With the closed shell configuration, it is virtually impossible to excite helium with common lasers. Only radiation in the EUV[8] enables the direct investigation of He_N [82–84]. So He_N offer a unique matrix, which is transparent over a wide wavelength range and enable the investigation of dopants under extremely cold conditions. Furthermore, electronic transitions are less broadened than in other matrixes and with the superfluidity of He_N, dopants are not trapped in different sites like in solid matrix spectroscopy [9, 85]. An exception are strong bondings between the dopant and the He, where a mechanism like freezing appears that localizes some He atoms around ions [9].

1.6 Atomic Bubble Model

In matrix isolation (Section 1.5), one goal is to minimize the influence of the environment by using noble gas matrices [6]. Compared to the bare atom natural linewidths of electronic transitions ($\sim 3\text{x}10^{-4}$ cm^{-1} [9]), spectral lines are broadened and shifted for dopants in or on He_N. The influence of the surrounding He_N during an electronic excitation can be described by the atomic bubble model, that was originally developed for impurities in bulk matrices [86, 87].
The Pauli repulsion repells the matrix He atoms and the dopant's electron density from each other. In liquid He, the electrons displace the matrix He atoms that form a spherical cavity around the dopant, also called "bubble" [68]. Most perturbation is caused by the first few solvation shells of He around the dopant, so this approach can be extended reliably to dopants in He_N [88]. In the center of larger droplets, the density is close to that of bulk liquid helium. Near the surface the density drops from 90 % to 10 % within ∼0.6 nm. A bubble formed in this region of high density-gradient is pushed toward the surface [68].

During an electronic excitation the bubble can be assumed stationary, since the time scale (picoseconds) of the electronic transition is shorter than the oscillation of the bubble [86]. Depending on the change in electron configuration during the transition, the influence of the matrix on spectral lines can vary from only a few cm^{-1} [89] (same

[8] Extreme ultraviolet

configuration for both involved states) up to a few hundred wave numbers [90, 91]. This is related to the change in orbital expansion during the excitation which interferes with the neighboring He and leads to a profound rearrangement of the matrix, while the state of helium is usually conserved upon rotational-vibrational excitation of a dopant [44]. As a rule of thumb, all electronic transitions including outermost electrons are shifted and broadened in the presence of a liquid or solid matrix. E.g., for Europium the active inner shell 5d←4f transition is shielded by the fully filled outermost 6s shell. Therefore, these transitions appear narrow (linewidths ∼10 cm^{-1}) also for Eu solvated in He_N [89]. Interestingly, the spectroscopic shift for 3d transition metal electronic transitions is dependent whether there is an odd or even number of 3d electrons for the excited state. For an odd number the shift is about 50 % less than an for even one (compare e.g., manganese $^6P^\circ[3d^5\ 4s\ 4p] \leftarrow {}^6S_{5/2}[3d^5\ 4s^2]$: 300-500 cm^{-1}, and chromium y^7P° $[3d^5 4s] \leftarrow a^7S_3$ $[3d^4 4s4p]$: 1900-4100 cm^{-1}, both in argon matrix) [92].

1.7 Transition Metals

Elements in the d-block of the periodic table (groups 3 - 12) are called *transition metals*. They have "*an incomplete d sub-shell, or* [...] *can give rise to cations with an incomplete d sub-shell.*"[93] In the periodic table they are surrounded by the s and p-blocks on either sides and represent the transition from the metallic character of the s-block elements to the non-metallic character of the p-block elements [94]. The subspecies of 3d transition metals are a very abundant species throughout the universe which increases the importance of detailed knowledge about the spectroscopic properties, also for astrophysics [13]. In technological applications, their hardness along with a high melting point makes them interesting and they show some well-defined similarities in physical and chemical properties [93]. Both investigated species, Cr and Cu in He_N, are members of the 3d transition metals.

1.7.1 Chromium

Chromium is an outstanding member among the transition metals. The name "*Chromium*" refers to the colors of its salts (greek: $\chi\rho\tilde{\omega}\mu\alpha$, color) and it was discovered in the mineral Crocoite[9] by Louis Nicolas Vauquelin (France) in 1797 (and almost at the same time by the German chemist Martin Heinrich Klaproth). Pure Cr could first be extracted by R.W. Bunsen in 1854 [96].
Cr is one of the more abundant elements on earth. Each year, approximately 10 million

[9] Crocoite consists of lead chromate (PbCrO4) and has a bright hyacinth-red color, used in the paint pigment *Chrome Yellow* [95].

tons are mined in the form of Chromit. Elementary Cr does only occur in meteoroids. Under the influence of ambient air, the passivating character prevents metal surfaces from oxidizing with a few atom layer thick protective oxide layer, which hinders the diffusion of oxygen into the underlying material. This corrosion resistance makes it an important alloying metal for stainless steel, whereas in steels for high speed tools Cr is added to improve the strengthening [96]. Cr compounds are widely used as catalysts in the field of organic chemistry, e.g., to perform dehydrogenation, isomerization, and polymerization of organic compounds [97–99]. In metallurgy, Cr is a member of the *refractory metals*, a group of metals with and extraordinarily resistance to heat and wear and melting points around 2000°C [100]. The Cr melting point lies at 1890°C and the boiling point at 2640°C [96]. Chromium has a relatively high vapor pressure compared to its high melting point. Therefore, it is an exception among the refractory metals where the high melting point is usually linked to a low vapor pressure [101]. Nevertheless, compared to other metals in the periodic system, high evaporation temperatures are needed to yield free Cr atoms [63]. To obtain these, several different methods were developed, like laser desorption [64], glow discharges [102], sputtering by an argon ion beam [103], and evaporation from electron impact heated crucibles [65]. The latter technique was used in this thesis to dope the He_N with Cr atoms (see Section 2.1.2).

Cr has four stable and two unstable isotopes, listed with their abundance or half-life times in Table 1.2. Isotopes with an even number of neutrons, like the most abundant ^{52}Cr, have no nuclear spin and are therefore well suited for ESR experiments due to the absence of a hyperfine structure (the hyperfine interaction constants for the odd isotopes can be found in Ref. [104]). Isotope shifts of the $y^7P^\circ_4 \leftarrow a^7S_3$ and $z^7P^\circ_{2,3,4} \leftarrow a^7S_3$ transitions (see below) lie in the range of $0 - 27{\cdot}10^{-3}$ cm^{-1} [104] and are thus not of concern. For the experiments, this reduces the focus to the most abundant isotope ^{52}Cr.

Table 1.2: Abundance or half life time (τ) of the six Cr isotopes and their nuclear spin (I).

Isotope	^{49}Cr	^{50}Cr	^{51}Cr	^{52}Cr	^{53}Cr	^{54}Cr
Abundance /τ	41.9 min.	4.35 %	27.70 d	83.79 %	9.50 %	2.36 %
I	5/2	0	7/2	0	3/2	0

The Cr electron configuration is:

$$[\mathrm{Ar}]\ 3d^5 4s^1$$

Chromium together with molybdenum are the only transition metals with only one unpaired electron in the 4/5 s orbital, while chromium and manganese are special chases for the 3d-4s configuration, as the 3d shell is half filled in both cases whereas the 4s is closed for Mn and open for Cr [24]. With the parallel orientation of all unpaired electrons,

the Cr atom exhibits a high magnetic moment of 6 μ_b ($\mu_B = \frac{e\hbar}{2m_e}$, Bohr magneton) [105]. In bulk phase, Cr is antiferromagnetic below the Néel temperature[10] (T_N = 311 K), and above it is paramagnetic [106, 107]. Another effect from the large number of electrons in the outer shells is the amount of 413 energy levels below the ionization limit (33 % are of even parity) [108]. An excerpt of the important states for this thesis is given in Table 1.3 and a Jablonksy diagram is shown Fig. 1.3. Comprehensive tabulated Cr levels and transitions can be found in Refs. [109–112]. To distinguish energy levels with equal assignment, they are ranked in energy and labeled with a small letter in front of the terms. Starting with the energetically lowest level, it numbers levels with even parity in alphabetical order ("a" to "z") and odd parity levels in reverse alphabetical order ("z" to "a"):

$$\begin{aligned} &\text{a,b,c...}^{2S+1}L_J \\ &\text{z,y,x...}^{2S+1}L_J^\circ \end{aligned} \tag{1.9}$$

L=0 and S=3 for the Cr ground state (a^7S_3) that yields a multiplicity M=7 (septet) due to the parallel spin configuration of the Cr outermost electrons ($3d^5 \uparrow 4s\uparrow$). Dipole allowed transitions from the a^7S_3 ground state are only possible to the z^7P° and y^7P° state, with the transition strengths and measured lifetimes given in Table 1.4. Energetically in between these two states lie the spin forbidden a^5P° state and the orbital forbidden z^7D° state (see Fig. 1.3). All other states in this region are both spin and orbital forbidden from the a^7S_3 ground state [77].

1.7.2 Cr_2

The role of the d-orbitals in the metal-metal bond of transition metal diatomics has been a controversial question for a long time [114, 115]. Moskovits et al. [116] recap that

> "*Although it is easy to generate clusters containing many tens of atoms* [...], *the complexity of the spectra which are being obtained with transition-metal diatomics has caused workers in the cluster field to stay at this first stop in the cluster journey somewhat longer than anticipated.*"[116]

and Morse [117] declares when writing about the predissociation process of Cr_2 observed by Bondybey, English [118], and Riley [18]

> "*From these studies it is clear that the photophysical and photochemical pathways in even diatomic molecules can be complicated.*"[117]

Hence, especially the chromium dimer was extensively studied [16, 22, 115, 117–122]. From a theoretical point of view, the Cr_2 sets a big challenge since its ground state

[10] Temperature, above which an antiferromagnetic or ferrimagnetic material becomes paramagnetic because the magnetic ordering of the atoms is destroyed by the thermal energy.

Table 1.3: Electron configuration and energy of relevant Cr states [109]. IP ... ionization potential.

Electron Configuration	Term	J	Energy [cm^{-1}]
$3d^5(^6S)4s$	a^7S	3	0.00
$3d^5(^6S)4s$	a^5S	2	7593.16
$3d^44s^2$	a^5D	0	7750.78
		1	7 810.82
		2	7 927.47
		3	8 095.21
		4	8 307.57
$3d^5(^4G)4s$	a^5G	2	20 517.40
		6	20 519.60
		3	50 520.92
		4	20 523.69
		5	20 523.94
$3d^5(^4P)4s$	a^5P	3	21 840.84
		2	21 847.88
		1	21 856.94
$3d^44s^2$	a^3P	0	23 163.27
		1	23 512.00
		2	24 093.16
$3d^5(^6S)4p$	z^7P°	2	23 305.01
		3	23 386.35
		4	23 498.84
$3d^5(^6S)4p$	z^5P°	3	26 787.50
		2	26 796.28
		1	26 801.93
$3d^4(^5D)4s4p(^3P^\circ)$	y^7P°	2	27 728.87
		3	27 820.23
		4	27 935.26
$3d^4(^5D)4s4p(^3P^\circ)$	y^5P°	1	29 420.90
		2	29 584.62
		3	29 824.75
$3d^5(^6S)4d$	e^7D	1	42 253.42
		2	42 254.52
		3	42 256.26
		4	42 258.37
		5	42 261.06
IP: $3d^5$	$^6S_{5/2}$		54 575.63
$3d^44s5s$	g^5D	0	54 646.20
		1	54 671.90
		2	54 818.55
		3	54 986.82
		4	55 209.01
$3d^44s5s$	e^3D	1	54 804.69
		2	54 974.64
		3	55 204.79

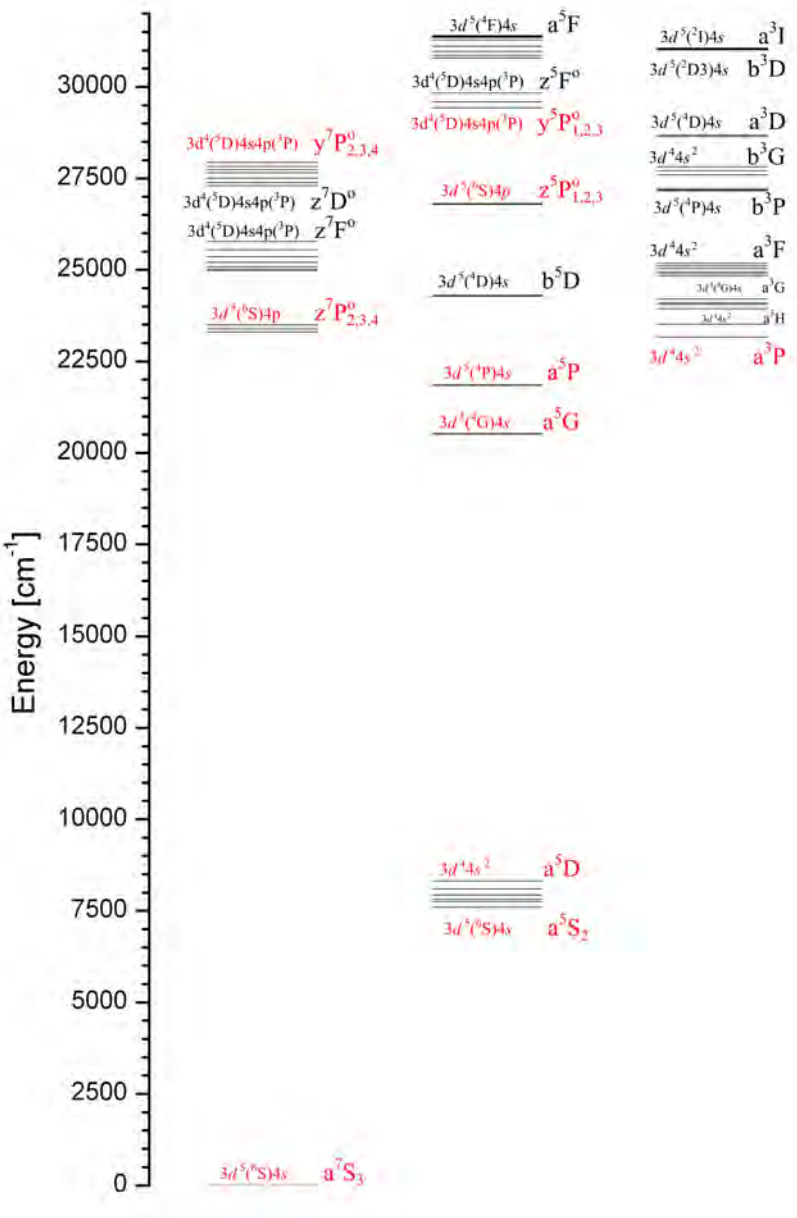

Figure 1.3: Jablonsky Diagram for Cr (singlet states not shown) from the a^7S_3 ground state up to an energy of 32000 cm^{-1}[112]. Levels listed in Table 1.3 are marked in red. The IP of Cr is 54 646.20 cm^{-1}.

Table 1.4: Literature parameters of the strong Cr ground state transitions.
λ ... Wavelength (Air), τ ... Lifetime,
A_{ki} ... Transition probability, P_{sat} ... Saturation intensity

Transition	Energy [109] [cm^{-1}]	λ [112] [nm]	τ [113] [ns]	A_{ki} [112] [1/s]	P_{sat} [104] [W/cm^2]
a^7S_3 - $z^7P^\circ_2$	23305.01	428.972	32.0(9)	3.16E+07	18
a^7S_3 - $z^7P^\circ_3$	23386.35	427.480	32.3(9)	3.07E+07	18
a^7S_3 - $z^7P^\circ_4$	23498.84	425.435	31.4(8)	3.15E+07	18
a^7S_3 - $y^7P^\circ_2$	27728.87	360.533	6.9(2)	1.62E+08	36
a^7S_3 - $y^7P^\circ_3$	27820.23	359.349	7.1(2)	1.50E+08	37
a^7S_3 - $y^7P^\circ_4$	27935.26	357.869	6.3(2)	1.48E+08	37

is one of the most complicated electronic structures that can be found among metal dimers [115, 122]. In the beginning of the theoretical consideration of Cr_2 it was suggested that the two Cr atoms do not bind and that their electrons are located at the two atoms in an antiferromagnetic fashion [114, 123]. Later on, the opposite was shown. The Cr-Cr bonding is one of the most extreme examples of metal-metal bonding with a formal bond order of six [119, 124]. The highly multiconfigurational $^1\Sigma_g^+$ ground state has the dominant configuration $\sigma_{3d}^2\pi_{3d}^4\delta_{3d}^4\sigma_{4s}^2$ (that weighs only 47 % of the total wavefunction)[125, 126]. In the Cr_2 molecule σ bonds are formed by the two s electrons and one pair of d electrons. Furthermore, two π type orbitals and two δ type orbitals are formed by the remaining d electrons which yields the formally sextuple bond and a $^1\Sigma_g^+$ ground state [118] with a magnetic moment of 0 μ_B [127]. Much theoretical effort was put into the study of the Cr_2 ground state, paying particular attention to the bond length, and also a great variety of experimental results were obtained for the dimer. A very short bond length of 1.68 Å [17, 121] with a binding energy of 1.42 eV (11450 cm^{-1})[120] was determined, which is significantly shorter than the bond length in the bulk body-centered-cubic (bcc) structure of 2.5 Å [128]. The $A^1\Sigma_u^+ \leftarrow X^1\Sigma_g^+$ transition energy was determined as 2.7 eV (21 753.2 cm^{-1}[129]) and a $\Delta\nu$=0 transition is favored by the Franck-Condon factor [118]. The transition lies about 1600 cm^{-1} lower in energy than the $z^7P^\circ \leftarrow a^7S_3$ atomic transition, denoting that the $A^1\Sigma_u^+$ state is more strongly bound than the ground state [15, 18]. The ionization potential of Cr_2 was found at 56 435 $\pm$ 8 cm^{-1} [129].

A manifold of absorption lines could be observed for dimers in gas phase or in matrix (see Table 1 of Ref. [119]). E.g., Moskovits et al. [19] concluded a metastable state to be populated after an excitation-relaxation cycle for Cr_2 in matrix, which was attributed to the high spin $^5\Sigma_g^+$ state (a^7S_3, a^7S_3). Such states are of special interest since He_N have the ability to specifically preserve high spin states, which was shown for species on the surface like triplet states of alkali metal dimers [21] and in the interior like

for silver dimers [20]. The lower state population is governed by a random formation process which can in principle also result in high spin states [20, 21]. With their six unpaired electrons per atom, Cr dimers are able to evolve spin states from multiplicity 1 to 13 and are therefore ideal objects to be studied. Elaborate calculations were done by K. Andersson [119] to simulate these lower and some excited state pair potentials (altogether 18), indicating that the interpretation of spectroscopic results might be challenging.

1.7.3 Small Cr_n Clusters

Small Cr_n aggregates are special compared to other 3d transition metal clusters. The growth is strongly controlled by the very robust binding nature of the dimer (see Section 1.7.2). Therefore, odd numbered clusters are formed of dimers plus an isolated atom, and even numbered clusters solely of dimers with strong intradimer- but weak interdimer bonding [22]. This odd-even effect also influences physical properties like the magnetic moment per atom [127] or the dissociation energies [130]. For clusters of n>11 the dimerization effect vanishes and they form in a bcc-like structure with larger Cr-Cr bond distances [22].
The chromium trimer was first examined theoretically by Anderson [131] in 1976 and experimentally by DiLella et al. [132] in 1982. Since then, results about the chromium trimer are somewhat controversial, where a detailed summary can be found in Ref. [133]. Much effort was made to examine the structural properties in theory [134, 135], as well as in experiments, primarily with Raman spectroscopy [132, 136]. Wang et al. [23] described the Cr_3 trimer as a dimer plus a loosely bound atom, having a $(\sigma_{3d}^2\pi_{3d}^4\delta_{3d}^4\sigma_{4s}^2)3d^54s^1$ electron configuration. The orbitals in the parentheses are assigned to the dimer and the attached atom therefore maintains all its six unpaired electrons. DFT calculations by Cheng and Wang [127] are intended to visualize these characteristics.

Small Cr_n clusters are antiferromagnetic, like in the bulk state, with a total magnetic moment of 0 μ_B, 6 μ_B, 0 μ_B, and 4.65 μ_B for n = 2, 3, 4, and 5, respectively [127, 135, 137]. Superparamagnetic properties were found for larger cooled (60-100 K) Cr clusters (n=20-133) by Payne et al. [138] when applying magnetic fields. Q. Wang et al. [24] propose with calculations, that the magnetic moment of small Cr clusters can be extensively increased by the addition of Nitrogen, yielding the total magnetic moment of 9 μ_B, 13 μ_B, 9 μ_B, and 3 μ_B for Cr_nN with n = 2, 3, 4, and 5, respectively. Due to the possibility of tailor made clusters inside He_N, these systems might be of interest for studies of magnetic particles in He_N.

1.7.4 Copper

In ancient times, the most important copper occurrences were on the island Cyprus[11], so it was called *aes cyprium* (Ore from Cyprus) which transformed to *aes cuprum* or *cuprum*. Copper is, besides Gold, the only metal which appears colored under normal conditions[12]. It is of interest because of its broad application in technology where it is also used extensively in electrical wiring and circuitry (approximately 50-60 %). Well known alloys like brass (60-90 % Cu, Zn) and bronze (>60 % Cu, Sn) consist to the largest part of Cu. It has the second best thermal (93.47 % of Ag) and electric (95.04 % of Ag) conductivity of all elements, while the both decrease strongly already with a low degree of impurities. The melting and boiling point lie at medium temperatures[13] of 1356.55 K and 2868.15 K, respectively, and like for Cr (see Section 1.4), copper vapor above the boiling point also contains Cu-dimers (Cu_2) [96, 139].

Cu has two stable isotopes (see Table 1.5) and is the first of the group 11 elements with Ag, Au, and Rg (Roentgenium) that contain a single electron in the outermost electron shell. The Cu electron configuration is:

$$[Ar]3d^{10}4s^1$$

Hence, its outermost shell is isoelectronic to potassium and results in $a^2S_{1/2}$ ground state.

Table 1.5: Abundance of the stable Cu isotopes with their nuclear spin (I).

Isotope	^{63}Cu	^{65}Cu
Abundance	69.17 %	30.83 %
I	3/2	3/2

Parameters of the two strong ground state transitions are listed in Table 1.6 and a Grotian diagram is shown in the results section (Section 3.7). As can be seen from Table 1.6, transition strengths are comparable to those of Cr (Table 1.4). The IP of Cu is 62 317.46 cm^{-1} [112]. Comprehensive tabulated properties of Cu levels and transitions can be found in Ref. [112].

[11] Due to the origin from Cyprus, the Greeks attributed it to the goddess Aphrodite.
[12] Under extremely pure conditions, also Ba, Cs, Ca, and Sr are also bright yellow to golden.
[13] In the field of metallurgy.

Table 1.6: Literature parameters of the strong Cu ground state transitions.
λ ... Wavelength (Air), τ ... Lifetime,
A_{ki} ... Transition probability, P_{sat} ... Saturation intensity

Transition	Energy [112] [cm^{-1}]	λ [112] [nm]	τ [104] [ns]	A_{ki} [112] [1/s]	P_{sat} [104] [W/cm^2]
$^2P^\circ_{1/2}$ - $^2S_{1/2}$	30 535.302	327.396	7.27	1.37E+08	49
$^2P^\circ_{3/2}$ - $^2S_{1/2}$	30 783.686	324.754	7.17	1.39E+08	51

1.8 Photoionization

Photoionization (PI) spectroscopy offers the possibility to investigate the properties of neutral atoms, molecules, and clusters upon excitation with photons that provide sufficient energy to ionize the target species. Advantages are a highly element selective excitation, the broad application on various target species, and a sensible detection due to the availability of efficient ion detectors (compared to, e.g., absorption- or fluorescence spectroscopy) [28]. Ions are usually recorded with commercially available detectors like channeltrons or microchannel plates, that convert an ion count into an electric pulse. The energy required for the detachment of one electron from the neutral is the first ionization energy (ionization potential (IP)), the second ionization energy is required to remove another electron, and so on. The IP is an element specific value that is strongly dependent on the filling of the valence electron shell and increases within one period from the alkali metal atoms to the noble gas atoms. The latter ones, which also include He, have the highest IP because of the fully filled electron shells.

The development of PI came hand in hand with the invention of the laser [140]. For a conventional light source, in the best case an intensity of a few $\frac{W}{cm^2}$ is available. For example, it would take on average 10^5 years to ionize a Xe atom with a two photon ionization of $\lambda = 193$ nm, that has an extremely low ionization rate in the order of $\sim 10^{-13} \frac{1}{s \cdot atom}$. With powerful ultra short pulsed lasers it was easily possible to ionize neutral species [141]. Using a pulse excimer laser (10^5 $\frac{mJ}{cm^2}$, 10 ns pulse duration), an intensity of 10^{11} $\frac{W}{cm^2}$ gives an ionization rate of $10^7 \frac{1}{s \cdot atom}$, which increases the Xe ionization probability to 10 % per laser pulse [141].

1.8.1 Single Photon Ionization

In the simplest case, the target species is excited by one photon from the ground state above its IP. So the electron (e^-) desorbs, leaving behind a positive ion (A^+). Excess energy is transformed to kinetic energy (ε) of the electron according to

$$\varepsilon = \mathrm{h}\nu - E_{IP}, \tag{1.10}$$

with the photon energy hν, and the IP energy E_{IP}. The whole ionization process reads as

$$A(nl) + \mathrm{h}\nu \rightarrow A^+ + e^-(\varepsilon l') \tag{1.11}$$

with n, the principal quantum number and l, the angular momentum of the electron in the bound state, and l', the angular momentum of the electron in the continuum state. For the ionization process $\Delta l = \pm 1$, according to the selection rules [141].

1.8.2 Multi Photon Ionization

The first to describe two photon processes was Maria Göppert-Mayer (1931, a student of Max Born) in her doctoral thesis [141]. Up to now, various ionization schemes were developed, where, according to G.S. Hurst et al. [142], five of them are sufficient to ionize ground sate atoms of all the known elements except helium and neon (see Fig. 4 and the table in Ref. [142]).
Resonance-enhanced multiphoton ionization (REMPI) is the most common case, which refers to the excitation of resonant transitions to intermediate states in advance of the ionization[14]. Due to the well defined intermediate levels the ionization will have a sharp resonance at characteristic photon energies [143]. The final ionization step can either happen nonresonantly into the ionization continuum or resonantly into autoionizing states. The latter open a further channel of increased ionization cross sections for specific photon energies (see Section 1.8.3).
Depending on the number of resonant transitions in these excitation paths, one is able to detect and identify rare isotopes with a relative abundance as low as 10^{-10}. In combination with a mass-selective ion detection (RIMS), the selectivity can be enhanced by factors up to 10^7. Therefore, photoionization spectroscopy is well suited for trace analysis or to analyze low concentrated probes [144]. Even organic samples, where concentrations are low[15] and influence from different other trace metals are dominant in other techniques, can be analyzed with a selectivity of $\geq 10^6 : 1$ [28].

Multi-photon excitation schemes require a relatively high laser fluence, that is easily achievable with pulsed lasers. Whereas for a one photon process the transition rate is proportional to the light intensity I, the rate $R_{\mathrm{ba}}^{(N)}$ for a N-multiphoton process is proportional to I^N [141]

$$R_{\mathrm{ba}}^{(N)} = \sigma_{\mathrm{ba}}^{(N)} \Phi^N \propto I^N \tag{1.12}$$

with the generalized cross section $\sigma_{ba}^{(N)}$ and the photon flux $\Phi = I/\hbar\omega$. To reach ionization saturation, a reasonable photon fluence at the transition frequency ω_{kn} has

[14] To distinguish this method from the non-selective ionization associated with x-rays and radioactivity it was initially called "resonance ionization spectroscopy" by G.S. Hurst et al. [142].
[15] E.g., chromium concentrations in the human body are quite low (<100 ppb) [28].

to be achieved which has to fulfill the condition [140]:

$$\Phi(\omega_{ba})[\frac{photons}{cm^2}] \geq \Phi^{ba}_{saturation} = \frac{1}{\sigma_{ba}} \tag{1.13}$$

Furthermore, the laser pulse duration must be shorter than the lifetime of the intermediate excited states to prevent relaxation.

To study Cr and Cu excitations, almost exclusively two photon ionization has been applied. The two major ionization schemes were used in course of this thesis (see Sections 3.4 and 3.6): one- and two-color resonant two-photon ionization (1CR2PI, 2CR2PI). In the 1CR2PI scheme all photons have the energy, whereas in the 2CR2PI scheme photons with two different wavelengths are involved. Both schemes were also used and described in literature [104]. For Cr, Hess and Harrison [102] used the 1CR2PI scheme when exciting the $y^7P^\circ_{2,3,4}$ state and ionizing the atom from this intermediate state with a second photon of the same color. Ground state excitations to the $z^7P^\circ_{2,3,4}$ state and subsequent ionization with a $\lambda = 308$ nm XeCl laser photon was used by Williams et al. [64] to study Cr in stainless steel samples.

1.8.3 Autoionization and Fano Resonances

Photoionization cross sections are increased by orders of magnitude upon transition to autoionization (AI) levels [143]. Compared to a direct transition to continuum states, the ionization including a resonant transition to autoionizing states has a larger excitation cross section, therefore leading to peaks in the PI spectrum as indicated in Fig. 1.4. The AI state is a doubly excited state, i.e., two electrons are excited at the same time. For an atom in such a state, the IP appears higher in energy than for singly excited atoms. The energy required for the excitation of both electrons is approximately the sum for exciting both individually, so the increase of the IP is simply the excitation energy of the second electron. Energy levels above the usual IP are called autoionizing states and can be populated with a resonant transition. A decay can either happen with the emission of a photon, nonradiative relaxation, or through AI. In the latter case, due to the correlation between the two excited electrons the energy is transferred from one to the other electron. Now, one electron is again in its ground state and the IP is shifted to the original value. The other electron is therefore lifted above the IP and detaches from the atom, resulting in a positively charged ion [145]. Figure 1.5 shows the schematic excitation of a multi electron atom leading to the ionization via an autoionizing state [146].

Overall, excitation of an atom above the IP can lead to three processes. Direct ionization, ionization upon excitation of an AI state, and, in principle, also radiative deexcitation of AI levels has to be taken into account [147]. Schematically this can be

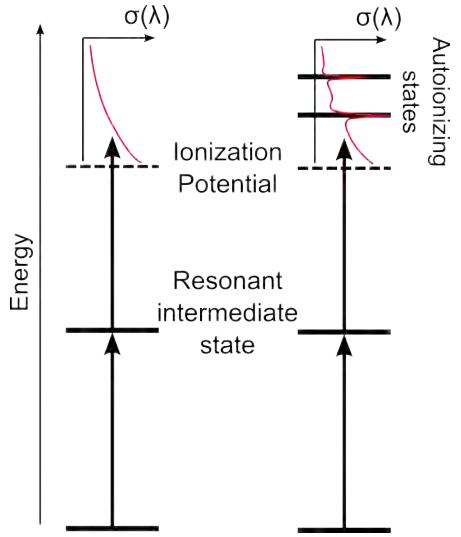

Figure 1.4: Schematic resonant multiphoton ionization schemes. Transitions into the ionization continuum have a decreasing cross section for increasing energies above the IP. Ionization through resonant autoionizing state transitions increase the cross section that adds to ionization through continuum states, resulting in sharp peaks in the spectrum. Inspired by Ref. [140].

described as follows [148]:

$$\mathrm{Cr} + N\mathrm{h}\nu \rightarrow \begin{cases} \mathrm{Cr}^{+} + e^{-} \\ \mathrm{Cr}^{\star\star} \begin{cases} \mathrm{Cr}^{+} + e^{-} \\ \mathrm{Cr}^{\star} + \mathrm{h}\nu \end{cases} \end{cases} \tag{1.14}$$

where N is the number of absorbed photons, $\mathrm{Cr}^{\star}$ a singly- and $\mathrm{Cr}^{\star\star}$ a doubly excited Cr state. Synchrotron radiation is used to excite AI states with a one-photon process [149], while "*two-color ionization schemes are particularly useful to access autoionization levels* [...]"[103] for multi-photon excitation (see Figs. 1.4 and 1.5), which is more

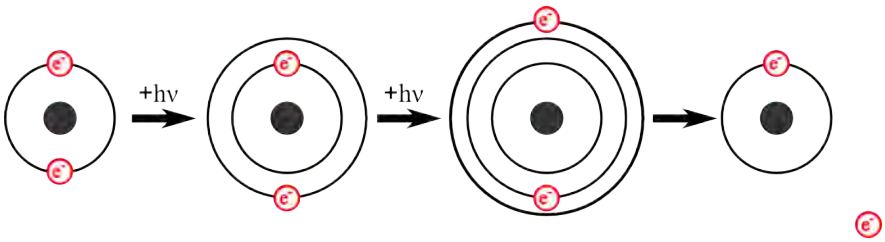

Figure 1.5: Autoionization caused by a two photon excitation. After two valence electrons are excited to energetically higher orbitals, one transfers its energy to the other that subsequently detaches. Based on Ref. [146].

convenient. It is highly improbable to have a system where both the first transition to an intermediate state and the transition to the AI state are of equal energy. Hence, for bare atom spectroscopy AI levels are usually excited by a so called $\omega + \omega_2^{AI}$ process that requires two photons of different energy (ω and ω_2)[104]. Using He_N (see Section 3.4), the broadening of the first transition for a Cr atom inside the droplet and the droplet mediated relaxation to energetically lower states [1, 2], enable the application of a one-color ionization scheme to observe AI transitions of Cr atoms. While scanning the wavelength over the broad, ground state transition band specific photon energies also meet the well defined transition energies from intermediate- to autoionizing states of ejected, bare atoms.

Autoionization peaks in the spectrum can exhibit an asymmetric line profile, which could first be explained by Fano and Cooper in 1961 [150, 151], therefore called *Fano resonances*. Because H. Beutler was the first to observe the asymmetric line shapes in the absorption spectra of atomic gases approximately 25 years earlier [152], they are sometimes called *Beutler-Fano profiles*. Fano resonances do not only appear in autoionizing transitions, but apply to very different fields like plasmonic nanostructures [153, 154], resonators [155] or classical systems [156]. In principle, such resonances occur when a final state can be accessed through different indistinguishable paths, where one of them includes a resonance [141].
When measuring the absorption of an atom above its ionization limit, resonant transitions to the doubly excited state cause peaks that add to on the continuum photoionization (Fig. 1.4). So two ionization paths contribute to the PI in this energy region: ionization through the doubly excited discrete state with a width of ΔE, and directly to the continuum states within the energy ΔE around the AI state. The wavefunction of these superimposed states is [145]

$$\psi(E) = c_1\psi_d(E) + c_2\psi_c(E) \tag{1.15}$$

with the wavefunctions of the discrete autoionizing state ψ_d and the continuum states ψ_c. The transition matrix element for the excitation from an initial state i (energy E_i) to the final state with energy E is [145]

$$M_{iE} = \int \psi_i^*(E_i)\mathbf{r}\psi(E)d^3\mathbf{r} = \int \psi_i^*(E_i)\mathbf{r}[c_1\psi_d(E) + c_2\psi_c(E)]d^3\mathbf{r}. \tag{1.16}$$

For the observed Cr AI transitions in Section 3.4, z^5P° is the initial state (ψ_i) and g^5D and e^3D the discrete doubly excited states (ψ_d). The absorption is proportional to the square of the transition matrix element, which therefore contains the interference term $2c_1M_{id}c_2M_{ic}$ that depends on the phase difference between the two wavefunctions ψ_d and ψ_c. While continuum state wavefunctions have a slowly changing phase, the discrete state wavefunction changes its phase by π when tuning across the resonance (E_0). This leads to constructive interference on one side of the resonance while they interfere

destructively on the other side [145]. Therefore, the peak maximum is shifted from the discrete unperturbed resonance E_0 by a factor F to E_0+F rather than appearing at E_0 [150]. The scattering cross section of the so-called *Fano profile* can be expressed as [145, 150]

$$\sigma_{Fano} = \frac{|(\psi(E)|R|\psi_i(E))|^2}{|(\psi_c(E)|R|\psi_i(E))|^2} = \frac{(q+\varepsilon)^2}{(1+\varepsilon^2)} = 1 + \frac{q^2+2q\varepsilon-1}{(1+\varepsilon^2)} \tag{1.17}$$

$$q = -\frac{D_1}{D_2 R_{12}}, \qquad \varepsilon = \frac{E-E_0}{\Gamma/2} \tag{1.18}$$

with ε, the reduced energy, E_0 the resonant energy, Γ the full width at half maximum of the resonance line, and the phenomenological shape parameter q. Figure 1.6 shows some resonance profiles for q values from zero to two. Overall, there are three special cases of resonance profiles [150]:

- $q = 0$ Antiresonance characteristic with a dip through at the resonance energy
- $0 < q < \infty$ Asymmetric resonance
- $q = \infty$ Lorentzian shaped resonance (typical for oscillating systems)

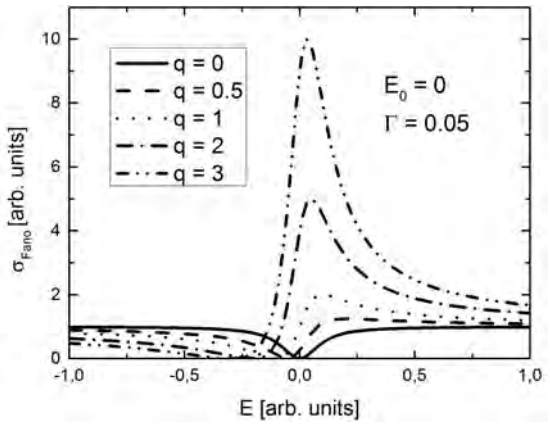

Figure 1.6: Fano resonance profiles for different line shape parameters q.

The phenomenological shape parameter q is determined by the transition strength to the bound state D_1, the transition strength to the continuum state D_2, and the coupling between these two states R_{12}. The product D_2R_{12} yields the transition amplitude to access the continuum state via the autoionizing state [145].
The lifetime of the autoionizing state τ is primarily determined by the autoionization rate into the continuum, that depends on the coupling to the continuum states. Values for this decay lie in the order of $\tau = 10^{-12}$ s, which is orders of magnitude shorter than for radiative decay to energetically lower states. The latter is therefore only of minor significance in this process [145]. Compared to levels which can only decay by radiative transitions, the short lifetime of AI states causes an increased transition

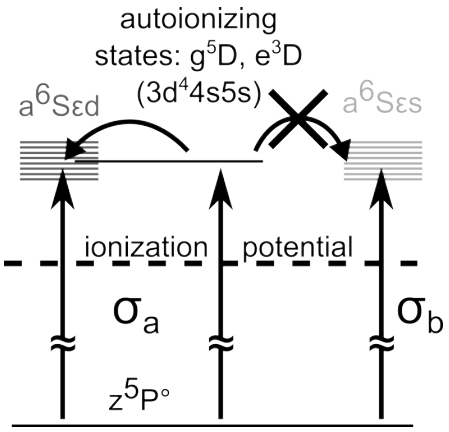

Figure 1.7: For Cr, the $a^6S\varepsilon d$ continuum states interfere with the g^5D and a^3D autoionizing states that are responsible for the Fano resonance (σ_a). Transitions to the $a^6S\varepsilon s$ continuum state are not affected by the interference and lead to an almost constant background signal (σ_b).

linewidth [140, 157].
In the ionization process, a second path, which includes the continuum states that do not interact with the AI states, is added to the Fano resonances. Because the angular momentum has to be preserved through the AI process, transitions into continuum states are restricted by the angular momentum selection rule. This results in two paths with the cross sections σ_a and σ_b, that are illustrated for Cr in Fig. 1.7. From the g^5D and e^3D ($3d^44s5s$) states, only transitions to the $^6S\varepsilon d$ continuum states are allowed ($\Delta l = \pm 1$). ^6S ($3d^5$) is the ion ground state, ε the kinetic energy of the electron, and d the angular momentum of the electron. This causes an overall ionization cross section of [150, 151]

$$\sigma = \sigma_a \left[\frac{(q+\varepsilon)^2}{(1+\varepsilon^2)}\right] + \sigma_b, \qquad \varepsilon = \frac{E - E_0}{\Gamma/2} \tag{1.19}$$

with the Fano resonance as first term. σ_b reveals a constant offset in the ionization spectrum that is not affected by the interference with discrete states.

1.9 Dissociation and Predissociation

He_N were doped with atoms and molecules, that can both be excited into energetically higher states with the absorption of a photon. The energy difference between two atomic states is well defined, like molecular transitions between two bound states that show discrete vibrational absorption bands. In contrast, photon energies exceeding the

molecular dissociation limit lead to a continuous absorption and fragmentation of the molecule. For states, which have a purely repulsive potential energy surface (PES), the process is called *direct dissociation* [158, 159]. The *photodissociation* process can be expressed as [158]

$$AB + N_{photon}\mathrm{h}\nu \rightarrow (AB)^{\star} \rightarrow A(\alpha) + B(\beta) + E_{trans} \tag{1.20}$$

where AB accounts for the parent molecule, N_{photon} the number of absorbed photons, $(AB)^{\star}$ the excited molecule before it breaks apart, and $A(\alpha)$, $B(\beta)$ the two fragments. The fragments are detected in the states α and β, assigned to the separate limit quantum states of the corresponding potential [159]. The excess energy is converted to kinetic energy (E_{trans}) of the fragments. It was shown for molecules in matrixes, that the separation process can be hindered with the dissipation of kinetic energy by the matrix. So, either the fragments are caged in one cavity and immediately recombine [160], or loose the kinetic energy, they penetrate the matrix until they thermalize and afterward recombine [81, 161].
Also for discrete absorbed photon energies, fragmentation can occur and the fragments are observed in the limit states of an energetically lower PES. When the molecule is excited into a bound state that can undergo a nonadiabatic transition to energies above the dissociation limit of a second state, it is called *indirect dissociation* or *predissociation* (Herzberg Type I, electronic predissociation, Fig. 1.8). The nonadiabatic transition involves the coupling of nuclear and vibronic motion, i.e., a break down of the Born-Oppenheimer approximation [159] ("*another way to express this state of affairs is to say that predissociation occurs on account of "tunneling"*"[162]). Because the states have to couple, not all bound states that have a higher energy than another state's continuous range of energies automatically predissociate. So, according to the Franck-Condon-Principle, both states have to be equal in total energy as well as in core distance at the crossing point. Crossing points can arise from avoided and real level crossings. A strong coupling between the two states can either be vibronic or purely electronic, like conical intersections. When there is no actual crossing and only very small coupling between the states, the transition can be enabled by a high density of vibrational states of the energetically lower state [61, 159, 162, 163].
The predissociation rate depends on the overlap of the vibrational wavefunctions of both states (the wavefunction of the dissociating state can be described with an Airy-Function), and is estimated from the absorption line broadening, the lifetime measurements of the excited state, or observation of fluorescence from the separate atom limit states. A maximum is found at the crossing point of the two potential curves resulting in sharp predissociation maxima. An overlap can also be present at the repulsive parts of the wavefunctions, where normally the PES are narrow but do not cross. In this case, the predissociation rate has no defined maximum but increases up to the direct dissociation of the energetic higher state [61, 163, 164].

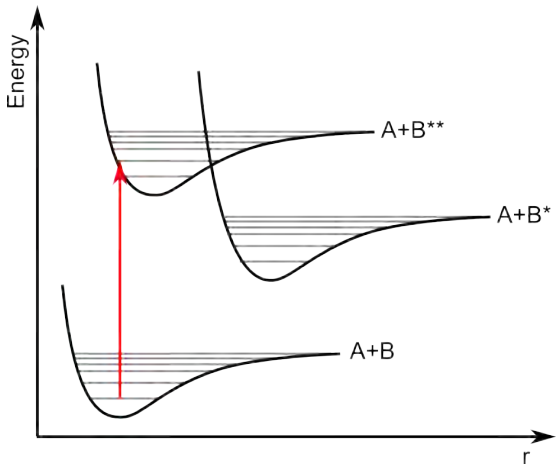

Figure 1.8: Example for a Herzberg Type I predissociation: After excitation (upwards pointing arrow) from the molecular ground state (separate limit states A+B) to the excited state (A+B**), nonadiabatic transition to the continuous range of energy levels of an energetically lower state leads to fragmentation into A+B*.

In analogy to Section 1.8.3, when the final state continuous range of energies lies above the molecule's first ionization potential, the predissociation process leads to ionization of the molecule. G. Herzberg called this "*phenomenon pre-ionization, in analogy to the term predissociation. However, many authors prefer the name autoionization.*" [162]

Besides the Herzberg Type I, also Herzberg Type II and III predissociation exist, which are not considered to be relevant for the results presented in Section 3.10. In the Herzberg Type II and III predissociation only one PES is involved. It has a potential well at close core distance and an energy barrier that blocks the dissociation channel. The latter can be caused by an avoided crossing with another state. The photon excites into a quasi-stable state inside the potential well, which can decay by either tunneling through the barrier (the only possibility for $\nu = 0$) or, if more than two atoms of the molecule are involved, the internal vibrational energy redistribution between various nuclear degrees of freedom lifts the molecule above the barrier. The latter case is also applicable to rotational energy surfaces, which is then called Herzberg Type III [158, 159, 162].

2 Experimental

In this chapter the experimental setups and procedures are elucidated. The Cluster Laboratory II (CLII)[1] with the He_N apparatus was set up by Markus Koch and Johannes Lanzersdorfer in course of their dissertation and diploma thesis, respectively. Therefore, solely parts and measurement techniques that were added to the setup or utilized for the first time are treated in more detail. The apparatus, the nozzle, and the laboratory are described briefly and the reader is referred to Refs. [51, 165, 166] for details.

2.1 Helium Nanodroplet Apparatus

The He_N apparatus consists of four differentially pumped vacuum chambers (typical vacuum pressures are listed in Table 2.1), each forming a group named after the designated function (see Fig. 2.1). He_N are produced in the source chamber (SC), doped in the pick-up chamber (PC), and analyzed by laser induced fluorescence (LIF) in the measurement chamber (MC). In a small separately pumped vacuum chamber attached to the end of the MC, a quadrupole mass spectrometer (QMS) (Balzers QMG 422) is located for mass analysis of the doped He_N. These detection systems enable to use the methods of beam depletion (BD), where after a resonant laser excitation of the dopant a decrease in the number of droplets arriving at the QMS is detected, undispersed LIF with a photomultiplier tube (PMT), dispersed LIF with a monochromator/spectrograph, or REMPI, where the dopants are photoionized and mass selectively analyzed. To provide a constant laboratory operation, a maintenance plan was created which can be found on the enclosed DVD ('Maintenance_CLII.docx').

2.1.1 Helium Nanodroplet Formation

He_N are formed by the supersonic expansion of high purity ^4He (99.9999 %, Grade 6.0, AirLiquide) through a closed cycle refrigerator (cold head: Leybold RGD1245,

[1] Address: Petersgasse 16, 8010 Graz, Room PHEG104

Table 2.1: Typical chamber vacuum pressures.

Chamber	p [mbar]
SC	$1.0{\cdot}10^{-4}$ - $1.5{\cdot}10^{-4}$
PC	$2{\cdot}10^{-6}$ - $7{\cdot}10^{-6}$
MC	$2{\cdot}10^{-7}$ - $1{\cdot}10^{-6}$
QMS	$5{\cdot}10^{-8}$ - $1{\cdot}10^{-7}$

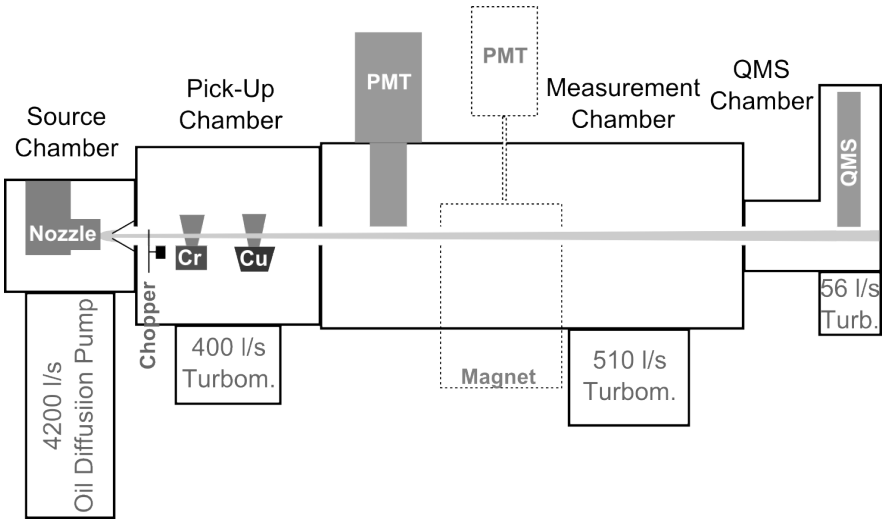

Figure 2.1: Schematic drawing of the helium droplet apparatus with the four separately pumped vacuum chambers. He_N are formed by the nozzle and doped with Cr or Cu atoms from the evaporation sources. The beam can be chopped for differential counting with the PMT or QMS. The position of the magnet and PMT, used for ESR measurements in Ref. [167], are indicated with dotted lines.

compressor: Leybold RW 4000 EU) cooled nozzle[2] with an orifice diameter of 5 μm. The stagnation pressure was set to 50 bar for all experiments. Nozzle temperatures are adjusted according to the required droplet size distribution in the range of 11 - 24 K (for droplet sizes see Section 1.3) with a proportional-integral-derivative (PID) controlled resistive heater. The source chamber is pumped by a 4200 l/s baffled oil-diffusion pump (Varian, HS 10) backed with a roots- (Leybold Ruvac WS500) and rotary vane (Alcatel T2100 SD) pump.
The center fraction of the He_N beam is extracted by a molecular beam skimmer[3] (d = 300 μm), and the collimated beam passes on to the pickup chamber where the high temperature evaporation sources are located. A rotating chopper wheel can interrupt the He_N beam periodically for differential measurements. The background signal, recorded when the chopper blocks the He_N beam and therefore hinders the transportation of the examined species to the detectors, is subtracted from the signal recorded when the chopper does not interfere the He_N beam. This differential measurement scheme was primarily used for electron-impact ionization recorded mass spectra, but neither for BD-, LIF-, nor PI experiments.

2.1.2 Helium Nanodroplet Doping with Crossed Beam Pick-up Sources

In the PC, the He_N beam passes regions filled with metal vapor to pick-up single atoms (Fig. 2.2). Two crucibles are used to evaporate bulk Cr and Cu. These are referred to as *high temperature evaporation sources* to distinguish them from low temperature sources used for the evaporation of alkali- and earth-alkali metals[4].
The Cr electron-bombardment evaporation source is described in detail in the master thesis and publication of Martin Ratschek [65, 169]. In brief, a tantalum crucible is isolated thermally and electrically from the common ground with two ceramic rods (Fig. 2.3). Below the crucible two heated filaments are located that emit electrons. These are accelerated toward the bottom of the crucible by a potential difference of 1 kV between the filaments and the crucible. Oven heating powers are adjusted by the filaments' electron emission current. The latter is dependent on the filament temperature that is controlled with the voltage across the filament pins. Bulk Cr inside the crucible is heated to temperatures in the range of 1300°C - 1700°C [65], which is lower than the melting point of Cr [96], but still sufficient to reach the required vapor pressure for single- and multi-atom doping (see Section 1.4). Heating loads in the order of 130 W - 200 W are used and have to be adjusted for every experimental run by recording the pick-up statistics (Cr^+, Cr_2^+,... ion yield as function of the heating power) with the QMS with

[2] The nozzle is connected to the cold end of the expander's second stage in a so-called Gifford-McMahon cycle that uses helium as a working medium [168].
[3] A thin walled cone with an orifice at the narrow end.
[4] For some preliminary experiments on Cr-Rb doping, also a low temperature pickup cell (see Ref. [51]) was in operation.

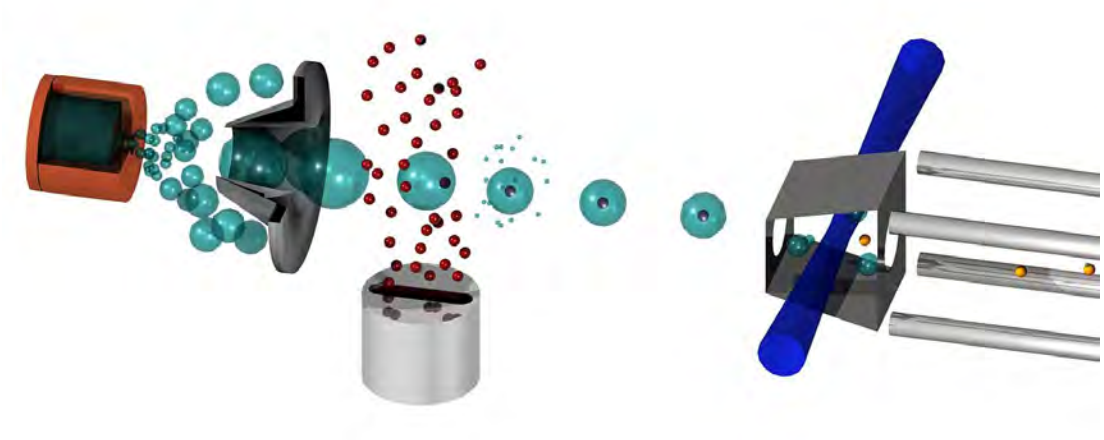

Figure 2.2: He_N (turquoise spheres) are formed by expanding ^4He through the nozzle (brown cylinder). The skimmer (grey cone) forms a beam that is doped with atoms (red spheres). These are evaporated from a heated crucible (gray cylinder) in a crossed pickup geometry. For PI measurements, the dopants can be photoionized with a laser (blue cylinder), extracted, and analyzed with the QMS (silver rods).

electron ionization (see e.g., Fig. 3 in Ref. [65]). The crucible is covered with a slitted lid that reduces the metal flow to the volume of the He_N beam and therefore decreases the contamination of the pick-up chamber. To prevent a heat-up of the vacuum chamber, radiation is dissipated by a cylindrical water cooled shield that encloses the crucible. The top of the shield is positioned between the crucible and the He_N beam and the Cr atoms emit through a slit in the cooling shield. Since this evaporation source is more difficult to operate than a low temperature oven, some practical instructions are provided in the Appendix B.2.

In collaboration with Alexander Volk and Markus Koch[5], a resistively heated evaporation source was engineered and built. A description of the Cu source layout and functionality can be found in the master thesis of Friedrich Lindebner [170]. Bulk Cu is filled in an alumina coated tungsten wire basket that is mounted between two copper blocks. These are connected to a high current power supply (EA-PS 9080-100), and ~300 W of electric power heat the crucible to temperatures around 1000°C [170]. The basket is again covered with a slitted lid where the atoms are emitted. Because of geometrical issues, here the He_N penetrate the cooling shield cylinder of the Cu source through two holes.

Both sources are designed in a crossed beam layout, meaning that the He_N beam is

[5]The majority of engineering was done by Alexander Volk.

Figure 2.3: Tantalum crucible of the Cr electron bombardment evaporation source. The crucible is covered with a reusable molybdenum lid where the Cr atoms are emitted through the slit. The short ceramic tubes at the ends of the long tube prevent them from being coated with metal.

crossed at almost right angles by the metal atoms. In contrast to other layouts where the He_N beam passes through the cells [165, 167], the crossed beam layout ensures that no free atoms originating from the evaporation sources can reach the detectors. Between the lid of the Cr source and the He_N beam the cooling shield is introduced and the lid of the Cu source is located approximately 10 mm below the He_N beam axis. The He_N beam has to pass baffles along the flight path from the source to the detectors. These are the chamber wall between pick-up and main chamber (hole radius $r = 2.5$ mm), the first LIF detector apertures ($r = 3$ mm) (see. Section 2.4.3), a microwave cavity ($r = 2$ mm), a LIF detection system ($r = 2.3$ mm), and the chamber wall between main chamber and the QMS chamber ($r = 3.8$ mm) [51]. All these baffles are positioned along the ∼1.4 m long flight path of the droplet beam to the QMS (for details see Ref. [51]), blocking all atoms originating from positions off the He_N beam axis.

2.1.3 Detectors

LIF is either recorded with a PMT or a monochromator attached to a fluorescence collection system. The excitation laser beam intersects the droplet beam at right angles and excites a resonant transition of the dopant atoms that subsequently emit fluorescence. The emitted light is collected and guided into the detector, as described in Section 2.4.3.
A QMS (Balzers, QMG 422), attached to the end of the measurement chamber was used for PI, BD, and electron impact ionization mass spectrometry. For PI, the electron source was switched off, whereas for BD and mass analysis the doped droplets were ionized with electrons from the QMS electron impact ionization source. Ions produced

in either case are extracted by an electric field, analyzed in the quadrupole rod system, and detected with a secondary electrons muliplier (SEM). When ionizing with the electron impact ionization source for detailed mass scans, the QMS parameters provided by the manufacturer are well chosen. For BD, where mass resolution is not that critical for the results, or PI, that dramatically changes the ionization process, empirical values were found which improved the signal by a factor of up to 6. The disadvantages are that the mass peak maxima are slightly shifted and not that well separated anymore, which does not have a significant influence on the results. The empirically determined QMS voltages are listed in Table 2.2.

Table 2.2: QMG 422 voltages for electron impact ionization (provided by the manufacturer for optimal resolution), BD (off-axis mounting), and PI (electron-source switched off).

Parameter	Manufacturer	BD	PI
V01	100	88	53
V02	70	70	60
V03	15.75	15	11.00
V04	9.00	10.5	6.25
V05	300	260	350
V06	300	300	330
V07	110	110	120

2.2 Pulsed Dye Laser

A pulsed dye laser (Lambda Physik, FL3002, specifications listed in Table 2.3), pumped with a XeCl excimer laser (Radiant Dyes, RD-200), is used to obtain laser pulses in the wavelength range of λ = 345 nm - 530 nm (dye laser), 315 nm - 330 nm (frequency doubled dye laser), and 308 nm (XeCl laser). The RD-200 is a very powerful excimer lasers with a repetition rate of up to 100 Hz and a nominal energy of up to 200 mJ per pulse[6].

The 308 nm beam is guided into the FL3002 Lambda Physik dye laser where it is split up in several parts. The first fraction pumps the oscillator. It consists of the lower part of a 20 mm dye cell, an end mirror, and a patented Lamda Physik grating setup [171] that determines the wavelength and should yield low amplified spontaneous

[6]Unfortunately, only about 90 mJ were reached which could have different reasons like the premixed operation gas, the fogging outcoupling mirror in the cavity, or simply a not practicable specified maximum output. The fogging mirror was cleaned which led to an increase from 30 to 90 mJ.

Table 2.3: Lambda Physik FL3002 Dye Lasers specifications [172].

Pulse energy	up to 15 mJ
Bandwidth	0.2 cm^{-1} (330-860 nm) Littrow-type oscillator (grating only)
Wavelength range	322 - 970 nm
Second harmonic generation	217 - 348 nm
Beam	divergence 0.5 mrad (typ.), diameter 2.5 mm (typ.)

emission (ASE). The monochromatic pulses are then guided into the upper part of the cuvette, used as preamplifier. There, the laser pulse is amplified before it reaches the main amplifier, a separate 40 mm dye cell. All three parts - the oscillator, preamplifier, and amplifier - are pumped by fractions of the 308 nm XeCl laser.

The problem using the FL3002 dye laser in the blue or UV region is the high ASE occurring when the grating should select wavelengths from the boundaries of the dye tuning ranges. Special caution should be given to ASE predominantly if the laser is optimized to maximum power output instead of low ASE (see also Ref. [172]). This can be seen in Fig. 2.4 where the laser is set to different wavelengths and the laser spectrum is recorded with a monochromator (either with the "SpectraPro250" for detailed scans or the "Ocean Optics USB 500" for live monitoring). A video of a wavelength scan can be found on the enclosed DVD ('Measurement_Video.avi'). An additional increase of ASE might be caused by the fondly called "Lambda Spot" [173]. Due to the high energy density on the grating, partial thermal destruction of the grating was caused in the early days of the laser that can reduce the wavelength selectivity and is typical for this type of laser. Significant misinterpretation of spectra can be caused when neglecting the ASE, as was investigated and documented by Lambda Physik [174] after Nogar and Keller [175] found weak sidebands in their R2PI spectra of Lu and blamed it on the laser.

The pulsed dye laser, used for examining Cr in He_N, was also used for BD and PI experiments on Cu atoms doped to the droplets. While photon energies obtained directly from the dyes (c.f. Table 2.3) are sufficient to excite the lowest strongly allowed ground state Cr transitions ($z^7P^\circ \leftarrow a^7S_3$, $y^7P^\circ \leftarrow a^7S_3$), the Cu ground state excitation (c.f. Fig. 3.22) requires photon energies close to the XeCl pump laser that are not directly accessible with the dyes. Therefore, second harmonic generation in a KDP crystal was used to double the frequency of the dye laser (dye: DCM). The crystal tilt angle has to be adjusted for every wavelength to meet the crystal phase-matching angle, which unfortunately causes problems in the ability to scan the wavelength and steering of the output laser beam[7]. For optimum energy outputs, scripts were implemented in the laser

[7] A detailed description of the solutions to overcome these problems can be found in the Master Thesis of Friedrich Lindebner [170]

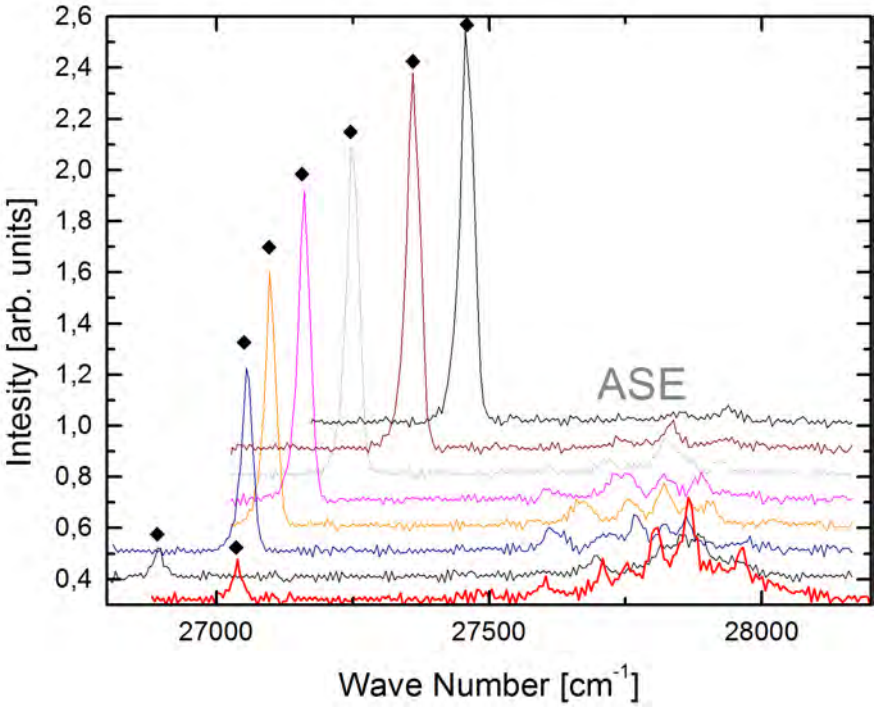

Figure 2.4: Laser spectra of the Lambda Physik FL3002 dye laser (dye: RDC360neu) recorded with a monochromator (SpectaPro250). The grating was set to different wavelengths (plots mutually shifted in vertical direction, laser marked with squares) where at the boundaries of the laser dye tuning range significant ASE appears at the central wavelength.

control program (Section 2.6.2) to automatically adjust the crystal tilt angle.

2.3 Beam Depletion

The ground state excitation spectra of the dopants were recorded, in addition to one and two color REMPI and LIF, with mass selected beam depletion (BD) (results in Sections 3.1, 3.2 and 3.9). When dopants inside the He_N are electronically excited by the laser photons, they are either ejected from the droplet (see Sections 3.1 and 3.4, [1, 2]) or transfer the excess energy to the droplet that is subsequently destroyed or shrinks upon evaporative cooling of He atoms from the surface. So, after a resonant excitation with the laser a reduction of dopants and He_N can be measured with the QMS (electron impact ionization). For Cr and Cu doped He_N it was found that a detection on the dopant mass is the most efficient method.
For BD, the laser beam can in principle be orientated either perpendicular or counter-propagating to the He_N beam. With a continuous wave (cw) laser, the He_N beam is constantly depleted which allows an efficient detection of the signal for a perpendicular orientation. In contrast, the laser beam should counterpropagate the He_N beam for pulsed lasers. In a perpendicular alignment the laser pulse would only interact with dopants that are present in the interaction volume during the short laser-on time, since relative to the laser pulse the He_N droplets are almost not moving. A counterpropagating orientation of the laser beam and the He_N beam increases the interaction volume to a maximum and enables to use the pulsed laser (Lambda Physik, FL3002) in this setup (Fig. 2.6). A ∼25 ns laser pulse (length ∼7.5 m) has the chance to excite the dopants along the whole He_N beam length. The He_N beam travels with approximately 400 m/s toward the QMS, which is located ∼1.4 m away from the source. Doppler shifts due to the propagation of the He_N in direction of the laser can be neglected because of the broad excitation features caused by the influence of the matrix (Section 1.5). As a result of the long interaction length of laser and droplet beam and the relatively slow velocity of the He_N beam, depletion can be recorded up to approximately 3 ms after the laser pulse (c.f. Fig. 2.5). To account for instabilities from the He_N- and evaporation source, a reference signal (same gate length) during the laser-off period was taken shortly after the full section of the depleted droplets has arrived at the detector. The depletion is evaluated from[8]

$$BD = Counts_{\text{Reference}} - Counts_{\text{Depleted}}. \tag{2.1}$$

The trigger for both gates is obtained from a fast photodiode and fed to a 2-channel digital counter (Stanford Research, SR400) that records the signal. The Cu depletion signal as a function of delay time between 0 and 7 ms after the trigger is shown in Fig. 2.5. The time scale shows a constant offset because of the setup-specific delay times.

To enable the laser beam to be guided counter-propagating to the He_N beam, the QMS

[8] Mind that the usual calculation of a background correction in the sense of $BD = Counts_{\text{Reference}} - Counts_{\text{Depleted}}$ yields a negative value.

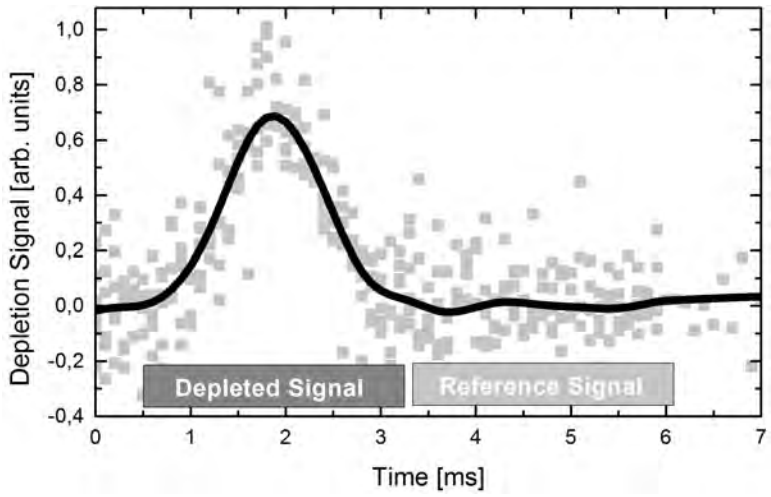

Figure 2.5: Time dependence of the Cu BD signal ($^2P^\circ_{1/2,3/2} \leftarrow ^2S_{1/2}$ excitation, $\tilde{\nu} = 57680\text{cm}^{-1}$). Typical counting gates for the depleted- and reference signal are indicated with gray boxes (c.f., Eq. (2.1)).

has to be orientated perpendicular to the He_N-laser beam axis because of geometric reasons. The Balzers crossbeam ion source has only one axis that does not interfere with any element of the QMS, which has to be in direction of the He_N- / laser beam. A vacuum chamber element was adapted to meet this geometric requirement and provides QMS alignment, a mount for the laser entrance window, and to attach a small (56 l/s) turbomolecular pump. A picture of the setup is shown in Fig. 2.6b and the technical drawings are provided in the Appendix A.1. In the experimental setup, the laser beam is guided from CLI toward the He_N-apparatus in CLII (see Fig. 2.6a). At the end of the measurement chamber, a cushion mounted marble slab is mounted to the frame of the apparatus. On the marble slab a mirror is fixed to guide the laser beam through a 2" 2° wedged fused silica window (Laseroptik, S-00994) counterpropagating to the He_N beam. Crude laser beam alignment was achieved with aid of the chopper wheel that is observed through a window on top of the pick-up chamber. Because the Cr-evaporation source cooling shield blocks the view to the chopper due to geometric reasons, a mirror was mounted inside the vacuum chamber. For proper antiparallel alignment the laser beam passes all apertures of the He_N beam and illuminates the closed chopper. Fine tuning of the beam path was done by steering the laser beam and simultaneously monitoring the depletion signal, which in most cases showed that a relatively good alignment was achieved already with the crude method.
The laser beam diameter is adjusted to the size of the apertures along the He_N flight path to maximise the overlap with the He_N beam. The laser fluence has to be kept low to reduce saturation effects. In Fig. 2.7, the Cr beam depletion signal for the $y^7P^\circ \leftarrow a^7S_3$ absorption is plotted in dependence on the laser power. The saturation laser fluence

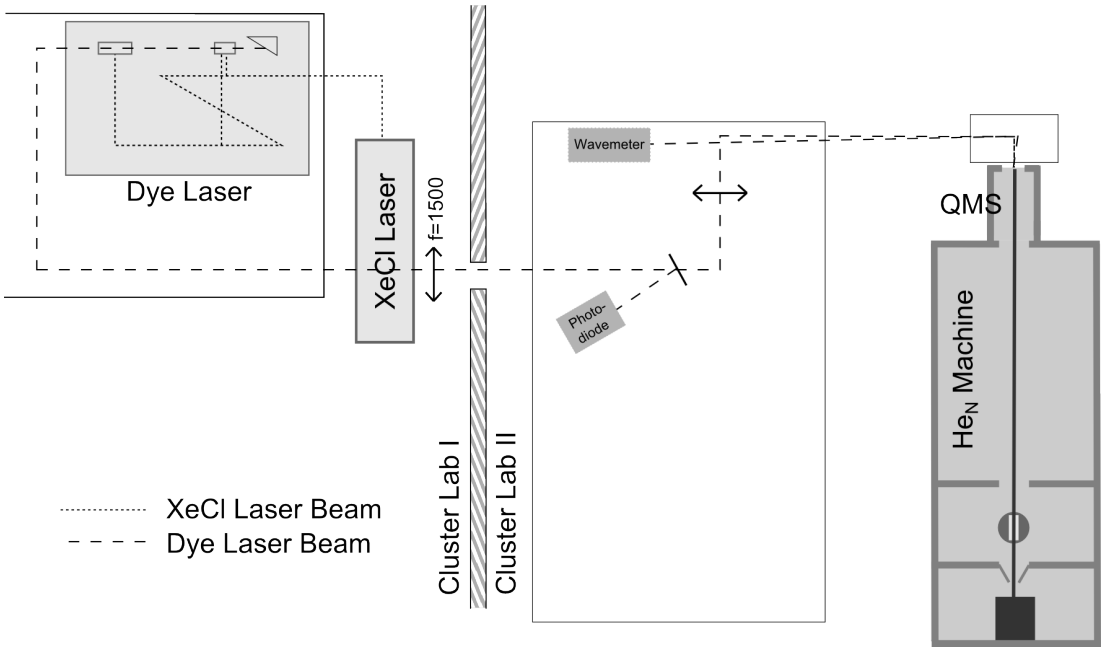

(a)

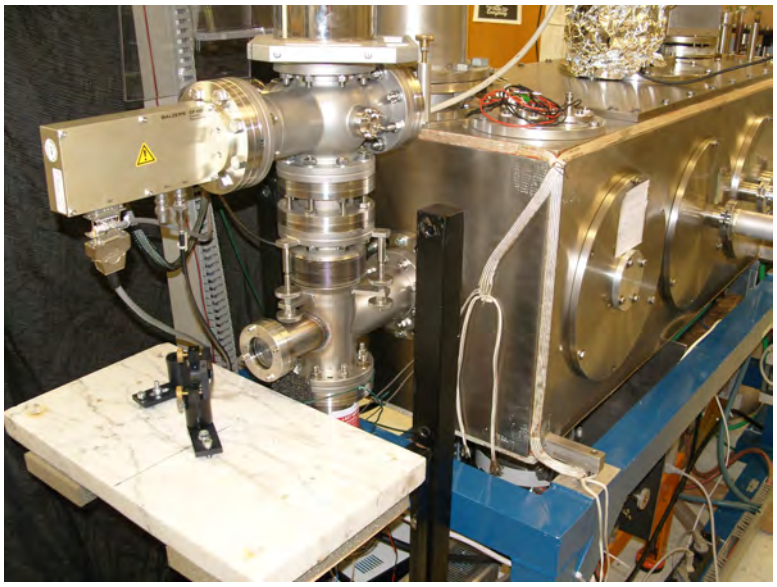

(b)

Figure 2.6: (a) Schematic setup for BD. The dye laser beam is transferred from CLI to CLII and counterpropagates the He_N beam. A reflex from a glass plate yields the trigger pulses for the counter. When possible, laser wavelengths were monitored with the pulsed wavelength meter from the laser reflex of the vacuum chamber entrance window. (b) Photograph of the QMS in the BD orientation. The laser beam is guided by the mirror (a cushion mounted marble slab is used to reduce vibrations) antiparallel to the He_N beam.

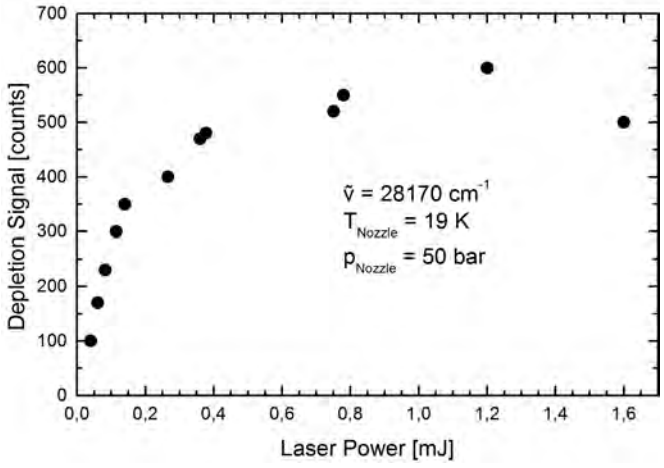

Figure 2.7: Saturation of the Cr in He_N $z^7P^\circ \leftarrow a^7S_3$ transition measured with beam depletion ($\tilde{\nu} = 28170 cm^{-1}$).

was estimated as approximately 1 mJ/cm^2 (with a beam cross section of 13 mm^2). Even when the width of the excitation band is considered, giving rise to an increased saturation fluence, this value seems very high regarding the bare atom ground state transition saturation intensity (Table 1.4). Hence, thes values should only be taken as a reference.

Depletion signals were recorded on the mass of the dopants, which enables a direct assignment of the absorption spectra to one specific species. When observing the decrease in ion counts on the mass of He, He_2, Cr, or CrHe, only a significant depletion was detected for Cr and He_2. Although the observation of the He_2 depletion was used by another group [176, 177], this signal was less pronounced than the dopant decrease. Reasons might be the reduced energy transfer to the droplet because of the efficient ejection (see Chapter 3), or experimental issues like the vacuum pressure in the QMS chamber (10^{-7} - 10^{-8} mbar) or doping of only a minor fraction of the He_N (all undoped droplets arrive at the detector).
Fig. 2.8 shows the Cr^+ depletion signal after the Cr $y^7P^\circ \leftarrow a^7S_3$ excitation for different nozzle temperatures (i.e., He_N sizes). The best depletion signal is obtained for nozzle temperatures around 20 K. A shift between the maxima of the absolute- and the depletion signal is observed, attributed to the droplet size dependence of the ejection mechanism being responsible for the depletion (see Section 3.2 for details).

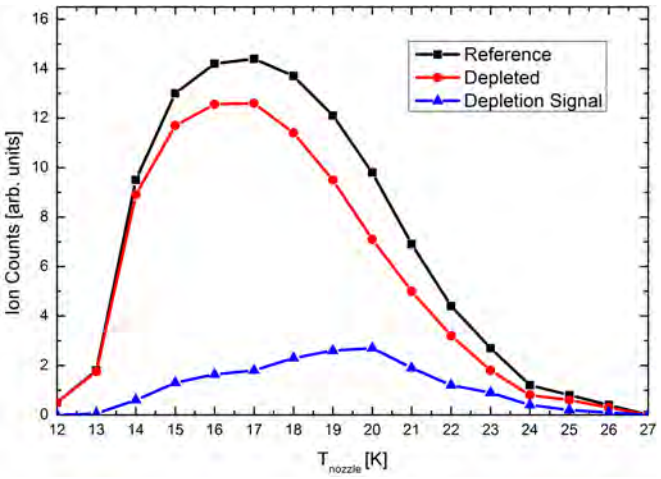

Figure 2.8: Absolute Cr^+ (m = 52 u) count rates of the reference- and depleted ($y^7P^\circ \leftarrow a^7S_3$ excitation, $\tilde{\nu} = 28\,170$ cm^{-1}) signal for different nozzle temperatures (i.e., droplet sizes). Equation (2.1) yields the absolute Cr^+ depletion signal.

2.4 Laser Induced Fluorescence

Cr atoms doped to He_N were resonantly excited into energetically higher electronic states. Subsequently, the atoms can relax radiatively to lower states upon emission of a photon. To detect this fluorescence, the emitted photons are collected over a large solid angle and guided toward a detector[9]. For undispersed LIF measurements a PMT was used as detector. Integrating photons over a wide energy range with a large detector yields a high sensitivity that enables the use of pulsed lasers (low pulse/pause ratio). By contrast, dispersed LIF allows the clear assignment of emission channels but required the use of a cw laser for detailed studies (low signal to noise ratio dispersed fluorescence measurements after the strong Cr $y^7P^\circ \leftarrow a^7S_3$ transition were also be performed with the pulsed laser). For first tests a monochromator with an attached photomultiplier was used which had a high detection efficiency but low resolution. Exact measurements were carried out with a cooled CCD camera attached to a spectrograph.

2.4.1 Undispersed Fluorescence

The strong fluorescence yield from Cr doped He_N after the $y^7P^\circ \leftarrow a^7S_3$ excitation enabled the observation of the undispersed LIF upon excitation with the pulsed dye laser. The pulsed dye laser has the ability to continuously scan wavelengths across the dye range (a scanable cw laser was not available in this wavelength region). The laser beam is

[9] The whole assembly is called *LIF detector* from now on.

guided from CLI to the He_N apparatus, in analogy to the BD and PI measurements (described in Sections 2.3 and 2.5). The laser crosses the He_N beam at right angles in the fluorescence collection region, where, because of the low laser beam quality, stray light is the dominating factor. The beam quality could be increased by introducing apertures on the way from CLI to CLII and baffles in the LIF detector baffle tube (see Fig. 2.10). Furthermore, the laser fluence has to be kept in the order of a few μJ per pulse by only using the dye laser oscillator and preamplifier.
Two different photomultiplier tubes were used for the measurements, depending on the characteristics required. Both were cooled to around -15°C with a Peltier cooled photomultiplier housing (TE-104TS-Rf). An EMI '9558 QB' photomultiplier (46 mm active diameter, 10 ns pulse rise time, 22 ns pulse full width at half maximum (fwhm) [178]) was chosen for single photon counting because of the matching spectral range with the Cr transitions and a large cathode for simple spatial adjustment. Time dependent fluorescence decay was measured with a fast response PMT (EMI 9863/350 QB, 9 mm active diameter, 2 ns pulse rise time, 3 ns pulse fwhm [178]). To separate the emission channels, fluorescence filters were introduced in front of the PMT. Spectral characteristics of the fluorescence filters were determined with a spectrograph (Ocean Optics, USB4000) and are listed in Table 2.4.

Table 2.4: Fluorescence filter transmission.

Filter	Transmission range [nm] (>50 % transmission)
350 nm Bandpass	<350 - 380
440 nm Bandpass	390 - 490
470 nm Lowpass	>470

The PMT output was amplified (EG&G Ortec, VT120A, 200 gain, 0 to -5 V non-inverting) and recorded with a digital counter (Stanford Research Systems, SR400). A detection gate of 60 ns after the laser pulse (c.f. Fig. 3.12) was set to reduce noise from the laser and ambient light during the long laser-off period between the pulses (∼10 ms for a 100 Hz repetition rate), triggered by the fast photodiode also used for BD (section 2.3).

2.4.2 Dispersed Fluorescence

Besides the knowledge about the excitation of Cr in He_N, observing the energetically resolved emission channels with dispersed LIF is a well established tool to get information about the performance of the examined species after the excitation. For dispersed LIF measurements, the two ground state excitations $z^7P^\circ \leftarrow a^7S_3$ and $y^7P^\circ \leftarrow a^7S_3$ were excited with a frequency doubled Ti:Sa laser and a Kr-Ion laser, respectively (results

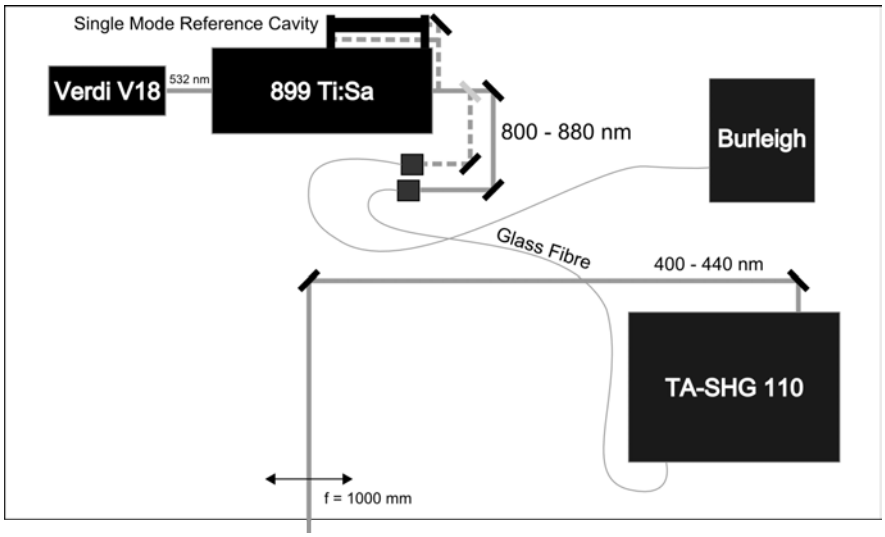

Figure 2.9: Setup for the frequency doubling of the Ti:Sa laser. TA-SHG 110 ... frequency doubling stage, Burleigh ... wavelength meter.

in Section 3.1). The Ti:Sa laser is pumped with a diode pumped solid state (DPSS) laser system (Coherent®, Verdi V18, $\lambda = 532$ nm) and has to be in single-frequency operation to double the photon frequency in an external cavity (Toptica, TA-SHG 110, KDP, $\lambda_{SHG} = 410\text{-}425$ nm) (see Fig. 2.9). The laser wavelength of the Ti:Sa laser is monitored with a wavelength meter (Burleigh, WA 1500). Wavelength adjustment is possible in a very limited range. To change the wavelength for more than ∼1 nm, the cavity has to be fully readjusted to meet the resonance conditions. A description to set up the Ti:Sa laser in single mode operation, fiber coupling, and adjustment of the frequency doubling stage is provided on the enclosed DVD ('Frequency_doubling.pdf').

The Kr-ion laser (Coherent®, Innova Sabre) 356.4 nm line was used (single line mode) to excite the Cr $y^7P^\circ \leftarrow a^7S_3$ transition in the droplet broadened excitation region for dispersed fluorescence studies. The laser was located in the basement[10] and guided over a long path (∼10 m) through a hole in the floor of CLII into the fluorescence collection region.
To determine the J-dependent population of the $y^7P^\circ_{2,3,4}$ state across the droplet broadened excitation band, the transition was excited with the pulsed laser at different wavelengths and the fluorescence recorded with the high resolution monochromator (see Fig. 3.10 in Section 3.3). In contrast to the undispersed fluorescence measurements (Section 2.4.1), no triggering of the detector is required for optimal signal to noise ratios due to the spectral separation of the fluorescence- and the excitation wavelengths.

[10]Prof. Windhold's lab.

Low resolution dispersed LIF spectra (Kr^+ excitation laser) were recorded with a PMT (EMI, 9558QB) attached to a 0.5 m focal length monochromator (Acton Research Corporation, SpectraPro-500). After exciting the strong $y^7P^\circ \leftarrow a^7S_3$ transition, the low resolution spectra gave first indications for three fluorescence branches (see Fig. 3.8). A better resolution was achieved with a Peltier cooled CCD camera (-100°C, LOT-Andor, iDUS DU401A BR-DD) attached to a high resolution spectrograph (GCA/McPherson Instrument, EUE-700). Each emission branch was recorded separately with an exposure time of approximately 20 minutes. The fluorescence lines were then evaluated with a curve fitting and peak fitting software (Fityk)[179] for the results presented in Table 3.1. For the results presented in section 3.1.4, the detection efficiency of the latter system was determined with a Hg discharge lamp (Acton Research Corporation, ms416, item No. 120...) previously calibrated with an Ocean Optics USB spectrometer. The latter one had been calibrated with a tungsten-band-lamp[11]. Knowing the intensities of the Hg discharge lamp lines, the detection efficiency of the whole system, consisting of LIF collection assembly, spectrograph, and CCD detector was calibrated.

2.4.3 Design and Construction of a LIF Detector Setup

A LIF detector setup was already available in the measurement chamber that was used for LIF, magnetic circular dichroism (MCD), and ESR measurements on Rb atoms doped to He_N (see Refs. [51, 165, 167, 180]). It is located between the magnet pole shoes [51] and consists of two hollow mirrors. A glass rod guides the collected light out of the vacuum chamber where it is imaged from the end of the glass rod on the photocathode of a PMT. This construction is useful for ESR measurements due to its compact and efficient light collection between the magnet's pole shoes. In contrast, it is not convenient for LIF measurements where no scanable magnetic field is required. The laser has to be guided through the interaction region very accurately with the disadvantage of increased stray light, the connection to a monochromator/spectrograph[12] is not very efficient, and the long distance from the nozzle decreases the He_N beam density.

Hence, a new LIF detector setup was constructed based on a lens system to overcome these limitations [180, 182]. A schematic cut through the measurement chamber is shown in Fig. 2.10 and detail drawings can be found in Appendix A.1. The lens system was designed and optimized for best efficiency and low costs with simulations carried out with 'WinLens3D Basic' from Qioptiq [183]. The simulation files can be found on the enclosed DVD. A four-lens system in combination with a concave mirror was chosen for a high collection efficiency from the fluorescence region with a diameter of

[11] Special thanks to Reinhold Hetzel from the group of Prof. Leising.

[12] Oriel Large Slit Bundle, Glass, Std. 11 mm ferrute, 0.8x9.7 mm Slit End Size, F/# 0.9, acceptance cone 68°, Model No. 77538 [181]

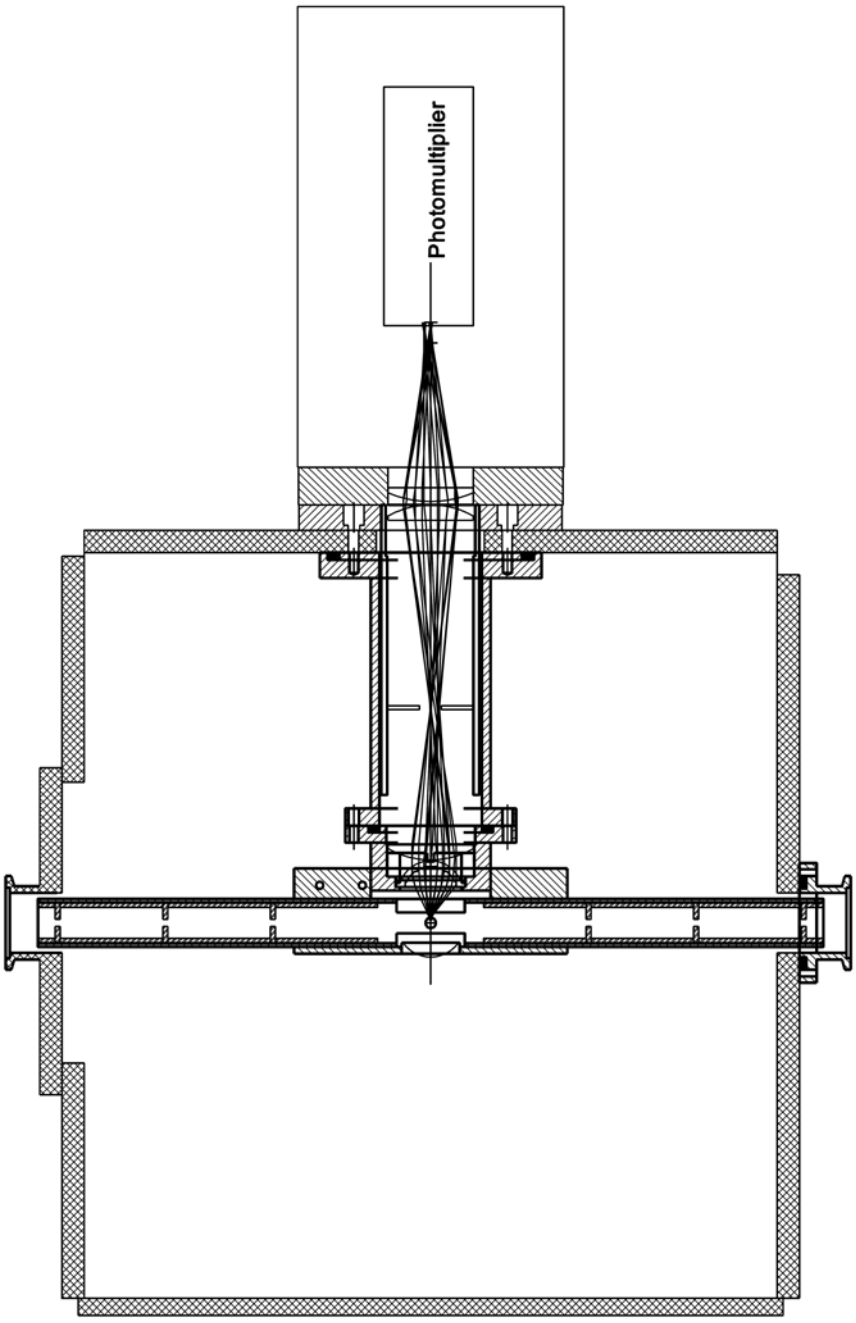

Figure 2.10: Cross-section through the measurement chamber and LIF collection assembly (He_N beam propagates into the plane of the drawing). The laser beam intersects the He_N beam in the center of the LIF detector system. Fluorescence light is collected and focused with four lenses on the photocathode of an end-on-PMT.

Table 2.5: Optical components used to construct the LIF collection system.

Part	Description	Distributor	Product Nr.	f [mm]	d [mm]	AR Coating
a 1	Concave Mirror (LIF)	Comar	10 SR 33	10	33,0	
a 2	Concave Mirror (MCD)	Comar	14 SR 50	14	50,0	
b	Glass Aspheric Condenser	Comar	29 AF 40	28,6	40,0	
c	Planoconvex Lens	Thorlabs	LA1050-A	100	50,8	350 - 700 nm
d	Planoconvex Lens	Thorlabs	LA1384-A	125	50,8	350 - 700 nm
e	Planoconvex Lens	Thorlabs	LA1979-A	200	50,8	350 - 700 nm

$\sim$3 mm [51] (Fig. 2.11d shows a test of the simulated configuration). It can be used with a photomultiplier or a monochromator/spectrograph and all parts of the assembly are listed in table 2.5. Also, chromatic aberrations were considered in the performed ray simulations that showed negligible influence on the focal planes.
Two different concave mirrors can be mounted underneath the intersection between He_N– and laser beam to collect light emitted into the lower hemisphere. The smaller mirror (part: a 1) has a shorter radius of curvature to cover a maximum solid angle for LIF measurements, while the larger one (part: a 2) covers a reduced solid angle but fits to the two permanent magnets that can be oriented along the laser beam (see Fig. 2.11b) for MCD measurements. These magnets are separated by a distance ring which keeps them parallel.
Light emitted into the upper hemisphere and light reflected from the concave mirror is collected from a large solid angle by a condensor lens (part: b) with a large numeric aperture. Currently, the lens material is B270 (transmission range 320 - 2600 nm [184]) because of economic reasons. For detection of UV light below 320 nm, it can be easily replaced with a fused silica lens. The lowest part of the tube system (Fig. 2.11c), which holds the condensor lens and provides the vacuum sealing (so all lenses except the lowest one can easily be changed during operation), can be replaced as a whole to mount other lenses or detectors in the He_N beam path, e.g., a TEM grid holder.
To shield ambient light and stray light from the entrance and exit windows the setup is equipped with a baffle tube along the laser beam. It is mounted, together with the concave mirror, on an aluminum block that is clamped to the tube system (Fig. 2.11a).

The parallel light beam, formed by the condensor lens, is focused with a second lens (part: c) into an intermediate image plane, where an aperture reduces the stray light collected from other sources than the fluorescence region (spatial filtering). The

intermediate image is focussed on the detector by a second pair of lenses (parts: c + d/e). Adaptation to both detectors is achieved by changing the uppermost lens. The lens (part d) focuses the light on the photocathode of the PMT while the other lens (part e) is chosen to meet the aperture of the monochromator (F/# = 4). Because the monochromator has to be oriented horizontally, the fluorescence light is reflected by a 1" mirror mounted on the monochromator just in front of the entrance slit. The LIF system can be equipped with a dummy stray light object in the He_N/laser interaction region (see Fig. 2.11a), that produces clearly visible light upon illumination with the laser to easily place the monochromator entrance slit in the lens system image plane. It consists of a glass rod with a small tip that can be introduced in the detection region (also under vacuum conditions).

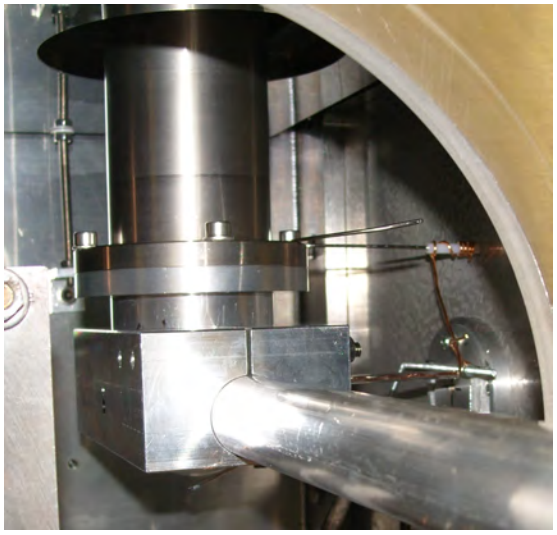

(a) LIF collection system.

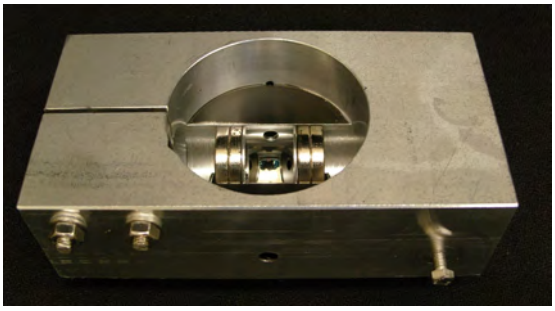

(b) LIF collector with permanent magnets for MCD measurements.

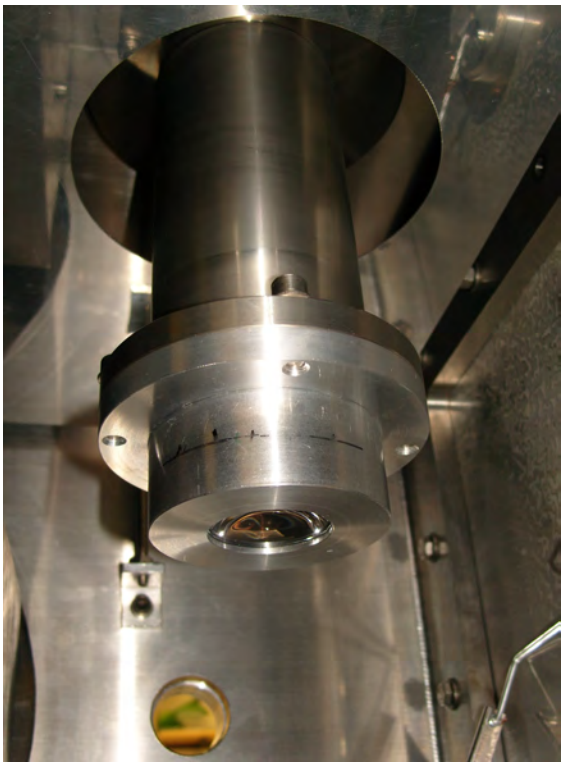

(c) LIF condensor lens with mount.

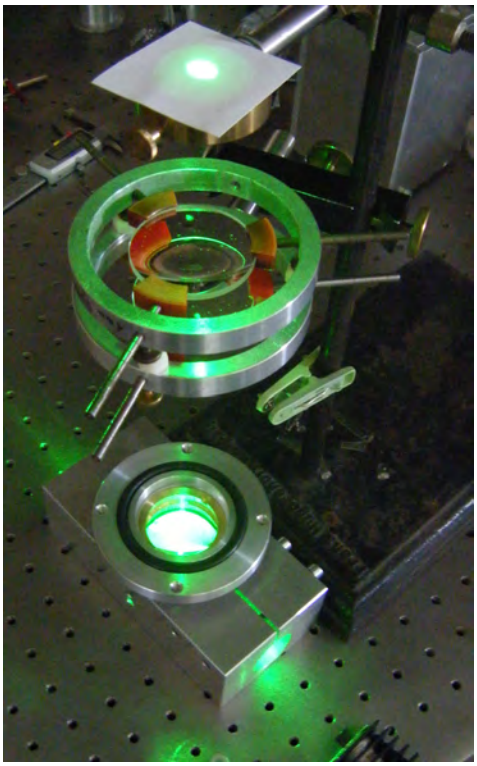

(d) Lenssystem test assembly.

Figure 2.11: Pictures of the newly designed LIF detector.

2.5 Photoionization

For photoionization experiments the QMS rod system is oriented in line with the He_N beam and the laser beam is guided to intersect the droplet beam at right angles inside the crossed beam ion source (e^- ionization deactivated, c.f. Figs. 2.2 and 2.12). This enables a mass selective ion detection for one- and two color REMPI (results in Sections 3.4 to 3.10). Photoions are continuously counted with a digital counter (Stanford Research Systems, SR400) connected to the discriminated output of the QMS[13]. Typical counting times are 1 s per data point because pulse-to-pulse power variations of the XeCl pump laser (100 Hz repetition rate) have a large effect on the dye laser output. It was found that signal averaging over 100 pulses represents the best compromise regarding the measurement time.
Only bare ions or ions with a few He atoms attached can be detected within the mass range of the QMS (< 500 u). At^+-He_N exceed the mass range and are missed. Hence, dopants have to detach from the droplet or destroy the droplet during the excitation and ionization process to be detected. The probability for these processes is dependent on the droplet size, which is determined by the He nozzle temperature. The latter also determines the He_N flow (see Section 1.3) and therefore is a critical parameter for PI of doped He_N. For the study of single atoms in He_N, best results were obtained with nozzle temperatures in the range of 18 - 20 K and a Cr source heating power of about 150 W. For dimer and cluster detection, nozzle temperatures around 15 K yield the best signal and slightly higher oven temperatures are beneficial. Nevertheless, the behavior can change strongly for each experimental run, so these values should only be taken as a reference and ideal parameters are to be determined individually.

For PI, the laser beam enters and exits the QMS chamber through two 1" windows (Fig. 2.12). In the beginning, both the entrance and exit windows were made of plane parallel fused silica which led to interference effects, resulting in wavelength dependent deviation of the PI signal especially for high resolution scans (primarily caused by the entrance window). A reduction of this effect can be achieved by either using anti-reflective coated- or wedged windows. Due to the wide spectral range used for PI, the entrance and exit windows were replaced with 3° wedged fused silica windows (Laseroptik, 25x6.35 mm, item number: S-01124) which reduced this effect. Reflections originating from both windows are used to record the dye laser wavelength. The laser pulse energy is simultaneously recorded with a laser power meter (Coherent®, FieldMaxII) located behind the exit window.
As indicated in Fig. 2.12a, for 2CR2PI both the XeCl laser beam and the dye laser beam are transferred to the apparatus. Mind that the lenses, indicated in Fig. 2.12a, have to be chosen and positioned individually for each experiment because the beam

[13]The discriminated output of the QMS is transformed to TTL pulses by a home-built photon counter (see Ref. [51]). The output from this counter is connected to the input of the SR400 that counts the ions (Fig. 2.16).

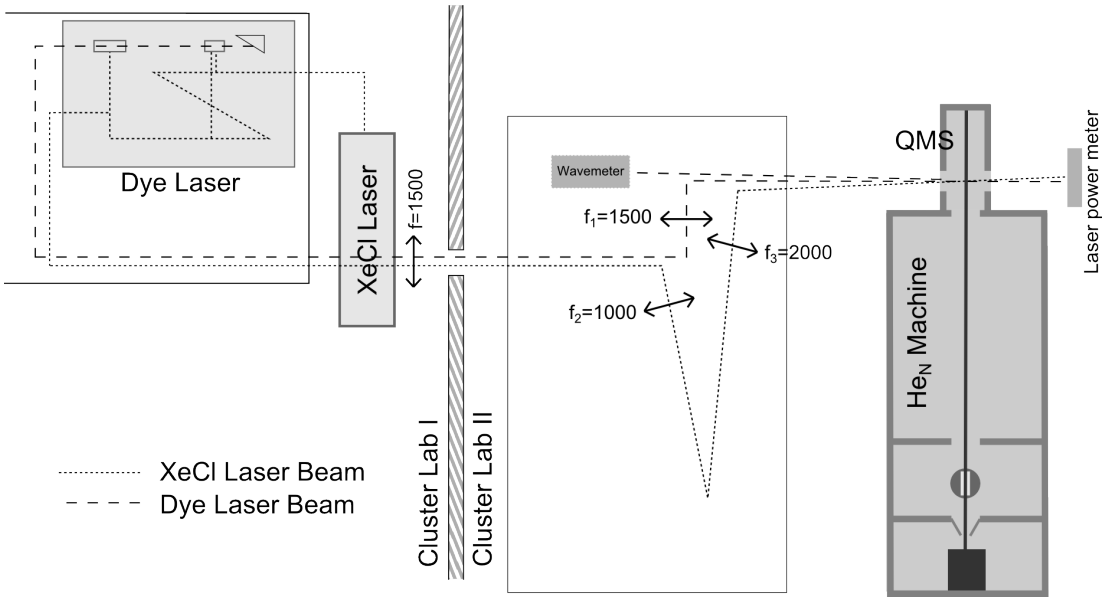

(a)

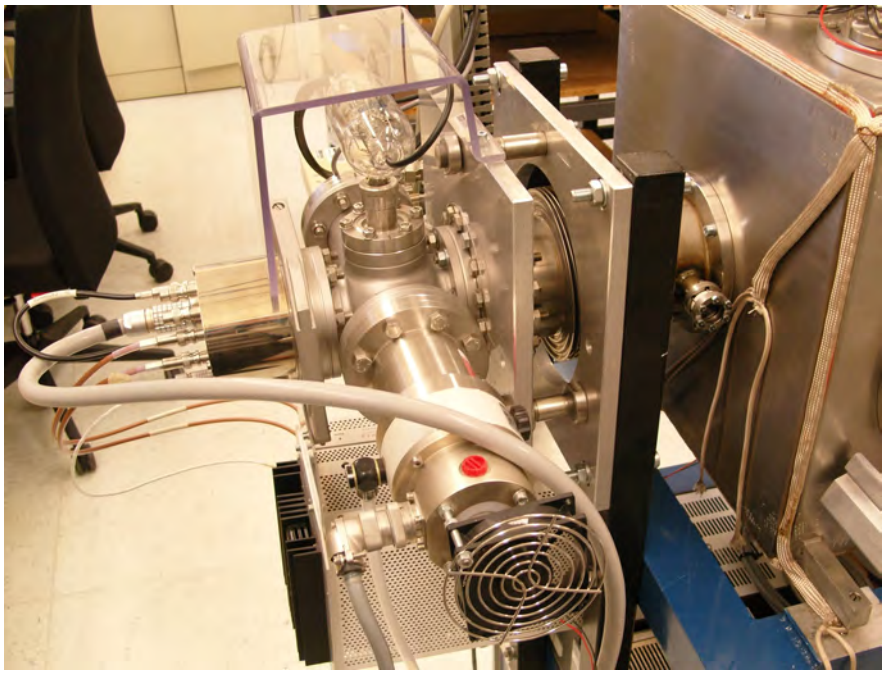

(b)

Figure 2.12: (a) Schematic setup for 2CR2PI measurements. The XeCl and dye laser beams are marked with dotted and dashed lines, respectively. For 1CR2PI only the dye laser beam was transferred to CL II. Laser tables are indicated a black rectangles and the f_{1-3} focal lengths should only be taken as reference. (b) Photograph of the QMS in the PI orientation. The rod system is oriented in line with the He_N beam and the laser beam enters the QMS chamber through the 1" entrance window and crosses the He_N beam at right angles.

parameters change with each adjustment of the laser (e.g., dye cell exchange). The XeCl laser pulses are delayed with respect to the dye laser pulses by a delay length to ionize the dopants after they are resonantly excited. Cr 2CR2PI spectra ($y^7P^\circ \leftarrow a^7S_3$) for different pulse delays are shown in Fig. 2.13c, where the best signal is achieved for a delay length of 2 - 3.5 m (≡7-12 ns). The XeCl laser can only ionize atoms which are in an intermediate state that is high enough in energy to reach the IP with one 308 nm photon. When the delay between the pulses is too short, only a small fraction of atoms is already resonantly excited to the intermediate state by the dye laser. If the delay exceeds the lifetime of the excited state (∼7 ns for y^7P°, see Table 1.4), the atoms have relaxed to energetically lower states that are not accessible for an ionization with the XeCl photon (Mind that the majority of atoms relax to the energetically lowest J substate of the initially excited state, rather than to other states [1]. Hence, the lifetime of the y^7P° state is decisive). Therefore, a delay which is in the order of the excited state's lifetime yields the best signal. The corresponding laser pulses with respect to the delay length are recorded with a fast photodiode and are shown in Fig. 2.13b. The individual laser pulses are shown in Fig. 2.13a.The photodiode's charging characteristic is not known, hence this should only be considered as a reference.

2.5.1 Cr_n Cluster Detection

The ion signal is usually low when recording REMPI spectra for the detection of $Cr_{2,3,\ldots}$. To increase the signal strength, the cluster excitation spectra (see Section 3.9) were recorded with a low QMS mass resolution to integrate the ions over a wider mass window (Δm ≈ 5 u, QMG 422 resolution parameter = 150, voltages according to Table 2.2). To demonstrate that Cr^+-He_n ($n \approx 13$) does not contribute to the Cr_2^+ signal, a mass spectrum was recorded (Fig. 2.14) while ionizing with REMPI on one of the strong peaks (see 3.28). The spectrum clearly shows an increased signal on the Cr^+ and $Cr_{2,3}^+$ mass, and a drop of signal in between. Additional peaks result from water fragments attached to the ions. The signal has the same characteristics but is lower when exciting in the broad dimer (and trimer) absorption band. In conclusion, the $y^5P_3^\circ \leftarrow a^5S_2$ transition peaks in the REMPI spectrum have to be attributed to Cr, Cr_2, or small Cr cluster (c.f. Section 3.10).

2.5.2 Evaluating Fano Resonances

A MATLAB® script was written to analyze the Fano profiles found for the AI peaks in the Cr 1CR2PI spectrum (Section 3.4). These resonances are caused by the interference between the autoionizing state wavefunction and continuum state wavefunctions (see

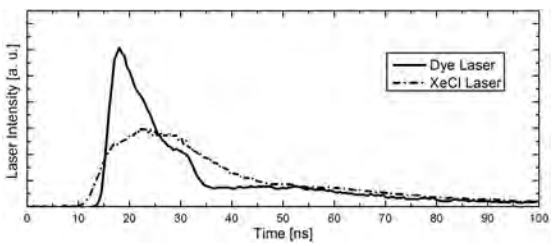

(a) Laser pulses of the dye- and XeCl laser. Signals were recorded separately.

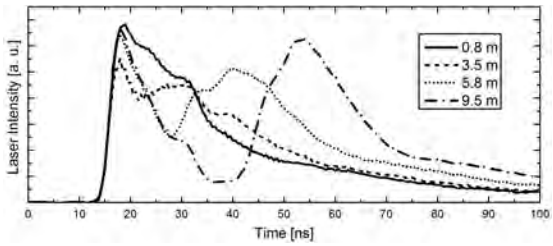

(b) Laser pulses in dependency on the delay length of the XeCl laser. The XeCl laser follows the dye laser.

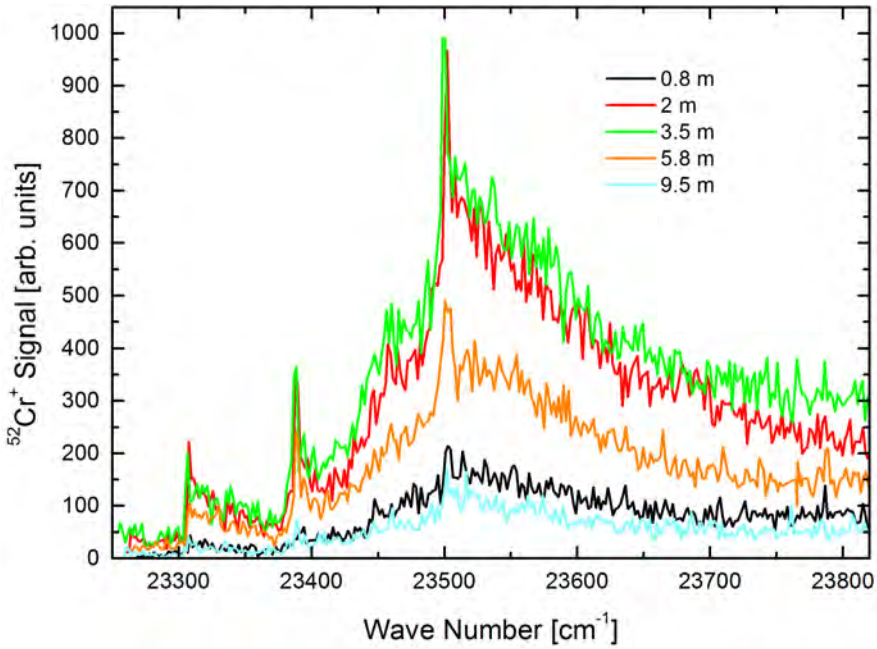

(c) Cr $z^7P^\circ \leftarrow a^7S_3$ 2CR2PI signal for different laser pulse delays.

Figure 2.13: Time delay between dye laser- and XeCl laser pulses optimized for maximum PI signal.

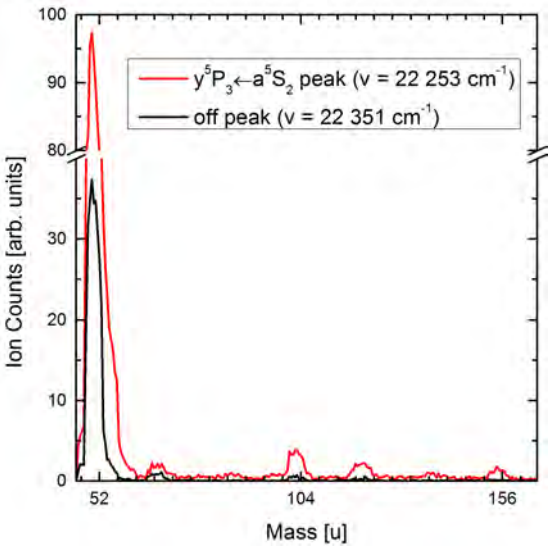

Figure 2.14: (a) Low resolution REMPI mass spectra with the laser set on the $y^5P_3^\circ \leftarrow a^5S_2$ transition ($\tilde{\nu} = 22\,253\text{cm}^{-1}$) or to $\tilde{\nu} = 22\,351\text{cm}^{-1}$ ($Cr_{2,3}$ excitation band).

Section 1.8.3). The line shape is modeled by [150]:

$$a + b\left[\frac{(q+\varepsilon)^2}{(1+\varepsilon^2)}\right] \tag{2.2}$$

$$\varepsilon = \frac{E - E_0}{\Gamma/2}. \tag{2.3}$$

The parameters were determined for a majority of the prominent AI peaks (see Table 3.2) using the MATLAB® iterative least squares fit routines 'nlinfit' and 'lsqcurvefit'. The script can be found on the enclosed DVD ('FanoFit.m'). In brief, every peak is fitted individually and start parameters have to be set for each. These include the values for the phenomenological shape parameter q, resonance energy E_0, linewith Γ, and the two parameters a and b. The droplet broadened $y^7P^\circ \leftarrow a^7S_3$ transition band is fitted prior to the Fano profile evaluation to account for the varying intermediate state population across the excitation region (see Fig. 3.14). This requires another two parameters in the pre-fit. The population of the z^5P° state[14] due to relaxation from the y^7P° state, and therefore the height of the AI peaks, is assumed to be proportional to the $y^7P^\circ \leftarrow a^7S_3$ transition strength (see chapters 3.4 and 3.1) represented by the broad structure. This influence shall be compensated by evaluating the ratio of $\frac{\text{AI Peak Signal}}{\text{Background}}$ instead of the raw peak signal, where the background signal is evaluated in the pre-fit.

[14]The different J population is assumed to be constant across the broadened $y^7P^\circ \leftarrow a^7S_3$ excitation.

The population corrected data is then deconvoluted with an assumed dye laser spectral width (0.2 cm^{-1}, see Table 2.3), derived from the specifications given in the FL3002 manual [172], and finally fitted with equations (2.2) and (2.3).
To show the credibility of the code, a benchmark test was performed with a data set from Ref. [185]. R. P. Madden and K. Colding [185] studied resonances in the photoionization continuum of He upon excitation with synchrotron radiation. The data points were extracted from the reference and a fit, neglecting a laser/slit correction in analogy to the approach described in Ref. [185], was performed. A comparison between the parameters from literature (Fig. 6 of Ref. [185]) and the parameters obtained with the MATLAB® script are shown in Fig. 2.15a. Clearly, the fitted resonance profile represents the data points very well and is in good accordance with the fitted resonance profile from Ref. [185]. As a consequence, also the calculated Fano parameters are within the uncertainty of the literature parameters, which proofs the reliability of the code. Hence, Fano profiles were found that resemble the experimental data well (Fig. 2.15b).

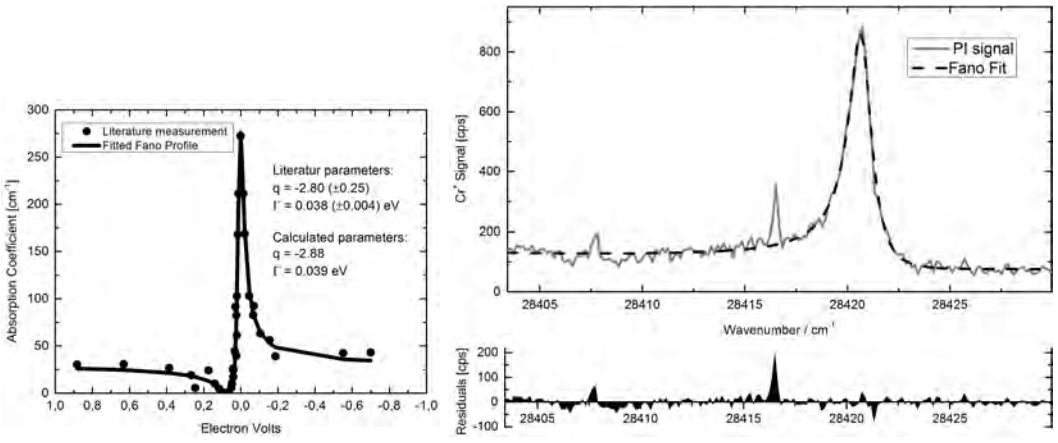

(a) (b)

Figure 2.15: (a) Benchmark test for the Fano profile fitting algorithm. The black curve is the fit of the data points (black dots) that were extracted from Ref. [185]. (b) Peak of the $g^5D_4 \leftarrow z^5P^\circ_3$ AI transition. The measured curve (gray line), the fitted Fano profile (dashed line), as well as the residual are plotted.

2.6 Data Acquisition and Control Programs

Two main programs were written to control the setup and record the signals. Both can be found on the enclosed DVD. An example of the device control- and data acquisition gateways for a typical BD experiment is illustrated in Fig. 2.16.

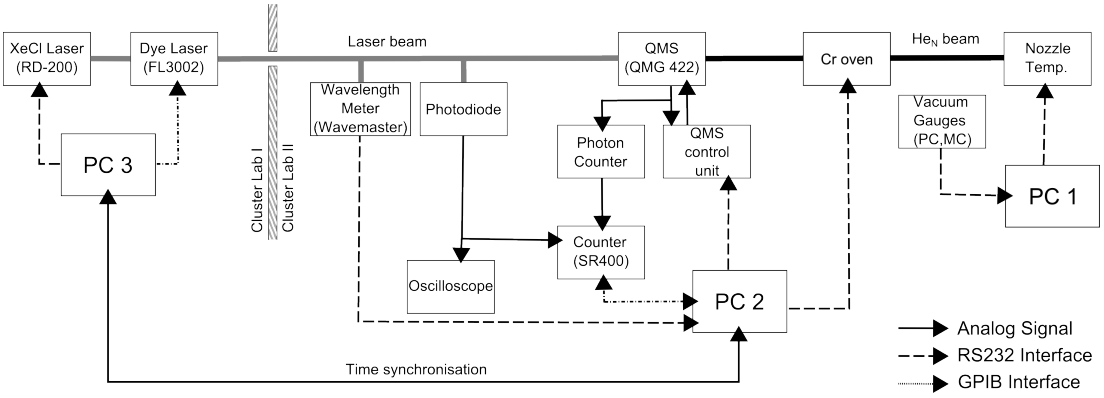

Figure 2.16: Illustration of the communication between the measurement devices used for a typical BD experiment. The arrows indicate the direction of control or signals. PC ... Personal Computer, Photon Counter ... Home-built photon counter used for TTL conversion.

2.6.1 Main Data Acquisition Program

All measurements with the pulsed dye laser were performed with a self-written LabVIEW program (PC 2 in Fig. 2.16). It was programmed from scratch and various functions were added to adapt the experimental requirements. The program allows to record signals from the digital counter (Stanford Research Systems, SR400) or from the analogue inputs of a data acquisition card (Meilhaus Electronic, ME-4660 PCI). The latter is also used for simultaneous monitoring the laser pulse energies or signals from devices with an analogue output (e.g., boxcar integrators, cw laser power meter). Laser wavelengths can either be recorded simultaneously from the wavelength meter (Coherent®, WaveMaster) or, for λ <400 nm, manually upon time synchronization with the pulsed dye laser program (see Section 2.6.2). The program is also capable to control and save the counter gate values, QMS values, or set TTL pulses for differential measurements.

2.6.2 Laser Remote Program

A MATLAB® script was written (PC 3 in Fig. 2.16) that allows to fully remote control the pulsed dye laser (Lamda Physik, FL3002). The laser GPIP drivers were adapted

from Ref. [186]. Laser wavelengths are determined by the grating angle that is adjusted with a stepper motor. The parameter for the grating order is set in the head of the script file, and the grating orders corresponding to the wavelength ranges can be found in a plot on the enclosed DVD ('GratingOrders.fig'). Scan speeds are set in steps/nm, where each step takes one second. The laser scan directions can also be changed to, e.g., check for experimental influence on the asymmetric line shapes of the Fano resonances. For slower scans above 10 steps/nm (which means a speed slower than 0.1 nm/second), a time interval is calculated from the scan speed when the command for a single motor step is sent to the laser. This enables an almost continuous scan with steps defined by the wavelength change of one motor step (∼0.02 nm [172]). Below a scan speed of 10 steps/nm (faster than 0.1 nm/second), this is not possible since the frequency of commands sent to the laser exceeds the laser's ability to execute them. So, every second the new stepper motor counts are calculated and sent to the laser, which results in a discontinuous, but faster scan.
Additionally to the position of the grating, the possibility to control the angle of the frequency doubling crystal was implemented and used for the photoionization of Cu atoms. Again, this angle is controlled by a stepper motor, where only a rough adjustment can be made in advance. Fine tuning of the angle has to be done manually by setting a vector of motor positions which is then recalled during the scan.
Wavelengths below 400 nm could not be determined with the wavelength meter (Coherent®, WaveMaser) but were estimated from the wavelength set on the laser. A relative offset of the set laser wavelength to the actual wavelength of ~0.3 nm was found and could be corrected[15] by changing the grating calibration constant stored in the laser electronics [172]. Since the two computers, one controlling the laser with the MATLAB® script in CLI and to other recording the measurement signal with a LabVIEW program in CLII, were not capable to interchange the wavelength information, the clocks of both PCs were synchronized to synchronize the laser wavelength in CLI with the recorded signal in CLII. The starting time of the measurement and the scan speed has to be set in both programs to calculate the current wavelength during the scan.

[15] Please mind that some diagrams shown in this thesis, which are not part of publications, might not be corrected for small wavelength uncertainties.

3 Results

This chapter contains the results in the form of texts and figures from the peer reviewed publications [1–4], one submitted manuscript [5], and selected further results. The sections are ordered according to the three major topics that were covered to study the transition metal (Cr and Cu) atoms and molecules in He_N[1]: First, the position (center – surface) and the behavior of Cr atoms upon excitation in He_N is studied with single photon excitation and monitoring the BD and LIF signal (Sections 3.1 to 3.3). The second part treats the performance of Cr and Cu doped to He_N upon REMPI with different ionization schemes (Sections 3.4 to 3.8). Interesting relaxation mechanisms are found and Fano resonances, resulting from the interference of an AI state with continuum states, are evaluated. Finally, the very unique performance of dissociation and geminate recombination for Cr dimers and small Cr cluster in He_N is probed with REMPI and presented in Section 3.9. Further spectral characteristics, that are also attributed to Cr dimers and small clusters, are discussed in Section 3.10.

[1]Hence, the reader should not be confused by the non-chronological order of the articles.

3.1 Electronic Relaxation after Resonant Laser Excitation of Cr in Superfluid Helium Nanodroplets [1]

The position of Cr in He_N is probed with BD and undispersed LIF. Dispersed LIF reveals the ejection of Cr after laser excitation of the two strong ground state transitions ($z^7P^\circ_{2,3,4} \leftarrow a^7S_3$ and $y^7P^\circ_{2,3,4} \leftarrow a^7S_3$). A complex pattern of relaxation pathways for chromium atoms in the cold helium environment are found, in which spin transitions and electronic transitions are involved that are forbidden for free atoms.
Sections 3.1.1 to 3.1.5 correspond to the publication "Electronic Relaxation after Resonant Laser Excitation of Cr in Superfluid Helium Nanodroplets" (The Journal of Physical Chemistry A **117** (2013), 9621-9625) by Andreas Kautsch, Markus Koch, and Wolfgang E. Ernst [1]. This article is part of the JPCA "Takeshi Oka Festschrift".

The author of this thesis had main contributions on:

- All measurement data
- Data evaluation and interpretation
- Writing the publication
- Figures and artwork

The contributions of the Co-authors and acknowledged persons listed below were:

- Markus Koch: Discussing the fluorescence decay time interpretation, proofreading of text, funding
- Wolfgang E. Ernst: Proofreading of text, supervision (experiment, publication), funding
- Friedrich Lindebner: Experimental assistance for improved dispersed LIF measurements
- Matthias Hasewend: Experimental assistance for preliminary undispersed LIF measurements

3.1.1 Abstract

Chromium (Cr) atoms embedded into helium nanodroplets (He_N) are ejected from the droplets upon photoexcitation. During ejection they undergo electronic relaxation resulting in bare Cr atoms in various excited states. In a study of the relaxation process we present absorption spectra observed via laser induced fluorescence and beam depletion as well as dispersed fluorescence spectra and time-resolved fluorescence measurements. Broad and shifted absorption structures were found for the strong $z^7P^\circ \leftarrow a^7S_3$ and $y^7P^\circ \leftarrow a^7S_3$ excitations from the ground state. Emission lines are, in contrast, very narrow, which indicates that fluorescence is obtained from bare excited Cr atoms after ejection. Upon excitation into the $y^7P^\circ_{2,3,4}$ states we observed fluorescence from $y^7P^\circ_2$, $z^5P^\circ_{1,2,3}$, and $z^7P^\circ_{2,3,4}$, indicating that these states are populated by electronic relaxation during the ejection processes. Relative population ratios are obtained from the intensities of individual spectral lines. Excitation into the $z^7P^\circ_{2,3,4}$ states resulted in fluorescence only from $z^7P^\circ_2$. Estimates of the time duration of the ejection process are obtained from time-resolved measurements.

3.1.2 Introduction

Chromium (Cr) is of astrophysical interest because of its presence in astronomical objects [187, 188] and in the solar spectrum [27]. Cr atoms and molecules have been isolated in rare gas matrixes for spectroscopic studies [75]. With regard to the free atoms, these studies find blueshifts and line broadenings of absorption spectra in the range of a few cm^{-1} to several 1000 cm^{-1}, depending on the change in electron configuration caused by the excitation. Matrix perturbations on Cr emission lines are found to be relatively small (<100 cm^{-1}). Upon excitation from the a^7S_3 ground state (electron configuration [Ar] $3d^54s^1$) via the two strong resonant transitions to $z^7P^\circ_{2,3,4}$ ($3d^54p$) and $y^7P^\circ_{2,3,4}$ ($3d^44s4p$), the Cr atoms were found to undergo complete electronic relaxation (also to states with different spin multiplicities) and fluorescence of matrix isolated Cr atoms was observed exclusively from other states than those originally excited.

In terms of matrix isolation, superfluid helium nanodroplets (He_N) combine many advantageous properties. Because of their low temperature of 0.37 K, their confinement character and very versatile doping possibilities, they have been popular for spectroscopic investigations of cold atoms, molecules and clusters [9]. We have recently succeeded in doping He_N with Cr atoms [65]. In a first spectroscopic study we identified the photoinduced ejection of bare Cr in the $z^5P^\circ_J$ (J= 1−3 being the total angular momentum quantum number) states [2]. The population ratios of the different J components could be obtained from an evaluation of the line strengths of transitions to autoionizing states.

In this work we present absorption spectra for the $z^7P^\circ_{2,3,4} \leftarrow a^7S_3$ and $y^7P^\circ_{2,3,4} \leftarrow a^7S_3$ excitations, which are obtained from laser induced fluorescence and beam depletion.

To further investigate the ejection and relaxation process, dispersed fluorescence spectra are presented. Finally, estimates for the duration of the ejection and relaxation process are obtained from time resolved laser induced fluorescence measurements.

3.1.3 Experimental

The experimental setup is based on a helium nanodroplet isolation spectroscopy apparatus described in detail elsewhere [165]. In brief, the helium nanodroplets are formed by a supersonic expansion of precooled (19 K) high purity He (99.9999%) from 50 bar to vacuum through a 5 μm nozzle (maximum of droplet size distribution: $\hat{N} \approx 1800$). The droplets pass through a 300 μm skimmer into a separately pumped pickup chamber in which chromium metal is evaporated by a home built high temperature electron bombardment source [65]. The Cr beam is crossed with the He_N beam at right angles along 10 mm of the He_N flight path. With this crossed beam geometry it can be ensured that no free atoms reach the detectors. The heating power of the Cr source is optimized for single atom pick up.

In the main chamber laser induced fluorescence (LIF) and laser induced detachment of Cr from He_N (i.e., beam depletion, BD) can be detected. For LIF measurements the beam of doped He_N is crossed by a laser beam at right angles. Baffle stacks are used to reduce stray light and ambient light. LIF light is collected by a combination of an aspheric lens (o.d. 40 mm, $f = 29$ mm) and a concave mirror (o.d. 33 mm, $f = 10$ mm). Collected light is guided through an aperture for spatial filtering and detected by a photomultiplier tube (PMT) (EMI 9558QB, EMI 9863/350QB). For time resolved fluorescence measurements band-pass or low-pass filters can be inserted in front of the PMT to monitor fluorescence light of individual transitions. Electronic pulses from the PMT are amplified (Ortec VT120A) and counted (Stanford Research Systems SR 400). When spectra are recorded with pulsed lasers (see below), a 60 ns detection gate is triggered by a fast photodiode. For time resolved LIF measurements a 5 ns counting gate is scanned in 1 ns steps. For dispersed fluorescence measurements the emitted light is passed through a monochromator (McPherson EU-700) with an attached CCD camera cooled to $-100\,^{\circ}C$ (LOT-Andor iDUS DU401A BR-DD). To compare intensities of emission lines from different excited states, we calibrated the detection system with a calibrated tungsten ribbon lamp.

To detect BD, a quadrupole mass spectrometer (QMS, Balzers QMG 422) is located at the end of the main chamber. The QMS rod system is oriented at right angles to the droplet beam so that the latter can be counterpropagated by a laser beam. Doped He_N are ionized by electron bombardment and ions are extracted toward the rod system, mass filtered, and finally detected by a secondary electron multiplier. The mass filter was set to 52 amu, the mass of the most abundant Cr isotope. Note that Doppler shifts due to the counter propagating arrangement can be neglected with respect to the

broadening of excitation lines inside He_N. Electronic pulses from the QMS are amplified (home built amplifier), discriminated and counted (Stanford Research Systems SR 400). Signal fluctuations due to source instabilities are reduced by applying a differential counting scheme (laser on QMS signal minus laser off QMS signal).

For BD, undispersed LIF, and time resolved fluorescence measurements, nanosecond laser pulses were used. The laser pulses were obtained from an excimer (XeCl, Radiant Dyes RD-EXC-200) pumped dye laser (Lambda Physik FL3002, dyes RDC 360 and Stilbene 3) with 20 ns pulse duration and 100 Hz repetition rate. For dispersed fluorescence measurements two different continuous wave (cw) laser systems were used. A frequency doubled Ti:sapphire laser (Coherent Verdi V18 pump laser, Coherent 899 in single mode and Toptica TA-SHG 110, maximum power output 150 mW) at 23600 - 23900 cm^{-1} was used for excitation into the z^7P° states, and a Kr ion laser (Coherent Innova Sabre, maximum power output 400 mW) at 28048.64 cm^{-1} was used for excitation into the y^7P° states.

3.1.4 Results and discussion

To discuss our results, we start with the characteristics of the excitation spectra followed by the observations of the fluorescence from the z^7P° ($3d^54p$) and y^7P° ($3d^44s4p$) states. For illustration, Fig. 3.1 displays a level diagram of Cr indicating excitation (upward pointing arrows), relaxation (dotted arrows), and fluorescence (downward pointing arrows) paths observed. Laser excitation around the strong transitions $z^7P^\circ_{2,3,4} \leftarrow a^7S_3$ (23305.01, 23386.35, and 23498.84 cm^{-1}) and $y^7P^\circ_{2,3,4} \leftarrow a^7S_3$ (27728.87, 27820.23, and 27935.26 cm^{-1}) leads to BD spectra as shown in Fig. 3.2. For the $y^7P^\circ \leftarrow a^7S_3$ transition the LIF excitation spectrum is also shown for comparison in the lower graph. Further broadening occurred in our experiments at higher laser fluence of the pulsed laser indicating saturation effects, e.g., in BD (115 μJ) compared to LIF (<10 μJ). The broad excitation band agrees with our former photoionization (PI) experiment [2]. Compared to free atom transitions, a blue shift of approximately 300 cm^{-1} is measured. Similar, but much stronger shifts, were observed for Cr dopants in matrixes (Ar, Kr) with up to 1400 cm^{-1} [75]. Furthermore, the peaks are broadened so that they give rise to one structure expanding over ~450 cm^{-1}. In matrix experiments, it was also not possible to resolve the J-splitting of lines due to the strong broadening [75]. For Ag in He_N, similarly shaped excitation structures were found [90]. The strongly shifted and broadened excitation can be taken as indication for the solvation of Cr inside the droplet. In a liquid or solid matrix it is a consequence of the orbital's size change from the ground to the excited state. Upon excitation into a larger orbital, strong Pauli repulsion of the surrounding helium causes the shift and the broadening [9, 86, 90].

The dispersed fluorescence after excitation into various parts of the z^7P° and the energetically lower side of the y^7P° excitation band are shown in Fig. 3.3 and Fig. 3.4,

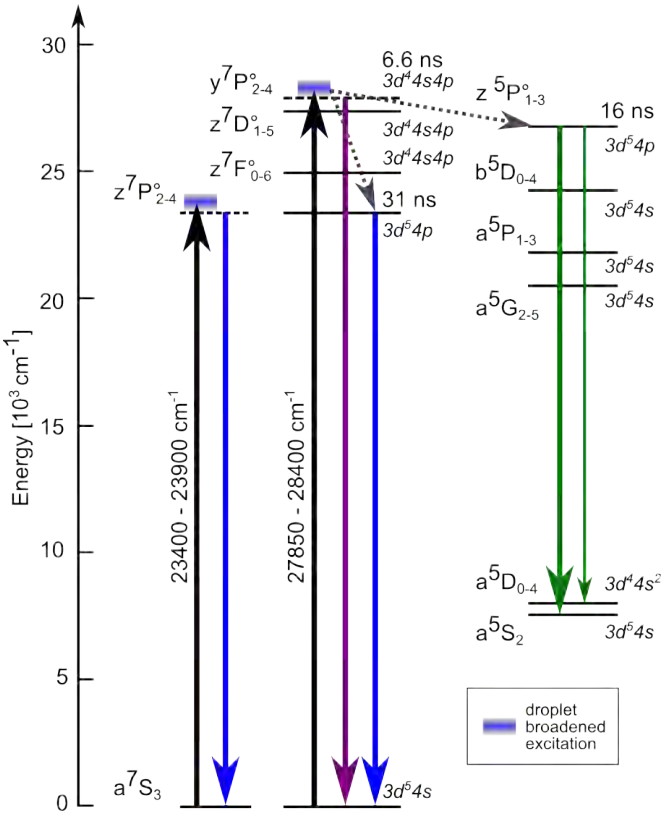

Figure 3.1: Level diagram of Cr and observed absorption and emission paths. Shaded rectangles indicate the excitation broadening due to the He_N and dashed lines stand for states where only emission from the lowest J substate could be observed. Nonradiative relaxation processes are marked as dotted arrows. Approximate lifetimes are shown next to some excited states of interest [108].

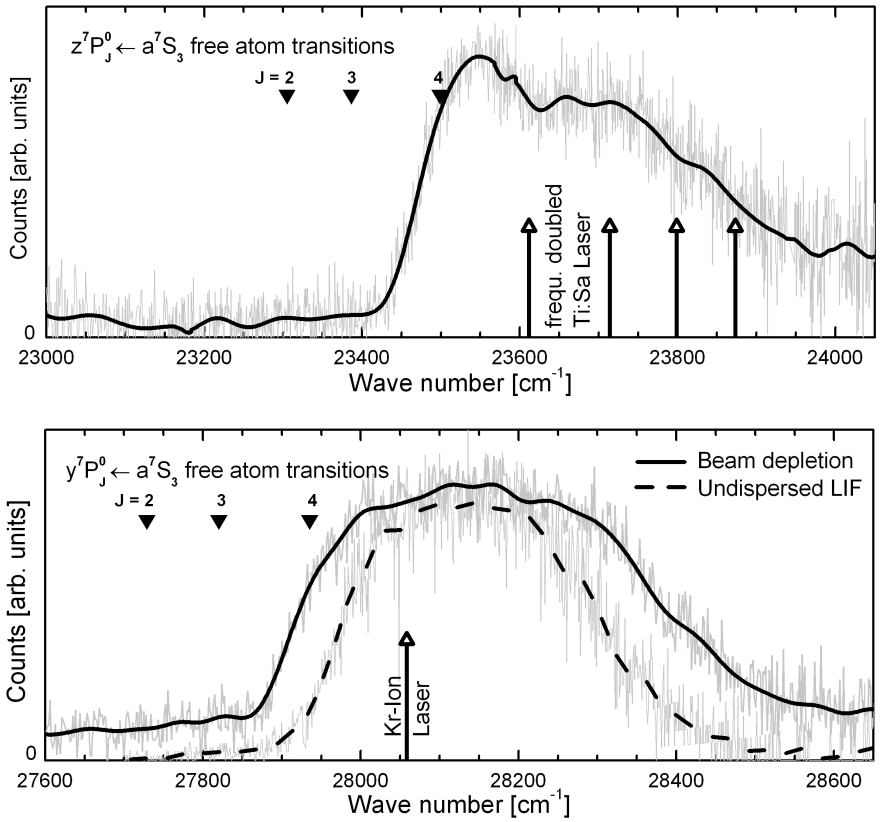

Figure 3.2: Beam depletion spectra of Cr atoms doped to He_N in the $z^7P^\circ \leftarrow a^7S_3$ and $y^7P^\circ \leftarrow a^7S_3$ transition region. For comparison, the lower graph shows the LIF detected excitation spectrum (dashed line). The measured signal (gray) is low pass FFT smoothed (black) and triangles indicate the free atom excitation transitions taken from Ref. [109]. Excitation wave numbers for dispersed LIF measurements using the Kr ion and frequency doubled Ti:sapphire lasers are indicated (cf. Figs. 3.3 and 3.4).

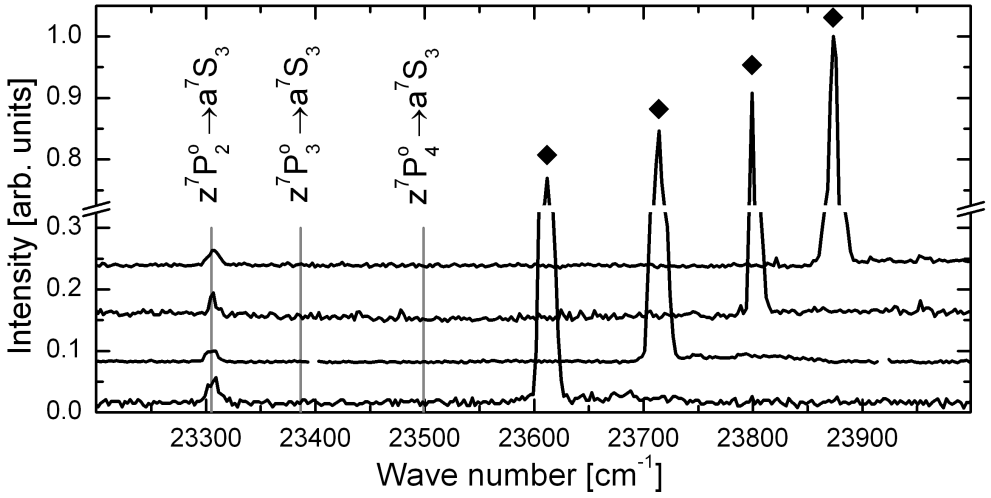

Figure 3.3: Dispersed fluorescence of Cr atoms upon excitation through the $z^7P^\circ \leftarrow a^7S_3$ transition inside He_N at differing photon energies (plots mutually shifted in vertical direction, laser marked with squares). Vertical lines indicate the free atom transitions $z^7P^\circ_{2,3,4} \rightarrow a^7S_3$[109].

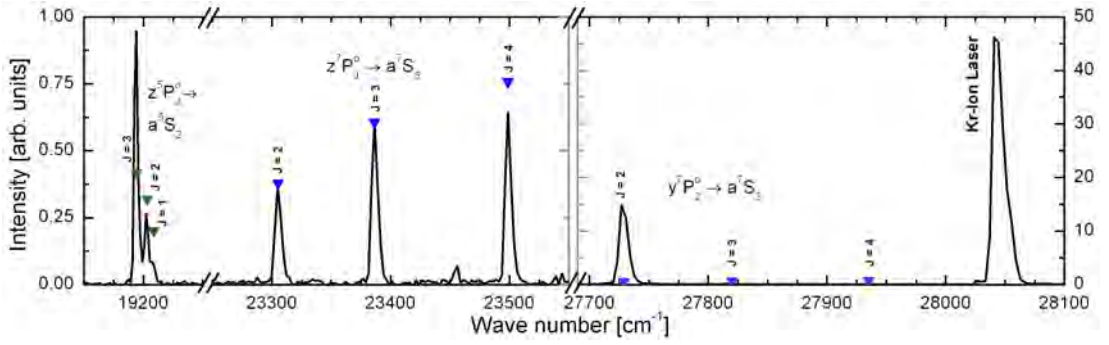

Figure 3.4: Spectrally resolved fluorescence of Cr atoms excited at 28056.6 cm^{-1} into the y^7P° state inside He_N. The bare Cr atom transitions $z^7P^\circ_{2,3,4} \rightarrow a^7S_3$, $y^7P^\circ_{2,3,4} \rightarrow a^7S_3$ and $z^5P^\circ_{1,2,3} \rightarrow a^5S_2$ are indicated by triangles [109]. Note the different intensity scales on the left and right panels. The feature at 23456 cm^{-1} is an artifact due to a faulty CCD response.

respectively. Scattered laser light serves as a reference marker. Clearly, all major emission [109] takes place at the free atom transition wavelengths within the relative uncertainty of the monochromator measurement (measured linewidths are shown in Table 3.1). If the emitting atoms were still attached to the droplets, line shifts and broadening beyond the resolution of the monochromator (4 - 8 cm^{-1}) should be observed. We conclude that all measured emission spectra result from free Cr atoms that had left the droplets.

With the laser excitation into z^7P° ($3d^54p$) or y^7P° ($3d^44s4p$) levels the related radiative emission to the ground state represents the dominant portion of the spectra. Matrix isolated Cr atoms show nonradiative energy relaxation mechanisms leading to no detectable fluorescence signals from these states [75]. On the other hand, from the $z^7P^\circ_{2,3,4} \rightarrow a^7S_3$ and $y^7P^\circ_{2,3,4} \rightarrow a^7S_3$ spin-orbit components only the energetically lowest transition is present ($z^7P^\circ_2 \rightarrow a^7S_3$, $y^7P^\circ_2 \rightarrow a^7S_3$). This phenomenon has no dependence on the excitation wavelength within the excitation region (Figures 3.2 and 3.3). So, a full relaxation within the J splitting of these excited states can be assumed and clearly bears the signature of the He_N influence. In our experiments, the fluorescence emission after the z^7P° excitation turned out to be very weak, which may be attributed to quenching processes. Contrary, after excitation into y^7P° the direct $y^7P^\circ_2 \rightarrow a^7S_3$ emission exceeds all other transitions in intensity.

Table 3.1: Peak areas and widths of the observed septet and quintet transitions. (*) marked values were manually set in the fitting routine. Data from literature [112] are applied for obtaining the relative population of states that is compared to PI results [2]. Uncertainties from fitting routines are given in parentheses.

Transition	Wave number [cm^{-1}] [109]	Measured area of emission line	Measured FWHM [cm^{-1}]	Relative intensity [112]	rel. LIF pop.	rel. PI pop. [2]	Free atom lifetime [ns] [108]
$z^5P^\circ_3 \rightarrow a^5S_2$	19194.34	7520(190)	3.7(1)	11000	0.64(2)	0.81(18)	16.2
$z^5P^\circ_2 \rightarrow a^5S_2$	19203.12	2070(70)	3.4*	8400	0.23(2)	0.15(3)	16.2
$z^5P^\circ_1 \rightarrow a^5S_2$	19208.77	710(40)	3.4*	5300	0.13(2)	0.04(4)	16.0
$z^7P^\circ_2 \rightarrow a^7S_3$	23305.01	4810(150)	6.3(2)	10000	0.35(2)		32.2
$z^7P^\circ_3 \rightarrow a^7S_3$	23386.35	7800(170)	6.1(2)	16000	0.35(2)		31.5
$z^7P^\circ_4 \rightarrow a^7S_3$	23498.84	8130(220)	6.1(2)	20000	0.30(2)		30.3
$y^7P^\circ_2 \rightarrow a^7S_3$	27728.87	274300(3300)	8.3(2)	13000	1.00		6.6
$y^7P^\circ_3 \rightarrow a^7S_3$	27820.23	0	-	17000	0.00		6.6
$y^7P^\circ_4 \rightarrow a^7S_3$	27935.26	0	-	19000	0.00		6.6

After excitation into the higher energetic y^7P° ($3d^44s4p$) band, also the energetically lower $z^7P^\circ_{2,3,4}$ ($3d^54p$) and $z^5P^\circ_{2,3,4}$ ($3d^54p$) states become populated and free atom allowed transitions from these levels contribute to the observed spectrum. In this case, emission from all substates is clearly present. Even weak transitions of $z^5P^\circ_{2,3} \rightarrow a^5D_{3,4}$

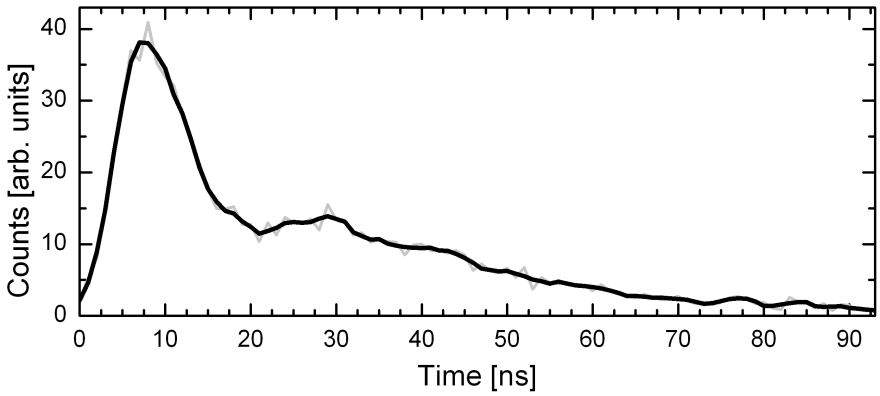

Figure 3.5: $z^5P^\circ \rightarrow a^5S_2$ fluorescence decay after a $y^7P^\circ \leftarrow a^7S_3$ excitation at 28090 cm^{-1}.

could be observed and show similar results. In our recent work [2], we found that the population of the J components decreases from the energetically lowest state ($z^5P^\circ_3$) to that of the energetically highest state ($z^5P^\circ_1$). This could be ascribed to the relaxation process during the ejection of the excited Cr* atom from the droplet. In agreement with this observation, an evaluation of the observed emission intensities in the present work on the basis of known free atom transition probabilities [112] yields very similar level populations as in Ref. [2] (Table 3.1). To obtain the relative populations (rel pop.) of the observed excited states, we fit the dispersed LIF lines in Fig. 3.4 with Gaussian functions. The obtained areas and full widths at half-maxima (FWHM) are listed in Table 3.1. The relative populations are then calculated as the ratios of measured areas to known relative intensities (the results are normalized for each multiplet). Analogously, the averaged relative population from the PI experiments [2] is normalized. Summation of the observed intensities within each multiplet reveals that the total population numbers for z^5P° and z^7P° are approximately equal. The $y^7P^\circ \rightarrow a^7S_3$ emission exceeds the other two transition pathways by more than an order of magnitude. A determination of exact ratios did not seem to be very reliable. The electronic relaxation from y^7P° to $z^7P^\circ_{2,3,4}$ involves a change from a $3d^4 4s4p$ configuration to $3d^5 4p$, similar to that in the relaxation to $z^5P^\circ_{1,2,3}$. Both correspond to forbidden transitions in the free atom becoming allowed due to the surrounding He. Calculations of the Cr-He potential curves could give a deeper insight into the mechanisms which are responsible for the observed relaxations.

For all three branches of emission, a linear increase of fluorescence intensity with laser power up to 9.5 W/cm^2 could be observed. In principle, this is not surprising, because the width of the excitation band is very large, giving rise to an increased saturation intensity.

To explore the time dependence of the relaxation and ejection processes, we monitored the time dependent decay of $y^7P^\circ_2 \rightarrow a^7S_3$ (27736.78 cm^{-1}), $z^7P^\circ \rightarrow a^7S_3$ ($\sim$23400 cm^{-1}),

and $z^5P^\circ \rightarrow a^5S_2$ ($\sim$19200 cm^{-1}) fluorescence after the 20 ns pulse excitation of the $y^7P^\circ \leftarrow a^7S_3$ Cr-in-He$_N$ band. Fig. 3.5 shows the quintet channel decay with a detection limited time resolution of 5 ns. First fluorescence emission is observed shortly after the laser pulse with a time delay barely outside our time resolution. As the low-pass filter reduced the stray light of the 28090 cm^{-1} excitation laser to the noise level of the detector system, the displayed signal resembles the time dependence of this fluorescence channel. A similar structure with two maxima followed by two different tails is observed on the $z^7P^\circ \rightarrow a^7S_3$ channels. The $y^7P^\circ \rightarrow a^7S_3$ fluorescence detection is more strongly biased by the strong laser excitation pulse due to the immediate neighborhood in wavenumber, which does not allow an unambiguous conclusion.

In the following we will summarize the observations and draw conclusions with regard to the relaxation processes.

3.1.4.1 A) Laser Excitation of the $y^7P^\circ \leftarrow a^7S_3$ Transition of Cr Attached to He$_N$

The absorption spectra have a width of about 400 cm^{-1} and are blue shifted by about 300 cm^{-1} compared to the free atom transitions, an observation that is in line with the previous conclusion that Cr is located inside the droplets [2]. After laser excitation, several fluorescence channels are observed with emission linewidths below the monochromator resolution (4 - 8 cm^{-1}), indicating that all emission takes place after ejection of Cr from the droplet. The *"most direct" channel* is represented by the $y^7P^\circ_2 \rightarrow a^7S_3$ fluorescence, irrespective of the excitation wavenumber within the 400 cm^{-1} bandwidth: Fast relaxation into the lowest J-level inside the droplet seems to be followed by ejection from the droplet. This pathway is chosen by the majority of the excited atoms. A *second channel* involves a normally spin-forbidden transition into $z^5P^\circ_{1,2,3}$ and ejection which we had also observed in our PI experiments [2]. In this process which is followed by a few percent of the atoms, the J-level population of $z^5P^\circ_{1,2,3}$ is observed with a similar to that in Ref. [2]. Time resolved measurements (Fig. 3.5) show a first emission peak shortly after the laser pulse. A second, weaker emission maximum follows about 20 ns after the first emission peak with a decay time of 23 $\pm$ 5 ns. The *third channel* is taken by another few percent of the excited atoms with relaxation into the $z^7P^\circ_{2,3,4}$ states followed by ejection and free atom fluorescence. All three J-levels appear about equally populated. Time resolved measurements reveal similar emission characteristics as observed for the quintet state channel. The delayed emission peak with respect to the first fluorescence maximum must be due to a combination of different processes. If Cr atoms inside droplets, excited to higher J-levels (i.e., J= 3,4) of $y^7P^\circ_J$, remain longer in the droplet while relaxing through lower J of y^7P° into z^7P° or z^5P° than those that were originally excited into $y^7P^\circ_2$, such timing of the emission could evolve.

3.1.4.2 B) Laser Excitation of the $z^7P^\circ \leftarrow a^7S_3$ Transition of Cr Attached to He_N

The large width of the excitation spectrum and its blue shift compared to the free atom transition is again in agreement with an in-droplet location of the atom, whereas the narrow fluorescence emission exclusively from the lowest J-level of z^7P° shows that the excited atoms quickly relax into the lowest spin-orbit state followed by ejection from the droplet. No other emission channels than $z^7P^\circ_2 \rightarrow a^7S_3$ are observed which is no surprise because all states that are lower in energy than z^7P° are metastable and would not radiatively decay as free atoms. As the emission after $z^7P^\circ \leftarrow a^7S_3$ excitation was rather weak, we were not able to perform time dependent measurements.

In summary, the excitation of a transition metal atom with rather complex electronic structure in a cold helium environment, is followed by fast relaxation processes involving both spin-orbit interaction and electronic state mixing. Detailed time-resolved measurements of all decay channels after subnanosecond excitation and detection (i.e., shorter PMT transition time) may allow us to collect the data that is necessary to develop a rate equation model for the relaxation of excited Cr in helium droplets.

3.1.5 Acknowledgement

We thank Friedrich Lindebner and Matthias Hasewend for experimental assistance. This work was supported by the Austrian Science Fund (FWF, Grant 22962-N20), as well as the European Commission and the Styrian Government within the ERDF program.

3.1.6 Table of Contents Graphic

The table of contents graphic of Ref. [1] (Fig. 3.6) visualizes the excitation of the solvated Cr a^7S_3 ground state atom with the laser (drawn in blue). The excitation into the $y^7P_{2,3,4}$ states is indicated with an upwards pointing arrow and the subsequent relaxations to the energetically lower states with dashed arrows. Levels drawn outside the droplet indicate the ejection of the Cr atom in the corresponding state. From these, the colored, downwards pointing arrows symbolize the bare atom radiative transitions to the a^7S_3 ground- or a^5S_2 metastable state. The color coding is linked to the markers in the fluorescence spectrum from Fig. 3.4. The latter is plotted vertically in Fig. 3.6 to symbolize that the excitation laser is higher in energy than the observed fluorescence.

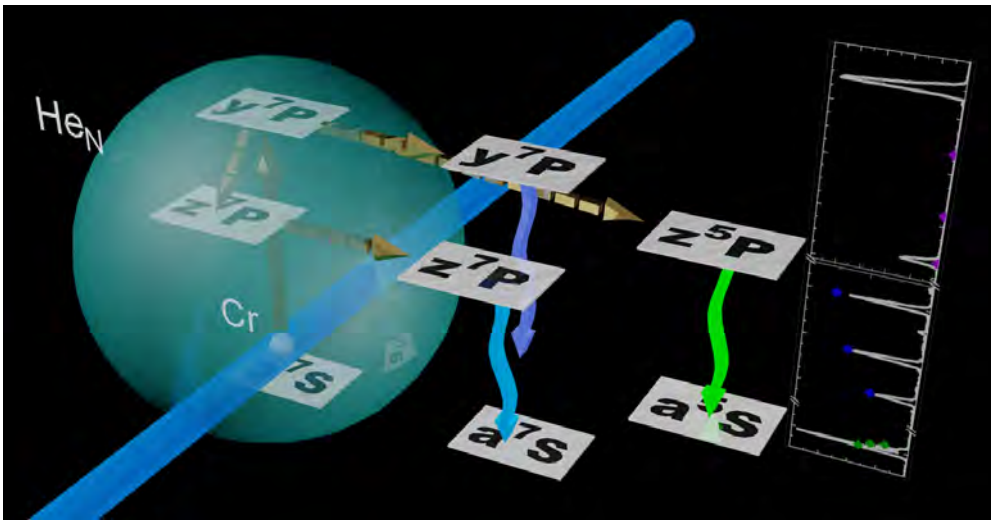

Figure 3.6: Table of contents graphic of Ref. [1]: "Electronic Relaxation after Resonant Laser Excitation of Cr in Superfluid Helium Nanodroplets".

3.2 Beam Depletion - He_N Size Influence

A clear dependence on the droplet size was observed for the depletion signal after the Cr $y^7P^\circ \leftarrow a^7S_3$ excitation (see Fig. 2.8). The best absolute depletion signal was found for nozzle temperatures around 20 K ($r_{droplet} = 2.46$ nm), as discussed in Section 2.3. Referring to the data shown in Fig. 2.8, a relative depletion signal is evaluated according to

$$BD_{\text{relative}} = \frac{BD_{\text{absolute}}}{Counts_{\text{Reference}}}. \tag{3.1}$$

BD_{absolute} is the depletion signal evaluated with Eq. (2.1) and $Counts_{\text{Reference}}$ the amount of Cr doped He_N arriving at the detector without depletion. The goal of the relative BD signal is to denote the reduced He_N flux for very large droplets or high nozzle temperatures.
The relative depletion signal (Eq. (3.1)) for different droplet sizes is plotted in Fig. 3.7 and shows a steady decrease with increasing droplet size. Below a radius of 1.5 nm (T_{nozzle} >24 K), the values are not reliable due to the low absolute signal strength.

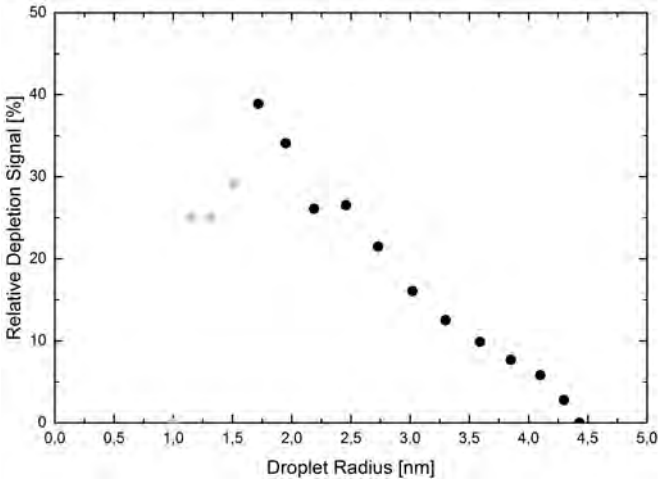

Figure 3.7: Relative Cr-depletion signal (Eq. (3.1)) for the $y^7P^\circ \leftarrow a^7S_3$ excitation ($\tilde{\nu} = 28\,170$ cm^{-1}) in dependence on the droplet size. Values with a high uncertainty are plotted in gray.

It is assumed that two mechanisms are responsible for this observation. First, when the Cr depletion is primarily caused by the ejection of the dopant from the droplet [1, 2], the He shell thickness around the solvated Cr influences the interaction time. If the excited atom has to penetrate more He, the chance to dissipate the excess energy increases. This goes in hand with the increased relaxation to energetically lower states, as suggested in Section 3.6. Dopants remaining in the larger He_N would not contribute to a depletion of the Cr^+ when they arrive at the detector. Alternatively, if depletion is caused by the destruction of droplets with the excess energy introduced by the photons,

smaller droplets can compensate less energy than the larger ones. At higher nozzle temperatures, the fraction of small droplets is increased (see Section 1.3), which means that the number of doped droplets destroyed by the release of the photon energy into the He_N is larger.

3.3 Laser Induced Fluorescence

Fluorescence after the $y^7P^\circ \leftarrow a^7S_3$ excitation of Cr atoms inside He_N is observed from the $y^7P^\circ_2$, $z^7P^\circ_{2,3,4}$, and $y^5P^\circ_{1,2,3}$ states (Section 3.1). Energetically lower states than initially excited are populated by nonradiative relaxation mediated by the droplet. Prior to the high resolution scans shown in Fig. 3.4, low resolution scans were recorded to explore the whole emission spectra (Fig. 3.8). Because of the low monochromator

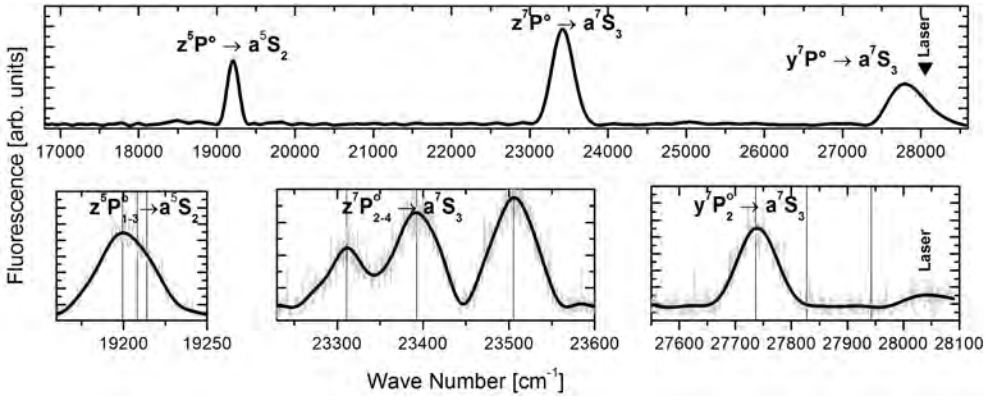

Figure 3.8: Low resolution LIF spectrum after excitation into the y^7P° state (c.f. Fig. 3.4) for a wide (top) and narrow (bottom) monochromator slit width. This spectrum is not corrected for the detection system efficiency.

resolution, the three $z^5P^\circ_{1,2,3} \rightarrow a^5S_2$ spin orbit components appear as one structure. By fixing the known fluorescence line positions [112], three Gaussian peaks were fitted to the structure (see Fig. 3.9a). When comparing the measured fluorescence to literature transition strengths [112], hints for an unequal J-population of the $z^5P^\circ_J$ state are found. From the high resolution spectrum (Fig. 3.4), a clear level population assignment was possible (see Fig. 3.9b) and the results are given in Table 3.1. Furthermore, also with 1CR2PI measurements, these relaxation dynamics are confirmed by evaluating the transitions to AI states (see Section 3.4).

Full relaxation to the lowest J=2 component of the initially excited state ($z^7P^\circ_J$ or $y^7P^\circ_J$) is present for Cr atoms in He_N over the whole droplet broadened excitation region [1]. Hence, it is impossible to distinguish between the excitation regions of the

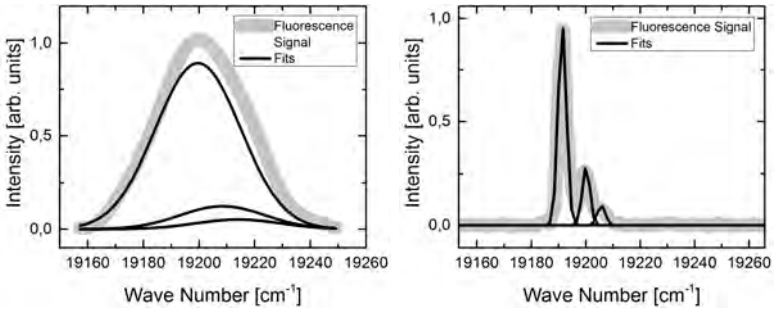

Figure 3.9: Fits for the fluorescence lines from the three $z^5P^\circ_{1,2,3} \rightarrow a^5S_2$ spin-orbit components recorded with (a) the low resolution monochromator (smoothed) and (b) the high resolution spectrograph.

J components with the experimental methods used. This is shown for the $z^7P^\circ \leftarrow a^7S_3$ transition in Fig. 3.3. As explained in Section 3.1, the same was observed for the $y^7P^\circ \leftarrow a^7S_3$ excitation, which is shown here in Fig. 3.10. The pulsed dye laser was used for excitation that caused an ASE peak at $\tilde{\nu} \approx 27800$ cm^{-1}.

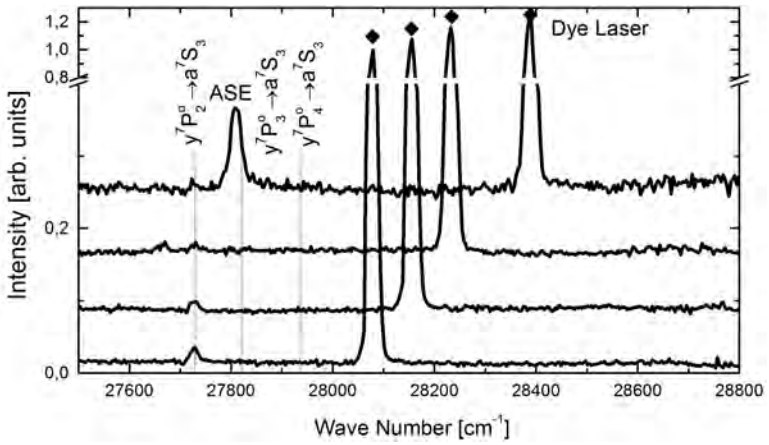

Figure 3.10: "*Dispersed fluorescence of Cr atoms upon excitation through the*" $y^7P^\circ \leftarrow a^7S_3$ "*transition inside* He_N *at differing photon energies (plots mutually shifted in vertical direction, laser marked with squares). Vertical lines indicate the free atom transitions*" [1] $y^7P^\circ_{2,3,4} \rightarrow a^7S_3$ [109]. The feature at $\tilde{\nu} \approx 27800$ cm^{-1} is caused by ASE of the laser.

Figure 3.11 shows the $y^7P^\circ_2 \rightarrow a^7S_3$, $z^7P^\circ \rightarrow a^7S_3$, and $z^5P^\circ_2 \rightarrow a^5S_2$ fluorescence peak heights with respect to the Kr-Ion laser intensity ($y^7P^\circ_2 \leftarrow a^7S_3$ excitation, $\tilde{\nu} = 28048.64$ cm^{-1}). The respective signals are recorded with the low resolution monochromator, therefore all J components of one transition contribute to the signal. Furthermore, the inten-

sities are not corrected for the wavelength dependent detector response. Clearly, the fluorescence intensity increases with laser intensity up to the maximum density of 9.5 W/cm^2 for all three branches of emission. The bare Cr $y^7P^\circ_2 \leftarrow a^7S_3$ saturation intensity (36 W/cm^2 [104]) is beyond the achieved laser intensity and, with the line broadening due to the He_N environment the transition strength is distributed over the whole broadened excitation. Hence, the spectral width of the laser only covers a fraction of the broad absorption band that further increases the saturation intensity.

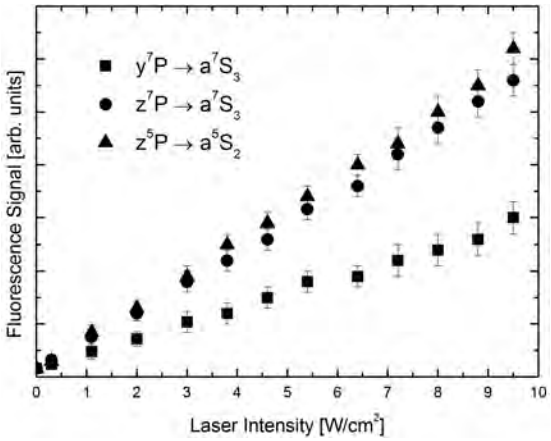

Figure 3.11: LIF intensity after the $y^7P \leftarrow a^7S_3$ excitation in dependence on the Kr-Ion laser intensity. Values are not corrected to the spectral detector response function.

After exciting the $y^7P^\circ \leftarrow a^7S_3$ Cr in He_N transition with the pulsed dye laser, the time dependent fluorescence decay was studied. Figure 3.12b shows the decay of the $y^7P^\circ_2 \rightarrow a^7S_3$, $z^7P^\circ \rightarrow a^7S_3$, and $z^5P^\circ \rightarrow a^5S_2$ fluorescence, as mentioned in Section 3.1. The signals were recorded with different fluorescence filters (see Table 2.4) in front of the PMT. In Fig. 3.12a, the black line represents the time dependent photon counts from the laser pulse and the Cr fluorescence. The gray line is the laser pulse, recorded while the He_N beam was blocked by the chopper that hinders the transportation of Cr to the detection region. Both signals are subtracted to obtain the time dependent fluorescence decay (Fig. 3.12b). Stray light from the laser almost saturates the PMT when the laser photons are not blocked by the BP 350 nm filter. Hence, the $y^7P^\circ_2 \rightarrow a^7S_3$ fluorescence signal is zero between 20 ns and 30 ns, but displays a trend toward the signal observed for the other emission channels. Laser photons are still not fully absorbed by the BP 440 nm filter, but are reduced which hinders the saturation of the detector.
All three fluorescence decay channels show an immediate onset with the laser pulse. This indicates that the relaxation to energetically lower states, enabled by the interaction with the He, has to happen on a very short time scale which is also proven with 1CR2PI (see 3.4).

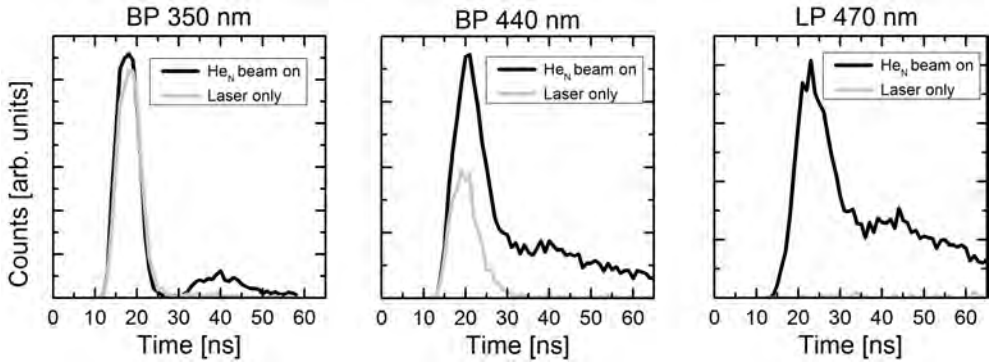

(a)

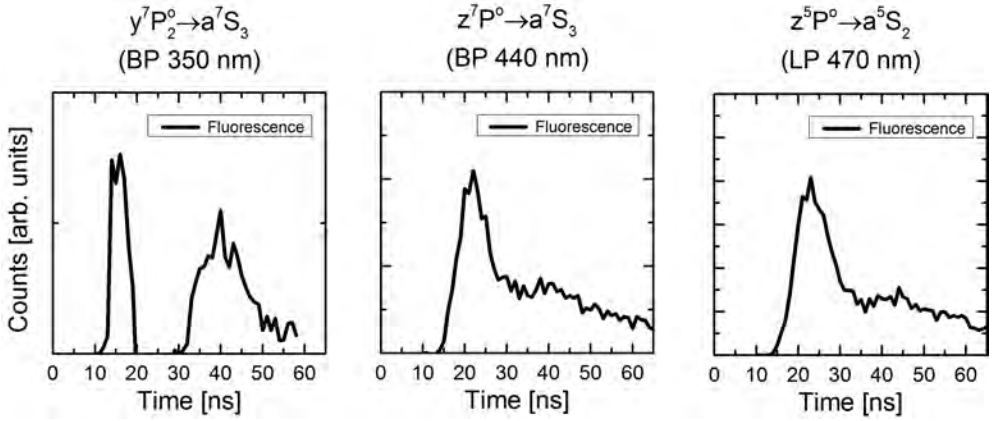

(b)

Figure 3.12: (a) Time evolution of the photon counts with different fluorescence filters in front of the PMT, for an excitation laser pulse at 28090 cm^{-1}. The gray line represents the laser (chopper closed) while the black line is the laser and the Cr fluorescence (chopper open). (b) Difference between the signals in (a), yielding the fluorescence decay of the three emission channels (Fig. 3.8). Time scales are not corrected for the PMT transit time and the charts are not to scale relative to each other.

3.4 Fano Resonances in Chromium Photoionization Spectra After Photoinduced Ejection From a Superfluid Helium Nanodroplet [2]

By applying one-color two-photon ionization, transitions to Cr autoionizing states are found. Relaxation to the intermediate $z^5P^\circ_{1,2,3}$ states after the ejection from the He_N, like observed with dispersed LIF, enabled the transitions to AI states and the observation of Fano resonances with a 1CR2PI scheme.
Sections 3.4.1 and 3.4.2 correspond to the publication "Fano Resonances in Chromium Photoionization Spectra After Photoinduced Ejection From a Superfluid Helium Nanodroplet" (Physical Review A **86** (2012), 033428-1 - 033428-4) by Andreas Kautsch, Matthias Hasewend, Markus Koch, and Wolfgang E. Ernst [2].

The author of this thesis had main contributions on

- All measurement data
- Data evaluation and interpretation
- Text in collaboration with Markus Koch
- Figure 3.14

The contributions of the Co-authors and acknowledged persons were:

- Matthias Hasewend: Experimental assistance
- Markus Koch: Text, Fig. 3.13, experimental collaboration, data evaluation and interpretation, calculating the $g^5D_{J_b} \leftarrow z^5P^\circ_{J_a}$ transition probabilities, funding
- Wolfgang E. Ernst: Proofreading of text, supervision (experiment, publication), funding
- Florian Lackner: Discussions

3.4.1 Abstract

The photoinduced ejection of atoms from superfluid helium nanodroplets is exploited to populate metastable atomic states which cannot easily be reached from the ground state.

We demonstrate this method with chromium (Cr) atoms which are located inside the droplet. The ejection is triggered by the $y^7P^\circ_{2,3,4} \leftarrow a^7S_3$ excitation. Due to relaxation during ejection we obtain bare, excited $Cr^\star$ atoms in the $z^5P^\circ_{1,2,3}$ states. The $Cr^\star$ atoms are photoionized into a region close above the threshold of the a^6S continuum of Cr II. Discrete autoionizing states ($g^5D_{2,3,4}$ and $e^3D_{1,2,3}$) embedded into the continuum are observed as sharp lines with characteristic, asymmetric line profiles. These Fano profiles provide information about the coupling of the autoionizing states to the continuum (autoionization rates) and cross sections for photoionization and resonant excitation. The $g^5D_{2,3,4} \leftarrow z^5P^\circ_{1,2,3}$ line strengths provide insight into the relaxation process, and we find that energetically lower J components of $z^5P^\circ_{1,2,3}$ are significantly more strongly populated.

3.4.2 Fano Resonances in Chromium Photoionization Spectra After Photoinduced Ejection From a Superfluid Helium Nanodroplet

The Fano effect, which arises from interference between different excitation paths, depicts a fundamental aspect of quantum mechanics and manifests itself in asymmetric spectral line profiles. This ubiquitous effect can be observed in photoionization (PI) when the continuum above the ionization threshold can be accessed from a lower state both directly and via a discrete autoionization state which is modified by the correlation interaction with the continuum. The line profile reveals valuable information about the transition strengths of the paths and the autoionization (AI) rate. Although discovered in atomic physics [150, 152], the Fano effect manifests itself in many areas such as electron and neutron scattering [189, 190], matrix isolation spectroscopy [191], photoabsorption in quantum well structures [192], and scanning tunneling spectroscopy [193]. The increasing interest in Fano resonances observed in nanoscale structures has very recently been summarized in a review article [194].

Chromium (Cr) is an outstanding member among the transition metals because of its huge magnetic moment of 6 μ_B arising from half-filled $3d$ and $4s$ subshells (ground-state electron configuration [Ar] $3d^5 4s^1$). Cr has recently attracted interest in astrophysics because of its presence in astronomical objects [188]. PI and electron–ion recombination calculations of neutral Cr have therefore been performed [104, 195], which are in need of experimental verification, especially for PI of excited, metastable states. Resonant two photon ionization of free Cr atoms was applied [104, and references therein], although no attention was devoted to AI states. Also, proposed PI schemes with higher efficiency due to the use of AI states [104] have not been realized experimentally so far.

Superfluid helium nanodroplets (He_N) serve as ideal cryogenic quantum matrix at 0.37 K and have been used for spectroscopic investigations of cold atoms, molecules, and clusters from the microwave regime to the vacuum ultraviolet [9]. Recently we demonstrated the doping of Cr atoms to He_N by mass spectrometry [65]. Most species are

solvated inside the He_N, where spectral features of electronic excitations are significantly broadened and shifted, although much less so than in other matrices. The weak but attractive interaction of the dopant with the He environment can become repulsive upon electronic excitation, leading to dopant ejection [90, 196]. Ejected bare atoms are then available in excited states for further spectroscopic investigations, as was demonstrated with the measurement of the *s* and *d* Rydberg series of Ag atoms [196]. The relaxation process mediated by the He environment is of particular interest, as it provides a way to populate metastable states which can not easily be accessed from the ground state.

Here we study the relaxation of excited $Cr^\star$ atoms upon the photoinduced ejection from He_N. From a line-shape analysis of Fano resonances observed in photoionization via AI states, we deduce the population ratios of different metastable J components, as well as AI rates and ratios of PI cross sections.

The setup follows the design of a He_N isolation spectroscopy apparatus [9, 165]. In the source chamber the He_N beam is formed by a supersonic expansion from a cooled nozzle (5 μm diameter, $p_0 = 50$ bar stagnation pressure, $T_0 = 20$ K temperature, droplet size $\hat{N} \approx 2000$). After collimation the He_N beam is crossed at right angles by an effusive Cr atom beam, facilitating the pickup of, on average, one Cr atom per droplet. The effusive Cr beam is obtained from our home-built electron bombardment source [65], which is heated typically to 1700 °C. It is important to point out that no bare Cr atoms can reach the PI region due to the crossed pickup geometry. The doped He_N then enters the extraction region of a quadrupole mass spectrometer (QMS, Balzers PPM 422), which is located in a separate vacuum chamber. PI is achieved by crossing the He_N beam at right angle with a laser beam. The laser beam is generated by a Lambda Physik 3002 FL dye laser, which is pumped by a pulsed XeCl excimer laser. To avoid saturation, the laser beam is attenuated to obtain a fluence of 0.5 mJ/cm^2 at the PI region. This setup allows us to perform resonance ionization spectroscopy of Cr–He_N complexes with mass-selective ion detection. The PI spectra here are exclusively recorded at 52 u, the mass of the most abundant Cr isotope. It is important to mention that the PI signal is obtained due to successive absorption of two photons at a certain laser wavelength, where the first excitation step takes place inside the He_N and the second step is the PI of the excited $Cr^\star$ atom.

The electron configuration of the Cr a^7S_3 ground state is $3d^5(^6S)4s$. As indicated in Fig. 3.13, Cr is excited via a strongly allowed transition [109, 197] to the $y^7P^\circ_{2,3,4}$ states ($3d^4(^5D)4s4p(^3P^\circ)$ configuration). As will be shown, we find nonradiative relaxation to the $z^5P^\circ_{1,2,3}$ ($3d^5(^6S)4p$) states. A second photon excites to $g^5D_{2,3,4}$ ($3d^44s5s$) and $e^3D_{1,2,3}$ ($3d^44s5s$) states, which lie within several hundred cm^{-1} above the lowest ionization limit at 54575.6 ± 0.3 cm^{-1} [198]. Both are thus energetically capable of electron emission to the a^6S ($3d^5$) level of Cr II.

Figure 3.14 shows the PI spectrum of Cr doped He_N. The droplet broadened feature of the $y^7P^\circ_{2,3,4}$ ($3d^44s4p$) ← a^7S_3 ($3d^54s$) transition is stretched over about 600 cm^{-1} to

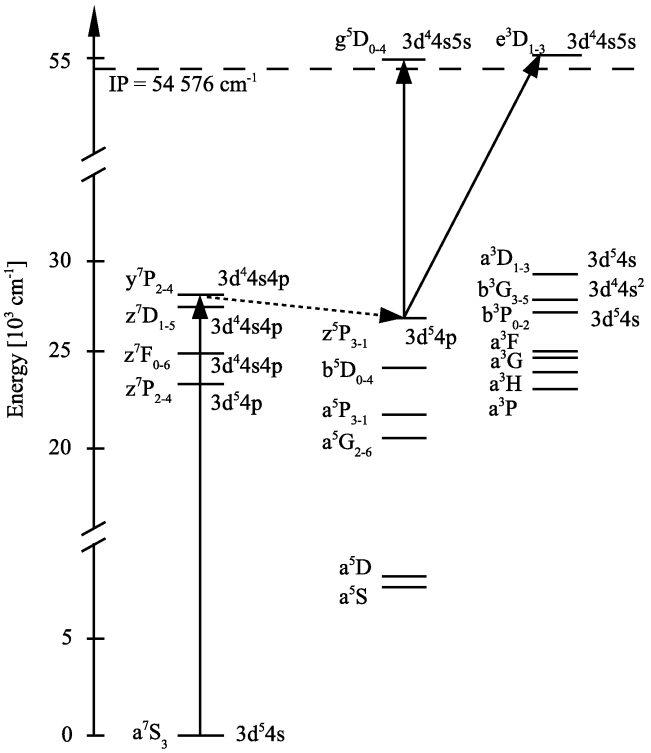

Figure 3.13: Energy-level diagram of gas-phase Cr atoms [109] depicting the laser excitations (solid arrow) and nonradiative relaxation (dashed arrow). Electron configurations are also given. IP indicates the ionization potential.

the blue side of the $y^7P^\circ_{2,3,4}$ states (indicated by vertical bars). This can be compared to the same Cr transitions in rare-gas matrices, where the broadening is about five times larger [75, 92]. It is found there that the spectral perturbation by the matrix strongly depends on the change in electron orbital size during the transition. Blue shifts and line broadenings vary from a few cm^{-1} to several $1000\,cm^{-1}$. Also, due to the matrix, optical transitions with spin and parity forbidden nature become allowed and nonradiative relaxations between systems with different spin multiplicities are observed [75]. In He_N, the Ag transitions $^2P^\circ_{1/2,3/2}$ ($4d^{10}5p$) $\leftarrow$ $^2S_{1/2}$ ($4d^{10}5s$) are broadened by about $500\,cm^{-1}$ ($^2P^\circ_{1/2}$) and $900\,cm^{-1}$ ($^2P^\circ_{3/2}$) [199].

In addition to the broad structure, very sharp spectral features are immediately evident in the spectrum. As indicated in detail at the bottom of Fig. 3.14, these can be identified as transitions of bare Cr atoms from the metastable $z^5P^\circ_{1,2,3}$ states to the $g^5D_{2,3,4}$ (red) and $e^3D_{1,2,3}$ (green) states. The absence of bare Cr atoms in the beam of doped He_N before laser excitation is proven by the lack of sharp features in the spectrum at the positions of the $^7P^\circ_{2,3,4}\leftarrow a^7S_3$ transitions (vertical black lines in Fig. 3.14, this transition is orders of magnitude stronger than other observed transitions [197]).

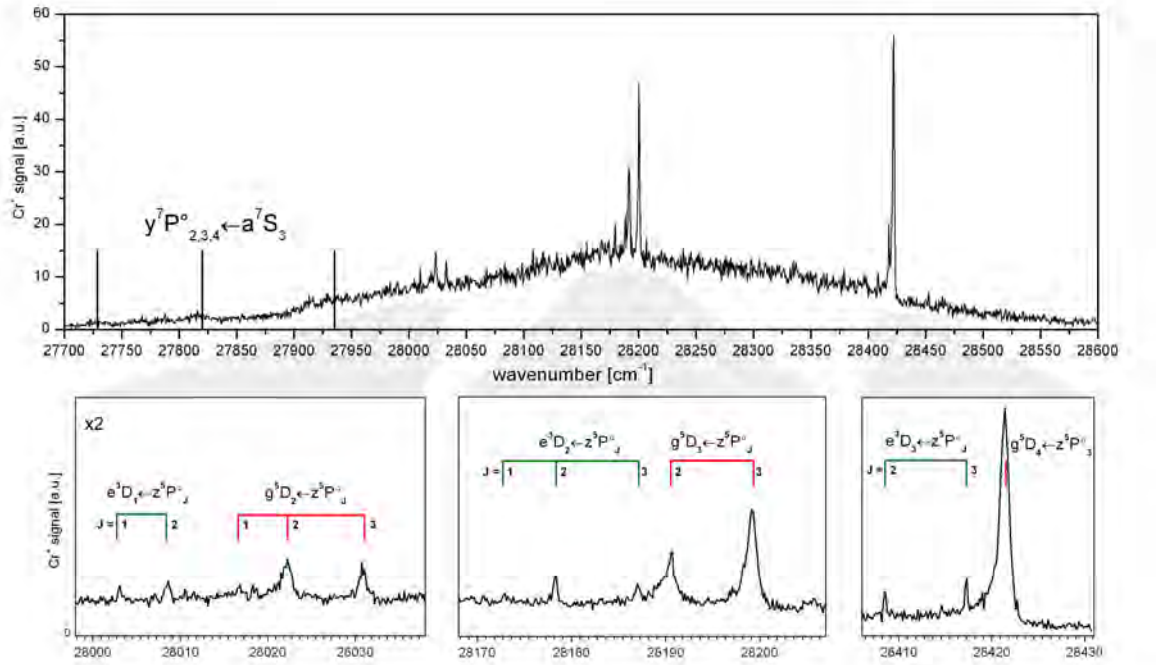

Figure 3.14: One-color two-photon PI spectrum of Cr doped He_N, detected at the Cr mass (52 u). The bare Cr atom transitions $y^7P^\circ_{2,3,4} \leftarrow a^7S_3$ are indicated as vertical lines at 27728.87, 27820.23, and 27935.26 cm^{-1}, respectively [109], and the droplet-broadened excitation is represented by the broad feature. The lower graphs show detailed scans of the AI transitions from $z^5P^\circ_{1,2,3}$ to $g^5D_{2,3,4}$ (red) and to $e^3D_{1,2,3}$ (green). A fit of the Fano line profile convoluted with a Gaussian function (see text) is shown as the dashed line. The spectrum has been normalized according to the laser pulse energy.

The first excitation step to $y^7P^\circ_{2,3,4}$ thus takes place exclusively inside He_N. The appearance of the Cr atom $g^5D_{2,3,4} \leftarrow z^5P^\circ_{1,2,3}$ and $e^3D_{1,2,3} \leftarrow z^5P^\circ_{1,2,3}$ transitions in the spectrum therefore proves that photoinduced ejection of bare, excited $Cr^\star$ atoms and the nonradiative relaxation $y^7P^\circ_{2,3,4} \rightarrow z^5P^\circ_{1,2,3}$ occur. For Ag atoms ejection from He_N upon electronic excitations, $^2P^\circ_{1/2,3/2} \leftarrow {}^2S_{1/2}$ has been observed [90, 196]. Spin relaxation after excitation to $^2P^\circ_{3/2}$ leads to excited $^2P^\circ_{1/2}$ atoms, facilitated by the $^2D_{5/2}$ state during $Ag^\star$–He exciplex formation [90, 200]. For the photoinduced ejection of Cr atoms from He_N we find a substantial change in electron configuration [$z^5P^\circ_{1,2,3}$ ($3d^5 4p$) $\leftarrow$ $y^7P^\circ_{2,3,4}$ ($3d^4 4s4p$)] during relaxation, which corresponds to a spin and parity forbidden transition. A similar relaxation process is observed for Cr in rare-gas matrices: upon excitation to the $y^7P^\circ_{2,3,4}$ states nonradiative relaxation to $a^5P_{1,2,3}$ ($3d^5 4s$), a^5G_{2-6} ($3d^5 4s$), and $a^3P_{0,1,2}$ ($3d^4 4s^2$) is observed [75]. The authors argue that the y^7P° states are shifted to higher energies due to the atom-matrix interaction potential, bringing them into resonance with other states that are less shifted. Between $y^7P^\circ_{2,3,4}$ and $z^5P^\circ_{1,2,3}$ of the free atom, several states are located: $b^3G_{3,4,5}$, $z^7D^\circ_{1-5}$, and $b^3P_{0,1,2}$. Altogether, the observed nonradiative relaxation $y^7P^\circ_{2,3,4} \rightarrow z^5P^\circ_{1,2,3}$ seems reasonable. Whether states close or below the $z^5P^\circ_{1,2,3}$ are as well populated needs further examination. Of special interest here are gerade states (e.g., $b^3G_{3,4,5}$, $b^3P_{0,1,2}$, $a^3F_{2,3,4}$, etc.) as they can not be reached from the ground state via one-photon excitation. Photoinduced ejection from He_N provides a unique method for spectroscopic investigations of such states.

Information about the mechanism of the relaxation process can be gained from the relative populations of the J components of $z^5P^\circ_{1,2,3}$, which are obtained by comparing measured and calculated absorption probabilities of the $g^5D_{J_b} \leftarrow z^5P^\circ_{J_a}$ transitions. Measured absorption probabilities $B_m(J_a, J_b)$ are obtained from the areas of the spectral lines in Fig. 3.14 [integration over a range of four times the full width at half maximum (FWHM) is considered] and relative calculated absorption probabilities $B_c(J_a, J_b)$ from the relation [141]

$$B_c(J_a, J_b) \propto (2J_b + 1) \left\{ \begin{array}{cc} L_a & J_a \; S \\ J_b & L_b \; 1 \end{array} \right\}^2 . \tag{3.2}$$

Relative values of B_m and B_c and their ratio B_m/B_c are listed in Table 3.2. The B_m/B_c ratios have similar values for transitions originating from states with the same J_a component, but vary significantly for different J_a. The population of J components of $z^5P^\circ_{1,2,3}$ increases by a factor of 5 from $J_a = 1$ to $J_a = 2$ and by the same factor from $J_a = 2$ to $J_a = 3$. This is in descending order of energy [109]: $z^5P^\circ_1$ ($26801.93\,cm^{-1}$) $> z^5P^\circ_2$ ($26796.28\,cm^{-1}$) $> z^5P^\circ_3$ ($26787.50\,cm^{-1}$). The same behavior is observed for transitions to e^3D, although less pronounced because of the weaker signal of these transitions and due to the fact that Eq. (3.2) is valid for transitions within the same multiplet, while $e^3D_{J_b} \leftarrow z^5P^\circ_{J_a}$ are quintet-to-triplet transitions. We thus conclude that the relaxation process of excited $Cr^\star$ during ejection from the droplet more strongly populates energetically lower J substates.

Table 3.2: Line parameters of the $g^5D_{0-4} \leftarrow z^5P^\circ_{1,2,3}$ transitions, as defined in the text. ME is the matrix element $\langle g^5 D_{J_b} | 1/r_{12} | a^6 S \varepsilon d \rangle$. The experimental uncertainty in the last digit is given in parentheses

$g^5D_{J_b}$	4	3	2	3	2	2
$z^5P^\circ_{J_a}$	3	3	3	2	2	1
B_m	1.00(2)	0.22(2)	0.03(2)	0.13(2)	0.07(2)	0.02(2)
B_c	1.00	0.26	0.04	0.73	0.45	0.45
$\frac{B_m}{B_c}$	1.00(2)	0.86(6)	0.73(45)	0.17(2)	0.15(4)	0.04(4)
q	-13(2)	-7(2)	-18(4)	-8(2)	-7(2)	4(4)
$\Gamma[\mathrm{cm}^{-1}]$	0.77(8)	0.85(8)	0.57(11)	0.96(10)	0.83(8)	0.61(12)
ME $[\mathrm{cm}^{-1}]$	0.35(3)	0.37(4)	0.30(6)	0.39(4)	0.36(4)	0.31(6)
A $[10^{11}\mathrm{s}^{-1}]$	1.4(1)	1.6(1)	1.1(2)	1.8(2)	1.6(2)	1.1(2)
$\frac{\sigma_a}{\sigma_b}$	0.27	0.14	0.003	0.05	0.04	0.04

Closer inspection of the $g^5D_{2,3,4} \leftarrow z^5P^\circ_{1,2,3}$ and $e^3D_{1,2,3} \leftarrow z^5P^\circ_{1,2,3}$ transitions in Fig. 3.14 reveals asymmetric line profiles, which are characteristic for transitions to discrete states embedded in a continuum of states. The Fano-type cross-section profile of a PI absorption line is represented by [150, 151]

$$\sigma = \sigma_a \left[\frac{(q+\varepsilon)^2}{(1+\varepsilon^2)} \right] + \sigma_b, \quad \varepsilon = \frac{E - E_0}{\Gamma/2}, \tag{3.3}$$

where q is a phenomenological shape parameter and Γ represents the line width. σ_a and σ_b are the PI cross sections to the interacting and non-interacting parts of the continuum [151] (see below). ε is the relative energy distance from the unperturbed line position E_0. The line parameters listed in Table 3.2 are obtained by fitting a convolution of Eq. (3.3) with a Gaussian function to the measured line profiles (dashed line in Fig. 3.14). The Gaussian function accounts for the estimated spectral width of the laser and has a FWHM of $0.2\,\mathrm{cm}^{-1}$. The shape of the Fano profile (on the sides of constructive and destructive interference) is comparable to the calculated PI cross section of this transition [195]. The predicted line width, however, is considerably larger. This may be caused by the uncertainty in the calculated spectrum as many lines in the close neighborhood of the transition are not assigned.

The lineshape parameters (q, Γ, σ_a and σ_b) represent a unique way to determine the sign and magnitude of the matrix elements for PI and AI according to the following considerations: AI of a discrete state (e.g., g^5D) above the ionization limit (a^6S) is possible into continuum states εl of nearly the same energy ε and the same angular momentum l. The corresponding configuration interaction matrix element (ME) is

connected to Γ by [151]

$$\Gamma = 2\pi \left\langle \mathrm{g^5D}_{J_\mathrm{b}} | 1/r_{12} | \mathrm{a^6S}\varepsilon\mathrm{d} \right\rangle^2 . \tag{3.4}$$

Calculated values of this ME are listed in Table 3.2, together with AI rates $A = 1/\tau = \Gamma/\hbar$ (τ is the lifetime of the AI states) [151]. The obtained $\mathrm{g^5D}$ AI rates are in good agreement with the calculated values of $2.0 \cdot 10^{11}\,\mathrm{s^{-1}}$ [104].

The asymmetry parameter q is determined by, additionally to the AI ME [Eq. (3.4)], the two different excitation paths, one from the lower state to the embedded discrete state ($\langle \mathrm{g^5D}_{J_\mathrm{b}} | \mu | \mathrm{z^5P}_{J_\mathrm{a}} \rangle$ [2]) and one from the lower state to the part of the continuum that mixes with the discrete state ($\langle \mathrm{a^6S}\varepsilon\mathrm{d} | \mu | \mathrm{z^5P}_{J_\mathrm{a}} \rangle$):

$$q = \frac{\langle \mathrm{g^5D}_{J_\mathrm{b}} | \mu | \mathrm{z^5P}_{J_\mathrm{a}} \rangle}{\pi \langle \mathrm{g^5D}_{J_\mathrm{b}} | 1/r_{12} | \mathrm{a^6S}\varepsilon\mathrm{d} \rangle \langle \mathrm{a^6S}\varepsilon\mathrm{d} | \mu | \mathrm{z^5P}_{J_\mathrm{a}} \rangle} \tag{3.5}$$

μ is the component of the dipole moment parallel to the photon polarization. If either the ME for PI or that for the transition from the lower to the upper discrete state is known (e.g., from saturation measurements or Hartree–Fock calculations) the other can be calculated. As indicated in Eq. (3.3), PI from the lower state ($\mathrm{z^5P^\circ}$) into two distinct parts of the continuum has to be considered: into the part of the continuum that interacts with the discrete state ($\mathrm{a^6S}\varepsilon\mathrm{d}$, $\sigma_\mathrm{a} \propto \langle \mathrm{a^6S}\varepsilon\mathrm{d} | \mu | \mathrm{z^5P}_{J_\mathrm{a}} \rangle^2$) and into the noninteracting part of the continuum ($\mathrm{a^6S}\varepsilon\mathrm{s}$, $\sigma_\mathrm{b} \propto \langle \mathrm{a^6S}\varepsilon\mathrm{s} | \mu | \mathrm{z^5P}_{J_\mathrm{a}} \rangle^2$). It is important to note, however, that other states (e.g., $\mathrm{b^3G}$, $\mathrm{z^7D}$ and $\mathrm{b^3P}$), which might be populated by nonradiative relaxation from $\mathrm{z^5P^\circ}$, could contribute to σ_b, but not to σ_a. The ratio $\sigma_\mathrm{a}/\sigma_\mathrm{b}$ (Table 3.2) is almost always below 10%, which indicates that other states in addition to $\mathrm{z^5P^\circ}$ are populated by the relaxation process.

In conclusion, we demonstrate an advanced photoionization method for Cr atoms with resonant transitions from high-lying metastable to autoionizing states. In the intermediate state, the energetically lower J substates turned out to be preferentially populated due to the non-radiative relaxation upon photoinduced ejection from a superfluid He nanodroplet. Autoionization rates of $1.1 - 1.8 \cdot 10^{11}\,\mathrm{s^{-1}}$ ($\mathrm{g^5D}$) were determined from Fano-shaped asymmetric lines with negative q values.

We thank Florian Lackner for helpful discussions. This work was supported by the Austrian Science Fund (FWF, Grant No. 22962-N20), as well as the European Commission and the Styrian Government within the ERDF program.

[2] In a zero order approximation [151], the mixing of the discrete state is neglected in the matrix element for the resonant transition.

3.5 Photoionization

3.5.1 Transitions to Autoionizing States

Transitions from the intermediate z^5P° state to the autoionizing g^5D and e^3D states were observed as sharp peaks in the 1CR2PI Cr spectrum. Because these transitions were observed for ejected bare atoms, they are restricted by the transition rules ΔJ = -1,0,1 and $\Delta S = 0$. Hence, quintet-triplet transitions are weaker, and transitions violating ΔJ = -1,0,1 are not observed. Transition energies were calculated from the known level energies [112] and are listed in table 3.3 (observed transitions are printed in bold).

Table 3.3: Energies of ΔJ allowed transitions from the z^5P° to the g^5D and e^3D [112] states. Observed transitions are printed in bold. Energies are given in cm^{-1}.

	Intermediate State	$z^5P^\circ_1$ 26801.93 cm^{-1}	$z^5P^\circ_2$ 26796.28 cm^{-1}	$z^5P^\circ_3$ 26787.50 cm^{-1}
AI State				
g^5D_0	54646,20 cm^{-1}	27844,27		
g^5D_1	54671,90 cm^{-1}	27869,97	27875,62	
g^5D_2	54818,55 cm^{-1}	**28016,62**	**28022,27**	**28031,05**
g^5D_3	54986,82 cm^{-1}		**28190,54**	**28199,32**
g^5D_4	55209,01 cm^{-1}			**28421,51**
e^3D_1	54804,69 cm^{-1}	**28002,76**	**28008,41**	
e^3D_2	54974,64 cm^{-1}	**28172,71**	**28178,36**	**28187,14**
e^3D_3	55204,79 cm^{-1}		**28408,51**	**28417,29**

3.5.2 Cr*-He Exciplex Formation During Ejection

Transitions to autoionizing states were attributed to free atoms because of their sharp peaks at the free atom transition energies. Similarly, the observation of sharp fluorescence lines (Section 3.1) is attributed to the same mechanism. To prove these results with another approach, mass scans were performed with the laser on the $g^5D_3 \leftarrow z^5P^\circ_3$ autoionization peak and slightly beside (+10 cm^{-1}). Both wavelengths are indicated in the spectrum in Fig. 3.15a. Ion counts (Fig. 3.15b) are integrated for each mass and plotted in Fig. 3.15c for better visibility. The Cr^+ isotopes appear in accordance with the natural abundances (4.3% ^{50}Cr, 83.8% ^{52}Cr, 9.5% ^{53}Cr, and 2.4% ^{54}Cr), and give rise to a constant background signal that is independent of small laser wavelength variations within the strong broadening of the ground state transition. The Cr^+ ion yield is increased for ionizing through the AI state after the $g^5D_3 \leftarrow z^5P^\circ_3$ transition, whereas the Cr^+-He signal is independent of the wavelength. The ejected bare atoms in

the $z^5P_3^\circ$ state have a larger ionization cross section when the photon energy meets the $g^5D_3 \leftarrow z^5P_3^\circ$ transition, giving a higher ion yield at the bare Cr masses. Cr^+-He can form from two ionization paths, that are again independent of low laser wavelength variations with the strong broadening of the ground state transition: A Cr ionized inside the droplet (path 1) destroys- or detaches from the droplet with a He atom remaining attached, or a $Cr^\star$-He exciplex leaves the droplet after the first excitation and is ionized into continuum states (path 2). For both paths, the AI is not accessible because that requires the $g^5D_3 \leftarrow z^5P_3^\circ$ bare atom transition in advance. The constant Cr^+-He ion signal therefore proves that solely bare atoms in the $z^5P_3^\circ$ are responsible for the AI peaks.

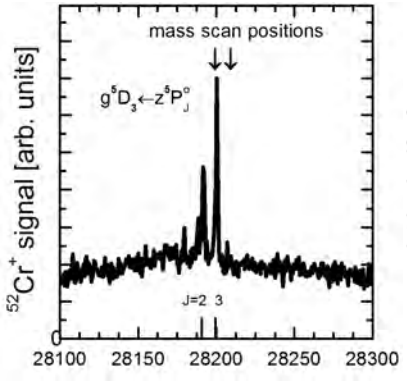

(a) Photon energy for the mass spectra.

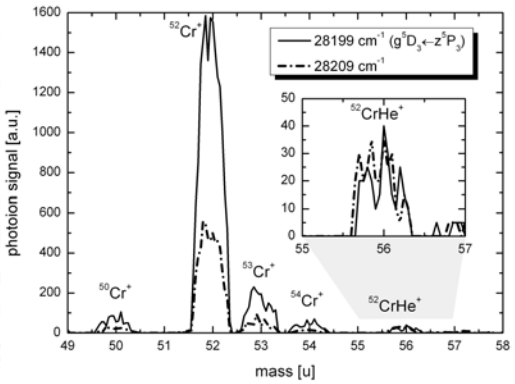

(b) Scans across the Cr^+ and $CrHe^+$ mass region.

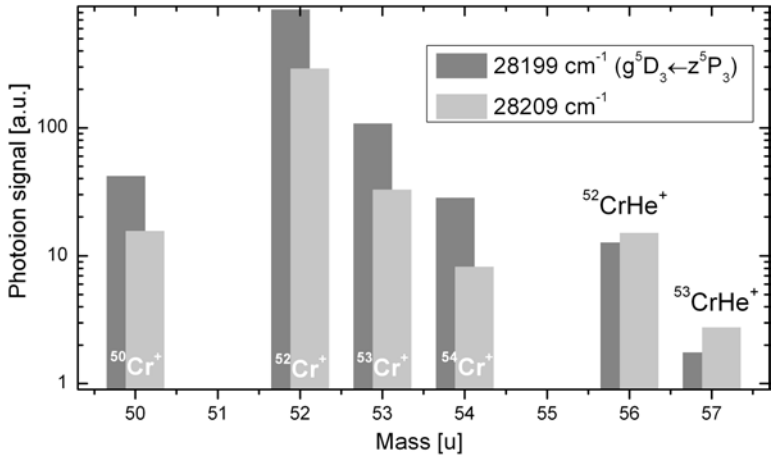

(c) Peak areas in 3.15b.

Figure 3.15: Mass scans for 1CR2PI of Cr in He_N at $\tilde{\nu} = 28\,199$ cm^{-1} and $\tilde{\nu} = 28\,209$ cm^{-1}.

3.6 One- and Two-Color Resonant Photoionization Spectroscopy of Chromium-Doped Helium Nanodroplets [3]

The results for one-color R2PI are now compared to two-color R2PI of Cr in He_N. With the XeCl laser present for two-color R2PI, the formation of $Cr^{\star}$-He_n exciplexes in different states is found. Furthermore, a systematic study of the z^5P state population with droplet size, obtained from the autoionization transition strength in 1CR2PI (see Section 3.4), is used to evaluate the properties of the relaxation processes.
Sections 3.6.1 to 3.6.6 correspond to the publication "One- and Two-Color Resonant Photoionization Spectroscopy of Chromium-Doped Helium Nanodroplets" by Markus Koch, Andreas Kautsch, Florian Lackner, and Wolfgang E. Ernst [3]. This article is part of the JPCA "A. W. Castleman, Jr. Festschrift".

The author of this thesis had main contributions on

- All measurement data
- Data evaluation and interpretation
- Preliminary version of text, collaboration for final text
- Figures and artwork

The contributions of the Co-authors and acknowledged persons were:

- Markus Koch: Final text, interpretation of relaxation mechanisms, funding
- Florian Lackner: *Introduction* text, collaboration for text
- Wolfgang E. Ernst: Proofreading of text, supervision (experiment, publication), funding
- Matthias Hasewend: Experimental assistance for 1CR2PI and preliminary 2CR2PI measurements
- Friedrich Lindebner: Experimental assistance for 2CR2PI measurements
- Johann V. Pototschnig: Discussing computational results
- Martin Ratschek: Discussing computational results

3.6.1 Abstract

We investigate the photoinduced relaxation dynamics of Cr atoms embedded into superfluid helium nanodroplets. One- and two-color resonant two-photon ionization (1CR2PI and 2CR2PI, respectively) are applied to study the two strong ground state transitions $z^7P^\circ_{2,3,4} \leftarrow a^7S_3$ and $y^7P^\circ_{2,3,4} \leftarrow a^7S_3$. Upon photoexcitation, $Cr^\star$ atoms are ejected from the droplet in various excited states, as well as paired with helium atoms as $Cr^\star$-He_n exciplexes. For the $y^7P^\circ_{2,3,4}$ intermediate state, comparison of the two methods reveals that energetically lower states than previously identified are also populated. With 1CR2PI we find that the population of ejected $z^5P^\circ_3$ states is reduced for increasing droplet size, indicating that population is transferred preferentially to lower states during longer interaction with the droplet. In the 2CR2PI spectra we find evidence for generation of bare Cr atoms in their septet ground state (a^7S_3) and metastable quintet state (a^5S_2), which we attribute to a photoinduced fast excitation-relaxation cycle mediated by the droplet. A fraction of Cr atoms in these ground and metastable states is attached to helium atoms, as indicated by blue wings next to bare atom spectral lines. These relaxation channels provide new insight into the interaction of excited transition metal atoms with helium nanodroplets.

3.6.2 Introduction

The advent of helium nanodroplets (He_N) has spawned many new vistas in the field of matrix isolation spectroscopy [9, 12]. Various fascinating spectroscopic experiments have been enabled by helium nanodroplet isolation spectroscopy, among them the study of the phenomenon of superfluidity from a microscopic perspective [201, 202] or the investigation of high-spin molecules [203–205]. Helium droplets as well as bulk superfluid helium [86] offer a unique spectroscopic matrix because of the weak interaction with dopants. He_N with an internal temperature of 0.37 K can be easily combined with many spectroscopic techniques. Utilizing the method of resonant multiphoton ionization (REMPI) spectroscopy for the investigation of doped helium nanodroplets is well established and has recently enabled the study of unusual alkali metal-(He_N) Rydberg complexes [50, 177, 206–208] as well as tailored molecules and clusters [209–211].
The investigation of complex magnetic phenomena in small nanoclusters is of interest for both fundamental theory of magnetism and the development of novel electronic devices. In this context, chromium (Cr) atoms with their huge magnetic moment [212] are of special interest. Cr nanoclusters exhibit a rich magnetic behavior and unusual properties, which are highly dependent on their geometric structure and spin configuration. A fundamental example of such an unusual and spin-dependent effect is the Kondo response of the triangular Cr trimer [213]. Helium nanodroplets are known to favor the formation of high-spin species [204], which may offer a convenient way for the selective preparation of high-spin Cr nanoclusters and their subsequent surface

deposition [55, 214] under soft landing conditions [215].
Recently, we started the investigation of Cr atoms and clusters embedded in He_N [1, 2, 65]. Mass spectroscopic studies demonstrated the formation of clusters consisting of up to 9 Cr atoms [65]. To gain deeper insight into the interaction between Cr atoms and the helium droplet, we focused on the spectroscopic study of single isolated Cr atoms in He_N. These experiments shine light on the influence of the droplet on the electronic structure of the Cr atom as well as photoinduced dynamics by utilizing various spectroscopic methods such as laser-induced fluorescence (LIF) spectroscopy, beam depletion (BD) spectroscopy and one-color resonant two-photon ionization (1CR2PI). Our previous studies cover the $y^7P^\circ_{2,3,4}$ and $z^5P^\circ_{1,2,3}$ states. The $y^7P^\circ_{2,3,4}$←a^7S_3 transition appears broadened ($600\,cm^{-1}$) and blue-shifted. In addition, transitions to discrete autoionizing (AI) states ($g^5D_{2,3,4}$ and $e^3D_{1,2,3}$), which are interacting with the ionization continuum [2], were observed. Dispersed LIF spectra recorded upon excitation to $y^7P^\circ_{2,3,4}$ show narrow band bare atom emission from the $y^7P^\circ_2$, $z^5P^\circ_{1,2,3}$, and $z^7P^\circ_{2,3,4}$ states [1]. Both observations demonstrate that a fraction of the Cr atoms is ejected from the droplets upon photoexcitation to the $y^7P^\circ_{2,3,4}$ states. These experiments show that the dynamic processes induced by photoexcitation are governed by nonradiative, droplet-mediated relaxation mechanisms that result in the formation of bare $Cr^\star$ atoms in various excited and metastable states.
In this article we extend our studies to previously uninvestigated spectral regimes. The utilization of two-color resonant two-photon ionization (2CR2PI) spectroscopy via the two strong ground state transitions ($z^7P^\circ_{2,3,4} \leftarrow a^7S_3$ and $y^7P^\circ_{2,3,4} \leftarrow a^7S_3$) offers new insights into the photoinduced dynamics of Cr-He_N and the interactions between Cr and He_N. 2CR2PI can be applied to energetically lower states due to the addition of a second laser with higher photon energy. In addition to the observation of bare atoms, we discuss the photoinduced generation of ground state Cr-He_n complexes and excited $Cr^\star$-He_n exciplexes. The formation of complexes consisting of excited atoms or molecules with several attached helium atoms is a general process initiated by the excitation of foreign species embedded in helium nanodroplets. These neutral "exciplexes" have been observed for example for surface bound atoms such as alkali metal [216–222] atoms and molecules and alkaline-earth metal atoms [223] as well as for species located inside the droplet [68, 90]. Here we show that not only bare Cr atoms relax into the quintet or septet ground state but also the observed Cr-He_n complexes. Different ionization pathways that are competing with relaxation mechanisms are reflected in the difference between 1CR2PI and 2CR2PI spectra. The study of the droplet size dependence of a selected transition shows additional characteristics about the relaxation and ejection mechanisms.

3.6.3 Experimental Section

The experimental setup has been described in detail in previous publications [1, 2, 4, 165]. In brief, the He_N beam is formed in a supersonic expansion of helium gas (purity 99.9999%) from a cooled nozzle (5 μm diameter, $p_0 = 50$ bar stagnation pressure, and $T_0 = 10 - 24$ K temperature). The droplet size is controlled by T_0 and follows a log–normal distribution with maximum values in the range $\hat{N} \approx 350$ ($T_0 = 24$ K) to $\hat{N} \approx 8300$ ($T_0 = 13$ K). The droplet beam is crossed at right angles along 10 mm of its path by an effusive Cr atom beam obtained from a home-built high temperature electron bombardment source arranged parallel below the droplet beam [65]. With this crossed beam geometry - and additional five small apertures to collimate the droplet beam - it can be ensured that no free atoms reach the detector. The heating power of the Cr source is optimized for single atom pick up (∼1700°C). The beam of Cr-doped He_N is crossed at right angles by laser beams inside the extraction region of a quadrupole mass spectrometer (QMS, Balzers QMG 422). This setup allows 1CR2PI and 2CR2PI mass spectroscopy where either the laser wavelength is scanned and the mass filter is set to the most abundant Cr isotope of 52 u (56 u for Cr–He) or the detected mass is scanned for a fixed laser wavelength. For 2CR2PI one laser is always kept at a constant wavelength of 308 nm (32 468 cm^{-1}).

For 1CR2PI the laser pulses are obtained from a dye laser (Lambda Physik FL3002, dyes: RDC 360 Neu for 27 600–28 800 cm^{-1}, Stilben 3 for 23 200–23 900 cm^{-1}, and Coumarin307 for 19 100–20 100 cm^{-1}) pumped by an excimer laser (Radiant Dyes RD-EXC-200, XeCl, 308 nm $\hat{=}$ 32468 cm^{-1}, ∼20 ns pulse duration, 100 Hz repetition rate). For 2CR2PI a fraction of the 308 nm light is branched off and guided to the ionization region. The temporal overlap with the ∼15 ns dye laser pulses is set to >10 ns. Both laser beams are moderately focused to a spot size of ∼5 mm^2. For the two-color experiment both lasers are attenuated best possible to reduce the probability of dopant ionization by photons of a single wavelength. Reasonable pulse energies were found within 0.3-0.6 mJ for all four laser wavelength regimes (Stilben 3, RDC 360 Neu, Coumarin 307, and XeCl laser).

In principle, R2PI occurs via the absorption of two photons, which can be of the same or of different colors (1CR2PI and 2CR2PI, respectively). The tunable laser is scanned across a resonant state while the ion yield is recorded as a function of laser wavelength. For 2CR2PI a second laser with constant wavelength is present. Relaxation mechanisms after the first absorption step have to be taken into account. The energy level diagram of selected Cr atomic states [109] is shown in Figure 3.16 together with various excitation and ionization paths for 1CR2PI and 2CR2PI. Due to the Cr ionization limit at 54 575.6 ± 0.3 cm^{-1} [198] a successive absorption of at least two photons is required for ionization. The first step of the R2PI scheme is an excitation from the a^7S_3 ground state (electron configuration: $3d^54s$) to the excited states $z^7P^\circ_{2,3,4}$

($3d^5 4p$) or $y^7P^\circ_{2,3,4}$ ($3d^4 4s4p$). The observed broadening and blue shift induced by the He_N are indicated as shaded areas above these levels. Both ground state excitations are accomplished by the tunable dye lasers in the regime of 23 200–23 900 cm^{-1} for $z^7P^\circ_{2,3,4}$ (red arrow in Figure 3.16) and 27 600–28 800 cm^{-1} for $y^7P^\circ_{2,3,4}$ (blue arrow). Upon excitation to $z^7P^\circ_{2,3,4}$ only a XeCl laser photon of 32 468 cm^{-1} (black arrow) has sufficient energy for ionization whereas for the $y^7P^\circ_{2,3,4}$ states photons of both the dye laser and the XeCl laser are able to ionize. The lower limit for PI with a single XeCl laser photon is marked by a dotted horizontal line. As indicated by the results, bare ground and metastable state Cr atoms and Cr-He_n complexes are produced in the course of 2CR2PI.

3.6.4 Results and discussion

3.6.4.1 $y^7P^\circ_{2,3,4} \leftarrow a^7S_3$ Excitation

We begin with the 2CR2PI excitation spectrum of the $y^7P^\circ_{2,3,4}$ ($3d^4 4s4p$) $\leftarrow a^7S_3$ ($3d^5 4s$) transition (bottom of Figure 3.17) because it can be compared with the 1CR2PI spectrum of our previous work (top of Figure 3.17) [2]. Cr^+ ions, which are detected at 52 u, are produced by in-droplet excitation with the tunable dye laser to the intermediate $y^7P^\circ_{2,3,4}$ states and subsequently ionized by a second photon either from the dye laser (1CR2PI) or from the XeCl laser (2CR2PI). In both $^{52}Cr^+$-spectra the width of the droplet broadened feature appears stretched over about 600 cm^{-1} to the blue side of the $y^7P^\circ_{2,3,4} \leftarrow a^7S_3$ bare atom transitions [109] (indicated by triangles in Figure 3.17). This is also in agreement with BD and LIF spectra [1]. As discussed in more detail in ref. [2], this broadening depends on the change in electron configuration and is moderate compared to the same Cr transitions obtained in heavy rare-gas matrices [75] and comparable to the excitation spectra of other atomic species in He_N [199]. Although the onset of the broad structure occurs at the same wavelength in both cases, the 2CR2PI spectrum shows an additional shoulder in the range of 27 900–28 100 cm^{-1} compared to the 1CR2PI spectrum. Upon in-droplet $y^7P^\circ_{2,3,4}$ excitation, ejection of bare Cr atoms in excited $z^5P^\circ_{1,2,3}$ states has previously been identified [1, 2]. We take this increased signal in the 2CR2PI spectrum as indication for additional relaxation to states below $z^5P^\circ_{1,2,3}$. Because of the higher photon energy available in 2CR2PI (XeCl laser at 32 468 cm^{-1}) as compared to 1CR2PI, a number of excited states that may be populated (e.g., a^3P, z^7P°, a^3H, b^5D, a^3G, a^3F, z^7P°, c.f., Figure 3.16) can add to the PI signal in the 2CR2PI scheme but not in 1CR2PI.

A 2CR2PI scan in the same spectral region with the mass filter tuned to the $^{52}Cr^+$-He mass (gray line in Figure 3.17, bottom) reveals a spectrum that is comparable in shape to the $^{52}Cr^+$ signal. This proves the formation of $Cr^\star$-He exciplexes during the relaxation–ejection process. The $^{52}Cr^+$-He signal is much weaker than that of $^{52}Cr^+$

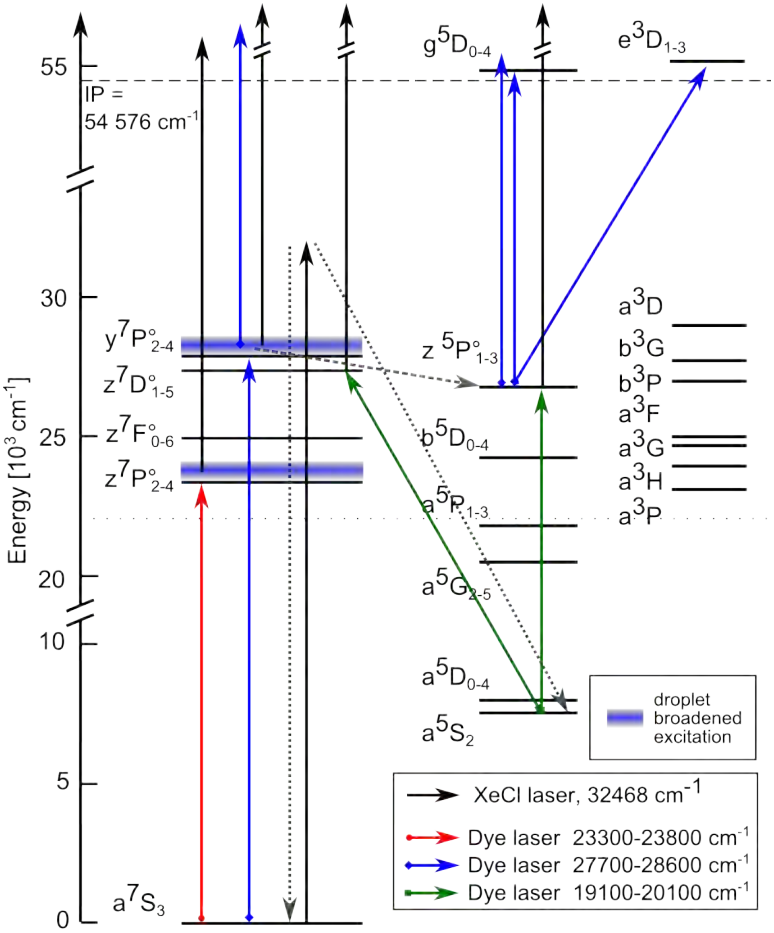

Figure 3.16: Energy level diagram for bare Cr atoms [109] showing 1CR2PI and 2CR2PI paths as combination of dye- and XeCl laser excitations and ionizations. The shaded areas above the $z^7P^\circ_{2,3,4}$ and $y^7P^\circ_{2,3,4}$ states indicate the droplet broadened and shifted excitation region. The dashed arrows indicate nonradiative relaxation paths. The dotted horizontal line at $22\,108\,\mathrm{cm}^{-1}$ marks the lower limit above which ionization with a single XeCl laser photon ($32\,468\,\mathrm{cm}^{-1}$) is possible.

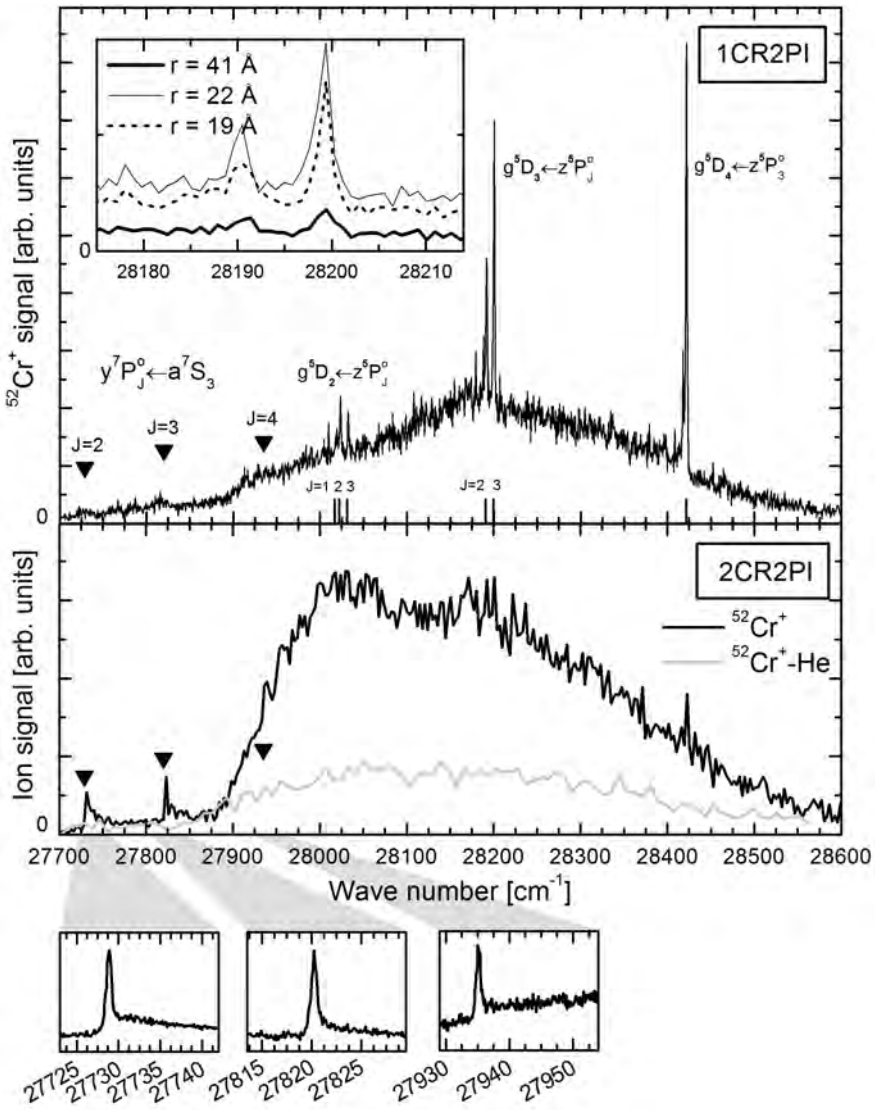

Figure 3.17: Top: 1CR2PI spectrum of the $y^7P^\circ_{2,3,4}$ ($3d^44s4p$) ← a^7S_3 ($3d^54s$) transition recorded by detecting $^{52}Cr^+$ [2]. Bare atom ground state transitions are indicated by triangles [109]. The sharp lines can be assigned to transitions of bare, excited atoms to autoionizing states. The spectrum was recorded with $T_0 = 20\,\mathrm{K}$, and the inset shows scans in the $g^5D_3 \leftarrow z^5P^\circ_{2,3}$ region for other droplet sizes. Bottom: 2CR2PI spectrum of the same transition at comparable conditions, detected at the $^{52}Cr^+$ mass (52 u, black curve) and $^{52}Cr^+$-He mass (56 u, gray curve). Different scaling factors are used for the two spectra. Detailed scans in the region of bare atom transitions are also shown.

(different scaling factors have been used for the two traces). However, no conclusions can be drawn about the $Cr^\star$ / $Cr^\star$-He ratio because excess energy of the ionizing photon leads to fragmentation of the exciplexes at an unknown rate.

The appearance of sharper features also depends on the ionization scheme. In the 1CR2PI spectrum (Figure 3.17, top) sharp lines above 28 000 cm^{-1} represent the bare atom transitions from the excited $z^5P^\circ_{1,2,3}$ to the autoionizing states $g^5D_{2,3,4}$ and $e^3D_{1,2,3}$, as described in detail in ref. [2]. These transitions are barely visible in the 2CR2PI spectrum (Figure 3.17, bottom black curve). Upon ejection of excited $Cr^\star$, the presence of XeCl radiation in the 2CR2PI scheme provides a second ionization channel. This leads to a strong increase of PI into the continuum that apparently outweighs the transition to an AI state by a second resonant dye laser photon. Below 28 000 cm^{-1}, narrow structures are present at the bare atom $y^7P^\circ_{2,3,4} \leftarrow a^7S_3$ line positions in the 2CR2PI spectrum but not at all in the 1CR2PI spectrum. These asymmetric lines with a wing on the blue side are present in neither the BD nor LIF spectra [1]. We take these features as proof for the generation of bare, ground state (a^7S_3) Cr atoms and Cr-He_n molecules related to XeCl laser excitation of the 2CR2PI scheme (see discussion below). Due to our crossed pickup geometry we can exclude that bare atoms reach the ionization region directly. This is proven by two facts: first, without helium droplets but with a heated Cr source, we see absolutely no ion signal and, second, the 1CR2PI spectrum (Figure 3.17, top) has no sharp features at the bare atom line positions. Furthermore, we identify resonant excitations of Cr quintet metastable states (see Figure 3.20), which cannot originate from the Cr source.

3.6.4.2 Droplet Size Dependence of Relaxation Mechanisms

The relaxation dynamics are influenced by the size of the droplets and we obtain information about this dependency from the 1CR2PI spectrum in the range of the $g^5D_3 \leftarrow z^5P^\circ_3$ AI transition (28 180–28 210 cm^{-1}, see inset of Figure 3.17). The AI peak height is proportional to the number of bare Cr atoms ejected from the droplet in the $z^5P^\circ_3$ state. The background signal, in contrast, corresponds to relaxation to other states that lie high enough in energy to be photoionized by the dye laser (e.g., y^7P°, b^3G, z^7D°, b^3P; note that all of these are higher in energy than $z^5P^\circ_3$). Also, $Cr^\star$-He_n exciplexes, even in case of a $z^5P^\circ_3$ Cr state, contribute to the background and not to the AI peak. Figure 3.18 shows the ratio of the AI peak height to the background. The peak height is obtained from a Gauss fit of the AI peak. Monitoring the ratio has the advantage that it is not influenced by variations of He_N flux with nozzle temperature. The AI peak height decreases almost by a factor of 3 with respect to the background for an increase of droplet radius from ∼15 to ∼46 Å. We take this as indication that for increasingly larger droplets relaxation to lower states than $z^5P^\circ_3$ occurs. In Ar matrices, where the perturbation by the host matrix is stronger and not limited in time because

of ejection, Cr excitation to z^7P° leads primarily to relaxation to a^3P states, which are lower in energy than states we find to be populated [75]. Although species on the He_N surface also show relaxation[216, 223, 224], our findings can be better compared to the Ag–He_N system, where excitation to the droplet broadened Ag $^2P_{3/2}$ structure leads to the ejection of bare Ag atoms in the $^2P_{1/2}$ state [90] and increasing the droplet size leads to an increase of Ag $^2P_{1/2}$ yield. The increased nonradiative transfer of population in excited Ag to the lowest excited state ($^2P_{1/2}$) for larger droplets supports our findings. In Cr the next lower state ($z^7F^\circ_6$) lies about 1000 cm^{-1} beneath $z^5P^\circ_3$, and within a few thousand wavenumbers, a multitude of states with all multiplicities can be found [109]. Increased relaxation to lower states for longer interaction with the helium droplet during ejection from larger droplets seems thus to be reasonable.

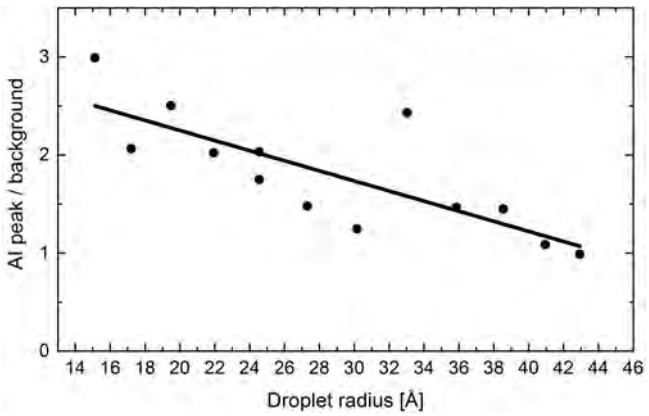

Figure 3.18: Ratio of atoms ionized through the g^5D_3 autoionization state ($g^5D_3 \leftarrow z^5P^\circ_3$ transition) to atoms ionized into continuum states in dependence on the droplet size. The line represents a linear fit and serves as guide to the eye.

3.6.4.3 $z^7P^\circ_{2,3,4} \leftarrow a^7S_3$ Excitation

The 2CR2PI spectrum via the $z^7P^\circ_{2,3,4}$ ($3d^54p$) as resonant intermediate state is shown in Figure 3.19 for the detection of $^{52}Cr^+$ (black) and $^{52}Cr^+$-He ions (gray). Upon comparison of the $^{52}Cr^+$ spectrum to beam depletion spectra [1], it becomes evident that for both techniques the droplet broadened feature has the same onset at about 23 400 cm^{-1} and that it extends several hundred wavenumbers to the blue. For the 2CR2PI spectrum the spectral shape is given by the combination of in-droplet excitation, subsequent relaxation, ejection from the droplet and, finally, ionization. Only z^7P° and a^3P lie high enough in energy to be ionized by a XeCl laser photon (32 468 cm^{-1}); relaxation to lower states will not contribute to the ion signal. We thus expect that a major part of the excited atoms relax to lower states and do not contribute to the 2CR2PI spectrum. The $^{52}Cr^+$-He signal above 23 400 cm^{-1}, although very weak,

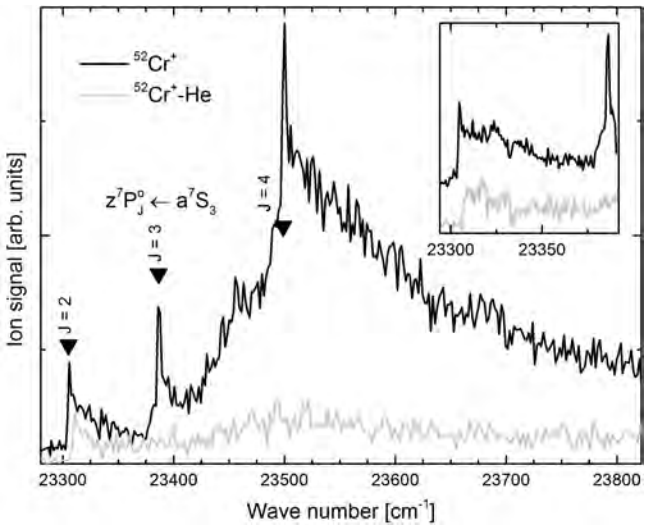

Figure 3.19: 2CR2PI excitation spectrum of the $z^7P^\circ_{2,3,4}$ ($3d^54p$) $\leftarrow$ a^7S_3 ($3d^54s$) transition ($T_0 = 20\,\mathrm{K}$, $\hat{N} = 1300$), recorded at the $^{52}Cr^+$ mass (52 u, black curve) and $^{52}Cr^+$-He mass (56 u, gray curve) with different scaling factors. The inset shows high resolution scans at both masses with vertical offsets. Bare atom $z^7P^\circ_{2,3,4} \leftarrow a^7S_3$ transitions [109] are indicated by triangles.

demonstrates the formation of $Cr^\star$-He exciplexes upon excitation to $z^7P^\circ_{2,3,4}$, as for $y^7P^\circ_{2,3,4}$ excitation above (Figure 3.17).

Similar to the $y^7P^\circ_{2,3,4}$ intermediate state, narrow spectral structures appear in the $^{52}Cr^+$ detected spectrum at the bare atom $z^7P^\circ_{2,3,4} \leftarrow a^7S_3$ line positions, also showing a wing toward higher wavenumbers. As will be discussed below, this is an indication for the presence of bare a^7S_3 Cr atoms and Cr-He_n ground-state molecules.

3.6.4.4 Formation of Quintet State Atoms

To examine the population of other states than the septet ground state, PI spectra were recorded with the dye laser scanning over the spectral regions of metastable quintet state transitions (green arrows in Figure 3.16) while the XeCl laser wavelength was fixed. As shown in Figure 3.20, we observe the population of the metastable a^5S_2 ($3d^54s$) state. In yet another wavelength range we find evidence for population of another metastable quintet state by identifying the bare atom transitions originating from a^5D ($3d^44s^2$) (not shown). This can be taken as another proof that the atoms cannot origin directly from the evaporation source but have to experience a droplet-mediated relaxation. Clearly, the spectrum in Figure 3.20 is dominated by the strong free atom $z^5P^\circ_{1,2,3}$ ($3d^54p$) $\leftarrow$ a^5S_2 ($3d^54s$) transition. The structure in the range of $19150\,\mathrm{cm}^{-1}$ to $19\,600\,\mathrm{cm}^{-1}$ is a superposition of a broad structure of unclear origin and sharp features at the bare atom

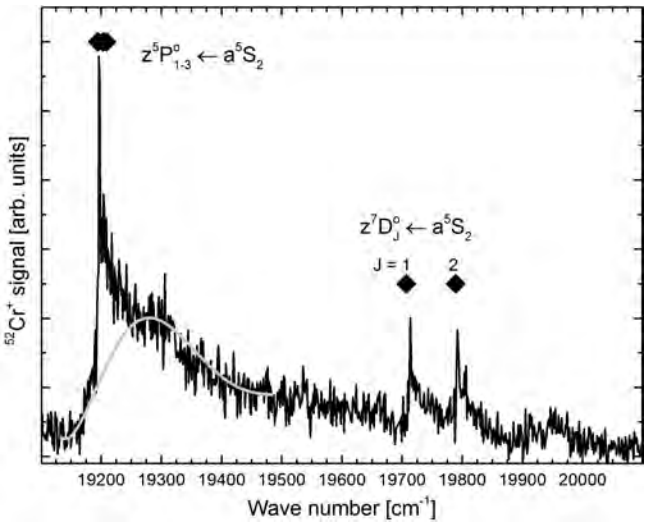

Figure 3.20: 2CR2PI excitation spectrum of the $z^5P^\circ_{1,2,3} \leftarrow a^5S_2$ and $z^7D^\circ_{1,2} \leftarrow a^5S_2$ transitions recorded at the $^{52}Cr^+$ mass (52 u). Bare atom transitions are indicated with squares [109]. The gray curve serves to indicate a broad structure of unknown origin.

$z^5P^\circ_{1,2,3} \leftarrow a^5S_2$ transitions. The broad structure is schematically indicated with a gray line, starting to the red side of the free atom transitions and having a weak maximum at 19 300 cm^{-1}. The wing to the blue side of the $z^5P^\circ_{1,2,3} \leftarrow a^5S_2$ feature has thus a width of ∼50 cm^{-1}. Within the observed energy region also the $z^7D^\circ_{1,2}$ ($3d^44s4p$) ← a^5S_2 ($3d^54s$) intercombination lines appear as sharp free atom transitions with wings to the blue side. We note that although these are intercombination lines, they are listed in literature for bare atoms [112].

3.6.4.5 Formation of Cr–He_n Complexes and $Cr^\star$-He Exciplexes

Multiphoton ionization schemes of Cr-He_N give rise to the detection of Cr^+-He_n complexes in our current study. The abundance of Cr^+-He_n with $n > 1$ is very low and the products are almost exclusively detected at the mass windows corresponding to Cr^+ atoms and Cr^+-He in the examined spectral regimes.
The formation of exciplexes, consisting of excited atoms or molecules with several attached helium atoms, has been observed upon photoexcitation for various species inside and on the surface of helium nanodroplets[68, 90, 216–219, 223]. In these experiments it has been shown that REMPI spectroscopy allows to draw conclusions on the formation of intermediate neutral exciplexes only with some reservation because it probes the resultant ionic complexes. If the ionizing laser photon energy is higher than the vertical ionization potential, the generated ionic complex can carry internal energy, which may cause the evaporation of helium atoms from the ionic complexes. Consequently, our

REMPI mass spectra do not necessarily reflect the abundance of exciplexes; moreover the number of He atoms attached to the dopant will be underestimated. In our experiments, the formation of Cr^*-He exciplexes is observed. The Cr^+-He spectra presented in Figures 3.17 and 3.19 have a similar shape as the droplet broadened transitions monitored at the Cr^+ mass window. This shows that Cr^*-He_n exciplexes are formed and ejected upon photoexcitation with the dye laser. In contrast to other helium droplet isolation experiments, we find evidence for the presence of ground state Cr-He_n complexes, which will be discussed in the following. These complexes are formed when the XeCl laser is present and are ionized by two-photon ionization; i.e., at least three photons are involved in the overall process that proceeds during the laser pulse duration (∼20 ns). A striking difference between the 2CR2PI and 1CR2PI spectra in Figure 3.17 is the emerging sharp spectral lines that correspond to the bare atom $y^7P^\circ_{2,3,4} \leftarrow a^7S_3$ transitions. The spectrally sharp transitions are accompanied by a small wing that extends toward the blue side. These spectral features are exclusively observed if the XeCl laser pulse is present. Similar transitions can be seen in the 2CR2PI spectra shown in Figures 3.19 and 3.20. Note that these features appear in addition to the droplet broadened structures and, especially, they are not present at the $y^7P^\circ_4 \leftarrow a^7S_3$ transition shown in the 1CR2PI spectrum (top Figure 3.17). In this region the dye laser excites a Cr-He_N transition but does not give rise to a sharp spectral line. Furthermore, the sharp spectral lines shown in Figure 3.17 accompanied by blue wings are only present if the QMS is set to the Cr bare atom mass window.
Evidence for the connection of the blue wings to the formation of Cr-He_n complexes can be seen in the inset of Figure 3.19 at the $z^7P^\circ_2$ ($3d^5 4p$) ← a^7S_3 ($3d^5 4s$) transition. Therein the Cr^+ and Cr^+-He ion yields are compared (Cr^+ is vertically offset and the two signals are scaled with different factors). It can be seen that in contrast to the Cr^+ signal, the small wing but not the sharp lines are observed at the Cr-He mass (the low abundance of Cr-He_2 forbids the recording of an excitation spectrum for the corresponding mass window). Hence the origin of the sharp peaks can be attributed unambiguously to bare atoms in the a^7S_3 state. The fact that the wings are present in both mass windows and that they are only observed in the 2CR2PI spectra demonstrates that they must originate from Cr-He_n ($n \geq 1$) products generated by a XeCl laser UV photon. It is important to note that in this spectral region, below the onset of the droplet broadened transition at 23 400 cm^{-1}, the signal corresponds exclusively to an excitation spectrum of products formed by the XeCl laser. Above 23 400 cm^{-1} the production of ground state Cr and Cr-He_n by the XeCl laser is competing with dye laser excitation of Cr-He_N. We think that the absence of pronounced wings in the Cr^+-He signal for the $z^7P^\circ_{3,4}$ ($3d^5 4p$) ← a^7S_3 ($3d^5 4s$) transitions in Figure 3.19 is related to the competition between these two excitation paths. Alternatively, the ability of excited Cr atoms to bind He atoms might be higher for the $z^7P^\circ_2$ state than for the $z^7P^\circ_{3,4}$ states. At the $y^7P^\circ_{2,3,4}$ ($3d^4 4s4p$) ← a^7S_3 ($3d^5 4s$) transitions in Figure 3.17 the signal-to-noise ratio in the Cr^+-He signal was unfortunately too low, which forbids a comparison to

the Cr^+ signal near the small blue wings.
The observation of these wings is remarkable because these Cr-He_n complexes must be in their electronic septet or quintet ground state. Recent calculations of our group [225] show that the lowest Cr-He quintet and septet states are very weakly bound (a few wavenumbers, only one vibrational level is supported) with large internuclear separation ($R_e > 5\,Å$). Calculations for coinage metals show that the binding energy rises with increasing number of helium atoms attached to the metal atom [88]. For the ground state, the coinage metals with their completely filled d-orbitals and one electron in the s-orbital, and chromium with its half-filled d-orbitals and one s-electron are very similar in their interaction with He atoms, which is dictated mainly by the electron in the s-orbital [225]. Consequently, the observed spectrum suggests that larger Cr-He_n complexes are formed upon UV excitation, followed by droplet-mediated relaxation via various routes into the electronic septet and quintet (and probably also into the triplet) ground states. Note that this process must be completed in less than 20 ns, the pulse duration of the synchronized excitation and ionization lasers. The observed narrow structures represent the spectral signature of a transition that originates from a very weakly bound ground state at large internuclear distances into the slightly repulsive part of an intermediate Cr-He_n state. This is expected from the Cr-He diatomic potential energy curves in ref. [225]. The excess energy of the laser and the internal energy of the formed Cr^+-He_n complex will cause fragmentation of the intermediate complexes, which explains the observation of mainly Cr^+ and Cr^+-He in the mass spectrum. Consequently, REMPI spectroscopy forbids conclusions on the size of the intermediate Cr-He_n complexes. From the present data we cannot exclude a surface migration of Cr atoms upon UV excitation. A similar scenario has been suggested for excited NO^* molecules on helium nanodroplets [68]. The investigated Cr transitions can be compared to the $4p \leftarrow 4s$ transition in potassium, which is located on the droplet surface [226]. Similar to Cr-He_n, the potassium transition exhibits a characteristic narrow, asymmetric shape as well as a coincidence of the bare atom transition with the rising edge of the droplet broadened transition. More sophisticated calculations will assist the assignment of the transitions to a small or large Cr-He_n parent complex.
On the basis of our data we cannot draw conclusions on the process that underlies the formation of ground state and metastable Cr atoms and Cr-He_n complexes because the spectral regime above the y^7P° state is not covered by our dye laser. We propose two different scenarios for the production of ground state and metastable Cr atoms and Cr-He_n. (i) Septet states are absent in the concerning spectral regime, but states with other multiplicities lie in the vicinity of the XeCl laser photon energy. Transitions from the septet ground state into states with other multiplicities, as they are observed for Cr (see Figure 3.20), may be excited and responsible for the production of ground state and metastable state complexes. (ii) At our experimental conditions, Cr dimers are present in a certain fraction of helium droplets. The excitation of a dimer transition in the concerning spectral region may give rise to the production of various products such

as Cr + Cr*-He_n, Cr* + Cr-He_n or Cr^*_2. The formation of Cr dimers is observed in helium nanodroplets [65], and their spectra will be explored in the near future.

3.6.5 Summary and Conclusion

Chromium atoms doped to superfluid helium nanodroplets are investigated with one- and two-color resonant two-photon ionization spectroscopy (1CR2PI and 2CR2PI, respectively) via the $y^7P^\circ_{2,3,4}$ resonant intermediate states and with 2CR2PI via the $z^7P^\circ_{2,3,4}$ states. We find two independent indications that nonradiative population transfer of excited $Cr^\star$ atoms mediated by the droplet takes place to lower states than previously identified [1, 2]. For the $y^7P^\circ_{2,3,4}$ intermediate states, comparison of 1CR2PI and 2CR2PI is possible and an additional shoulder observed with 2CR2PI indicates the population of $Cr^\star$ states that are too low in energy to be detected with 1CR2PI. Additionally, a decrease of $z^5P^\circ_3$ population of bare $Cr^\star$ atoms for increasing droplet size also points toward relaxation to energetically lower states as the duration of interaction with helium during ejection is increased. The formation of $Cr^\star$-He_n exciplexes upon in-droplet excitation of y^7P° and z^7P° is demonstrated by the fact that the excitation spectra obtained with Cr^+ and Cr^+-He detection are identical.

All 2CR2PI spectra reveal sharp lines at the bare atom positions, which we attribute to the presence of the 308 nm XeCl laser. A fast (< 20 ns) excitation-relaxation cycle produces bare Cr atoms in the septet ground state (a^7S_3) as well as metastable quintet (a^5S_2 and a^5D) states, which are subsequently probed by 2CR2PI. All of these lines show a wing on their blue side, which indicates the presence of ground and metastable Cr-He_n molecules. In addition, the detection of Cr^+-He ions in spectral regions of the $z^7P^\circ_2 \leftarrow a^7S_3$ wing verifies the presence of ground state Cr-He_n complexes. Given the weak binding energy of ground-state septet and quintet Cr-He diatomic molecules [225] and the presumably only slightly stronger bond of Cr-He_n complexes [88], this observation is remarkable as it demonstrates that a complete relaxation to the Cr ground state has to take place inside the droplet.

The complex electronic structure of the Cr atom leads to even more complex electronic structure inside a helium droplet due to the perturbation by the surrounding helium. Several different relaxation channels to repulsive states that cause an ejection from the droplet might compete. The fact that Cr ions with attached helium atoms are detected in our experiments suggests that Cr-He_n formation needs to be considered for the explanation of relaxation pathways and the description of the dynamics of Cr atoms inside helium droplets, calling for more sophisticated theoretical models. The Cr-He potential energy curves calculated in our group [225] can serve as a starting point for this task. Finally, it cannot be decided from our current data if ground state Cr atoms and Cr-He_n complexes originate from excitation of single Cr atoms inside He_N

or a photoinduced dissociation of Cr dimers inside the droplet. Photoexcitation of Cr dimers is subject of our current research.

3.6.6 Acknowledgement

We thank Matthias Hasewend and Friedrich Lindebner for experimental support as well as Johann V. Pototschnig and Martin Ratschek for helpful discussions. This work was supported by the Austrian Science Fund (FWF, Grant 22962-N20), as well as the European Commission and the Styrian Government within the ERDF program.

3.6.7 Table of Contents Graphic

The table of contents graphic (Fig. 3.21) shows a collage of Fig. 3.16 and Fig. 3.17 from the manuscript. Schematic drawings of the bare atom, small Cr-He_n, and Cr solvated in He_N are placed in the spectrum to indicate which part they contribute to. The arrows symbolize whether the spectral feature originates from a bare atom or a Cr-He_n complex in the ground state, or from the droplet broadened excitation for Cr atoms solvated inside He_N (indicated with a shaded rectangle).

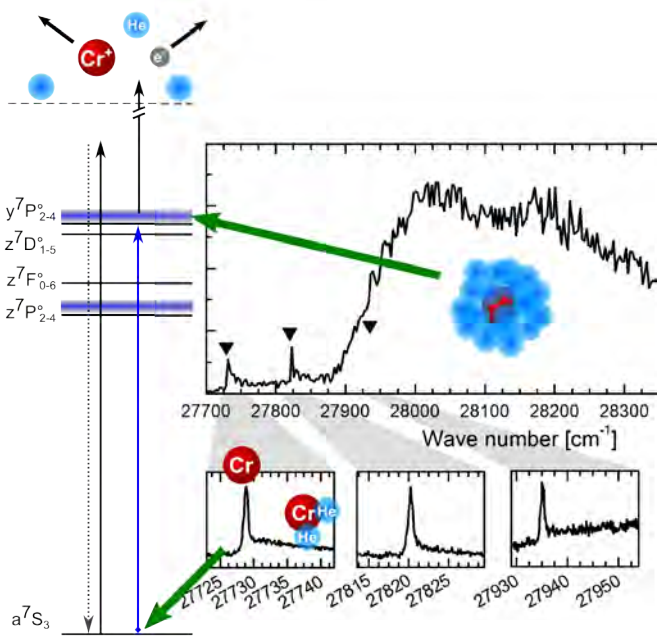

Figure 3.21: Table of contents graphic of Ref. [3]: "One- and Two-Color Resonant Photoionization Spectroscopy of Chromium-Doped Helium Nanodroplets".

3.7 Laser Ionization and Spectroscopy of Cu in Superfluid Helium Nanodroplets [4]

The electronic excitation and relaxation behavior of copper atoms doped to He_N and the formation of small copper clusters is probed with two-color two-photon ionization. Relaxation and ejection mechanisms, similar to Cr in He_N, are observed and the spectral features of small Cu-He_n complexes are compared to simulated spectra from literature [88].
Sections 3.7.1 to 3.7.6 correspond to the publication "Laser Ionization and Spectroscopy of Cu in Superfluid Helium Nanodroplets" (International Journal of Mass Spectrometry **365-366** (2014), 255 - 259) by Friedrich Lindebner, Andreas Kautsch, Markus Koch, and Wolfgang E. Ernst [4]. It is part of a special issue in honor of Tilmann Märk.

The author of this thesis had main contributions on

- All measurement data (except mixed CrCu clusters)
- Data interpretation
- Text
- Content of figures

The contributions of the Co-authors and acknowledged persons listed below were:

- Friedrich Lindebner: Preparation and assistance for experiments, experiments for mixed CrCu clusters, data evaluation, editing of figures and artwork, proofreading of text
- Markus Koch: Proofreading of text, funding
- Wolfgang E. Ernst: Proofreading of text, supervision (experiment, publication), funding

3.7.1 Abstract

Mass and optical spectroscopic methods are used for the analysis of copper (Cu) atoms and clusters doped to helium nanodroplets (He_N). A two-color resonant two-photon

ionization scheme is applied to study the Cu $^2P^\circ_{1/2,3/2} \leftarrow ^2S_{1/2}$ ground state transition. The absorption is strongly broadened for Cu atoms submerged inside helium nanodroplets and a comparison with computed literature values is provided. An observed ejection of the dopant from the droplet is triggered upon excitation, populating energetically lower states. The formation of Cu_n clusters up to Cu_7 inside helium nanodroplets was observed by means of electron impact ionization mass spectroscopy.

3.7.2 Introduction

Helium nanodroplets (He_N) have drawn attention from theoreticians and experimentalists alike, as they offer a confined, transparent, and weakly interacting matrix for a well defined analysis of dopants at low temperatures (0.4 K) [9]. The systematic spectroscopic interrogation of foreign atoms has proven to be a powerful technique for the examination of the dopant properties, as well as a probe for the behavior of the quantum liquid itself [9]. Mass analysis of ionization fragments from atom and cluster doped or pure He_N, has been widely used to monitor dynamic processes influenced by the superfluid helium environment [2, 9, 196, 219, 227–229].

Besides the very well known technical importance of Cu, applications have been developed in the biosciences where single Cu atom resonance ionization mass spectrometry (RIMS) was used to nondestructively handle and manipulate plant cells that accumulate foreign atoms [230]. Formation of small Cu_n clusters inside He_N will enable the study of high spin states where hardly any data is available but has been shown for alkali and silver dimers and alkali trimers attached to He_N [20, 21, 205, 209]. One of our goals is the deposition and investigation of structural and magnetic properties of Cu_n clusters on surfaces as these might differ considerably from those of both their atomic constituents and bulk matter [214, 231].

Most experimental and theoretical studies of metal doped He_N are concerning alkali atoms. It is well established that alkali atoms reside on the droplet surface [9, 21, 66, 232] because of their large van der Waals radius, while most other atoms are dissolved inside the droplet [1, 2, 90, 196, 199]. Helium can be viewed as a probe to explore the electronic structure of an excited atom [233] and the solvation of atoms inside He_N can be extracted from absorption broadenings and line shifts [9, 88]. The $(n\text{-}1)d^{10}$ ns electron configuration of coinage metal atoms can be considered alkali like, so these species are well suited for spectroscopic analysis and were already doped to various matrices. In He droplet experiments, preferably silver was used as a single atom dopant [90, 91, 196] or to form larger clusters [214, 234]. Doping of Cu was reported for the investigation of the bonding between Cu_n clusters and organic molecules [235], the formation of unusual Cu_n clusters [231], and Cu was also implanted in a He fountain [236]. Matrix isolated copper was found to undergo nonradiative relaxation and fluorescent emission on forbidden lines [237] where transitions of valence electrons show a strong broadening and blueshift,

while inner-shell transitions are practically unshifted [238]. An investigation of the solubility of coinage metals suggests that shell formation around the dopant is expected with the onset of a second shell for more than 25 He atoms and the formation of a compact solvation shell for larger clusters [88].

We were able to measure the absorption of the Cu-He_N system to provide comparison to theoretical studies [88, 233]. An $\omega_1+\omega_2$ Resonance Ionization Spectroscopy (RIS) scheme is used to study the excitation with one photon utilizing a resonant transition from the ground state and a second photon providing the energy to ionize, a scheme that was also used in free Cu atom spectroscopy [104] for bare atoms. Here we present the results from a mass selective laser spectroscopic study of the first strong ground state excitation of Cu doped He_N and mass spectroscopic observation of small Cu_n clusters formed inside the droplets.

3.7.3 Experimental

The experimental setup follows the design of a HElium NanoDroplet Isolation (HENDI) spectroscopy apparatus described in detail in previous publications [2, 165]. He_N are formed by a supersonic expansion of He gas (purity 99.9999%) through a cooled nozzle (closed cycle two-stage cryocooler, T_0 = 13-20 K nozzle temperature, p_0 = 5 MPa stagnation pressure, d_0 = 5 µm orifice diameter) into vacuum. The He condenses to form clusters following a log-normal size distribution with, under these conditions, typical maxima in the distribution of $\hat{N}_{p_0,T_0} = \hat{N}_{5,13-20}$ = 7 200 - 1 400 atoms and r = 4.3-2.5 nm (mean droplet size $\bar{N}$ = 21 200 - 4 000). As the spectroscopic linewidth of dopant transitions is partially due to inhomogeneous broadening from the droplet size distribution, the largest intensity within the linewidth has to be assigned to the droplet size represented by the maximum of the log-normal size distribution. For this reason, we prefer to list the maxima rather than the average sizes (see also for details ref. [50]). The droplets pass a skimmer (d = 300 µm) to shape a He_N beam traveling toward a pickup oven located in a separately pumped vacuum chamber where the He_N statistically pick up one or more Cu atoms. The resistively heated Cu evaporation source consists of a tungsten wire heated alumina (Al_2O_3) coated crucible covered with a slitted molybdenum lid with a slit length of 25 mm, arranged parallel below the droplet beam. Gas phase Cu atoms are emitted from the slit and intersect the He_N beam at right angles, hence the crossed beam geometric layout - including 5 small apertures to collimate the droplet beam - ensures that no free atoms reach the detection region 1.4 m downstream. For the doping with single Cu atoms, oven temperatures of typically 1000 - 1100°C are necessary in this setup. For the formation of Cu_n clusters inside He_N, the experimental conditions are chosen to favor the pickup of, on average, more than one Cu atom per droplet, meaning higher crucible temperatures (1100 - 1300°C) and large droplets ($\hat{N}_{5,13.5} \approx$ 6 800 corresponding to an average size of $\bar{N}$ = 18 300). A quadrupole

mass spectrometer (QMS, Balzers QMG 422) with counter (Stanford Research SR400) is located at the end of the main vacuum chamber. It can be oriented in two ways to intersect the He_N beam with a laser beam either at right angles for photoionization (PI) or antiparallel for beam depletion (BD) measurements. For analysis of the embedded Cu_n clusters by means of electron impact ionization mass spectroscopy, the QMS is equipped with a crossed beam electron bombardment ion source. Here, the He_N beam is chopped for differential counting with a home-built two channel counter.

For the Cu excitation in the UV spectral region, the radiation from an excimer (XeCl, Radiant Dyes RD-EXC-200) pumped dye laser (Lambda Physik FL3002, dye DCM) with ∼25 ns pulse duration and 100 Hz repetition rate is frequency doubled with a KDP crystal (second harmonic generation, SHG). Excitation wavelengths are determined from the fundamental wavelength measured with a wavemeter (Coherent Wavemaster). For Resonant two Photon Ionization (R2PI), part of the excimer laser beam ($\lambda = 308$ nm) is coupled out of the dye laser pump beam and guided toward the HENDI apparatus simultaneously with the tunable dye laser beam. Both are focused and overlapped inside the ionization region of the QMS (laser fluence: SHG $\approx 7\,\mathrm{mJ/cm^2}$, XeCl $\approx 5\,\mathrm{mJ/cm^2}$). The R2PI and BD spectra presented are exclusively recorded at 63 u, the mass of the most abundant Cu isotope. For the observation of photoionized fragments, the mass filter is scanned while ionization is accomplished with fixed laser wavelengths. Overall, this setup allows us to perform resonance ionization spectroscopy of Cu-He_N complexes with mass selective ion detection and electron impact ionization mass spectroscopy.

The Cu ground state ($^2S_{1/2}$) electron configuration is [Ar]$3d^{10}4s$. In principle, the ground state absorption measurement follows the simple R2PI excitation scheme (see Fig. 3.22) of ref. [104]. For all atoms solvated inside He_N, the first resonant excitation step is accomplished by the dipole allowed transitions D1 ($\tilde{\nu} = 30\,535\,\mathrm{cm^{-1}}$) and D2 ($\tilde{\nu} = 30\,783\,\mathrm{cm^{-1}}$) [112] to the $^2P^\circ_{1/2}$ and $^2P^\circ_{3/2}$ (electron configuration: $3d^{10}4p$) states, respectively. The Cu II limit lies at $\tilde{\nu} = 62\,317\,\mathrm{cm^{-1}}$ which cannot be reached from the $Cu^\star$ intermediate $^2P^\circ_{1/2,3/2}$ states with a photon of $\tilde{\nu} < 31\,782\,\mathrm{cm^{-1}}$ and is thus accomplished by the absorption of a XeCl laser photon ($\tilde{\nu} = 32\,468\,\mathrm{cm^{-1}}$).

3.7.4 Results and discussion

3.7.4.1 Resonant two photon ionization of Cu-He_N

A number of characteristic absorption features is observed with R2PI, as one laser is scanned from 30 470 $\mathrm{cm^{-1}}$ to 32 120 $\mathrm{cm^{-1}}$ while the second laser is kept constant at 32 468 $\mathrm{cm^{-1}}$. In the upper panel of figure 3.23 the recorded spectrum is plotted together with the computed vertical excitation spectra for $CuHe_{12}$ (dotted blue curve) and $CuHe_{100}$ (dashed red curve) [88] in the $^2P^\circ_{1/2,3/2} \leftarrow {}^2S_{1/2}$ transition energy region. The ions are detected exclusively at the mass of the most abundant ^{63}Cu isotope. Most

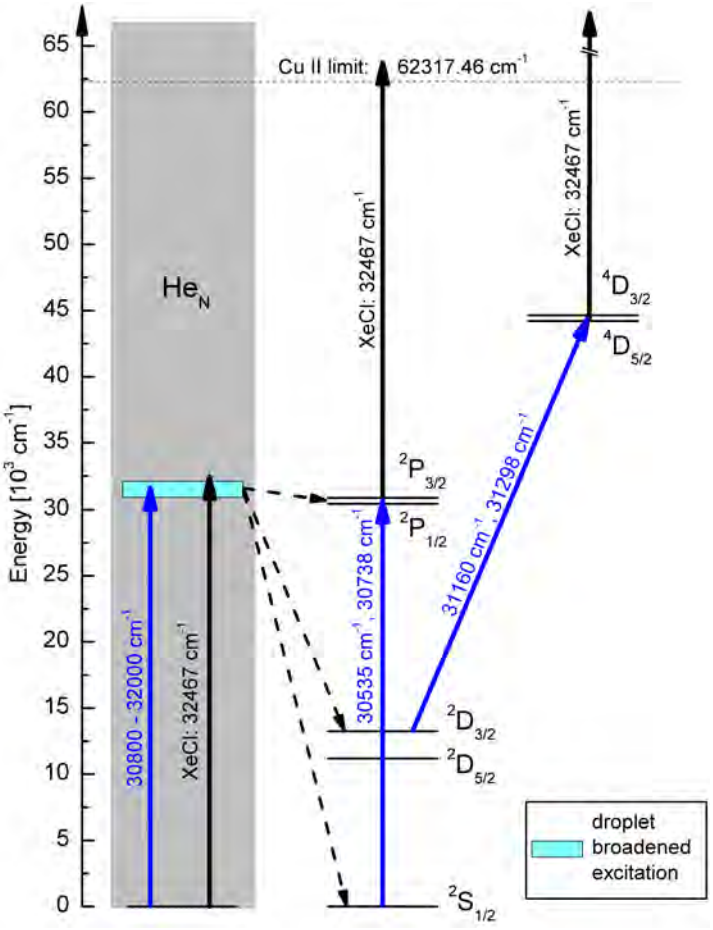

Figure 3.22: Energy-level diagram of Cu with the observed absorption paths indicated (upwards pointing arrows). The shaded rectangle indicates the excitation broadening due to the He_N and the dashed arrows stand for nonradiative relaxation processes. Note that the $^2P^\circ_{1/2,3/2}$ and $^4D^\circ_{5/2,3/2}$ spin-orbit splitting is not drawn to scale.

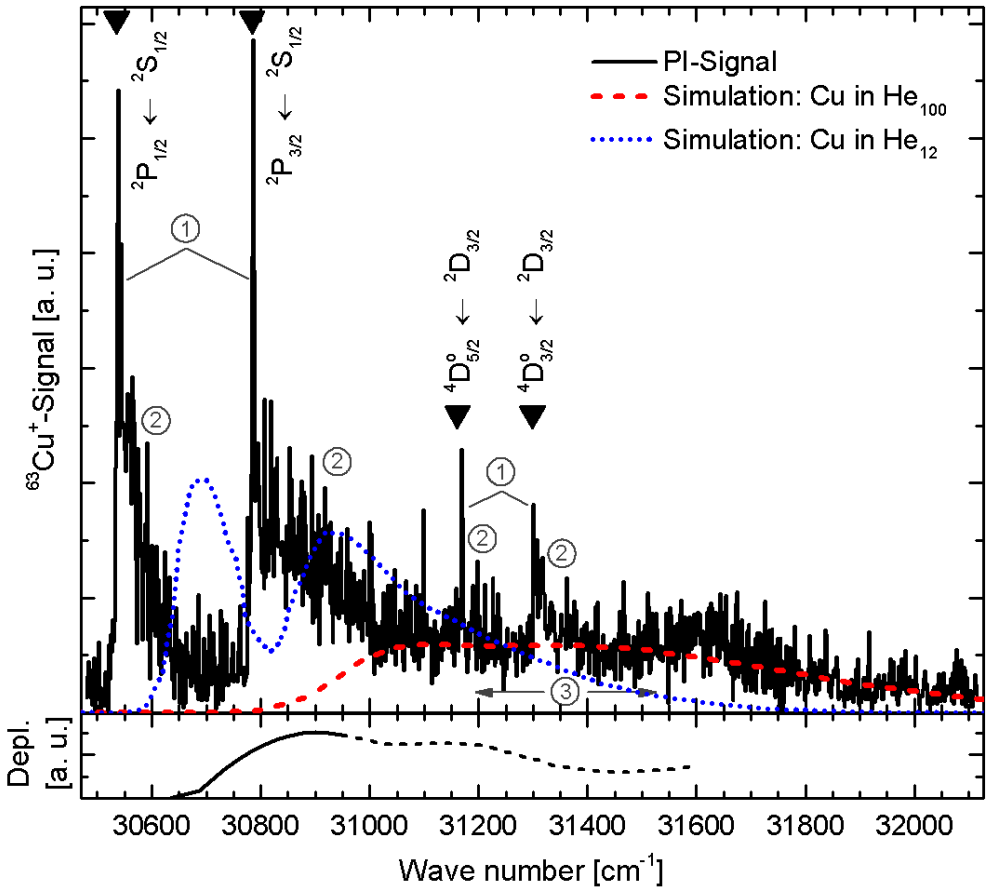

Figure 3.23: Top: Two-color two-photon ionization spectrum of Cu doped He_N (mean radius 3.9 nm) in the energy region of the $^2P^\circ_{1/2,3/2} \leftarrow {}^2S_{1/2}$ ground state transition. The free atom transition energies are indicated with triangles. Computed absorption spectra for $CuHe_{100}$ (dashed red) and $CuHe_{12}$ (dotted blue) are redrawn from ref. [88] and scaled for best comparability. Numbers correspond to the features described in the text. Bottom: Beam depletion spectrum of Cu doped He_N. The dashed signal might not be considered reliable due to large noise.

obviously, it consists of (1) sharp peaks at the catalogued Cu gas phase transition energies which are (2) broadened on their high energy side by up to ∼200 cm^{-1} wide shoulders. These features are discussed below, while first the broad structure (3) stretching over ∼900 cm^{-1} between $\tilde{\nu} = 30\,900\,cm^{-1}$ and $\tilde{\nu} = 31\,800\,cm^{-1}$ is treated.

In Fig. 3.23, the broad band (3) ranging from 30 900 to 31 800 cm^{-1} is assigned as $^2P^\circ_{1/2,3/2} \leftarrow ^2S_{1/2}$ excitation of Cu inside the droplet, in reasonable agreement with the calculation of Cargnoni and Mella [88] for $CuHe_{100}$. This is characteristic for outer shell transitions of atoms surrounded by the droplet. Cavities are formed around the dopant and a qualitative understanding of spectral line broadening and shift is provided by the size-dependent energy of the atomic bubble state. During the orbital expansion of a vertical electronic excitation the He atoms inside the cluster cannot readjust their positions [88] so the Pauli repulsion from the surrounding matrix strongly perturbs the dopant valence electron orbitals.

The solvation of metal atoms inside He_N is often described using the model by Ancilotto et al. [66] which aims to predict the solvation of a dopant with a dimensionless parameter of $\lambda \geq 1.9$. The calculated value of $\lambda = 2.9$ [70] for Cu atoms inside He_N and the distinct Cu-He well depth of -28.4 μhartree (-0.77 meV) estimated with ab initio ground state pair potentials [88] is qualitatively supported by our experimental findings. Because of the similar outer shell electron configurations [88, 90], similarities between the Cu-He and Ag-He interaction potentials were found [88] which leads to comparable computational and experimental results, apart from the two spin-orbit components that are clearly separated in the case of Ag due to the larger spin-orbit splitting.

The first laser excitation is accomplished while the Cu atom resides inside a droplet with $\hat{N}_{5,15} = 5\,200$ He atoms (r = 3.9 nm). The observed broad and blueshifted absorption (3) agrees well with the simulated absorption for a cluster size of $n = 100$ He atoms [88]. Only the first two solvation shells around the Cu are accounted for to play a role for the excitation shift [88], and further influence for larger cluster sizes is dismissed by the authors. Recent calculations by Mateo et al. [91] revealed that spectra of impurities like Ag, fully solvated inside large enough droplets, are independent of the droplet size and comparable to doped bulk liquid helium. To our knowledge, no experimental data is available for excitation spectra of atomic Cu solvated in bulk liquid He.

Beam depletion measurements (Fig. 3.23, bottom panel) which are sensitive to the initial ground state single photon absorption of Cu inside He_N neglect any photon-induced secondary effects described below. The BD spectrum shall be compared to the computed $CuHe_{100}$ (dashed red curve) vertical excitation spectrum representing the in-droplet excitation best. The onset of the droplet broadened structure lies approximately $100\,cm^{-1}$ to the red of the computed absorption, reaching the maximum absorption level already at $30\,800\,cm^{-1}$. So we attribute the deviation from computational results [88] either to saturation effects in the experiment [1] or to the uncertainty in the Lax

approximation, that tends to slightly overestimate the energy gaps due to the lack of zero point energy corrections.

While the broad absorption band originating from Cu inside He_N can be well assigned, we will now discuss the strongly increased ion yield (1) at and (2) in the vicinity of the free atom ground and excited state transitions. As described above, the experimental setup prevents free atoms from reaching the PI-region from the evaporation source. We hold a photo-induced ejection mechanism responsible for the production of un- and weakly perturbed Cu atoms, like it was predicted by F. Cargnoni and M. Mella in the form of a "spit out" from the droplet following the $^2P^\circ_{1/2,3/2} \leftarrow {}^2S_{1/2}$ excitation [88]. The spin changing D-D transition ($\Delta L = 0$, $\Delta S = 1$) should be dipole forbidden but has a low free atom transition strength [112] and as in other doped helium droplet spectroscopy [206], may even become more allowed in the presence of the helium environment. The relatively intense signal from the $^4D^\circ_{3/2,5/2} \leftarrow {}^2D_{3/2}$ transitions points toward a strong population of the metastable $^2D_{3/2}$ state. Exciplexes which form when one or several host atoms (helium) penetrate into the nodal region of the excited valence electron's density distribution [238], are responsible for a fast nonradiative relaxation due to the crossing of the $^2\Sigma^+$, $^2\Pi_{1/2}$, $^2\Pi_{3/2}$ and the $^2\Sigma^+$, $^2\Pi_{1/2}$, $^2\Pi_{3/2}$, $^2\Delta_{3/2}$, $^2\Delta_{5/2}$ potential energy curves of the Cu-He diatomic which converge asymptotically to the atomic ^2P and ^2D doublets [233], respectively. The exciplex formation is particularly favored for alkali and coinage metal atoms because of the dumbbell-shaped nP orbitals. The elucidated mechanism might also be extended to nonresonant excitation in the vicinity of the resonant state. One excimer laser photon may provide excitation near the resonant transition (see Fig. 3.22) and lead to ejection and relaxation of a Cu atom. After relaxation, the Cu atoms experience a repeated resonant excitation followed by ionization. Free Cu atoms accompanying the Cu doped He_N beam were never observed by us and are not expected due to our "crossed beam" pickup-geometry. The sharp lines (1) at the wavenumbers of the free Cu $^2P^\circ_{1/2} \leftarrow {}^2S_{1/2}$ and $^2P^\circ_{3/2} \leftarrow {}^2S_{1/2}$ transitions indicate that within the pulse length of our laser ($\sim$25 ns) a Cu atom can be excited inside the droplet, be ejected from the droplet, relax to the ground state, and be resonantly ionized through the two ^2P states. Furthermore, the spectrum in Fig. 3.23 shows spectral bands extending from the free atom transitions toward higher wavenumbers (2). They have a similar shape as the simulated bands by Cargnoni and Mella [88] for Cu in He_{12}, which are nevertheless shifted by about 130 cm^{-1} to the blue, about the same amount as the shift for simulated Cu-He_{100} against our depletion band. We conclude that our measured bands (2) derive from small Cu-He_n ($n = 1, 2, 3$) complexes ejected from the droplet along with the free atoms mentioned above. While our ion mass scans only show $(CuHe)^+$ and $(CuHe_2)^+$, recent calculations of Cargnoni et at. [233] predict that the $Cu^\star(^2P)$ state is capable of binding up to 5 He atoms. Simulations of excitation spectra of the complexes CuHe to $CuHe_5$ would shine more light on our observations. The overall agreement between the calculations [88] and our spectra is certainly not perfect but shows the right tendency

considering the complexity of the system. The deviation of 100 to 130 cm^{-1} is similar as in the case of Ag atoms solvated in He_N [88, 199].

3.7.4.2 Electron impact ionization of Cu_nHe_N

Fig. 3.24 (upper panel) shows an electron impact ionization mass spectrum of Cu doped He_N from Cu_2^+ to Cu_7^+. The formation of Cu_n clusters is confirmed by the distinct patterns according to the isotopic composition of ^{63}Cu and ^{65}Cu. A comparison with the calculated binomial distribution for the Cu_7^+ cluster is shown in the lower panel of Fig. 3.24. Cluster sizes of up to seven Cu atoms were observed, limited by the maximum QMS detection range. The energy introduced by the pickup of seven copper atoms can be estimated according to Lewerenz et al. [239] (discussed in more detail in Ref. [65]) and leads to the evaporation of 2 700 ± 100 He atoms, together with the binding energy of the Cu_7 cluster [240] a total number of 17 000 ± 2 000 He atoms are evaporated during the Cu_7 cluster formation. This is realistic since, according to the log-normal distribution ($\hat{N}_{5,13.5} \approx 6\,800$), 38% ± 5% of the droplets are of sufficient size to survive the formation of Cu_7. Odd-even cluster ion yield oscillations are apparent in the signal integrated over each specific isotopic cluster composition, but are less prominent than observed for Ag [234]. These oscillations can be attributed to the electronic shell structure of the coinage metal clusters, where a cluster with an even number of electrons (odd numbered cluster ion) is more stable than one with an odd number of electrons (even numbered cluster ion) [241]. However, due to various different contributions of droplet size dependent electron impact ionization of Cu_n inside He_N, possibly accompanied by fragmentation, we note that the real Cu_n flux rate cannot easily be deduced from the measured Cu_n^+ ion yield. Finally, the pickup of water from the residual gas in the vacuum chamber leads to the occurrence of patterns between the cluster masses, originating from $Cu_n(H_2O)_m^+$ compounds and their fragments. An investigation of the electronic properties of such metal-water clusters in the gas phase was recently reported [242]. Further equidistant peaks, separated by 4 u, correspond to the well known He_N fragment ions.

Successive doping of the droplet beam with Cr [65] and Cu leads to the formation of mixed metal clusters inside the He_N. CrCu, $CrCu_2$, Cu_2Cr, and $CrCu_3$ were successfully detected by means of electron impact ionisation mass spectroscopy. These species are promising candidates for spectroscopic investigation on He_N, as only little data is available [243] and the mixed clusters may possess interesting magnetic properties [244].

3.7.5 Conclusions

In this work, we examine the absorption and relaxation mechanisms of Cu atoms embedded inside He_N by means of laser ionization spectroscopy with mass selective

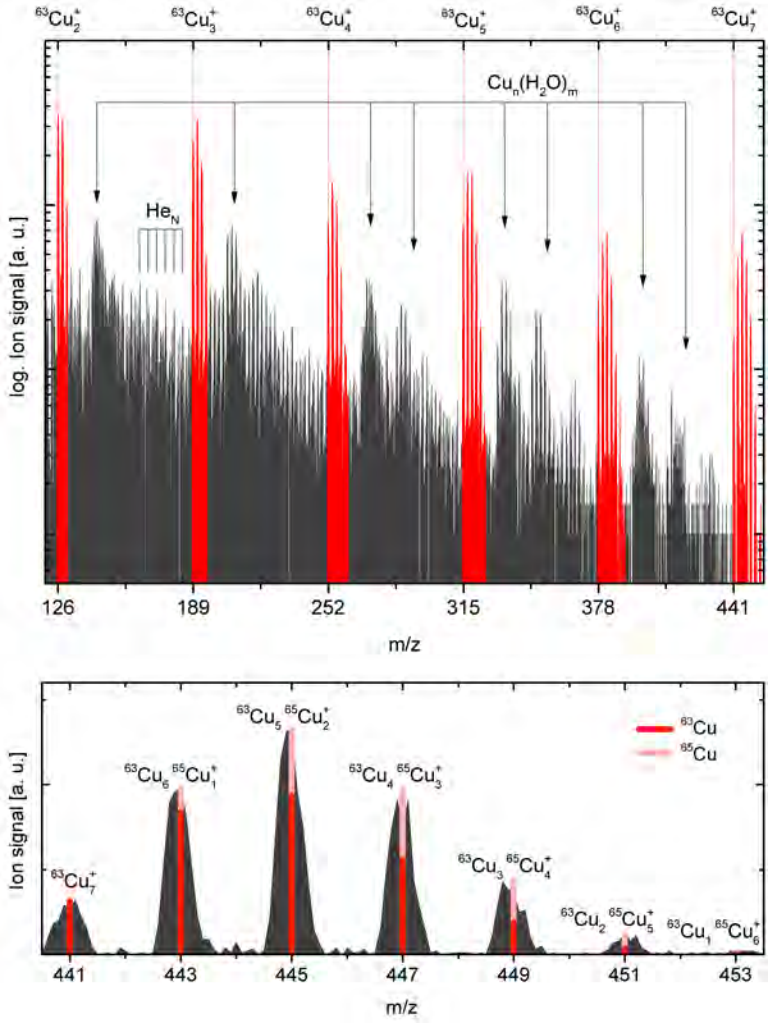

Figure 3.24: Top figure: Mass spectrum of Cu_n clusters (red pattern) embedded inside He_N, detected by electron impact ionization. Bottom figure: Comparison of measured and calculated isotopic composition of the Cu_5 cluster.

detection and compare them to computational results from literature [88]. A broad and approximately 700 cm^{-1} blueshifted absorption band is observed as depletion spectrum and is assigned to Cu atoms solvated inside the droplets. Predicted photoinduced ejection was observed including the relaxation to the ground and intermediate ^2D states together with the formation of small Cu-He_n clusters. For a better comparison with calculations, the computation of absorption spectra for Cu-He_n clusters with less than 12 He atoms or for Cu atoms residing on the droplets surface would be helpful.

The successful formation of small Cu_n clusters and $Cu_n(H_2O)_m^+$ compounds inside He_N was shown for up to seven Cu atoms and evidence is provided that a significant fraction of the droplets survive this cluster formation. This will allow systematic spectroscopic studies of electronic spectra of these systems.

3.7.6 Acknowledgment

The research was supported by the Austrian Science Fund (FWF) under grant number 22962-N20 and by the European Commission and the Styrian Government within the ERDF program.

3.7.7 Table of Contents Graphic

The table of contents graphic[3] [4] in Fig. 3.25 visualizes (from left to right) the excitation of the solvated Cu $^2S_{1/2}$ ground state atom with the laser (drawn in red) that causes the ejection of the Cu atom. The atom is ionized by the same laser which leads to the detachment of an electron.

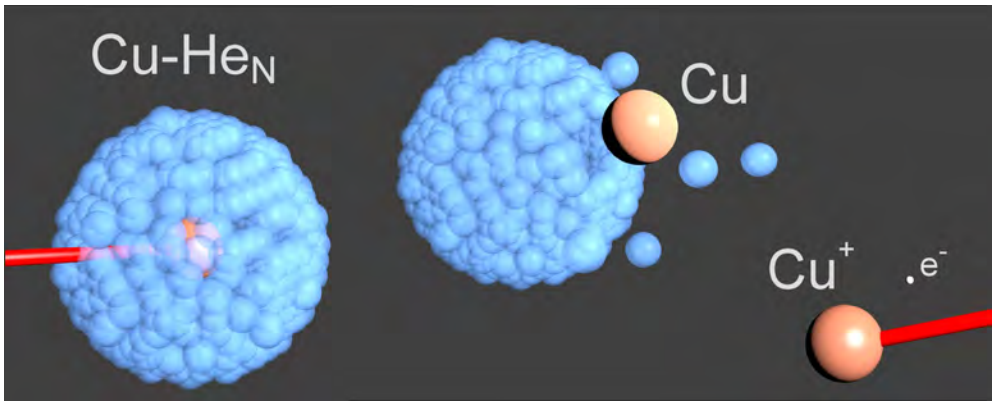

Figure 3.25: Table of contents graphic of Ref. [4]: "Laser Ionization and Spectroscopy of Cu in Superfluid Helium Nanodroplets".

[3] Artwork created by Friedich Lindebner

3.8 Spectroscopic Proof for the Absence of Bare Atoms from the Evaporation Sources

Besides the geometric considerations from Section 2.1.2, the observations from Sections 3.6 and 3.7 are now taken to formulate a spectroscopic proof, that no bare atoms from the evaporation sources reach the detection region. The Cu $^4D^\circ_{3/2,5/2} \leftarrow {}^2D_{3/2}$ transitions (see Fig. 3.23) clearly show the characteristics of free atoms, giving rise to sharp peaks at the cataloged transition energies. Similarly, this is the case for the Cr $z^5P^\circ_{1,2,3} \leftarrow a^5S_2$ and $z^7D^\circ_{1,2} \leftarrow a^5S_2$ transition peaks (Fig. 3.20). From the evaporation source it is not to be expected to obtain atoms in another than the ground state, so an electronic excitation has to happen in advance to reach the metastable $^2D_{3/2}$ (Cu) or a^5S_2 (Cr) state. For the excitation of free atoms into this metastable states, the energy has to meet exactly a ground state transition, which is neither the case for the dye laser at the $^4D^\circ_{3/2,5/2} \leftarrow {}^2D_{3/2}$ (Cu), $z^5P^\circ_{1,2,3} \leftarrow a^5S_2$ (Cr), or $z^7D^\circ_{1,2} \leftarrow a^5S_2$ (Cr) transition, nor the XeCl laser. So at least these bare atom transitions have to originate from an atom originally influenced by a droplet. This idea shall also be extended to the Cr and Cu ground state transitions. To evidence this, the laser was set to the free atom $^2P^\circ_{3/2} \leftarrow {}^2S_{1/2}$ Cu transition energy. While observing the Cu^+ ion yield corresponding to the bare atom transition peak maximum in Fig. 3.23, the chopper was closed which interrupts the droplet beam between the nozzle and the Cu evaporation source (see Fig. 2.1). This does not influence the path between the oven and the QMS. No ion counts were detected when the chopper was closed so no free atoms from the evaporation source contributed to the signal.

3.9 Photoinduced Molecular Dissociation and Photoinduced Recombination Mediated by Superfluid Helium Nanodroplets [5]

Besides the study of single Cr and Cu atoms in He_N, the He_N-assisted formation of Cr_2 and small Cr clusters is used to investigate the photoinduced dynamics of these species with REMPI. A whole cycle of photoinduced molecular dissociation, stable spatial separation of the fragments, and, finally, photoinduced recombination is observed. With mass resolved photoionization spectroscopy, the spectral evidence for the separation of dimer fragments to a surface bound and a solvated position after photoexcitation, as well as the geminate recombination with the initial partner upon photoionization of the surface located fragment is probed. In addition, an evidence that this process can be generalized also for small Cr clusters is presented.
Sections 3.9.1 to 3.9.3 correspond to a manuscript (submitted to a peer-reviewed journal) with the title "Photoinduced Molecular Dissociation and Photoinduced Recombination Mediated by Superfluid Helium Nanodroplets" by Andreas Kautsch, Markus Koch, and Wolfgang E. Ernst [5].

The author of this thesis had main contributions on

- All measurement data
- Data evaluation and interpretation
- Article text
- Figures and artwork

The contributions of the Co-authors and acknowledged persons listed below were:

- Markus Koch: Contribution and proofreading of text, discussing data, funding
- Wolfgang E. Ernst: Proofreading of text, supervision (experiment, publication), funding
- Friedrich Lindebner: Experimental assistance
- Martin Ratschek: Comparison with computational results [225, 245]
- Johann Potoschnig: Comparison with computational results [225, 245]
- Florian Lackner: Proofreading of text

3.9.1 Abstract

We present photoinduced chemical reaction dynamics of cold, isolated Cr_2 molecules in helium nanodroplets (He_N), exploiting the quantum state specific spatial separation

of solvated and surface locations on the droplet. The molecules are excited to achieve dissociation to a ground state (a^7S_3) and a metastable state (a^5S_2) atom. State specific spatial separation, in combination with efficient translational cooling to avoid ejection, causes the ground state atom to be solvated inside the droplet while the metastable atom migrates to the surface. A barrier between the two reactants formed by the He_N prevents recombination. We apply a resonance-enhanced multiphoton ionization scheme including the $y^5P^\circ_{1,2,3} \leftarrow a^5S_2$ atom transition to the surface atom in order to verify its location and separation from the solvated counterpart. This transition to a different quantum state and its subsequent ionization triggers solvation followed by geminate recombination, which is verified by the detection of Cr_2^+ molecular ions.

3.9.2 Photoinduced Molecular Dissociation and Photoinduced Recombination Mediated by Superfluid Helium Nanodroplets

He_N are a well-established tool for the spectroscopic investigation of isolated, ultracold (0.4 K) atoms, molecules, and clusters [9] and offer a unique method for cold chemistry on a single molecule level. The spatial separation of surface located and solvated dopant locations in He_N provides a promising approach to control and monitor chemical reactions, especially if the location is state specific and can thus be changed by photoexcitation. In this letter we demonstrate a complete cycle of photoinduced molecular dissociation, spatial separation of the fragments to a fully solvated and a stable, surface bound state and finally, photoinduced geminate recombination of the fragments.

Increasing interest in exploring chemical reactions in He_N originates from the ability to stabilize and investigate radical reaction intermediates [11, 246–248] or confine dissociation fragments to the volume of the droplet [81, 161]. High cooling rates permit efficient relaxation of excited molecules [161], the formation and stabilization of metastable clusters [249, 250], or aggregation of weak Van der Waals bound complexes [251]. Shallow energy barriers along reaction pathways can lead to trapping in local reactive potential-energy surface minima [248] which can be overcome by photo-activation to trigger chemical reactions [252, 253]. The location of a dopant is dictated by the interaction with helium (the pair potential) and can be estimated by the dimensionless Ancilotto parameter [66]. While the majority of atoms and molecules in their ground state are located inside the droplet, an electronic transition from the ground state to an excited state can initiate migration from inside to the droplet surface. This has been observed, for example, for Ag [91, 196, 254], Cu [4, 88], Cr [1–3], CF_3 [255, 256], and NO [68]. Usually, surface migration is followed by desorption from the droplet, only for NO* there was indication that the excited molecule remains in a surface-bound state [68]. For droplets doped with both surface located and solvated species the helium matrix can form a barrier that prevents molecule formation or clustering, even in the presence of long range Van der Waals interaction [257]. On the other side, Van der Waals forces

between solvated noble gas atoms and surface-located alkaline earth metal atoms can be exploited to overcome the separating character of He_N [258, 259]. Transition from a surface location to solvation was achieved for the HCN-Sr complex (and vice versa for HCN-Ca) by vibrational excitation [260], and in general, surface-located species migrate inside the droplet upon ionization [219, 261, 262].

Here we demonstrate that photoexcitation of solvated Cr_2 molecules results in dissociation to one atom in a solvated state (a^7S_3) and a second atom in a surface bound state (a^5S_2). Both fragments are sufficiently cooled to prevent ejection from the droplet. A resonant three photon ionization scheme is applied to the surface atom to verify its location and, at the same time, trigger solvation and recombination with its original partner.

Chromium clusters (Cr_2 - Cr_4) are formed inside helium nanodroplets by the pickup of single Cr atoms. The setup follows a Helium Nanodroplet Isolation (HENDI) apparatus, described in detail in Ref. [165]. In brief, He_N are formed by the supersonic expansion of high purity ^{4}He gas through a cooled nozzle (diameter d = 5 μm, stagnation pressure p_0 = 50 bar). Droplet sizes follow a log-normal distribution with a distribution maximum of $\hat{N}$ = 6 300 He atoms (mean droplet size $\bar{N}$ = 16 000) for a nozzle temperature of 14 K. The collimated He_N beam is crossed at right angles by an effusive beam of Cr atoms from an electron bombardment Cr oven [65] beneath the He_N beam. This setup ensures that no free atoms reach the detection region. Heating powers were experimentally adjusted to favor the pick-up of several atoms per droplet.

Excitation spectra of the Cr_n-He_N (n=2-4) complexes are recorded with beam depletion (BD) and resonance-enhanced multiphoton ionization (REMPI) spectroscopy. A quadrupole mass spectrometer (QMS, Balzers QMG 422) is attached at the end of the measurement chamber to facilitate mass selective ion detection. Laser pulses are obtained from an excimer (XeCl, Radiant Dyes RD-EXC-200, 308 nm, ∼20 ns pulse duration) pumped dye laser (Lamda Physik, FL3002, dye: Coumarin 2). For BD, the laser beam counter propagates the He_N beam. Laser excitation of Cr_2 causes the reduction of Cr_2 molecules arriving at the QMS by various mechanisms like helium evaporation due to dissipation of excess energy. For REMPI, the laser beam intersects the doped He_N beam at right angles in the extraction region of the QMS. The mass window of the QMS is set to integrate the signal of the Cr_n^+ isotopes and Cr_n^+-He around the central cluster mass to increase the signal. To further increase the signal quality, two color REMPI was used in addition to one color REMPI. Therefore, a fraction of the 308 nm pump laser light is overlapped with the dye laser.

In Fig. 3.26 the Cr_2 potential energy curves [119, 120] and Cr atom energy levels [112] that are of relevance for the presented experiment are shown, together with an excitation-ionization scheme indicated with arrows. The first step in this scheme is excitation of ground state Cr_2 ($4s\sigma_g^2 3d^{10}$) inside He_N via the $A^1\Sigma_u^+ \leftarrow X^1\Sigma_g^+$ transition. The excited $A^1\Sigma_u^+$ state correlates to one ground state (a^7S_3, $3d^5 4s$) and one excited (z^7P°, $3d^5 4p$)

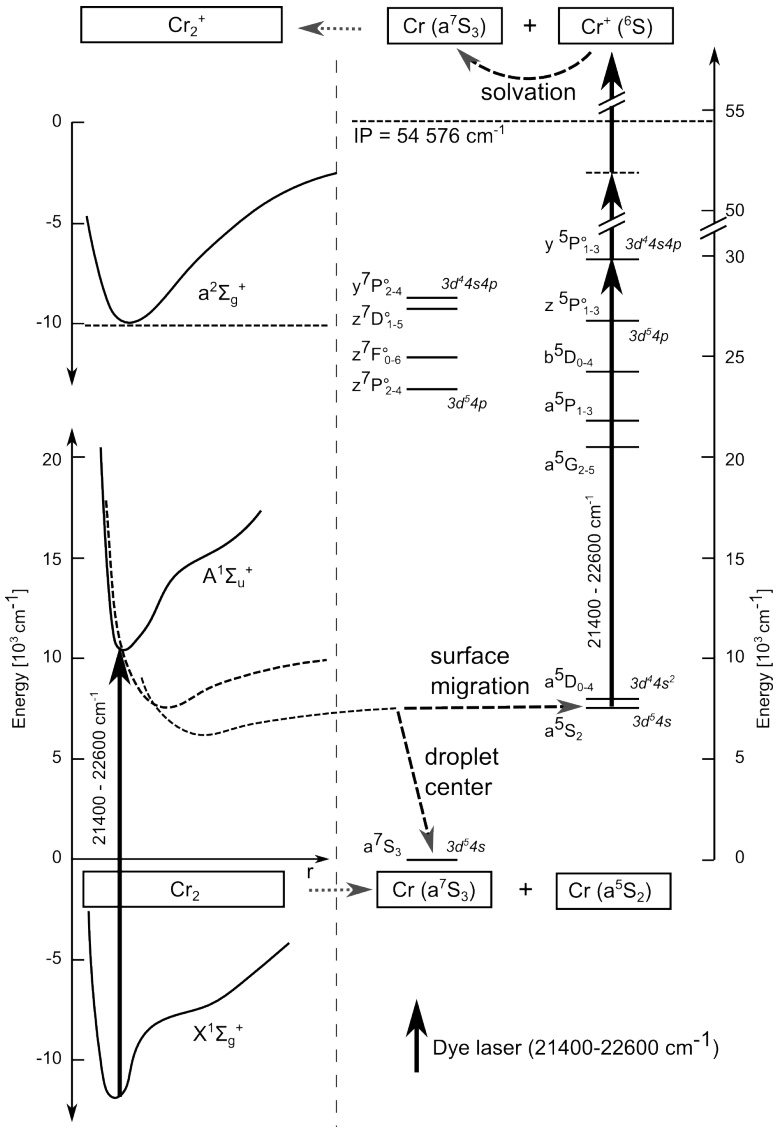

Figure 3.26: Cr_2 and Cr_2^+ potential energy curves [119, 120] (left) and Cr atom energy levels [112] (right). An ionization scheme is indicated by a combination of solid arrows (laser excitation) and dashed arrows (relaxation). Upon Cr_2 excitation to the $A^1\Sigma_u^+$ state inside He_N the molecule undergoes relaxation to predissociating states resulting in Cr (a^7S_3) and Cr (a^5S_2) atom states. While the first remains solvated inside the droplet, the latter migrates to the surface where it is ionized by a resonant three photon scheme. This triggers solvation and recombination to Cr_2^+.

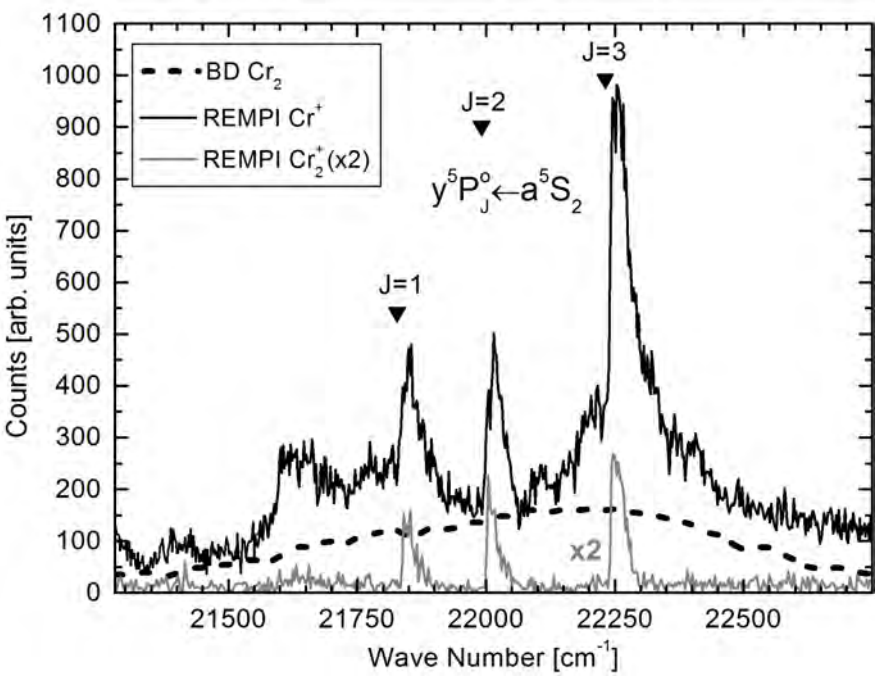

Figure 3.27: BD (dashed line) and one color REMPI spectra in the range of the Cr_2 $A^1\Sigma_u^+ \leftarrow X^1\Sigma_g^+$ transition. For REMPI, photoions are detected at the mass of Cr^+ (black solid line) and Cr_2^+ (gray solid line, multiplied by 2). The bare Cr atom $y^5P^\circ_{1,2,3} \leftarrow a^5S_2$ transition energies are indicated with triangles [112].

Cr atom, and, as will be shown below, dissociates via internal conversion to form an a^7S_3 and an a^5S_2 atom.

The spectra representing this process are shown in Figs. 3.27 and 3.28. Fig. 3.27 shows the Cr_2 BD spectrum (dashed line) and the one color REMPI spectra for the detection of Cr^+ (black solid line) and Cr_2^+ (gray solid line). The broadened in-droplet $A^1\Sigma_u^+ \leftarrow X^1\Sigma_g^+$ Cr_2 ground state excitation appears as a band in the BD spectrum, stretching from 21500 to 22600 cm^{-1}. We note that the Cr_2 might additionally be formed in higher multiplicities as it was observed for Ag_2 [20] in He_N. However, currently we cannot identify other multiplicities. For the strongly bound Cr_2 singlet ground state (binding energy = 1.42 eV (11450 cm^{-1})[120]), the majority of droplets are expected to survive the formation for a size distribution maximum of $\hat{N} = 6300$ and an energy of 5 cm^{-1} dissipated per evaporated He atom. In gas phase, the $A^1\Sigma_u^+ \leftarrow X^1\Sigma_g^+$ Cr_2 transition is observed at an energy of 21751 cm^{-1} (0-0 band, 2.7 eV) [17, 18, 118]. Cr_2 excitation spectra in other solid rare gas matrices yield usually shifted and broadened spectral features, but cannot provide a consistent picture about the magnitude of the shift, because of different trapping sites [15, 77, 85, 136, 263].

The REMPI spectrum for Cr^+ detection (Fig. 3.27, black solid line) resembles the

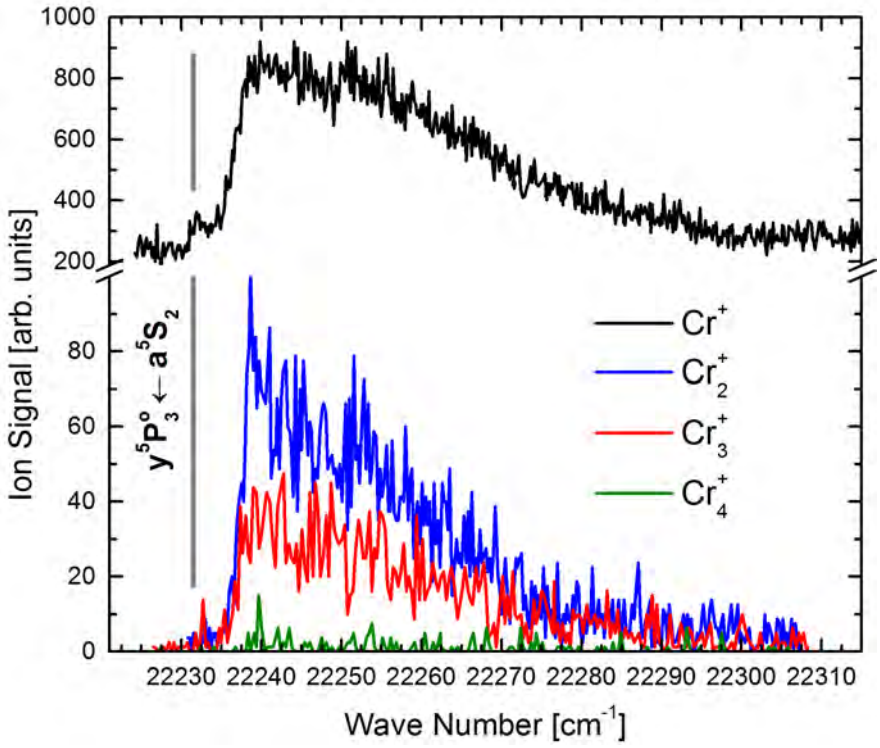

Figure 3.28: High resolution REMPI scan of the $y^5P^o_3 \leftarrow a^5S_2$ transition for detection of $Cr^+_{1,2,3,4}$ ions (two-color ionization scheme with the XeCl laser at 308 nm as second wavelength). The bare Cr atom $y^5P^o_3 \leftarrow a^5S_2$ transition energy is indicated with a vertical line [112].

Cr_2 band but shows three extra peaks and additional structures. Remarkably, the three pronounced peaks can be assigned to Cr atom $y^5P^\circ_{1,2,3} \leftarrow a^5S_2$ transitions (indicated by triangles [112]), pointing toward dissociation of Cr_2 upon excitation. Photoinduced dissociation in He_N has been observed for various species [203, 256, 258].

Predissociation of Cr_2 upon excitation to $A^1\Sigma_u^+$ has been observed in gas phase [18, 118, 119] and in matrix [15]. It was concluded, that the $A^1\Sigma_u^+$ state is crossed by at least one perturbing state and one predissociation state, where possible assignments were discussed by Andersson [119]. Riley et al. [18] propose the nonradiative transition from the $A^1\Sigma_u^+$ to another bound state. The latter is rapidly dissociated by a state correlating to the separate atom limit states Cr (a^7S_3) and Cr (a^5S_2, a^5D) [18]. From our results we clearly identify the population of the a^5S_2 atom state and assign the following dissociative process:

$$Cr_2(X^1\Sigma_g^+) \xrightarrow{h\nu} Cr_2(A^1\Sigma_u^+) \longrightarrow Cr(a^7S_3) + Cr(a^5S_2) \tag{3.6}$$

Because the in-droplet $A^1\Sigma_u^+ \leftarrow X^1\Sigma_g^+$ molecule band overlaps in energy with the atom $y^5P^\circ_{1,2,3} \leftarrow a^5S_2$ transition peaks, the Cr atoms in their metastable a^5S_2 state can be resonantly excited (c.f. Fig. 3.26). The lifetime of the final y^5P° state is with ∼70 ns [108] much longer than the laser pulse duration, and is not expected to be reduced by the He_N influence [217]. Excited $Cr^\star$ (y^5P°) can be photoionized by absorption of two photons and Cr^+ ions are detected upon detachment from the droplet.

The fate after dissociation is dictated by the interaction of the (metastable) Cr atoms with He atoms [225, 245]. In principle, the atoms can remain solvated inside the He_N, stay bound on the surface, or detach from the He_N with a certain probability to take a few He atoms along. Since the droplet acts as a heat bath, kinetic energy can be dissipated to prevent ejection [81, 161]. An excess energy of about 0.4 eV (3200 cm^{-1}), given by the difference of excitation energy and the dissociation limit, can be compensated by the evaporation of 640 He atoms. So the location of the dopants after dissociation (inside He_N, on its surface) is governed by the electronic states of the atoms. As observed for single Cr atoms in earlier experiments [1–3] and as predicted by theoretical studies [225, 245], the ground state (a^7S_3) atom remains solvated inside the droplet. The metastable state (a^5S_2) atom, in contrast, favors a surface position, which is suggested by DFT calculations (Ref. [245]) and can be confirmed by the observed excitation line shape. To this end we present a high resolution scan of the $y^5P^\circ_3 \leftarrow a^5S_2$ transition for the detection of Cr^+ to Cr_4^+ in Fig. 3.28. Although one color and two color REMPI give equal results, the latter provides a better signal to noise ratio and was thus chosen. One 308 nm photon is used for ionization of excited y^5P° state atoms instead of two dye laser photons (c.f. Fig. 3.26). At the bare atom transition energy (indicated with a vertical line in Fig. 3.28), the absence of sharp atomic lines proves that hardly any atoms are ejected from the droplet upon dissociation, encouraging the interpretation in terms of the effective kinetic energy dissipation upon predissociation.

Relative to the bare atom transition energy, the onset of the main feature is shifted approximately 5 cm^{-1} to the blue. A maximum is reached at 22240 cm^{-1} followed by an almost steady signal decrease, giving a total peak width of ∼50 cm^{-1}. These spectral characteristics are comparable to transitions of heavier alkali metal atoms that reside in a surface dimple [165, 257, 264], which allows us to identify the surface position for the a^5S_2 atom experimentally. We thus conclude that Cr a^5S_2 atoms are stable on the He_N surface, where they are available for further excitation.

We consider it important to mention that Cr $y^5P^\circ_{1,2,3}$←a^5S_2 excitation observed here on the He_N surface is of completely different nature than the z^5P°←a^5S_2 excitation of bare Cr atoms and small Cr-He_n (n=1,2,...) exciplexes observed in our previous studies [3]. This becomes obvious by comparing the corresponding line shapes. In the two color REMPI scheme in Ref. [3], 308 nm excitation and droplet mediated relaxation results in bare a^5S_2 Cr atoms and Cr-He_n exciplexes, both being ejected from the He_N. The corresponding excitation spectrum is composed of a sharp atom line accompanied by a wing to the blue (due to Cr-He_n). Here, in contrast, we see no signal at the bare atom line position (Fig. 3.28) and observe the onset of the peak 5 cm^{-1} to the blue. Although the XeCl laser was present for recording the spectra in Fig. 3.28, a bare atom transition peak is completely missing. We achieve this by letting the dye laser pulse precede the XeCl laser pulse and thereby prevent the 308 nm photon initiated process.

The characteristic $y^5P^\circ_{1,2,3}$←a^5S_2 transition peaks are also present in the REMPI spectra when employing Cr_2^+ detection (see Figs. 3.27 and 3.28), with exactly the same position and shape as for Cr^+ detection. This is even more surprising, because the Cr $y^5P^\circ_{1,2,3}$←a^5S_2 transition obviously has to be a step in the ionization process leading from Cr_2 to Cr_2^+. The observation becomes plausible when we build on our conclusions from before, namely that upon Cr_2 dissociation the a^5S_2 atom is residing on the surface while the a^7S_3 atom remains solvated inside the droplet. After resonant ionization of the surface atom with the $y^5P^\circ_{1,2,3}$←a^5S_2 transition as the first step (see Fig. 3.26), the Cr^+ ion has a fair chance to be pulled inside the He_N [219, 245, 262] where it recombines with its original partner to form Cr_2^+. Forming the Cr_2^+ $a^2\Sigma_g^+$ ground state ($Cr(^7S)$+$Cr^+(^6S)$ with binding energy = 1.30 eV [120]), releases approximately the same amount of energy to the droplet as the initial Cr_2 formation, again evaporating ∼2100 He atoms. A certain fraction of the droplets is now completely evaporated by this energy input which produces detectable, bare Cr_2^+ ions [81]. Remaining Cr_2^+ doped droplets that survived are not detected within the QMS mass window.

We mention that in addition to the $Cr+Cr^+ \rightarrow Cr_2^+$ recombination, another excitation path is possible, although, unlikely. According to DFT calculations [245], Cr y^5P° atoms have a stable position on the surface and inside the He_N, with a small energy barrier in between. Hence, Cr (y^5P°) atoms might move back inside the droplet to form an excited $Cr_2^\star$ molecule with the Cr (a^7S_3) ground state atom. As above, evaporation of a certain fraction of the droplets and subsequent two photon ionization would lead to

Cr_2^+ detection. Since the recombination process is confined to the volume of the droplet irrespective of the recombination path, this also proves the location of the a^5S_2 atom to be on the droplet.

Now we consider He_N doped with $Cr_{3,4}$ clusters. Fig. 3.28 shows that at the $y^5P_3^\circ \leftarrow a^5S_2$ transition also Cr_3^+ and Cr_4^+ ion clusters are detected. This means, that He_N doped with Cr_3 and Cr_4 (probably also $Cr_5, ...$) clusters can undergo a similar excitation process as Cr_2, including the characteristic REMPI of a surface located atom and subsequent recombination with the solvated fragments. Because of the strong Cr_2 bonding nature, Cr_3 is composed of a dimer plus a loosely bonded atom [23, 127] and Cr_4 of two dimers with strong intradimer but weak interdimer bonding [22]. This dimerization effect controls the cluster growth up to Cr_{11}, yielding similarities between the ground state photoabsorption spectra of dimers and small chromium cluster [22, 85, 136]. The detection of Cr_3^+ and Cr_4^+ therefore suggests that the Cr_2 dissociation process and surface migration of one atom is not disturbed by the presence of a further Cr atom or dimer in the droplet.

As depicted in Fig. 3.27, the spectrum detected on Cr^+ exhibits a broad background (Cr^+ signal between the $y^5P_{1,2,3}^\circ \leftarrow a^5S_2$ peaks), which is not present for detection on Cr_2^+, Cr_3^+, and Cr_4^+. Cr^+ ions contributing to the broad photoion background may originate from dissociated highly excited or ionized Cr dimers. The origin of the structure stretching from 21550 to 21700 cm^{-1} is not clear, but might be caused by resonant enhanced ionization of Cr_2 in competition with the predissociative pathway.

In conclusion, we have investigated the electronic $A^1\Sigma_u^+ \leftarrow X^1\Sigma_g^+$ excitation of Cr_2 molecules located inside He_N with beam depletion and resonant multiphoton ionization spectroscopy. The ionization spectra show, in addition to the droplet broadened molecular excitation structure, three pronounced peaks which we allocate to the $y^5P_{1,2,3}^\circ \leftarrow a^5S_2$ Cr atom transitions. The lineshape (50 cm^{-1} width and the 5 cm^{-1} blueshift of their onset with respect to the bare atom lines) leads us to the conclusion that the Cr_2 molecule dissociates upon excitation [18] into a solvated, ground state (a^7S_3) atom and a surface-located, metastable (a^5S_2) atom. The latter is ionized by resonance-enhanced multiphoton ionization. Surprisingly, we detect these three $y^5P_{1,2,3}^\circ \leftarrow a^5S_2$ atom peaks not only at the Cr^+ ion mass, but also at $Cr_{2,3,4}^+$ masses. Cr_2^+ detection demonstrates that during or upon photoionization a fraction of the surface atoms migrates back inside the droplet to recombine with their ground state counterpart. From the $Cr_{3,4}^+$ detection we conclude that this pairwise dissociation and surface migration process is not disturbed by the presence of additional Cr atoms, a fact which we attribute to the strong dimerization effect in small Cr clusters [22].

The elucidated mechanisms open a possibility for photoinduced chemistry mediated by He_N. Chemical reactions in He_N doped with both surface located (e.g., alkali-metal or alkaline earth metal atoms) and solvated species could be triggered by photoexcitation

of the latter to a surface located state. The bond formation can then be followed, e.g., with time-resolved femtosecond spectroscopy.

3.9.3 Acknowledgment

The authors thank Friedrich Lindebner for experimental assistance as well as Martin Ratschek and Johann V. Pototschnig for computational support and Florian Lackner for careful reading. The research was supported by the Austrian Science Fund (FWF) under grant number 22962-N20 and by the European Commission and the Styrian Government within the ERDF program.

3.9.4 Table of Contents Graphic

The table of contents graphic in Fig. 3.29 shows the whole process of photoinduced molecular dissociation of Cr_2, state dependent spatial separation of the Cr atoms, photoionization of the surface located atom, the solvation of the Cr^+ ion, and finally, the recombination forming a bare Cr_2^+. The REMPI spectrum from Fig. 3.28, which played a key role in the analysis, is shown in the background.

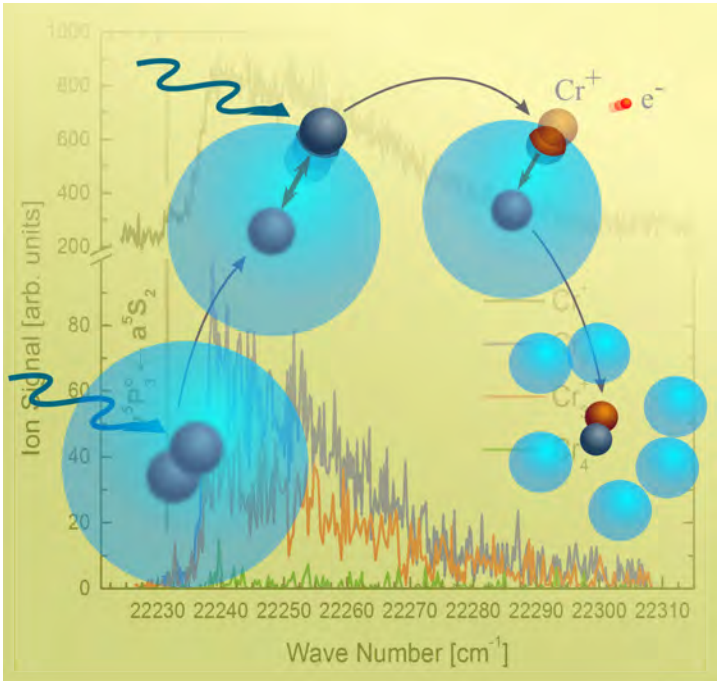

Figure 3.29: Table of contents graphic of Ref. [5]: "Photoinduced Molecular Dissociation and Photoinduced Recombination Mediated by Superfluid Helium Nanodroplets".

3.10 Cr Dimer and Cluster Transitions

Figure 3.30 shows a two color REMPI spectrum for the detection of Cr^+ and Cr_2^+ over a wide photon energy range. First, the Cr^+ spectrum is considered. The XeCl 308 nm fluence was kept low to minimize the Cr ejection and relaxation process discussed in Section 3.6. Still, the sharp peaks at the bare atom transition energies, spread over the whole spectrum, are a result of the XeCl initiated process. Hence, on the low energy side the spectral features from Fig. 3.20 are found. From 21450 - 22600 cm^{-1} the spectrum corresponds to the energy range covered in the one color REMPI spectrum of Section 3.9 (Fig. 3.27). By comparing the two spectra, it is obvious that the sharp bare atom lines at 21500 cm^{-1} and 22650 cm^{-1} are missing in the one color REMPI spectrum due to the absence of the XeCl laser initiated processes. In contrast, the $y^5P^\circ \leftarrow a^5S$ transitions of Cr atoms located on the surface after the Cr_2 dissociation, are also the dominant features in the two color REMPI spectrum here. The broad structure from 22750 - 23200 cm^{-1} could not be clearly assigned so far.
Considering the whole Cr^+ spectrum, the broad structures begin at energies around 21500 cm^{-1}, although no strong Cr ground state excitations are possible below an energy of 23305 cm^{-1} ($z^7P^\circ \leftarrow a^7S_3$). Hence, these bands are attributed to the Cr dimer and small Cr cluster transitions, as shown with Cr_2 BD between 21450 cm^{-1} and 22600 cm^{-1} (see Fig. 3.27). To support this conclusion, the Cr_2^+ spectrum is now considered. The $y^5P^\circ \leftarrow a^5S$ transition peaks are again dominant as described in Section 3.9. Although the noise level is high, the onset of an increased Cr_2^+ signal can be estimated to energies around 21500 cm^{-1}, and a slight indication of the broad structures from the Cr^+ is present. The low Cr_2^+ signal is attributed to the dissociation of Cr_2 during REMPI. Contrary, no Cr_2^+ would be detected if solely a single atom was involved in the excitation process.
A similar, unassigned structure is found in the region of the $z^7P^\circ_{2,3,4} \leftarrow a^7S_3$ transition. Figure 3.31 shows the one and two color REMPI spectrum for the detection of Cr^+. The two color REMPI spectrum (gray line) from 23300 - 23800 cm^{-1} corresponds to the spectrum shown in Fig. 3.19. To the high energy side of the $z^7P^\circ \leftarrow a^7S_3$ Cr in He_N transition, a weak structure is present that is clearly dominant in the one color REMPI spectrum (black line). No Cr transition lies in this energy region, so it is suggested that the structure corresponds to a Cr_2 or Cr cluster transition.
Figure 3.32 shows a spectrum recorded with a strongly focused dye laser beam. The e^7D_{1-5} states are populated from the a^7S_3 ground state through a virtual state with two photons of the same energy. A third photon from the laser pulse provides enough energy to reach the Cr IP (54 576 cm^{-1}). The non-resonant two-photon e^7D_{1-5} ($3d^54d$) $\leftarrow$ a^7S_3 ($3d^54s$) transitions appear as narrow sharp peaks at (half of) the energy of the catalogued bare atom transition energies. In contrast to all sharp free atom transitions described above, neither the XeCl laser was present nor a resonant single photon Cr ground state transition can be excited with the dye laser photons. Also, like it is typical

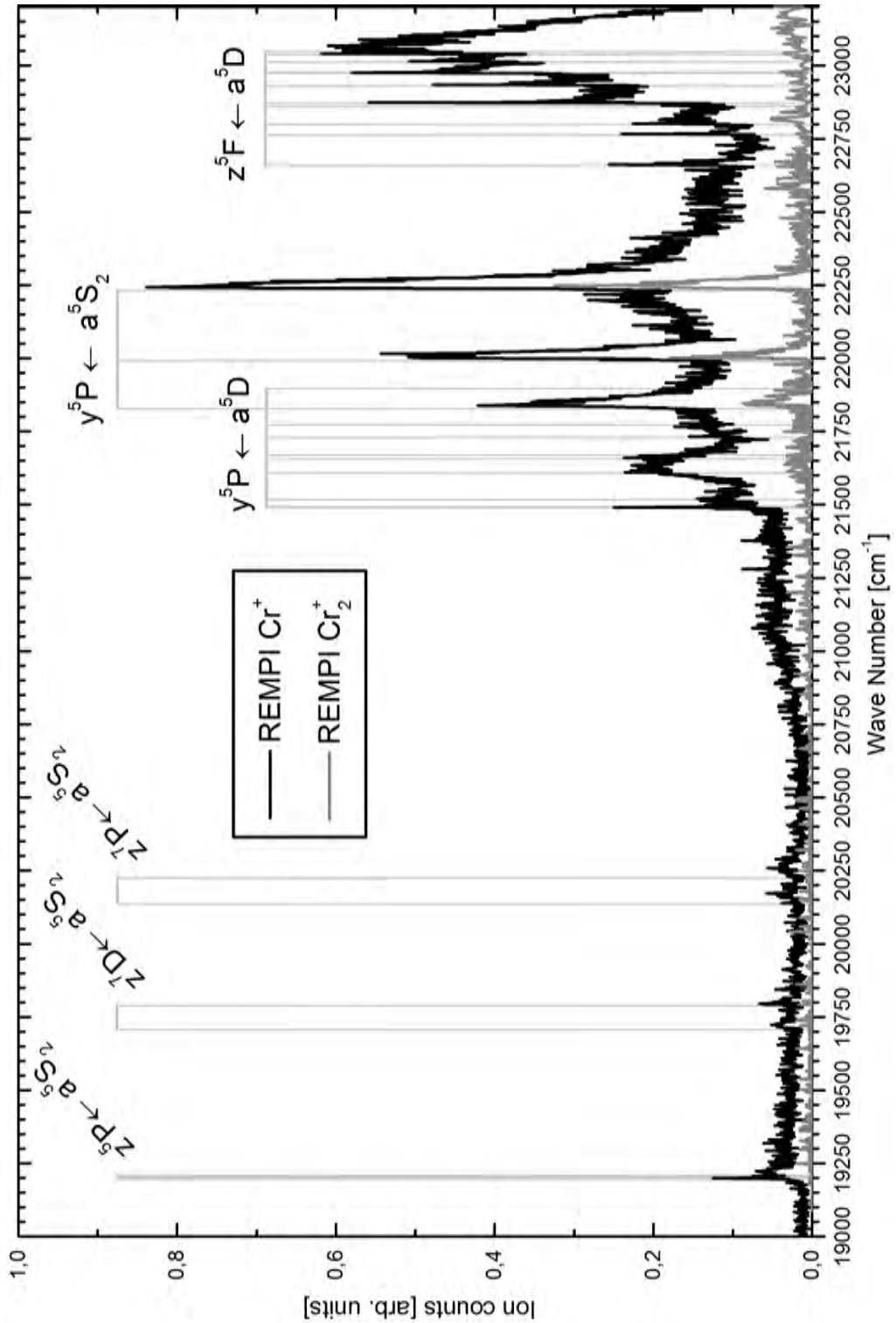

Figure 3.30: Two-color REMPI spectrum for the detection of Cr^+ and Cr_2^+. The signals are not to scale relative to each other. Bare atom transition energies are indicated with vertical lines [112].

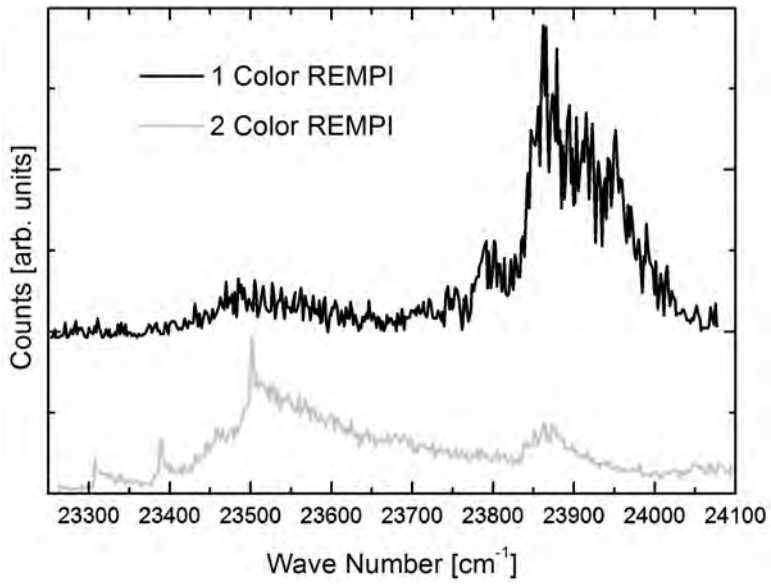

Figure 3.31: One- and two-color REMPI spectrum for the detection of Cr^+ in the region of the $z^7P^\circ_{2,3,4} \leftarrow a^7S_3$ transition energies. The plots are mutually shifted in vertical direction and not drawn to scale relative to each other.

when the XeCl laser is absent, no wings to any side are observed. That these lines are caused by atoms solvated inside the He_N is unlikely according to all the previous observations. A. Bartelt et al. observed narrow absorption lines for Eu solvated in He_N, caused by the weak interaction of the involved electrons with the helium bubble because they are shielded by the outermost $6s^2$ shell [89]. Although these were declared as the narrowest lines observed inside He_N, they still had a linewidth of $\sim$10 cm^{-1}.
Hence, it is suggested that there is an ejection mechanism present also after the excitation with a $\bar{\nu} \approx 21130$ cm^{-1} photon. When having a close look at Fig. 3.30, a low intensity structure is noticeable, stretching from 20750 cm^{-1} to 21500 cm^{-1}. This could be caused by a weak dimer or cluster absorption, populating a state that dissociates in two ground state atoms. If this is the case, the kinetic energy of the fragments is too high to be dissipated by the droplet, resulting in bare ground state atoms. Still, this interpretation should be considered with caution because of the high laser fluence used.

A clear assignment of all these broad structures might be challenging, since the formation of Cr_2 is not restricted to its singlet ground state. Ag_2 solvated inside He_N were found in the triplet and singlet state [20] which showed that the formation of triplet state systems is not restricted to surface locations [9, 21]. In contrast to alkali atoms, no selection mechanism preferring one configuration is present so the state population is only governed by the random formation and the lifetime of the metastable state. Hence, a great manifold of PES (see Ref. [119]) causes very different excitation paths.

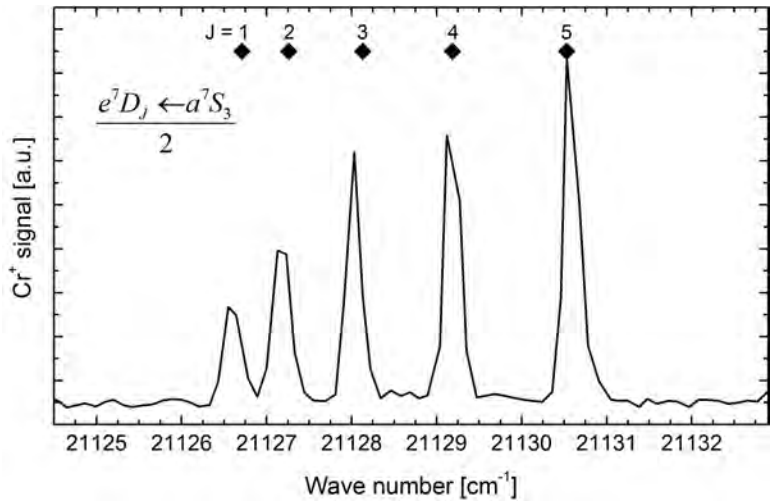

Figure 3.32: 1CR3PI spectrum of Cr doped He_N with the non-resonant two-photon $e^7D_{1-5} \leftarrow a^7S_3$ transition as intermediate step. The laser photon energy is plotted on the abscissa. Two photons of the energy marked with squares, are required for the Cr $e^7D_{1-5} \leftarrow a^7S_3$ transition.

To give a possibility to relate the $y^5P_3^\circ \leftarrow a^5S_2$ transition peak to Cr_2, Fig. 3.33a shows the REMPI spectra from Fig. 3.28 for different nozzle temperatures. The strong signal for low temperatures, i.e., larger droplet sizes, indicates the cause of the structures by Cr dimers or clusters. Only larger droplets can dissipate sufficient energy to survive the formation process of Cr dimers that are the parent species for dissociation and subsequent surface migration of the a^5S atoms.
Figure 3.33b shows the pick-up statistics probed with electron impact ionization (Cr^+ and Cr_2^+ detection) and PI (Cr^+ detection, $\tilde{\nu}$ =22241.6 cm^{-1}). Both pick-up statistics were recorded sequentially because of experimental reasons, but comparable conditions were carefully chosen (see heating power). The PI signal is in quite good concordance with the Cr_2 pickup statistics, especially when considering that cluster fragmentation upon electron impact ionization [65] can shift the monomer signal to slightly higher heating power.

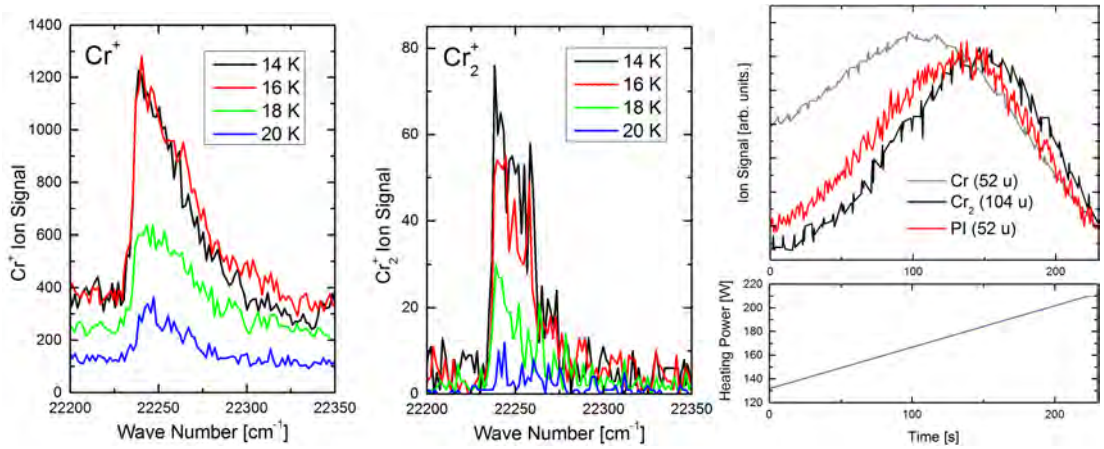

(a) (b)

Figure 3.33: (a) REMPI spectrum of the $y^5P_3^\circ \leftarrow a^5S_2$ transition for different nozzle temperatures and detection of Cr^+ (left) and Cr_2^+ (right). (b) PI signal for Cr^+ detection ($\tilde{\nu}$ =22241.6 cm^{-1}) compared to the Cr and Cr_2 pickup statistics recorded with electron bombardment ionization.

4 Summary and Outlook

Helium nanodroplets (He_N) serve as ideal containers to examine isolated species in a cold, superfluid matrix (0.37 K). With laser spectroscopy and mass spectrometry a variety of mechanisms were observed after the photoexcitation of chromium (Cr) and copper (Cu) atoms, dimers, and small clusters doped to He_N. These include mechanism such as relaxation to states with different multiplicities, the ejection from the He_N, the relocation on the He_N, the formation of small M-He_n (M = Cr, Cu) complexes and excited $M^\star$-He_n exciplexes, or the photoinduced dissociation and photoinduced recombination of Cr_2 and Cr clusters.

He_N are produced in a supersonic expansion of He gas through a cooled nozzle (T_0 = 21 - 13 K, $\hat{N}$ = 1 000 - 7 200 He atoms, p_0 = 50 bar) and doped with Cr and Cu atoms from high temperature evaporation sources in a crossed beam setup. After the pick-up of several atoms by one droplet, also metal dimers and small clusters are formed in the droplet.

With respect to the bare atom transitions, spectral excitation features of the strong ground state transitions (Cr: z,y^{7}P°←a^{7}S$_3$; Cu: ^{2}P°←^{2}S$_{1/2}$) are blue shifted by 200 - 300 cm^{-1} and broadened by 400 - 700 cm^{-1} [1–4]. This is observed with beam depletion (BD), laser induced fluorescence (LIF), or resonance-enhanced multiphoton ionization (REMPI). The observations are taken as indication for the solvation of both species inside the droplet. After the excitation with a laser photon, the atoms are found relaxing to energetically lower states because of the influence of the He matrix. Simultaneously, they are ejected from the droplet. For Cr, after the **y^{7}P° ← a^{7}S$_3$ excitation** inside the He_N, the population of the energetically lower z^{5}P°$_{1,2,3}$ and z^{7}P°$_{2,3,4}$ states is observed. The population distribution of the z^{5}P°$_{1,2,3}$ substates is found to be shifted toward the energetically lowest J=3 substate. In contrast, the z^{7}P°$_{2,3,4}$ states are equally populated. From the initially excited y^{7}P°$_{2,3,4}$ state, fluorescence is exclusively observed from the lowest J=2 substate independent of the excitation energy within the droplet broadened excitation band. Laser excitation of the **z^{7}P° ← a^{7}S$_3$ transition** shows a similar blueshift and broadening but leads to only weak fluorescence from the z^{7}P°$_2$ state. This can be attributed to quenching effects in the droplet or relaxation into dark states. All emission lines are narrow and at their bare atom transition energies, indicating the ejection of the bare Cr atoms after the relaxation. The relaxation and ejection allows the observation of transitions from the intermediate z^{5}P° state to autoionizing states in a 1CR2PI scheme [2]. The transition lines are found to have the shape of Fano

resonances [150], which originate from the interference between different excitation paths and are observed when the continuum above the ionization threshold can be accessed from a lower state both directly and via a discrete autoionizing state. The result are asymmetric spectral line profiles that are evaluated for the Cr $g^5D_{2,3,4} \leftarrow z^5P^\circ_{1,2,3}$ and $e^3D_{1,2,3} \leftarrow z^5P^\circ_{1,2,3}$ transitions.
With two-color resonant two-photon ionization (2CR2PI) of Cr and Cu doped to He_N, the used XeCl excimer laser initiates a photoinduced fast excitation-relaxation cycle that populates energetically lower levels than identified with the other methods [3, 4]. These include the a^7S_3 ground- and a^5S_2 metastable state. Furthermore, besides the ejected bare atoms, some helium atoms remain attached to a fraction of the metal atoms causing 50 cm^{-1} broad blue wings next to the bare atom spectral lines in the PI spectrum.
Cr_2 and small Cr clusters are formed in He_N after the multiple pick-up of atoms by one droplet. These show the very peculiar effect of photoinduced dissociation, spatial separation on the He_N, and photoinduced geminate recombination, which could be probed with REMPI [5]. After the Cr_2 ground state transition into a predissociative state, the molecule is dissociated forming one ground state- and a metastable state atom. While the a^7S_3 ground state atom remains solvated inside, a surface position is energetically favored for the atom in the a^5S_2 metastable state. After REMPI of the latter, the ion has an attractive potential with the He_N and geminate recombination with the other Cr atom is observed. This process could also be observed for small Cr clusters which is attributed to the strong dimerization effect, i.e., strong intradimer but weak interdimer bonding [119], upon cluster formation.

The found mechanisms offer a profound basis for the study of further transition metal atoms, dimers, and clusters doped to He_N. Ejection and relaxation mechanisms have also been observed for Ag in He_N [196] and are likely to apply to other transition metal atoms in He_N. These processes allow to access states other than the excited or can influence the fluorescence yield. The photoinduced control of the reactants' positions on the droplet can be useful to influence the outcome of chemical reactions, that benefit from the cold temperature of the droplet [246–248]. Furthermore, this could also allow time-dependent studies of reactions in a cold and weakly interacting matrix like He_N.

Bibliography

[1] A. Kautsch, M. Koch, W. E. Ernst. Electronic Relaxation After Resonant Laser Excitation of Cr in Superfluid Helium Nanodroplets. *The Journal of Physical Chemistry A* **117** (2013), 9621–9625.
DOI: 10.1021/jp312336m. Takeshi Oka Festschrift

[2] A. Kautsch, M. Hasewend, M. Koch, W. E. Ernst. Fano Resonances in Chromium Photoionization Spectra After Photoinduced Ejection From a Superfluid Helium Nanodroplet. *Physical Review A* **86** (2012), 033428–1 – 033428–4.
DOI: 10.1103/PhysRevA.86.033428

[3] M. Koch, A. Kautsch, F. Lackner, W. E. Ernst. One- and Two-Color Resonant Photoionization Spectroscopy of Chromium-doped Helium Nanodroplets. *The Journal of Physical Chemistry A* (2014), in press.
DOI: 10.1021/jp501285r. A. W. Castleman, Jr. Festschrift

[4] F. Lindebner, A. Kautsch, M. Koch, W. E. Ernst. Laser Ionization and Spectroscopy of Cu in Superfluid Helium Nanodroplets. *International Journal of Mass Spectrometry* **365-366** (2014), 255 – 259.
DOI: 10.1016/j.ijms.2013.12.022. Special issue: Tilmann Märk

[5] A. Kautsch, M. Koch, W. E. Ernst. Photoinduced Molecular Dissociation and Photoinduced Recombination Mediated by Superfluid Helium Nanodroplets. (2014), submitted.

[6] T. Bally. *Matrix Isolation. - in: Reactive Intermediate Chemistry.* edited by R. A. Moos, M. S. Platz, and M. Jones, Jr., John Wiley & Sons, Hoboken, New Jersey, 2004.

[7] J. Arnó, J. W. Bevan. *Infrared Spectroscopy in Supersonic Free Jets and Molecular Beams. - in: Jet Spectroscopy and Molecular Dynamics.* edited by J.M. Hollas and D. Phillips, Chapman and Hall, Glasgow, 1994.

[8] M. D. Morse. *Supersonic Beam Sources. - in: Atomic, Molecular, and Optical Physics: Atoms and Molecules. Volume 29B: Experimental Methods in the Physical*

Sciences. edited by F. B. Dunning and R. G. Hulet, Academic Press, San Diego, 1995.

[9] C. Callegari, W. E. Ernst. *Helium Droplets as Nanocryostats for Molecular Spectroscopy - from the Vacuum Ultraviolet to the Microwave Regime. - in: Handbook of High-Resolution Spectroscopy*. Vol. 3, p. 1551-1594. Edited by F. Merkt and M. Quack, John Wiley & Sons, Chinchester, 2011.

[10] E. Whittle, D. A. Dows, G. C. Pimentel. Matrix Isolation Method for the Experimental Study of Unstable Species. *The Journal of Chemical Physics* **22** (1954), 1943–1943.
DOI: 10.1063/1.1739957

[11] J. Küpper, J. M. Merritt. Spectroscopy of Free Radicals and Radical Containing Entrance-channel Complexes in Superfluid Helium Nanodroplets. *International Reviews in Physical Chemistry* **26** (2007), 249–287.
DOI: 10.1080/01442350601087664

[12] J. P. Toennies, A. F. Vilesov. Spectroscopy of Atoms and Molecules in Liquid Helium. *Annual Review of Physical Chemistry* **49** (1998), 1–41.
DOI: 10.1146/annurev.physchem.49.1.1

[13] B. Sonntag, P. Zimmermann. XUV Spectroscopy of Metal Atoms. *Reports on Progress in Physics* **55** (1992), 911.
DOI: 10.1088/0034-4885/55/7/002

[14] M. Beller, C. Bolm (Editors). *Transition Metals for Organic Synthesis, Vol. 1, 2nd Edition*. Wiley-VCH, Weinheim, 2004.

[15] M. J. Pellin, D. M. Gruen. Emission, Ground, and Excited State Absorption Spectroscopy of Cr_2 Isolated in Ar and Kr Matrices. *The Journal of Chemical Physics* **79** (1983), 5887–5893.
DOI: 10.1063/1.445758

[16] S. M. Casey, D. G. Leopold. Negative Ion Photoelectron Spectroscopy of Chromium Dimer. *The Journal of Physical Chemistry* **97** (1993), 816–830.
DOI: 10.1021/j100106a005

[17] D. L. Michalopoulos, M. E. Geusic, S. G. Hansen, D. E. Powers, R. E. Smalley. The Bond Length of Chromium Dimer. *The Journal of Physical Chemistry* **86** (1982), 3914–3916.
DOI: 10.1021/j100217a005

[18] S. J. Riley, E. K. Parks, L. G. Pobo, S. Wexler. The A←X Transition in Cr_2: Predissociation, Isotope Effects, and the 1–1 Sequence Band. *The Journal of Chemical Physics* **79** (1983), 2577–2582.
DOI: 10.1063/1.446169

[19] M. Moskovits, W. Limm, T. Mejean. A Weakly Bound Metastable State of Cr_2: Possible Evidence for a Double Minimum Ground State. *The Journal of Chemical Physics* **82** (1985), 4875–4879.
DOI: 10.1063/1.448658

[20] A. Przystawik, P. Radcliffe, S. Göde, K. H. Meiwes-Broer, J. Tiggesbäumker. Spectroscopy of Silver Dimers in Triplet States. *Journal of Physics B: Atomic, Molecular and Optical Physics* **39** (2006), S1183.
DOI: 10.1088/0953-4075/39/19/S25

[21] G. Auböck, J. Nagl, C. Callegari, W. E. Ernst. Triplet State Excitation of Alkali Molecules on Helium Droplets: Experiments and Theory. *The Journal of Physical Chemistry A* **111** (2007), 7404–7410.
DOI: 10.1021/jp070891y

[22] J. I. Martínez, J. A. Alonso. Theoretical Study of the Photoabsorption Spectrum of Small Chromium Clusters. *Physical Review B* **76** (2007), 205409.
DOI: 10.1103/PhysRevB.76.205409

[23] L.-S. Wang, H. Wu, H. Cheng. Photoelectron Spectroscopy of Small Chromium Clusters: Observation of Even-Odd Alternations and Theoretical Interpretation. *Physical Review B* **55** (1997), 12884–12887.
DOI: 10.1103/PhysRevB.55.12884

[24] Q. Wang, Q. Sun, B. K. Rao, P. Jena, Y. Kawazoe. Nitrogen-Induced Magnetic Transition in Small Chromium Clusters. *The Journal of Chemical Physics* **119** (2003), 7124–7130.
DOI: 10.1063/1.1607958

[25] F. Stienkemeier, K. K. Lehmann. Spectroscopy and Dynamics in Helium Nanodroplets. *Journal of Physics B: Atomic, Molecular and Optical Physics* **39** (2006), R127.
DOI: 10.1088/0953-4075/39/8/R01

[26] C. E. Moore, M. G. J. Minnaert, J. Houtgast. *The Solar Spectrum 2935 Å to 8770 Å*. 61. US Government Printing Office, Washington, 1966.

[27] D. E. Blackwell, S. L. R. Menon, A. D. Petford. Measurement of Relative Oscillator-Strengths for Cr-I Lines .1. Measures for Transitions From Levels a^7S_3(0.00 eV), a^5S_2(0.94 eV) and a^5D_{0-4} (0.96-1.03 eV). *Monthly Notices of the Royal Astronomical Society* **207** (1984), 533–546.

[28] R. C. Estler, N. S. Nogar. Chromium Determination in NIST Standard Urine by Resonance Ionization Mass Spectrometry. *Spectrochimica Acta Part B: Atomic Spectroscopy* **48** (1993), 663 – 669.
DOI: 10.1016/0584-8547(93)80070-B

[29] K. Bartschat, R. H. G. Reid, P. G. Burke, H. P. Summers. Electron Impact Ionization of Neutral Chromium. *Journal of Physics B: Atomic, Molecular and Optical Physics* **23** (1990), L721.
DOI: 10.1088/0953-4075/23/21/010

[30] M. Bures, J. Jacquinot, K. Lawson, M. Stamp, H. P. Summers, D. A. D'Ippolito, J. R. Myra. Impurity Release from the ICRF Antenna Screens in JET. *Plasma Physics and Controlled Fusion* **33** (1991), 937.
DOI: 10.1088/0741-3335/33/8/005

[31] M. A. Seeds, D. E. Backman. *Astronomy: The Solar System and Beyond*. Cengage Learning, Belmont, USA, 6th Edition, 2009.

[32] R. K. Kochhar. French Astronomers in India During the 17th - 19th Centuries. *Journal of the British Astronomical Association* **101** (1991), 95–100.

[33] The British Association Meeting at Edinburgh. *Nature* **4** (1871), 261–278.
DOI: 10.1038/004261a0

[34] G. Gienow, P. Gienow. *Materia Medica der Urelemente Teil 2*. epubliWiley, Berlin, 2010.

[35] H. Kamerlingh Onnes. Experiments on the Condensation of Helium by Expansion. *Communications from the Physical Laboratory of the University of Leiden* (1908), 744.

[36] H. Kamerlingh Onnes. The Condensation of Helium. *Nature* **77** (1908), 581.
DOI: 10.1038/077581a0

[37] P. Kapitza. Viscosity of Liquid Helium Below the λ-Point. *Nature* **141** (1938), 74.
DOI: 10.1038/141074a0

[38] D. D. Osheroff, R. C. Richardson, D. M. Lee. Evidence for a New Phase of Solid He^3. *Physical Review Letters* **28** (1972), 885–888.
DOI: 10.1103/PhysRevLett.28.885

[39] E. G. Lewars. *Modeling Marvels, Computational Anticipation of Novel Molecules*. Springer, 2008.

[40] J. C. Kotz, P. M. Treichel, J. Townsend. *Chemistry and Chemical Reactivity*. Cengage Learning, Belmont, CA, 2008.

[41] R. E. Grisenti, W. Schöllkopf, J. P. Toennies, G. C. Hegerfeldt, T. Köhler, M. Stoll. Determination of the Bond Length and Binding Energy of the Helium Dimer by Diffraction from a Transmission Grating. *Physical Review Letters* **85** (2000), 2284–2287.
DOI: 10.1103/PhysRevLett.85.2284

[42] V. Pierrard. Evaporation of Hydrogen and Helium Atoms from the Atmospheres of Earth and Mars. *Planetary and Space Science* **51** (2003), 319 – 327.
DOI: 10.1016/S0032-0633(03)00014-X

[43] W. G. Stuber, D. W. Studer, A. R. Winters. Pure Liquid Helium Produced from Crude Helium Feed - Providing Refrigeration for Two-step Purificn. by Compression and Expansion of Purified Helium in Liquefier. Patent: US4659351-A ; GB2185808-A ; AU8768028-A ; GB2185808-B, 1987.

[44] J. P. Toennies, A. F. Vilesov. Superfluid Helium Droplets: A Uniquely Cold Nanomatrix for Molecules and Molecular Complexes. *Angewandte Chemie International Edition* **43** (2004), 2622–2648.
DOI: 10.1002/anie.200300611

[45] E. W. Becker, R. Klingelhöfer, P. Lohse. Strahlen aus Kondensiertem Helium im Hochvakuum. *Zeitschrift Naturforschung Teil A* **16** (1961), 1259.

[46] H. Buchenau, E. L. Knuth, J. Northby, J. P. Toennies, C. Winkler. Mass Spectra and Time-of-flight Distributions of Helium Cluster Beams. *The Journal of Chemical Physics* **92** (1990), 6875–6889.
DOI: 10.1063/1.458275

[47] E. L. Knuth, U. Henne. Average Size and Size Distribution of Large Droplets Produced in a Free-jet Expansion of a Liquid. *The Journal of Chemical Physics* **110** (1999), 2664–2668.
DOI: 10.1063/1.477988

[48] M. Lewerenz, B. Schilling, J. Toennies. A New Scattering Deflection Method for Determining and Selecting the Sizes of Large Liquid Clusters of ^{4}He. *Chemical Physics Letters* **206** (1993), 381 – 387.
DOI: 10.1016/0009-2614(93)85569-A

[49] J. Harms, J. P. Toennies, F. Dalfovo. Density of superfluid helium droplets. *Physical Review B* **58** (1998), 3341–3350.
DOI: 10.1103/PhysRevB.58.3341

[50] F. Lackner, G. Krois, M. Koch, W. E. Ernst. Rubidium on Helium Droplets: Analysis of an Exotic Rydberg Complex for $N^* < 20$ and $0 \leq L \leq 3$. *The Journal of Physical Chemistry Letters* **3** (2012), 1404–1408.
DOI: 10.1021/jz300381y

[51] M. Koch. *Magnetic Resonance Spectroscopy of Single Alkali-Metal Atoms Isolated in Superfluid Helium Nanodroplets*. Dissertation, Graz University of Technology, 2009.

[52] F. Lackner. *Rydberg States of Alkali-Metal Atoms on Superfluid Helium Nanodroplets*. Dissertation, Graz University of Technology, 2012.

[53] M. Mudrich, F. Stienkemeier. Photoionizaton of Pure and Doped Helium Nanodroplets. *ArXiv e-prints* (2014). ArXiv:1406.4697

[54] M. Barranco, R. Guardiola, S. Hernández, R. Mayol, J. Navarro, M. Pi. Helium Nanodroplets: An Overview. *Journal of Low Temperature Physics* **142** (2006), 1–81.
DOI: 10.1007/s10909-005-9267-0

[55] L. F. Gomez, E. Loginov, A. F. Vilesov. Traces of Vortices in Superfluid Helium Droplets. *Physical Review Letters* **108** (2012), 155302.
DOI: 10.1103/PhysRevLett.108.155302

[56] J. Tiggesbäumker, F. Stienkemeier. Formation and Properties of Metal Clusters Isolated in Helium Droplets. *Physical Chemistry Chemical Physics* **9** (2007), 4748–4770.
DOI: 10.1039/B703575F

[57] J. Gspann. Helium Microdroplet Transparency in Heavy Atom Collisions. *Physica B+C* **108** (1981), 1309 – 1310.
DOI: 10.1016/0378-4363(81)90953-0

[58] A. Scheidemann, J. P. Toennies, J. A. Northby. Capture of Neon Atoms by ^{4}He Clusters. *Physical Review Letters* **64** (1990), 1899–1902.
DOI: 10.1103/PhysRevLett.64.1899

[59] M. Hartmann, R. E. Miller, J. P. Toennies, A. F. Vilesov. High-Resolution Molecular Spectroscopy of van der Waals Clusters in Liquid Helium Droplets. *Science* **272** (1996), 1631–1634.
DOI: 10.1126/science.272.5268.1631

[60] V. Mozhayskiy, M. N. Slipchenko, V. K. Adamchuk, A. F. Vilesov. Use of Helium Nanodroplets for Assembly, Transport, and Surface Deposition of Large Molecular and Atomic Clusters. *The Journal of Chemical Physics* **127** (2007) 094701.
DOI: 10.1063/1.2759927

[61] W. Demtröder. *Molekülphysik: Theoretische Grundlagen und experimentelle Methoden.* Oldenbourg Wissenschaftsverlag München, 2003.

[62] K. Hilpert, R. Ruthardt. Determination of the Dissociation Energy of the Cr_2 Molecule. *Berichte der Bunsengesellschaft für physikalische Chemie* **91** (1987), 724–731.
DOI: 10.1002/bbpc.19870910707

[63] R. Speiser, H. L. Johnston, P. Blackburn. Vapor Pressure of Inorganic Substances. III. Chromium Between 1283 and 1561 °K. *Journal of the American Chemical Society* **72** (1950), 4142–4143.
DOI: 10.1021/ja01165a082

[64] M. W. Williams, D. W. Beekman, J. B. Swan, E. T. Arakawa. Detection of Trace Elements with Resonance Ionization and Time-of-flight Mass Spectrometry. *Analytical Chemistry* **56** (1984), 1348–1350.
DOI: 10.1021/ac00272a033

[65] M. Ratschek, M. Koch, W. E. Ernst. Doping Helium Nanodroplets with High Temperature Metals: Formation of Chromium Clusters. *The Journal of Chemical Physics* **136** (2012) 104201.
DOI: 10.1063/1.3692330

[66] F. Ancilotto, P. B. Lerner, M. W. Cole. Physics of Solvation. *Journal of Low Temperature Physics* **101** (1995), 1123–1146.
DOI: 10.1007/BF00754527

[67] R. M. Bowley. Discussion of the Surface Tension of Liquid Helium. *Journal of Physics C: Solid State Physics* **3** (1970), 2012.
DOI: 10.1088/0022-3719/3/10/002

[68] E. Polyakova, D. Stolyarov, C. Wittig. Multiple Photon Excitation and Ionization of NO in and on Helium Droplets. *Journal of Chemical Physics* **124** (2006), 214308–1 – 214308–11.
DOI: 10.1063/1.2198844

[69] J. V. Pototschnig. *Theoretical investigation of the interaction between Chromium and Helium.* Master Thesis, Graz University of Technology, 2012.

[70] M. Mella, M. C. Colombo, G. Morosi. Ground State and Excitation Dynamics in Ag Doped Helium Clusters. *The Journal of Chemical Physics* **117** (2002), 9695–9702.
DOI: 10.1063/1.1518472

[71] J. Reho, U. Merker, M. R. Radcliff, K. K. Lehmann, G. Scoles. Spectroscopy of Mg Atoms Solvated in Helium Nanodroplets. *The Journal of Chemical Physics* **112** (2000), 8409–8416.
DOI: 10.1063/1.481444

[72] F. Stienkemeier, A. F. Vilesov. Electronic spectroscopy in He droplets. *The Journal of Chemical Physics* **115** (2001), 10119–10137.
DOI: 10.1063/1.1415433

[73] L. Andrews, M. Moskovits (Editors). *Chemistry and Physics of Matrix-Isolated Species.* North-Holland, Amsterdam, 1989.

[74] H. Wiggenhauser, D. M. Kolb, H. H. Rotermund, W. Schrittenlacher, W. Schroeder. Fluorescence Spectroscopy in the Nanosecond Range for Matrix-Isolated Cu Atoms and Dimers. *Chemical Physics Letters* **122** (1985), 71 – 75.
DOI: 10.1016/0009-2614(85)85480-4

[75] M. J. Pellin, D. M. Gruen, T. Fisher, T. Foosnaes. Emission, Optical–Optical Double Resonance, and Excited State Absorption Spectroscopy of Matrix Isolated Chromium and Molybdenum Atoms. *The Journal of Chemical Physics* **79** (1983), 5871–5886.
DOI: 10.1063/1.445757

[76] M. Moskovits, J. E. Hulse. The UV-Visible Spectra of Copper Atoms Isolated in Various Matrixes. *The Journal of Physical Chemistry* **85** (1981), 2904–2912.
DOI: 10.1021/j150620a011

[77] M. Vala, R. Pyzalski, J. Shakhsemampour, M. Eyring, J. Pyka, T. Tipton, J. C. Rivoal. Moment Analysis for Absorption and Magnetic Circular Dichroism Bands of Atomic P ← S Transitions: Application to Matrix-Isolated Chromium. *The Journal of Chemical Physics* **86** (1987), 5951–5957.
DOI: 10.1063/1.452480

[78] R. J. V. Zee, J. W. Weltner. ESR of the $^6\Sigma$ CrCu Molecule at 4°K. *The Journal of Chemical Physics* **74** (1981), 4330–4333.
DOI: 10.1063/1.441674

[79] R. J. V. Zee, C. A. Baumann, J. W. Weltner. ESR of Chromium Metal Atoms and Molecules in Matrices. *The Journal of Chemical Physics* **82** (1985), 3912–3920.
DOI: 10.1063/1.448882

[80] L. B. J. Knight, A. Mouchet, W. Beaudry, M. Duncan. High-temperature Generation and ESR Matrix Isolation Studies of ZnF and CdF in Neon and Argon Matrices. *Journal of Magnetic Resonance* **32** (1978), 383 – 390.
DOI: 10.1016/0022-2364(78)90053-7

[81] A. Braun, M. Drabbels. Photodissociation of Alkyl Iodides in Helium Nanodroplets. III. Recombination. *The Journal of Chemical Physics* **127** (2007) 114305.
DOI: 10.1063/1.2767263

[82] R. Fröchtenicht, U. Henne, J. P. Toennies, A. Ding, M. Fieber-Erdmann, T. Drewello. The Photoionization of Large Pure and Doped Helium Droplets. *The Journal of Chemical Physics* **104** (1996), 2548–2556.
DOI: 10.1063/1.471009

[83] D. S. Peterka, J. H. Kim, C. C. Wang, L. Poisson, D. M. Neumark. Photoionization Dynamics in Pure Helium Droplets. *The Journal of Physical Chemistry A* **111** (2007), 7449–7459.
DOI: 10.1021/jp0710032

[84] D. Buchta, S. R. Krishnan, N. B. Brauer, M. Drabbels, P. O'Keeffe, M. Devetta, M. Di Fraia, C. Callegari, R. Richter, M. Coreno, K. C. Prince, F. Stienkemeier, J. Ullrich, R. Moshammer, M. Mudrich. Extreme ultraviolet ionization of pure He nanodroplets: Mass-correlated photoelectron imaging, Penning ionization, and electron energy-loss spectra. *The Journal of Chemical Physics* **139** (2013) 084301.
DOI: 10.1063/1.4818531

[85] J. Derouault, M. Dalibart. Photo-induced Inter-conversion Reactions Between Atoms and Small Aggregates of Chromium Trapped in Argon Matrices. *Zeitschrift für Physik D - Atoms, Molecules and Clusters* **19** (1991), 211–214. DOI: 10.1007/BF01448294

[86] P. Moroshkin, A. Hofer, A. Weis. Atomic and Molecular Defects in Solid ^{4}He. *Physics Reports* **469** (2008), 1 – 57. DOI: 10.1016/j.physrep.2008.06.004

[87] A. P. Hickman, W. Steets, N. F. Lane. Nature of Excited Helium Atoms in Liquid Helium: A Theoretical Model. *Physical Review B* **12** (1975), 3705–3717. DOI: 10.1103/PhysRevB.12.3705

[88] F. Cargnoni, M. Mella. Solubility of Metal Atoms in Helium Droplets: Exploring the Effect of the Well Depth Using the Coinage Metals Cu and Ag. *The Journal of Physical Chemistry A* **115** (2011), 7141–7152. DOI: 10.1021/jp112408d

[89] A. Bartelt, J. Close, F. Federmann, K. Hoffmann, N. Quaas, J. Toennies. The UV-Absorption of Europium Atoms Embedded in Helium Nanodroplets. *Zeitschrift für Physik D - Atoms, Molecules and Clusters* **39** (1997), 1–2. DOI: 10.1007/s004600050101

[90] E. Loginov, M. Drabbels. Excited State Dynamics of Ag Atoms in Helium Nanodroplets. *The Journal of Physical Chemistry A* **111** (2007), 7504–7515. DOI: 10.1021/jp0716278

[91] D. Mateo, A. Hernando, M. Barranco, E. Loginov, M. Drabbels, M. Pi. Translational Dynamics of Photoexcited Atoms in ^{4}He Nanodroplets: The Case of Silver. *Physical Chemistry Chemical Physics* **15** (2013), 18388–18400. DOI: 10.1039/C3CP52221K

[92] D. M. Mann, H. P. Broida. Ultraviolet Absorption Spectra of Transition Metal Atoms in Rare-gas Matrices. *The Journal of Chemical Physics* **55** (1971), 84–94. DOI: 10.1063/1.1675564

[93] A. D. McNaught, A. Wilkinson. *IUPAC. Compendium of Chemical Terminology, 2nd ed. (the "Gold Book").* Blackwell Scientific Publications, Oxford, 1997.

[94] M. Satake. *Chemistry of Transition Elements.* Discovery Publishing House, New Delhi, 1994.

[95] P. Frances (Editor). *Nature Guide Rocks and Minerals.* Dorling Kindersley Limited, London, 2012.

[96] H. H. Binder. *Lexikon der chemischen Elemente: Das Periodensystem in Fakten, Zahlen und Daten (German Edition).* S. Hirzel, Stuttgart, 1999.

[97] M. P. McDaniel. *Chapter 3 - A Review of the Phillips Supported Chromium Catalyst and Its Commercial Use for Ethylene Polymerization. - in: Advances in Catalysis*, Vol. 53 of *Advances in Catalysis.* edited by B. C. Gates and H. Knözinger, Academic Press, 2010.
DOI: 10.1016/S0360-0564(10)53003-7

[98] F. Aubriet, J.-F. Muller, C. Poleunis, P. Bertrand, P. G. D. Croce, P. Grange. Activation Processes and Polyethylene Formation on a Phillips Model Catalyst Studied by Laser Ablation, Laser Desorption, and Static Secondary Ion Mass Spectrometry. *Journal of the American Society for Mass Spectrometry* **17** (2006), 406 – 414.
DOI: 10.1016/j.jasms.2005.11.008

[99] M. S. Kumar, N. Hammer, M. Rønning, A. Holmen, D. Chen, J. C. Walmsley, G. Øye. The Nature of Active Chromium Species in Cr-catalysts for Dehydrogenation of Propane: New Insights by a Comprehensive Spectroscopic Study. *Journal of Catalysis* **261** (2009), 116 – 128.
DOI: 10.1016/j.jcat.2008.11.014

[100] International Journal of Refractory Metals and Hard Materials. (accessed 27.05.2014)
`http://www.journals.elsevier.com/international-journal-of-refractory-metals-and-hard-materials/`

[101] B. Edenhofer, J. W. Bouwman. *Vacuum Heat Treatment. - in: Steel Heat Treatment Handbook, Second Edition.* edited by G. E. Totten and M. A.H. Howes, Marcel Dekker, New York, 1997.

[102] K. R. Hess, W. W. Harrison. Laser Resonance Ionization in a Glow Discharge. *Analytical Chemistry* **58** (1986), 1696–1702.
DOI: 10.1021/ac00121a021

[103] O. Gobert, T. Gibert, B. Dubreuil, P. Gelin, J. L. Debrun. Photoionization Cross Sections in Resonance Ionization Mass Spectrometry of Sputtered Metal Atoms: Applications to Material Analysis. *Journal of Applied Physics* **70** (1991), 7602–7607.
DOI: 10.1063/1.349716

[104] E. Saloman. A Resonance Ionization Spectroscopy/Resonance Ionization Mass Spectrometry Data Service. II-Data Sheets for Al, Ca, Cs, Cr, Co, Cu, Kr, Mg, Hg and Ni. *Spectrochimica Acta Part B: Atomic Spectroscopy* **46** (1991), 319 – 378.
DOI: 10.1016/0584-8547(91)80035-2

[105] M. Tomza. Prospects for Ultracold Polar and Magnetic Chromium-Closed-Shell-Atom Molecules. *Physical Review A* **88** (2013), 012519.
DOI: 10.1103/PhysRevA.88.012519

[106] R. Hafner, D. Spišák, R. Lorenz, J. Hafner. Magnetic Ground State of Cr in Density-functional Theory. *Physical Review B* **65** (2002), 184432.
DOI: 10.1103/PhysRevB.65.184432

[107] H. P. J. Wijn (Editor). *Magnetic Properties of Metals: d-Elements, Alloys and Compounds (Data in Science and Technology)*. Springer, Berlin Heidelberg, 1991.

[108] J. Cooper, N. Gibson, J. Lawler. Radiative Lifetimes in Cr I by Laser Induced Fluorescence. *Journal of Quantitative Spectroscopy and Radiative Transfer* **58** (1997), 85 – 92.
DOI: 10.1016/S0022-4073(97)00028-9

[109] J. Sugar, C. CORLISS. Atomic-Energy Levels of the Iron-Period Elements - Potassium Through Nickel. *Journal of Physical and Chemical Reference Data, Supplement No. 2* **14** (1985), 1.

[110] S. M. Younger, J. R. Fuhr, G. A. Martin, W. L. Wiese. Atomic Transition Probabilities for Vanadium, Chromium, and Manganese (a Critical Data Compilation of Allowed Lines). *Journal of Physical and Chemical Reference Data* **7** (1978), 495–629.
DOI: 10.1063/1.555576

[111] M. Mazari, W. W. Buechner, A. Sperduto. Energy Levels in Chromium-52. *Physical Review* **107** (1957), 1383–1386.
DOI: 10.1103/PhysRev.107.1383

[112] A. Kramida, Yu. Ralchenko, J. Reader and NIST ASD Team (2012). NIST Atomic Spectra Database (ver. 5.0), [Online]. Available: http://physics.nist.gov/asd [2013, May 16]. National Institute of Standards and Technology, Gaithersburg, MD.

[113] U. Becker, H. Bucka, A. Schmidt. Lifetime Measurements of Excited Chromium-I Levels. *Astronomy* **59** (1977), 145–149.

[114] M. M. Goodgame, W. A. Goddard. The "Sextuple" Bond of Chromium Dimer. *The Journal of Physical Chemistry* **85** (1981), 215–217.
DOI: 10.1021/j150603a001

[115] E. Thomas III, J. Murray, C. O'Connor, P. Politzer. The Cr_2 Molecule: Some Perspectives. *Journal of Molecular Structure: THEOCHEM* **487** (1999), 177 – 182.
DOI: 10.1016/S0166-1280(99)00152-9

[116] M. Moskovits, W. Limm, T. Mejean. Dichromium Revisited: A Resonance Raman Study of Cr_2 Isolated in Argon, Krypton and Xenon Matrixes. *The Journal of Physical Chemistry* **89** (1985), 3886–3890.
DOI: 10.1021/j100264a024

[117] M. D. Morse. Clusters of Transition-Metal Atoms. *Chemical Reviews* **86** (1986), 1049–1109.
DOI: 10.1021/cr00076a005

[118] V. E. Bondybey, J. H. English. Electronic Structure and Vibrational Frequency of Cr_2. *Chemical Physics Letters* **94** (1983), 443 – 447.
DOI: 10.1016/0009-2614(83)85029-5

[119] K. Andersson. The Electronic Spectrum of Cr_2. *Chemical Physics Letters* **237** (1995), 212 – 221.
DOI: 10.1016/0009-2614(95)00328-2

[120] C.-X. Su, D. A. Hales, P. B. Armentrout. The Bond Energies of Cr_2 and Cr_2^+. *Chemical Physics Letters* **201** (1993), 199 – 204.
DOI: 10.1016/0009-2614(93)85056-T

[121] M. Brynda, L. Gagliardi, B. O. Roos. Analysing the Chromium-Chromium Multiple Bonds Using Multiconfigurational Quantum Chemistry. *Chemical Physics Letters* **471** (2009), 1 – 10.
DOI: 10.1016/j.cplett.2009.02.006

[122] N. Desmarais, F. A. Reuse, S. N. Khanna. Magnetic Coupling in Neutral and Charged Cr_2, Mn_2, and CrMn Dimers. *The Journal of Chemical Physics* **112** (2000), 5576–5584.
DOI: 10.1063/1.481183

[123] S. P. Walch, C. W. Bauschlicher, B. O. Roos, C. J. Nelin. Theoretical Evidence for Multiple 3d Bonding in the V_2 and Cr_2 Molecules. *Chemical Physics Letters* **103** (1983), 175–179.
DOI: 10.1016/0009-2614(83)80376-5

[124] A. Noor, G. Glatz, R. Müller, M. Kaupp, S. Demeshko, R. Kempe. Metal-Metal Distances at the Limit: Cr-Cr 1.73 Å - the Importance of the Ligand and its Fine Tuning. *Zeitschrift für anorganische und allgemeine Chemie* **635** (2009), 1149–1152.
DOI: 10.1002/zaac.200900175

[125] F. Ruiperez, M. Piris, J. M. Ugalde, J. M. Matxain. The Natural Orbital Functional Theory of the Bonding in Cr_2, Mo_2 and W_2. *Physical Chemistry Chemical Physics* **15** (2013), 2055–2062.
DOI: 10.1039/C2CP43559D

[126] B. O. Roos. The Ground State Potential for the Chromium Dimer Revisited. *Collection of Czechoslovak Chemical Communications* **68** (2003), 265 – 274.
DOI: 10.1135/cccc20030265

[127] H. Cheng, L.-S. Wang. Dimer Growth, Structural Transition, and Antiferromagnetic Ordering of Small Chromium Clusters. *Physical Review Letters* **77** (1996), 51–54.
DOI: 10.1103/PhysRevLett.77.51

[128] C. Kittel. *Introduction to Solid State Physics*. John Wiley & Sons, 1995.

[129] B. Simard, M.-A. Lebeault-Dorget, A. Marijnissen, J. J. ter Meulen. Photoionization Spectroscopy of Dichromium and Dimolybdenum: Ionization Potentials and Bond Energies. *The Journal of Chemical Physics* **108** (1998), 9668–9674.
DOI: 10.1063/1.476442

[130] C.-H. Su, P. B. Armentrout. Collision-induced dissociation of Cr_n^+ (n=2-21) with Xe: Bond energies, dissociation pathways, and structures. *The Journal of Chemical Physics* **99** (1993), 6506–6516.
DOI: 10.1063/1.465842

[131] A. B. Anderson. Structures, Binding Energies, and Charge Distributions for Two to Six Atom Ti, Cr, Fe, and Ni Clusters and Their Relationship to Nucleation and Cluster Catalysis. *The Journal of Chemical Physics* **64** (1976), 4046–4055.
DOI: 10.1063/1.432013

[132] D. P. DiLella, W. Limm, R. H. Lipson, M. Moskovits, K. V. Taylor. Dichromium and Trichromium. *The Journal of Chemical Physics* **77** (1982), 5263–5266.
DOI: 10.1063/1.443794

[133] B. N. Papas, H. F. Schaefer. Homonuclear Transition-Metal Trimers. *The Journal of Chemical Physics* **123** (2005) 074321.
DOI: 10.1063/1.2006090

[134] A. Bérces. The Structures and Vibrational Frequencies of Small Clusters of Transition Metal and Main Group Elements a Gradient Corrected Density Functional Study. *Spectrochimica Acta Part A: Molecular and Biomolecular Spectroscopy* **53** (1997), 1257 – 1272.
DOI: 10.1016/S1386-1425(97)00024-3

[135] C. Kohl, G. F. Bertsch. Noncollinear Magnetic Ordering in Small Chromium Clusters. *Physical Review B* **60** (1999), 4205–4211.
DOI: 10.1103/PhysRevB.60.4205

[136] L. Fang, B. Davis, H. Lu, J. R. Lombardi. Resonance Raman Spectroscopy of Mass Selected Chromium Trimers in an Argon Matrix. *The Journal of Physical Chemistry A* **105** (2001), 9375–9378.
DOI: 10.1021/jp011248t

[137] P. Ruiz-Díaz, J. L. Ricardo-Chávez, J. Dorantes-Dávila, G. M. Pastor. Magnetism of Small Cr Clusters: Interplay Between Structure, Magnetic Order, and Electron Correlations. *Physical Review B* **81** (2010), 224431.
DOI: 10.1103/PhysRevB.81.224431

[138] F. W. Payne, W. Jiang, L. A. Bloomfield. Magnetism and Magnetic Isomers in Free Chromium Clusters. *Physical Review Letters* **97** (2006), 193401.
DOI: 10.1103/PhysRevLett.97.193401

[139] J. R. Davis (Editor). *ASM Specialty Handbook: Copper and Copper Alloys*. ASM International, 2001.

[140] V. S. Letokhov. *Laser Control of Atoms and Molecules*. Oxford University Press, 2007.

[141] I. V. Hertel, C. P. Schulz. *Atom-, Molekul- Und Optische Physik 1*. Springer-Lehrbuch. Springer, Berlin, 2008.

[142] G. S. Hurst, M. G. Payne, S. D. Kramer, C. H. Chen. Counting the Atoms. *Physics Today* **33** (1980), 24–29.

[143] G. S. Hurst, M. G. Payne. *Principles and applications of resonance ionisation spectroscopy*. A. Hilger, 1988.

[144] http://www.techniklexikon.net/d/ionisationsspektroskopie/ ionisationsspektroskopie.htm. (accessed 02.02.2014)

[145] W. Demtröder. *Atoms, Molecules and Photons*. Springer, Berlin, 2 Edition, 2010.

[146] W. Demtröder. *Laser Spectroscopy: Basic Concepts and Instrumentation*. Advanced Texts in Physics. Springer, 2003.

[147] K. Franzreb, J. Fine. The Significance of Autoionization Processes During Nonresonant One-Color Two-Photon Ionization of Neutral Silver and Copper Atoms at $\lambda = 248$ Nm. *Nuclear Instruments and Methods in Physics Research Section B: Beam Interactions with Materials and Atoms* **83** (1993), 266 – 274. DOI: 10.1016/0168-583X(93)95937-Z

[148] K. Tegeder, R. Lincke. Photoionisationsmessungen an Atomstrahlen. *Zeitschrift für Physik* **247** (1971), 51–59. DOI: 10.1007/BF01557854

[149] K. Godehusen, T. Richter, P. Zimmermann, M. Martins. Ion-Charge Resolved 3p Photoabsorption Measurements of Atomic Cr. *Journal of Physics B: Atomic, Molecular and Optical Physics* **36** (2003), L387. DOI: 10.1088/0953-4075/36/21/L03

[150] U. Fano. Effects of Configuration Interaction on Intensities and Phase Shifts. *Physical Review* **124** (1961), 1866–1878. DOI: 10.1103/PhysRev.124.1866

[151] U. Fano, J. W. Cooper. Line Profiles in the Far-UV Absorption Spectra of the Rare Gases. *Physical Review* **137** (1965), A1364–A1379. DOI: 10.1103/PhysRev.137.A1364

[152] H. Beutler. Über Absorptionsserien von Argon, Krypton und Xenon zu Termen zwischen den beiden Ionisierungsgrenzen $^2P^\circ_{3/2}$ und $^2P^\circ_{1/2}$. *Zeitschrift für Physik* **93** (1935), 177–196. DOI: 10.1007/BF01365116

[153] P. Fan, Z. Yu, S. Fan, M. L. Brongersma. Optical Fano Resonance of an Individual Semiconductor Nanostructure. *Nature Materials* **13** (2014), 471–475. DOI: 10.1038/NMAT3927

[154] D. E. Nikonov, A. m. c. Imamoğlu, M. O. Scully. Fano Interference of Collective Excitations in Semiconductor Quantum Wells and Lasing Without

Inversion. *Physical Review B* **59** (1999), 12212–12215.
DOI: 10.1103/PhysRevB.59.12212

[155] T.-T. Le, L. Cahill. Generation of Two Fano Resonances Using 4x4 Multimode Interference Structures on Silicon Waveguides. *Optics Communications* **301-302** (2013), 100 – 105.
DOI: 10.1016/j.optcom.2013.03.051

[156] Y. S. Joe, A. M. Satanin, C. S. Kim. Classical Analogy of Fano Resonances. *Physica Scripta* **74** (2006), 259.
DOI: 10.1088/0031-8949/74/2/020

[157] S. Baier, M. Martins, B. R. Muller, M. Schulze, P. Zimmermann. Investigation of Autoionizing Levels in the Ag I Spectrum Populated by a Combination of Discharge and Laser Excitation. *Journal of Physics B: Atomic, Molecular and Optical Physics* **23** (1990), 3095.
DOI: 10.1088/0953-4075/23/18/012

[158] R. Schinke. *Photodissociation Dynamics: Spectroscopy and Fragmentation of Small Polyatomic Molecules (Cambridge Monographs on Atomic, Molecular and Chemical Physics)*. Cambridge University Press, 1993.

[159] G. W. F. Drake (Editor). *Springer Handbook of Atomic, Molecular, and Optical Physics*. Springer, 2005.

[160] U. Buck. Photodissociation of Hydrogen Halide Molecules in Different Cluster Environments. *The Journal of Physical Chemistry A* **106** (2002), 10049–10062.
DOI: 10.1021/jp0208079

[161] D. Stolyarov, E. Polyakova, C. Wittig. Photoexcitation of NO_2 in He_n Droplets above the Gas-phase Dissociation Threshold. *The Journal of Physical Chemistry A* **108** (2004), 9841–9846.
DOI: 10.1021/jp040310u

[162] G. Herzberg. *The Spectra and Structures of Simple Free Radicals - an Introduction to Molecular Spectroscopy*. Dover Publications, New York, revised. Edition, 1971.

[163] H. Haken, H. C. Wolf. *Molekülphysik und Quantenchemie*. Springer-Verlag Berlin Heidelberg, 1994.

[164] J. L. McHale. *Molecular Spectroscopy*. Prentice Hall, 1st Edition, 1998.

[165] M. Koch, J. Lanzersdorfer, C. Callegari, J. S. Muenter, W. E. Ernst. Molecular Beam Magnetic Resonance in Doped Helium Nanodroplets. A Setup for Optically Detected ESR/NMR in the Presence of Unresolved Zeeman Splittings. *The Journal of Physical Chemistry A* **113** (2009), 13347–13356.
DOI: 10.1021/jp9041827

[166] J. Lanzersdorfer. *Assembly and Test of a Helium Cluster Beam Apparatus for Magnetic Field Studies of Atom and Molecule Doped Helium Nanodroplets.* Master Thesis, Institute of Experimental Physics, Graz University of Technology, 2008

[167] M. Koch, G. Auböck, C. Callegari, W. E. Ernst. Coherent Spin Manipulation and ESR on Superfluid Helium Nanodroplets. *Physical Review Letters* **103** (2009), 035302.
DOI: 10.1103/PhysRevLett.103.035302

[168] W. E. Gifford, R. C. Longsworth. *in: Advances in Cryogenic Engineering Proceedings of the 1965 Cryogenic Engineering Conference Rice University Houston, Texas August 23-25, 1965.* edited by K. D. Timmerhaus, Springer US, Boston, MA, 1966.

[169] M. Ratschek. *Doping Helium Droplets: Development of a High-Temperature Pickup Source.* Master Thesis, Graz University of Technology, 2010.

[170] F. Lindebner. *Spectroscopic Investigation of Cu and Cr Doped Helium Nanodroplets.* Master Thesis, Graz University of Technology, 2013.

[171] H. Buecher, H. Kneipp, U. Stamm. Abstimmbarer Laseroszillator Tunable laser oscillator. DE Patent 4,302,378, 1994.

[172] Lambda Physik. Manual for FL3002 pulsed dye laser.

[173] Oral communication with Dr. Kurt Iskra (29.02.2012)

[174] M. Przybylski, B. Otto, H. Gerhard. Spectral Purity of a FL 3002 Dye Laser Measured with a High-Resolution Monochromator. *Lambda Highlights* **11** (1988), 3.

[175] N. S. Nogar, R. A. Keller. Effect of Very Weak Laser Sidebands on Optical Spectra Involving Easily Saturable Intermediate States. *Analytical Chemistry* **57** (1985), 2992–2993.
DOI: 10.1021/ac00291a053

[176] E. Loginov, L. F. Gomez, A. F. Vilesov. Formation of Core-Shell Silver-Ethane Clusters in He Droplets. *The Journal of Physical Chemistry A* **117** (2013),

11774 – 11782.
DOI: 10.1021/jp402614s

[177] E. Loginov, L. F. Gomez, N. Chiang, A. Halder, N. Guggemos, V. V. Kresin, A. F. Vilesov. Photoabsorption of Ag_N (N =∼ 6-6000) Nanoclusters Formed in Helium Droplets: Transition from Compact to Multicenter Aggregation. *Physical Review Letters* **106** (2011), 233401.
DOI: 10.1103/PhysRevLett.106.233401

[178] ET Enterprises. (accessed 11.02.2014)
`www.et-enterprises.com`

[179] M. Wojdyr. Fityk: A General-purpose Peak Fitting Program. *Journal of Applied Crystallography* **43** (2010), 1126 – 1128.
DOI: 10.1107/S0021889810030499

[180] J. Lanzersdorfer. *Assembly and Test of a Helium Cluster Beam Apparatus for Magnetic Field Studies of Atom and Molecule Doped Helium Nanodroplets.* Master Thesis, Graz University of Technology, 2008.

[181] O. Instruments. Product catalog: Rectagular to circular fiber bundles. (accessed 19.04.2012)
`https://www.newport.com`

[182] J. Kändler. *Messung zur Ladungsverteilung in Erdalkalihalogeniden.* Dissertation, Freie Universität Berlin, 1988.

[183] Qioptiq. (accessed 04.07.2011)
`http://www.winlens.de/`

[184] Comar Optics Ltd. (accessed 04.11.2011)
`http://www.comaroptics.com/technical/optical-materials`

[185] R. P. Madden, K. Codling. 2-Electron Excitation States in Helium. *Astrophysical Journal* **141** (1965), 364.
DOI: 10.1086/148132

[186] T. Spinka. Lambda-Physik FL3002 GPIB Instrument Drivers, 2007. (accessed 04.07.2014)
`http://www.mathworks.com/matlabcentral/fileexchange/19944-lambda-physik-fl3002-gpib-instrument-drivers/content/FL3002DyeLaserControl/GPIB_Wrapper/DevClear.m`

[187] M. Kromer, S. A. Sim, M. Fink, F. K. R. pke, I. R. Seitenzahl, W. Hillebrandt. Double-Detonation Sub-Chandrasekhar Supernovae: Synthetic Observables for Minimum Helium Shell Mass Models. *The Astrophysical Journal* **719** (2010), 1067 – 1082.
DOI: 10.1088/0004-637X/719/2/1067

[188] D. E. Welty, T. Simon, L. M. Hobbs. Spatial and Temporal Variations in Interstellar Absorption Towards HD 72127AB. *Monthly Notices of the Royal Astronomical Society* **388** (2008), 323–334.
DOI: 10.1111/j.1365-2966.2008.13389.x

[189] R. K. Adair, C. K. Bockelman, R. E. Peterson. Experimental Corroboration of the Theory of Neutron Resonance Scattering. *Physical Review* **76** (1949), 308–308.
DOI: 10.1103/PhysRev.76.308

[190] J. A. Simpson, U. Fano. Classification of Resonances in the Electron Scattering Cross Section of Ne and He. *Physical Review Letters* **11** (1963), 158–159.
DOI: 10.1103/PhysRevLett.11.158

[191] M. Chergui, N. Schwentner, V. Chandrasekharan. Fano profiles on multiphonon continua in electronic transitions of matrix-isolated NO. *Physical Review Letters* **66** (1991), 2499–2502.
DOI: 10.1103/PhysRevLett.66.2499

[192] J. Faist, F. Capasso, C. Sirtori, K. W. West, L. N. Pfeiffer. Controlling the Sign of Quantum Interference by Tunnelling from Quantum Wells. *Nature* **390** (1997), 589 – 591.
DOI: 10.1038/37562

[193] V. Madhavan, W. Chen, T. Jamneala, M. F. Crommie, N. S. Wingreen. Tunneling into a Single Magnetic Atom: Spectroscopic Evidence of the Kondo Resonance. *Science* **280** (1998), 567–569.
DOI: 10.1126/science.280.5363.567

[194] A. E. Miroshnichenko, S. Flach, Y. S. Kivshar. Fano Resonances in Nanoscale Structures. *Reviews of Modern Physics* **82** (2010), 2257–2298.
DOI: 10.1103/RevModPhys.82.2257

[195] S. N. Nahar. Photoionization and Electron-ion Recombination of Cr I. *Journal of Quantitative Spectroscopy and Radiative Transfer* **110** (2009), 2148 – 2161.
DOI: 10.1016/j.jqsrt.2009.04.015

[196] F. Federmann, K. Hoffmann, N. Quaas, J. D. Close. Rydberg States of Silver: Excitation Dynamics of Doped Helium Droplets. *Physical Review Letters* **83** (1999), 2548–2551.
DOI: 10.1103/PhysRevLett.83.2548

[197] G. A. Martin, J. R. Fuhr, L. W. Wiese. *Atomic transition probabilities scandium through manganese*. Published by the American Chemical Society and the American Institute of Physics for the National Bureau of Standards, 1988.

[198] M. C. E. Huber, R. J. Sandeman, E. F. Tubbs. The Spectrum of Cr I Between 179.8 and 200 nm Wavelengths, Absorption Cross Sections, and Oscillator Strengths. *Proceedings of the Royal Society of London. Series A, Mathematical and Physical Sciences* **342** (1975), 431–438.

[199] A. Bartelt, J. D. Close, F. Federmann, N. Quaas, J. P. Toennies. Cold Metal Clusters: Helium Droplets as a Nanoscale Cryostat. *Physical Review Letters* **77** (1996), 3525–3528.
DOI: 10.1103/PhysRevLett.77.3525. Indium, Silver

[200] Z. J. Jakubek, Q. Hui, M. Takami. Condensation of He Gas on Optically Excited Ag Atoms Below the Critical Temperature (T<5.2K). *Physical Review Letters* **79** (1997), 629–632.
DOI: 10.1103/PhysRevLett.79.629

[201] S. Grebenev, J. P. Toennies, A. F. Vilesov. Superfluidity Within a Small Helium-4 Cluster: The Microscopic Andronikashvili Experiment. *Science* **279** (1998), 2083 – 2086.
DOI: 10.1126/science.279.5359.2083

[202] J. Tang, Y. Xu, A. R. W. McKellar, W. Jäger. Quantum Solvation of Carbonyl Sulfide with Helium Atoms. *Science* **297** (2002), 2030–2033.
DOI: 10.1126/science.1073718

[203] J. Higgins, C. Callegari, J. Reho, F. Stienkemeier, W. E. Ernst, K. K. Lehmann, M. Gutowski, G. Scoles. Photoinduced Chemical Dynamics of High-Spin Alkali Trimers. *Science* **273** (1996), 629 – 631.
DOI: 10.1126/science.273.5275.629

[204] J. Higgins, W. E. Ernst, C. Callegari, J. Reho, K. K. Lehmann, G. Scoles, M. Gutowski. Spin Polarized Alkali Clusters: Observation of Quartet States of the Sodium Trimer. *Physical Review Letters* **77** (1996), 4532–4535.
DOI: 10.1103/PhysRevLett.77.4532

[205] A. W. Hauser, G. Auböck, W. E. Ernst. *Jahn-Teller Effect and Spin-Orbit Coupling in Heavy Alkali Trimers - in: Vibronic Interactions and the Jahn-Teller Effect: Theory and Applications*, Vol. 23 of *Springer Series: Progress in Theoretical Chemistry and Physics*. edited by M. Atanasov, C. Daul, and P. Tregenna-Piggott, Springer, 2012.

[206] F. Lackner, G. Krois, M. Theisen, M. Koch, W. E. Ernst. Spectroscopy of ns, nP, and nD Rydberg Series of Cs Atoms on Helium Nanodroplets. *Physical Chemistry Chemical Physics* **13** (2011), 18781–18788.
DOI: 10.1039/C1CP21280J

[207] F. Lackner, G. Krois, W. E. Ernst. Rydberg-Ritz Analysis and Quantum Defects for Rb and Cs Atoms on Helium Nanodroplets. *Molecular Physics* **111** (2013), 2118–2125.
DOI: 10.1080/00268976.2013.788792

[208] E. Loginov, C. Callegari, F. Ancilotto, M. Drabbels. Spectroscopy on Rydberg States of Sodium Atoms on the Surface of Helium Nanodroplets. *Journal of Physical Chemistry A* **115** (2011), 6779–6788.
DOI: 10.1021/jp111146n

[209] J. Nagl, G. Auböck, A. W. Hauser, O. Allard, C. Callegari, W. E. Ernst. Heteronuclear and Homonuclear High-Spin Alkali Trimers on Helium Nanodroplets. *Physical Review Letters* **100** (2008), 063001.
DOI: 10.1103/PhysRevLett.100.063001

[210] M. Mudrich, O. Bünermann, F. Stienkemeier, O. Dulieu, M. Weidemüller. Formation of Cold Bialkali Dimers on Helium Nanodroplets. *The European Physical Journal D* **31** (2004), 291–299.
DOI: 10.1140/epjd/e2004-00139-6

[211] G. Krois, J. V. Pototschnig, F. Lackner, W. E. Ernst. Spectroscopy of Cold LiCa Molecules Formed on Helium Nanodroplets. *The Journal of Physical Chemistry A* **117** (2013), 13719–13731.
DOI: 10.1021/jp407818k

[212] B. O. Roos, A. C. Borin, L. Gagliardi. Reaching the Maximum Multiplicity of the Covalent Chemical Bond. *Angewandte Chemie International Edition* **46** (2007), 1469–1472.
DOI: 10.1002/anie.200603600

[213] T. Jamneala, V. Madhavan, M. Crommie. Kondo Response of a Single Antiferromagnetic Chromium Trimer. *Physical Review Letters* **87** (2001), 256804–

1 – 256804–4.
DOI: 10.1103/PhysRevLett.87.256804

[214] A. Volk, P. Thaler, M. Koch, E. Fisslthaler, W. Grogger, W. E. Ernst. High Resolution Electron Microscopy of Ag-Clusters in Crystalline and Non-Crystalline Morphologies Grown Inside Superfluid Helium Nanodroplets. *The Journal of Chemical Physics* **138** (2013) 214312.
DOI: 10.1063/1.4807843

[215] P. Thaler, A. Volk, M. Ratschek, M. Koch, W. E. Ernst. Molecular Dynamics Simulation of the Deposition Process of Cold Ag-Clusters under Different Landing Conditions. *Journal of Chemical Physics* **140** (2014) 044326.
DOI: 10.1063/1.4862917

[216] F. R. Brühl, R. A. Trasca, W. E. Ernst. Rb-He Exciplex Formation on Helium Nanodroplets. *Journal of Chemical Physics* **115** (2001), 10220–10224.
DOI: 10.1063/1.1410118

[217] J. Reho, C. Callegari, J. Higgins, W. E. Ernst, K. K. Lehmann, G. Scoles. Spin-Orbit Effects in the Formation of the Na-He Excimer on the Surface of He Clusters. *Faraday Discuss.* **108** (1997), 161–174.
DOI: 10.1039/A706108K

[218] M. Theisen, F. Lackner, W. E. Ernst. Cs Atoms on Helium Nanodroplets and the Immersion of Cs^+ Into the Nanodroplet. *The Journal of Chemical Physics* **135** (2011) 074306.
DOI: 10.1063/1.3624840

[219] M. Theisen, F. Lackner, W. E. Ernst. Forming Rb^+ Snowballs in the Center of He Nanodroplets. *Physical Chemistry Chemical Physics* **12** (2010), 14861–14863.
DOI: 10.1039/C0CP01283A

[220] C. P. Schulz, P. Claas, F. Stienkemeier. Formation of $K^\star He$ Exciplexes on the Surface of Helium Nanodroplets Studied in Real Time. *Physical Review Letters* **87** (2001), 153401–1 – 153401–4.
DOI: 10.1103/PhysRevLett.87.153401

[221] G. Droppelmann, O. Bünermann, C. P. Schulz, F. Stienkemeier. Formation Times of RbHe Exciplexes on the Surface of Superfluid versus Normal Fluid Helium Nanodroplets. *Physical Review Letters* **93** (2004), 023402–1 – 023402–4.
DOI: 10.1103/PhysRevLett.93.023402

[222] C. Giese, T. Mullins, B. Grüner, M. Weidemüller, F. Stienkemeier, M. Mudrich. Formation and Relaxation of RbHe Exciplexes on He Nanodroplets Studied by Femtosecond Pump and Picosecond Probe Spectroscopy. *Journal of Chemical Physics* **137** (2012), 244307–1 – 244307–7.
DOI: 10.1063/1.4772749

[223] E. Loginov, M. Drabbels. Spectroscopy and Dynamics of Barium-Doped Helium Nanodroplets. *Journal of Chemical Physics* **136** (2012), 154302.
DOI: 10.1063/1.3701565

[224] L. Fechner, B. Gruner, A. Sieg, C. Callegari, F. Ancilotto, F. Stienkemeier, M. Mudrich. Photoionization and Imaging Spectroscopy of Rubidium Atoms Attached to Helium Nanodroplets. *Physical Chemistry Chemical Physics* **14** (2012), 3843–3851.
DOI: 10.1039/C2CP22749E

[225] J. V. Pototschnig, M. Ratschek, A. W. Hauser, W. E. Ernst. An Ab Initio Study of the CrHe Diatomic Molecule: the Effect of Van Der Waals Distortion on a Highly Magnetic Multi-electron System. *Physical Chemistry Chemical Physics* **16** (2014), 9469–9478.
DOI: 10.1039/C4CP00559G

[226] F. Stienkemeier, J. Higgins, C. Callegari, S. Kanorsky, W. Ernst. Spectroscopy of Alkali Atoms (Li, Na, K) Attached to Large Helium Clusters. *Zeitschrift für Physik D - Atoms, Molecules and Clusters* **38** (1996), 253–263.
DOI: 10.1007/s004600050090

[227] H. Schöbel, C. Leidlmair, P. Bartl, S. Denifl, T. D. Märk, O. Edit, P. Scheier. Electron Ionization of Superfluid Helium Nanodroplets Doped with C_{60} and Small Molecules. *Journal of Physics: Conference Series* **388** (2012), 012044.
DOI: 10.1088/1742-6596/388/1/012044

[228] H. Schöbel, P. Bartl, C. Leidlmair, S. Denifl, O. Echt, T. Märk, P. Scheier. High-Resolution Mass Spectrometric Study of Pure Helium Droplets, and Droplets Doped with Krypton. *The European Physical Journal D* **63** (2011), 209–214.
DOI: 10.1140/epjd/e2011-10619-1

[229] F. Ferreira da Silva, P. Bartl, S. Denifl, O. Echt, T. D. Mark, P. Scheier. Argon Clusters Embedded in Helium Nanodroplets. *Physical Chemistry Chemical Physics* **11** (2009), 9791–9797.
DOI: 10.1039/B913175B

[230] N. S. Nogar, R. C. Estler. Chromium Detection by Laser Desorption and Resonance Ionization Mass Spectrometry. *Analytical Chemistry* **64** (1992), 465–468.
DOI: 10.1021/ac00029a003

[231] L. F. Gomez, L. F., E. Loginov, A. Halder, V. V. Kresin, A. Vilesov. Formation of Unusual Copper Clusters in Helium Nanodroplets. *International Journal of Nanoscience* **12** (2013), 1350014.
DOI: 10.1142/S0219581X13500142

[232] L. An der Lan, P. Bartl, C. Leidlmair, H. Schöbel, S. Denifl, T. D. Märk, A. M. Ellis, P. Scheier. Submersion of Potassium Clusters in Helium Nanodroplets. *Physical Review B* **85** (2012), 115414.
DOI: 10.1103/PhysRevB.85.115414

[233] F. Cargnoni, A. Ponti, M. Mella. Coinage Metal Exciplexes with Helium Atoms: A Theoretical Study of M*(2L)He_n (M = Cu, Ag, Au; L = P,D). *Physical Chemistry Chemical Physics* **15** (2013), 18410–18423.
DOI: 10.1039/C3CP50250C

[234] F. Federmann, K. Hoffmann, N. Quaas, J. Toennies. Spectroscopy of Extremely Cold Silver Clusters in Helium Droplets. *The European Physical Journal D* **9** (1999), 11–14.
DOI: 10.1007/PL00010922

[235] P. L. Stiles, R. E. Miller. Structures and Bonding Nature of Small Monoligated Copper Clusters (HCN-Cu_N, N = 1-3) Through High-Resolution Infrared Spectroscopy and Theory. *The Journal of Physical Chemistry A* **110** (2006), 10225–10235.
DOI: 10.1021/jp063187a

[236] E. Vehmanen, V. Ghazarian, C. Sams, I. Khachatryan, J. Eloranta, V. A. Apkarian. Injection of Atoms and Molecules in a Superfluid Helium Fountain: Cu and Cu_2He_n (n = 1, ..., ∞). *The Journal of Physical Chemistry A* **115** (2011), 7077–7088.
DOI: 10.1021/jp1123986

[237] G. A. Ozin, S. A. Mitchell, J. Garcia-Prieto. Fluorescence Spectroscopy and Photoprocesses of Copper, Cu and Cu_2 in Rare Gas Matrixes. *The Journal of Physical Chemistry* **86** (1982), 473–479.
DOI: 10.1021/j100393a012

[238] P. Moroshkin, V. Lebedev, A. Weis. Vibronic Transitions of Atomic Bubbles in Condensed ^{4}He. *Journal of Low Temperature Physics* **162** (2011), 710–717. DOI: 10.1007/s10909-010-0304-2

[239] M. Lewerenz, B. Schilling, J. P. Toennies. Successive Capture and Coagulation of Atoms and Molecules to Small Clusters in Large Liquid Helium Clusters. *The Journal of Chemical Physics* **102** (1995), 8191–8207. DOI: 10.1063/1.469231

[240] M. Kabir, A. Mookerjee, A. Bhattacharya. Structure and Stability of Copper Clusters: a Tight-Binding Molecular Dynamics Study. *Physical Review A* **69** (2004), 043203. DOI: 10.1103/PhysRevA.69.043203

[241] I. Katakuse, T. Ichihara, Y. Fujita, T. Matsuo, T. Sakurai, H. Matsuda. Mass Distributions of Copper, Silver and Gold Clusters and Electronic Shell Structure. *International Journal of Mass Spectrometry and Ion Processes* **67** (1985), 229 – 236. DOI: 10.1016/0168-1176(85)80021-5

[242] C. Braun. *Time-Resolved Photoelectron Spectroscopy of Mass-Selected Metal-Water Clusters*. Dissertation, University of Konstanz, 2012.

[243] C. A. Baumann, R. J. V. Zee, J. W. Weltner. ESR of Bimetallic Transition-Metal Molecules at 4 K. I. CrCu, CrAg, and CrAu. *The Journal of Chemical Physics* **79** (1983), 5272–5279. DOI: 10.1063/1.445715

[244] M. Wang, B. Wang, Z. Chen. Magnetic Coupling Interaction for Mixed Transition Metal Dimer: Ab Initio MRCI(SD) + Q Investigation on CrCu. *Chemical Physics Letters* **435** (2007), 5 – 9. DOI: 10.1016/j.cplett.2006.12.037

[245] M. Ratschek, J. V. Pototschnig, A. W. Hauser, W. E. Ernst. Solvation and Spectral Line Shifts of Chromium Atoms in Helium Droplets based on a Density Functional Theory Approach. *Journal of Physical Chemistry A* (2014), in press. DOI: 10.1021/jp5034036

[246] J. M. Merritt, J. Kupper, R. E. Miller. Entrance Channel X-HF (X = Cl, Br and I) Complexes Studied by High-resolution Infrared Laser Spectroscopy in Helium Nanodroplets. *Physical Chemistry Chemical Physics* **7** (2005), 67–78. DOI: 10.1039/B415427D

[247] J. M. Merritt, S. Rudić, R. E. Miller. Infrared Laser Spectroscopy of CH_3—HF in Helium Nanodroplets: The Exit-channel Complex of the F + CH_4 Reaction. *The Journal of Chemical Physics* **124** (2006) 084301.
DOI: 10.1063/1.2168450

[248] S. Rudić, J. M. Merritt, R. E. Miller. Infrared Laser Spectroscopy of the CH_3HCN Radical Complex Stabilized in Helium Nanodroplets. *The Journal of Chemical Physics* **124** (2006) 104305.
DOI: 10.1063/1.2170087

[249] K. Nauta, R. E. Miller. Nonequilibrium Self-Assembly of Long Chains of Polar Molecules in Superfluid Helium. *Science* **283** (1999), 1895–1897.
DOI: 10.1126/science.283.5409.1895

[250] K. Nauta, R. E. Miller. Formation of Cyclic Water Hexamer in Liquid Helium: The Smallest Piece of Ice. *Science* **287** (2000), 293 – 295.
DOI: 10.1126/science.287.5451.293

[251] W. K. Lewis, C. M. Lindsay, R. E. Miller. Ionization and Fragmentation of Isomeric Van Der Waals Complexes Embedded in Helium Nanodroplets. *Journal of Chemical Physics* **129** (2008), 201101.
DOI: 10.1063/1.3025917

[252] G. E. Douberly, J. M. Merritt, R. E. Miller. IR-IR double resonance spectroscopy in helium nanodroplets: Photo-induced isomerization. *Physical Chemistry Chemical Physics* **7** (2005), 463 – 468.
DOI: 10.1039/B417553K

[253] T. Liang, S. D. Flynn, A. M. Morrison, G. E. Douberly. Quantum Cascade Laser Spectroscopy and Photoinduced Chemistry of Al-$(CO)_n$ Clusters in Helium Nanodroplets. *Journal of Physical Chemistry A* **115** (2011), 7437 – 7447.
DOI: 10.1021/jp203367t

[254] N. B. Brauer, S. Smolarek, E. Loginov, D. Mateo, A. Hernando, M. Pi, M. Barranco, W. J. Buma, M. Drabbels. Critical Landau Velocity in Helium Nanodroplets. *Physical Review Letters* **111** (2013), 153002.
DOI: 10.1103/PhysRevLett.111.153002

[255] A. Braun, M. Drabbels. Imaging the Translational Dynamics of CF_3 in Liquid Helium Droplets. *Physical Review Letters* **93** (2004), 253401.
DOI: 10.1103/PhysRevLett.93.253401

[256] A. Braun, M. Drabbels. Photodissociation of Alkyl Iodides in Helium Nanodroplets. I. Kinetic Energy Transfer. *The Journal of Chemical Physics* **127** (2007) 114303.
DOI: 10.1063/1.2767261

[257] J. Poms, A. W. Hauser, W. E. Ernst. Helium Nanodroplets Doped with Xenon and Rubidium Atoms: A Case Study of Van Der Waals Interactions Between Heliophilic and Heliophobic Dopants. *Physical Chemistry Chemical Physics* **14** (2012), 15158 – 15165.
DOI: 10.1039/C2CP42333B

[258] A. Masson, M. Briant, A. Hernando, N. Halberstadt, J.-M. Mestdagh, M.-A. Gaveau. Fluorescence Emission of Ca-Atom From Photodissociated Ca_2 in Ar-Doped Helium Droplets. I. Experimental. *The Journal of Chemical Physics* **137** (2012) 184310.
DOI: 10.1063/1.4762836

[259] E. Lugovoj, J. P. Toennies, A. Vilesov. Manipulating and enhancing chemical reactions in helium droplets. *The Journal of Chemical Physics* **112** (2000), 8217–8220.
DOI: 10.1063/1.481426

[260] G. E. Douberly, P. L. Stiles, R. E. Miller, R. Schmied, K. K. Lehmann. $(HCN)_mM_n$ (M = K, Ca, Sr): Vibrational Excitation Induced Solvation and Desolvation of Dopants in and on Helium Nanodroplets. *The Journal of Physical Chemistry A* **114** (2010), 3391–3402.
DOI: 10.1021/jp908834m

[261] L. An der Lan, P. Bartl, C. Leidlmair, R. Jochum, S. Denifl, O. Echt, P. Scheier. Solvation of Na^+, K^+, and Their Dimers in Helium. *Chemistry - A European Journal* **18** (2012), 4411–4418.
DOI: 10.1002/chem.201103432

[262] X. Zhang, M. Drabbels. Communication: Barium Ions and Helium Nanodroplets: Solvation and Desolvation. *The Journal of Chemical Physics* **137** (2012) 051102.
DOI: 10.1063/1.4743900

[263] E. P. Kündig, M. Moskovits, G. A. Ozin. Matrix Synthesis and Characterisation of Dichromium. *Nature* **254** (1975), 503–504.
DOI: 10.1038/254503a0

[264] G. Auböck, J. Nagl, C. Callegari, W. E. Ernst. Electron Spin Pumping of Rb Atoms on He Nanodroplets via Nondestructive Optical Excitation. *Physical Review Letters* **101** (2008), 035301.
DOI: 10.1103/PhysRevLett.101.035301

Appendix

A.1 Technical Drawings

The technical drawings of the parts mounted to the experimental setup are presented in this chapter. All drawings are also stored on the enclosed DVD (Appendix B.3).

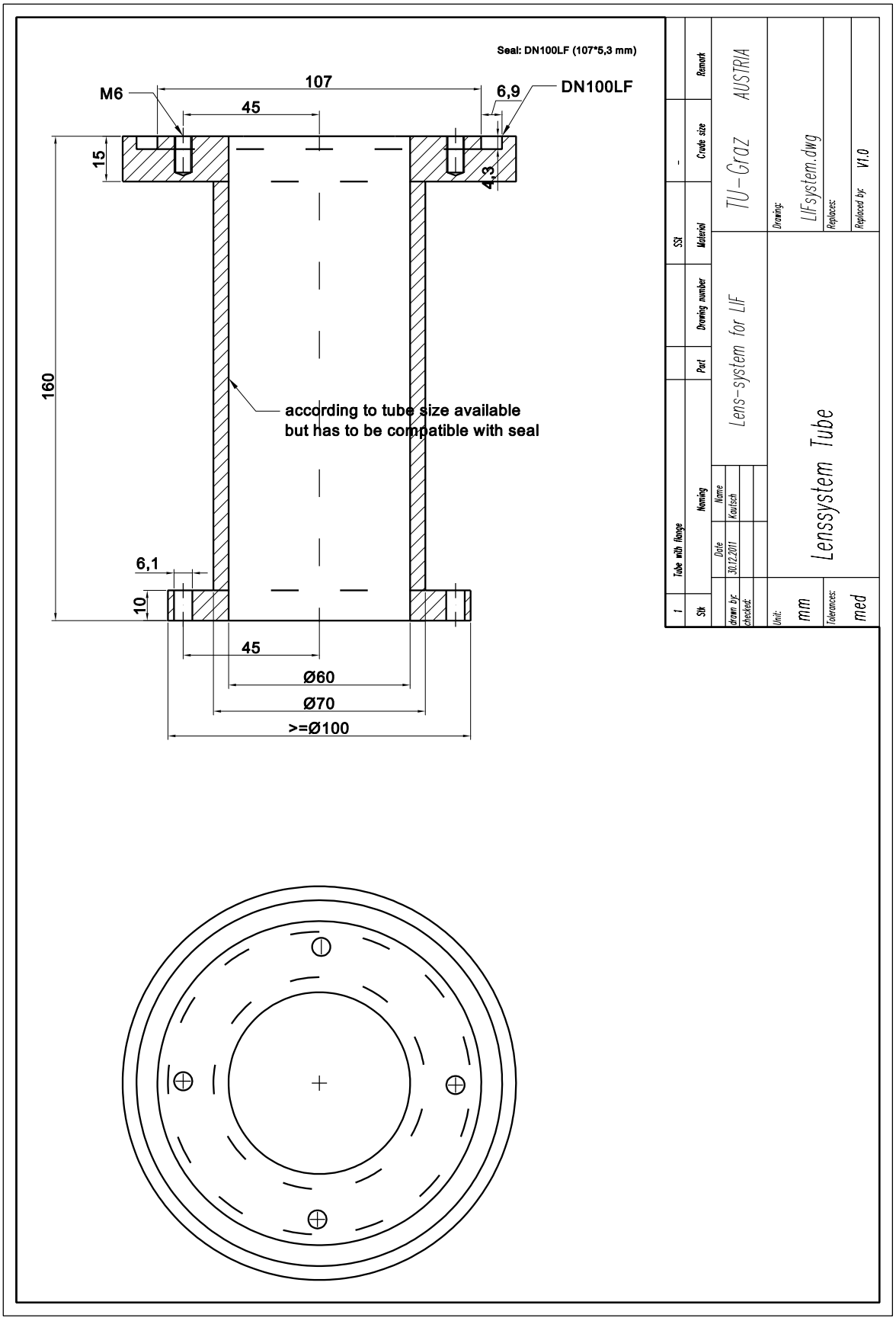
Seal: DN100LF (107*5,3 mm)
M6
107
45
6,9
DN100LF
15
4,3
160
according to tube size available
but has to be compatible with seal
6,1
10
45
Ø60
Ø70
>=Ø100
1
Tube with Flange
Stk
Norming
Part
Drawing number
SSt
-
Material
Crude size
Remark
Lens-system for LIF
TU-Graz AUSTRIA
Drawing:
LIFsystem.dwg
Replaces:
Replaced by:
V1.0
Name
Date
drawn by:
Kautsch
30.12.2011
checked:
Unit:
mm
Tolerances:
med
Lenssystem Tube

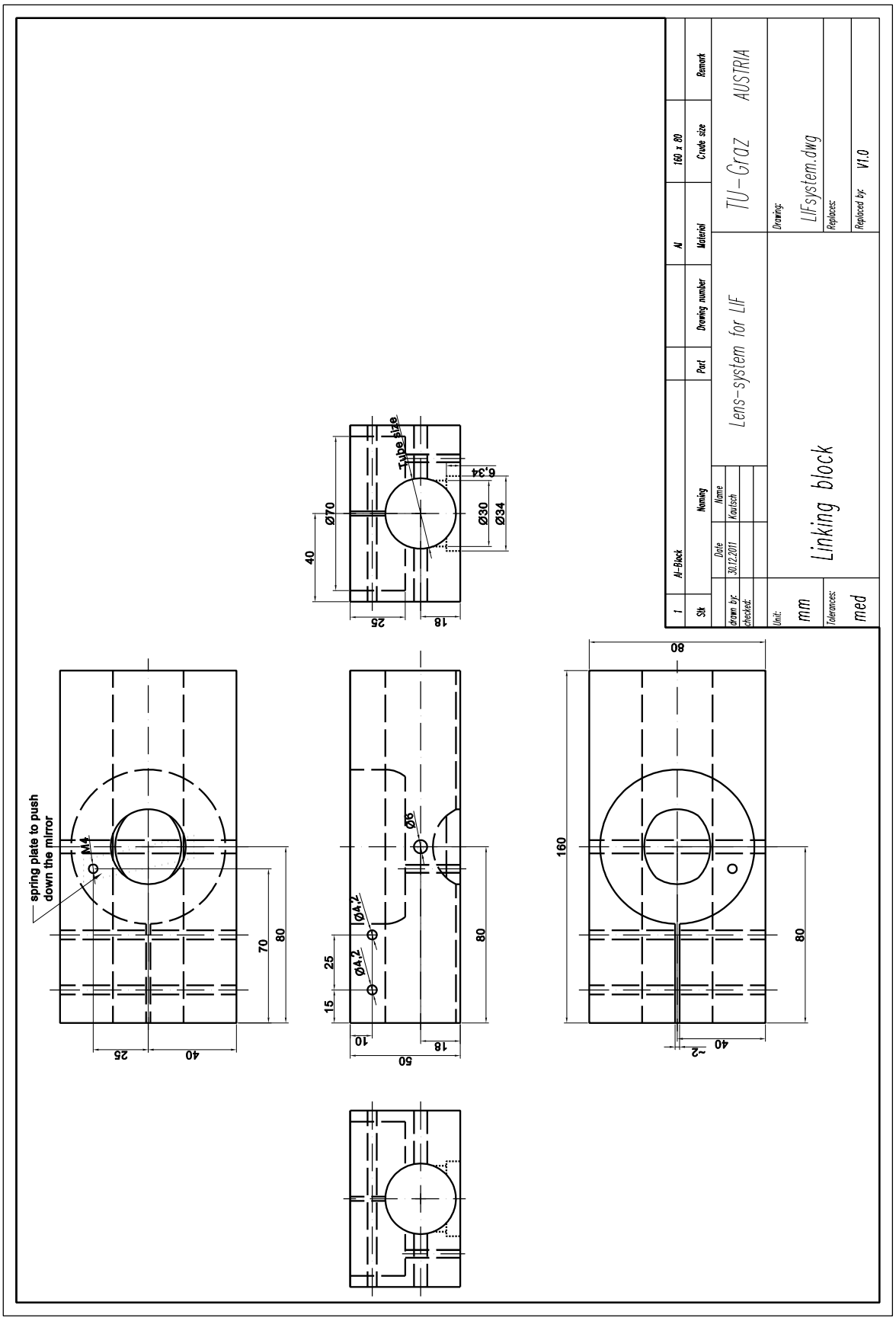
spring plate to push down the mirror
M4
Ø70
40
Tube size
6.34
Ø30
Ø34
25
18
Ø6
Ø4.2
Ø4.2
25
15
10
18
50
80
70
80
25
40
160
80
80
40
2
1
Al-Block
Stk
Norming
Part
Drawing number
Al
Material
160 x 80
Crude size
Remark
Lens-system for LIF
TU-Graz AUSTRIA
Date
Name
drawn by:
30.12.2011
Kautsch
checked:
Unit:
mm
Linking block
Drawing:
LIFsystem.dwg
Tolerances:
med
Replaces:
Replaced by:
V1.0

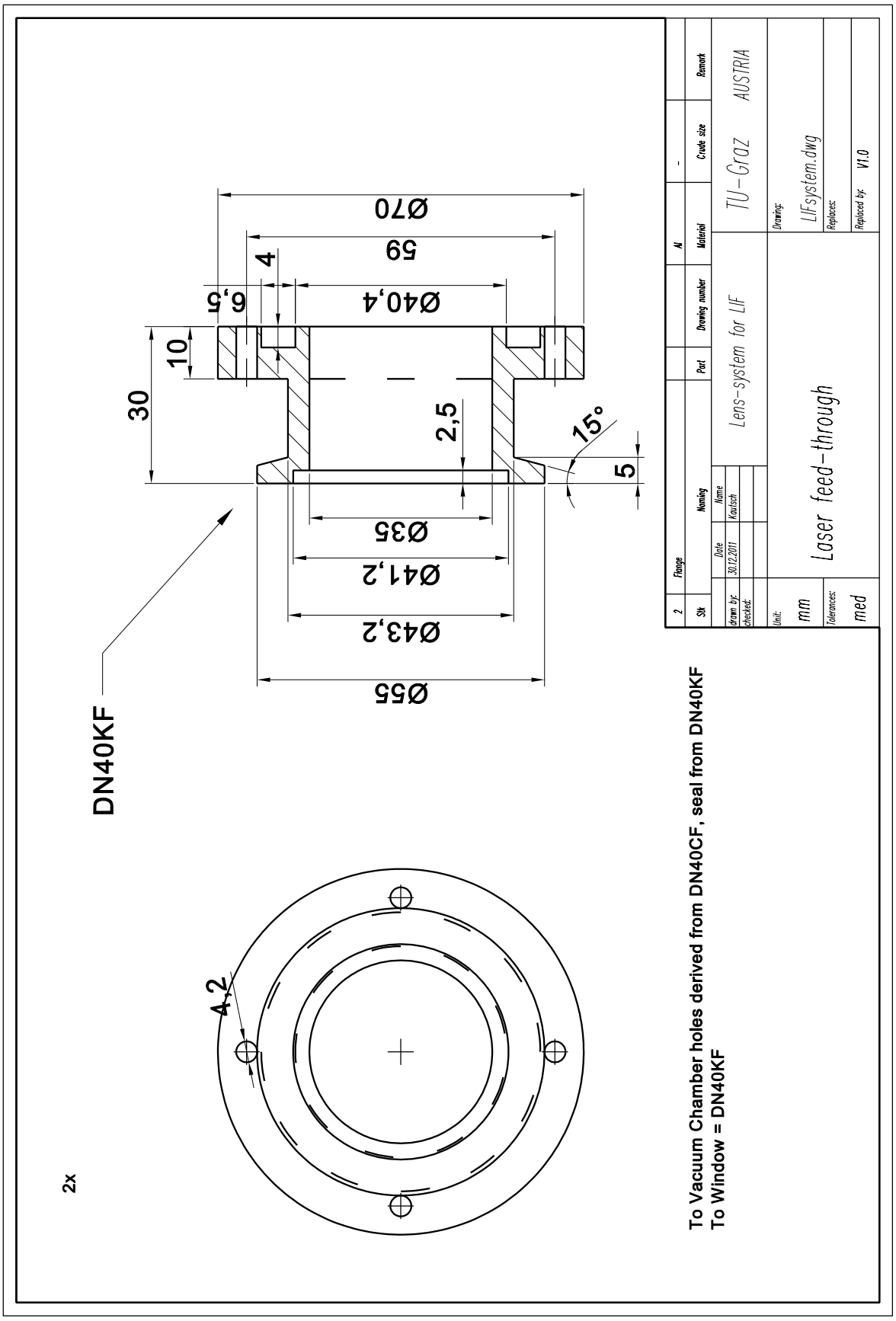
2x
4,2
DN40KF
Ø70
59
4
6,5
Ø40,4
10
30
2,5
15°
5
Ø35
Ø41,2
Ø43,2
Ø55
To Vacuum Chamber holes derived from DN40CF, seal from DN40KF
To Window = DN40KF
2
Flange
Stk
Naming
Part
Drawing number
Material
Al
Crude size
-
Remark
Lens-system for LIF
TU-Graz AUSTRIA
Date
Name
drawn by:
30.12.2011
Kautsch
checked:
Unit:
mm
Laser feed-through
Drawing:
LIFsystem.dwg
Tolerances:
med
Replaces:
Replaced by:
V1.0

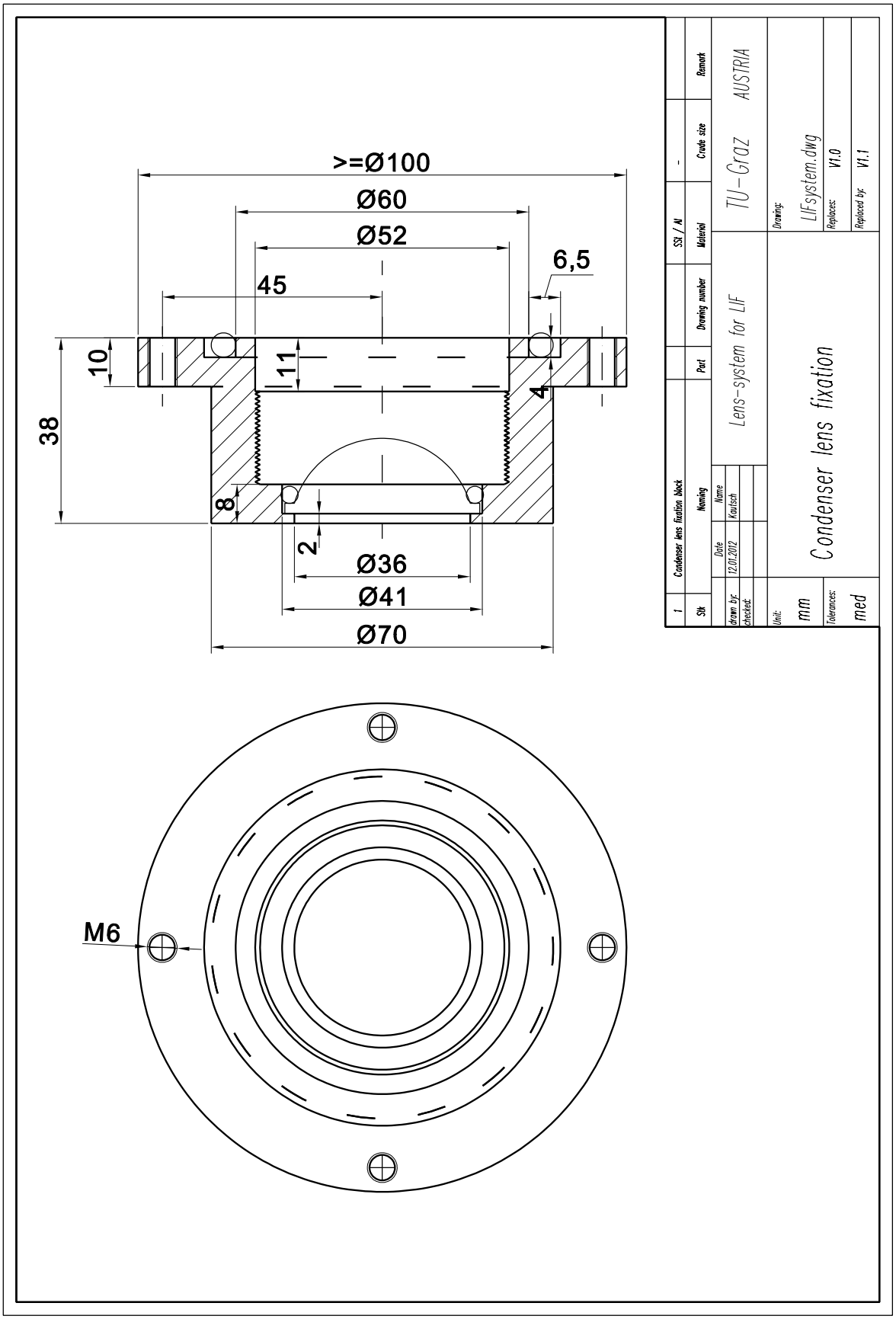
>=Ø100
Ø60
Ø52
6,5
45
10
11
4
38
8
2
Ø36
Ø41
Ø70
M6
1
Condenser lens fixation block
Stk
Naming
Part
Drawing number
Material
SSt / Al
-
Crude size
Remark
Lens-system for LIF
TU-Graz AUSTRIA
Date
Name
drawn by:
12.01.2012
Kautsch
checked:
Unit:
mm
Tolerances:
med
Condenser lens fixation
Drawing:
LIFsystem.dwg
Replaces:
V1.0
Replaced by:
V1.1

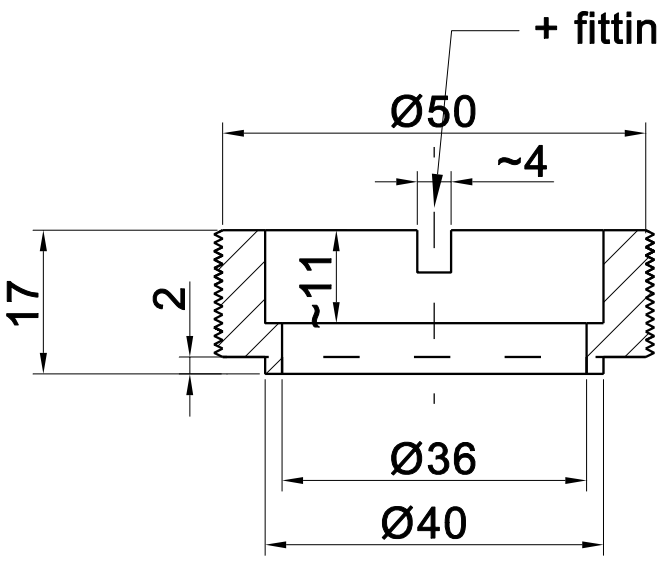

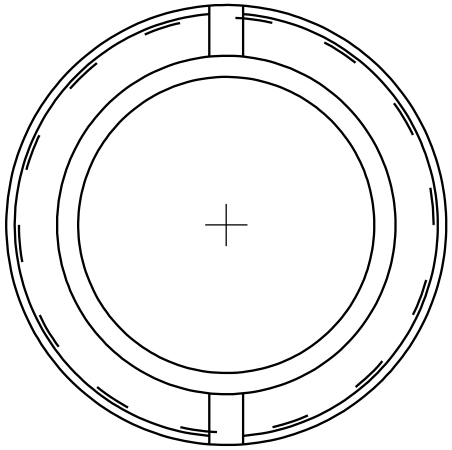

1	Condenser lens fixation sqeezer			Brass	-	
Stk	Naming	Part	Drawing number	Material	Crude size	Remark

	Date	Name		
drawn by:	12.01.2012	Kautsch	Lens-system for LIF	TU-Graz AUSTRIA
checked:				

Unit:		Drawing:
mm	Seal Squeezer	LIFsystem.dwg
Tolerances:		Replaces: V1.0
med		Replaced by: V1.1

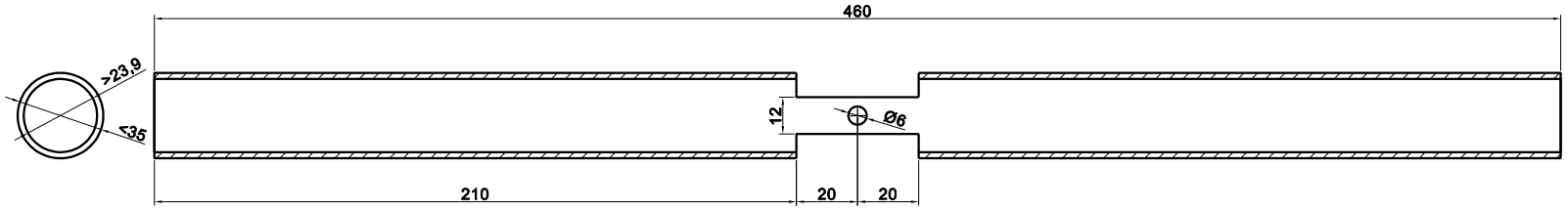

Stk	Naming	Part	Drawing number	Material	Crude size	Remark
1	Tube			Al	-	

	Date	Name
drawn by:	30.12.2011	Kautsch
checked:		

Lens-system for LIF

TU-Graz AUSTRIA

Unit: mm

Tolerances: med

Shielding Tube

Drawing: LIFsystem.dwg

Replaces:

Replaced by: V1.0

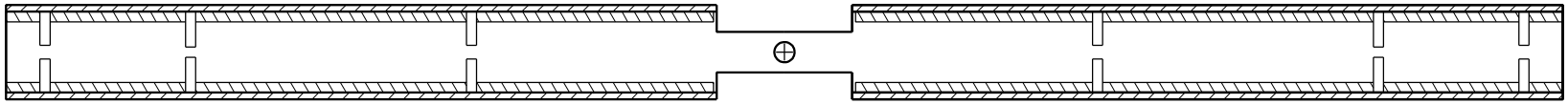

Distance tubes inside (black anodized):
2 x 10 mm
2 x 40 mm
2 x 70 mm
2 x 80 mm

Stk	Naming	Part	Drawing number	Material	Crude size	Remark
8	Tube			Al	-	

	Date	Name		
drawn by:	01.02.2012	Kautsch	Lens-system for LIF	TU-Graz AUSTRIA
checked:				

Unit: mm	Distance tubes	Drawing: LIFsystem.dwg
Tolerances: med		Replaces:
		Replaced by: V1.0

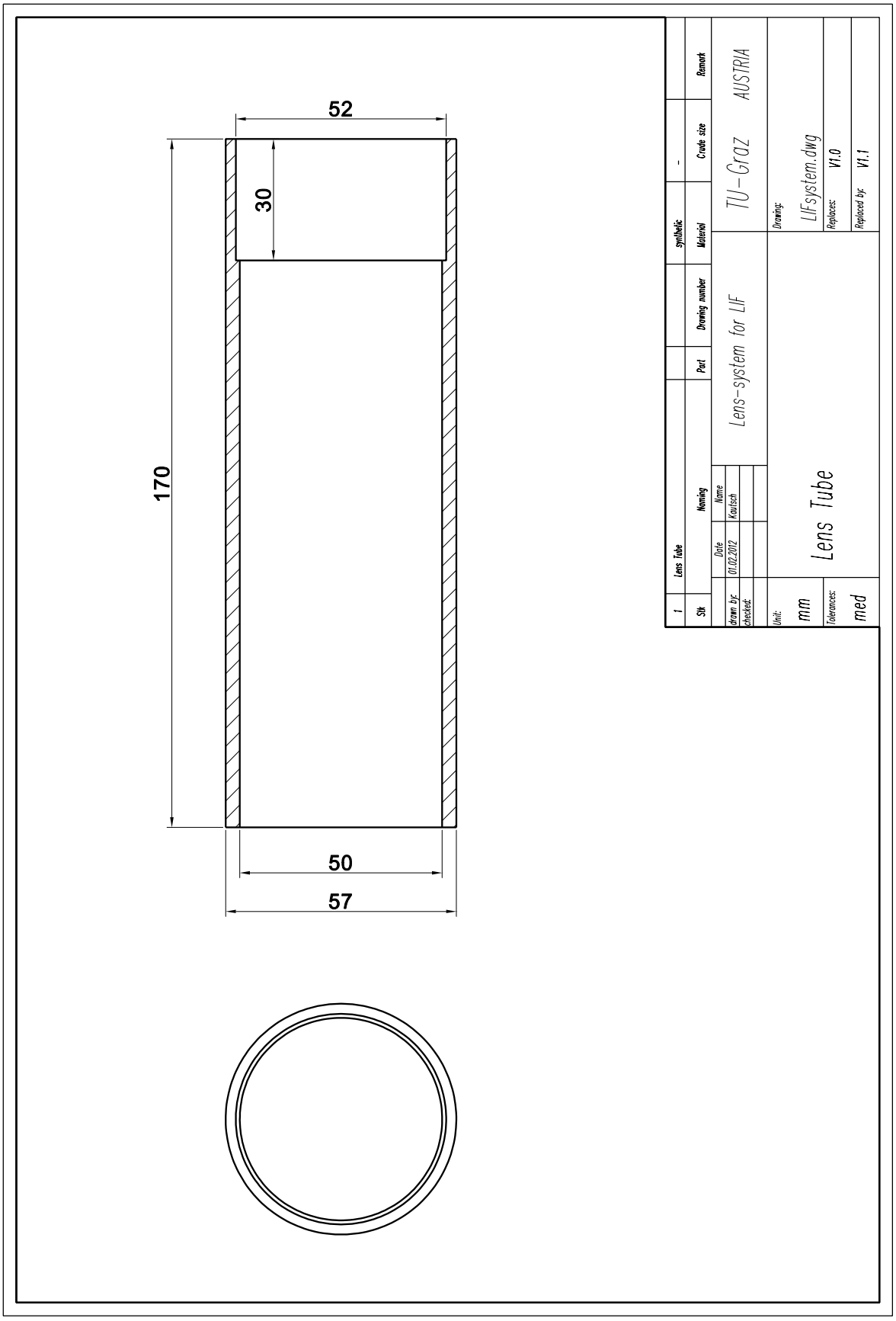
52
30
170
50
57
1
Lens Tube
Stk
Naming
Part
Drawing number
synthetic
Material
-
Crude size
Remark
Lens-system for LIF
TU-Graz AUSTRIA
Date
Name
drawn by:
01.02.2012
Kautsch
checked:
Unit:
mm
Lens Tube
Drawing:
LIFsystem.dwg
Tolerances:
mid
Replaces:
V1.0
Replaced by:
V1.1

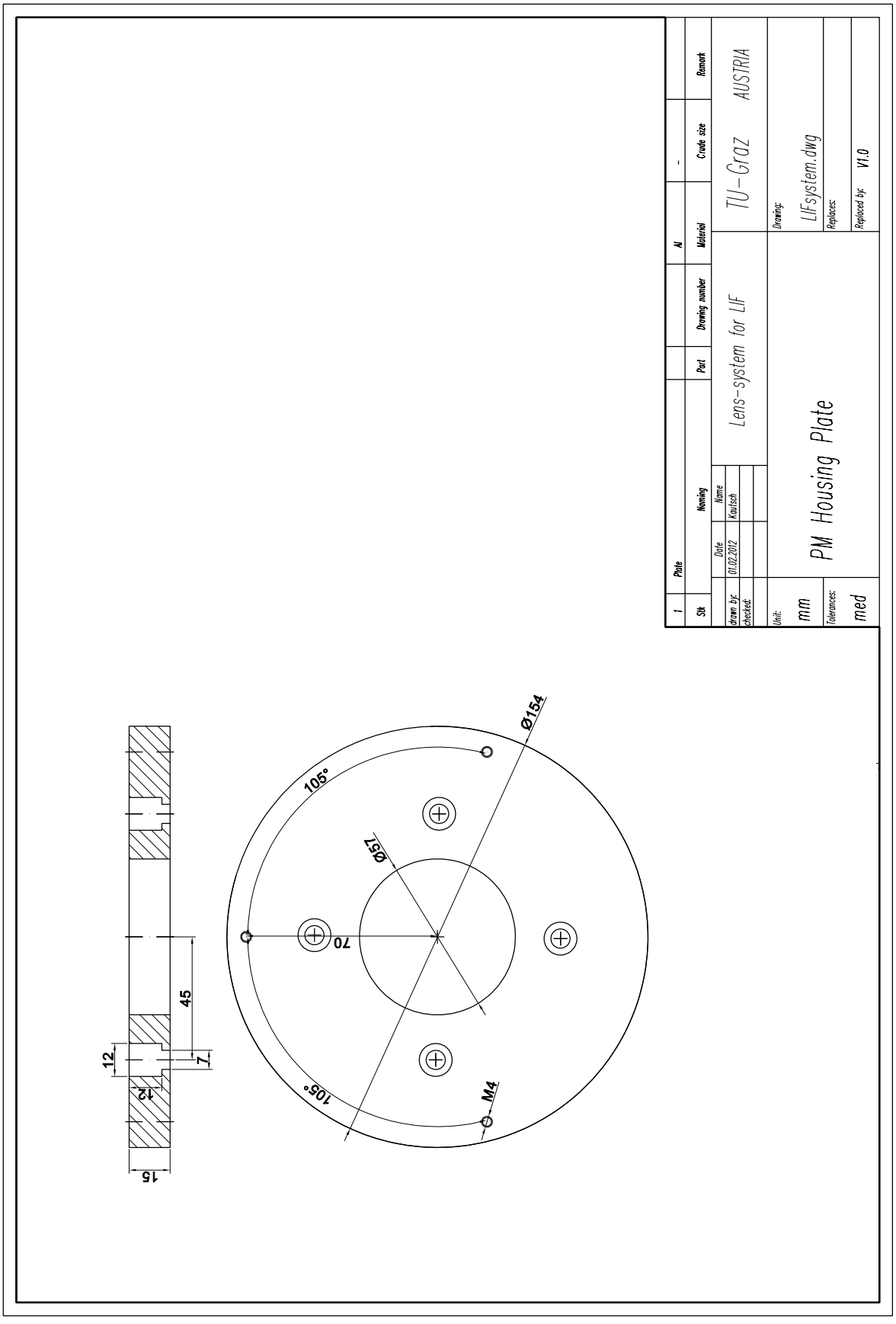
Ø154
105°
Ø90
70
105°
M4
45
12
7
2
15
1
Plate
Stk
Naming
Part
Drawing number
Al
Material
-
Crude size
Remark
Lens-system for LIF
TU-Graz AUSTRIA
Date
Name
drawn by:
01.02.2012
Kautsch
checked:
Unit:
mm
PM Housing Plate
Drawing:
LIFsystem.dwg
Tolerances:
med
Replaces:
Replaced by:
V1.0

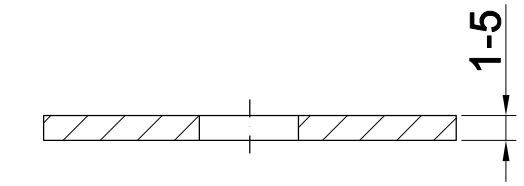

one each Ø 8, 10, 12, 15

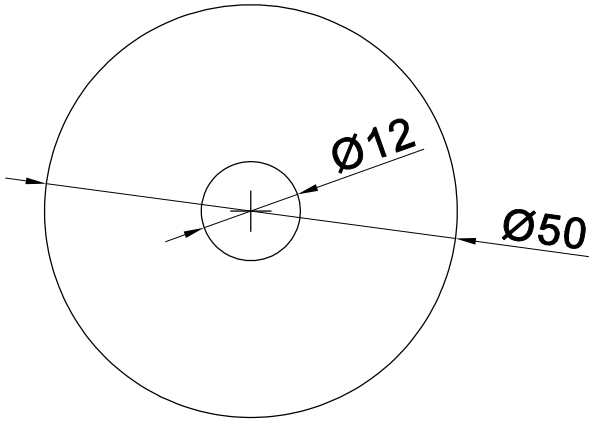

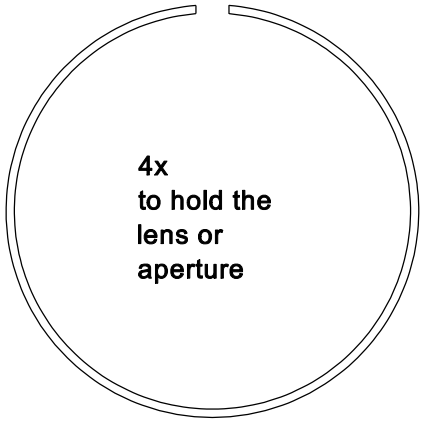

Stk	Naming	Part	Drawing number	Material	Crude size	Remark
1	Plate			synthetic block	-	
4	Tension Ring			spring steel Ø1 mm	-	

	Date	Name		
drawn by:	01.02.2012	Kautsch	Lens-system for LIF	TU-Graz AUSTRIA
checked:				

Unit: mm	Aperture + Tension Ring	Drawing: LIFsystem.dwg
Tolerances: med		Replaces:
		Replaced by: V1.0

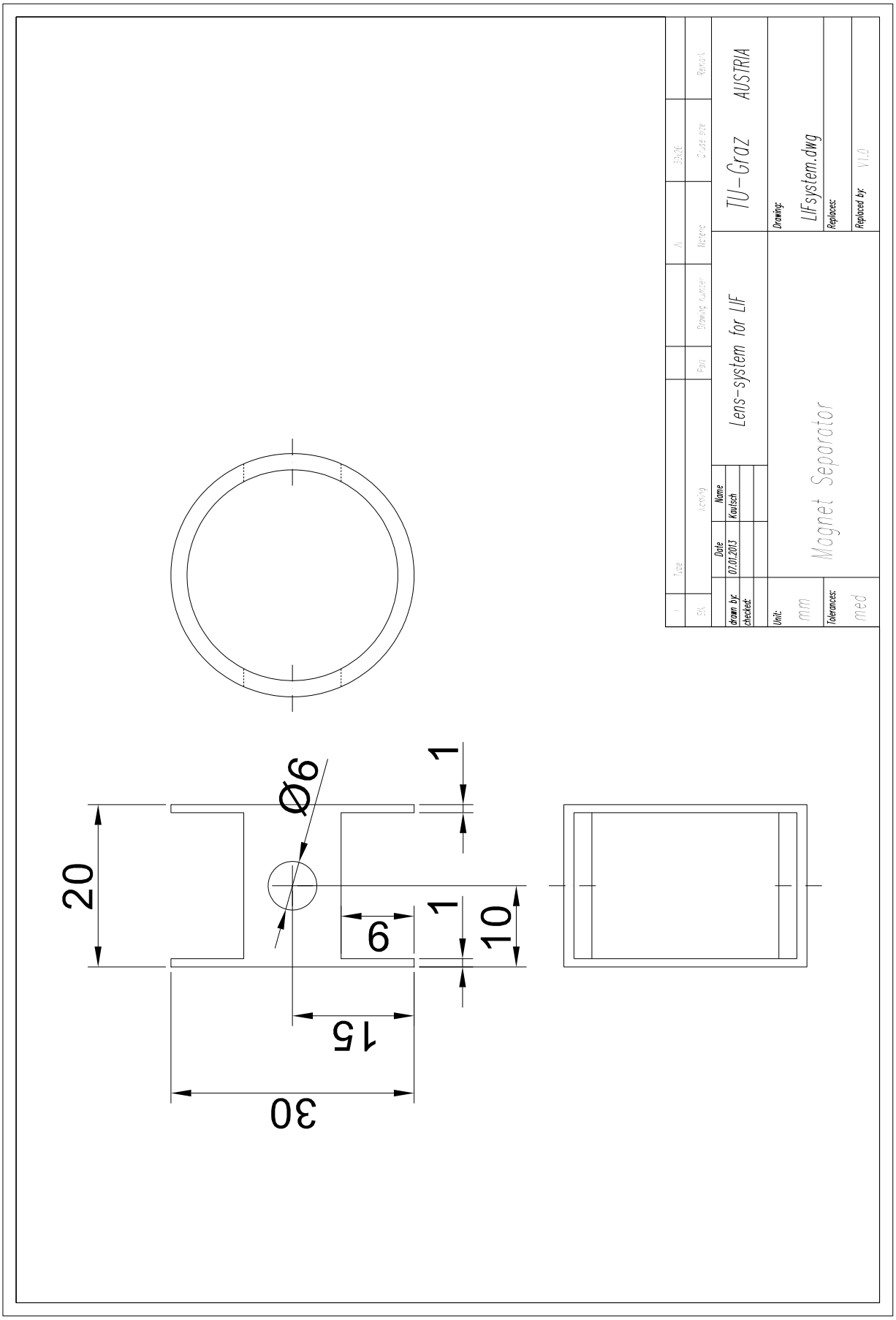
Ø6
1
20
9
1
10
15
30
Lens-system for LIF
Magnet Separator
TU-Graz AUSTRIA
LIFsystem.dwg
Name
Kaulisch
Date
07.01.2013
drawn by:
checked:
Unit:
mm
Tolerances:
med
Replaced by:
V1.0

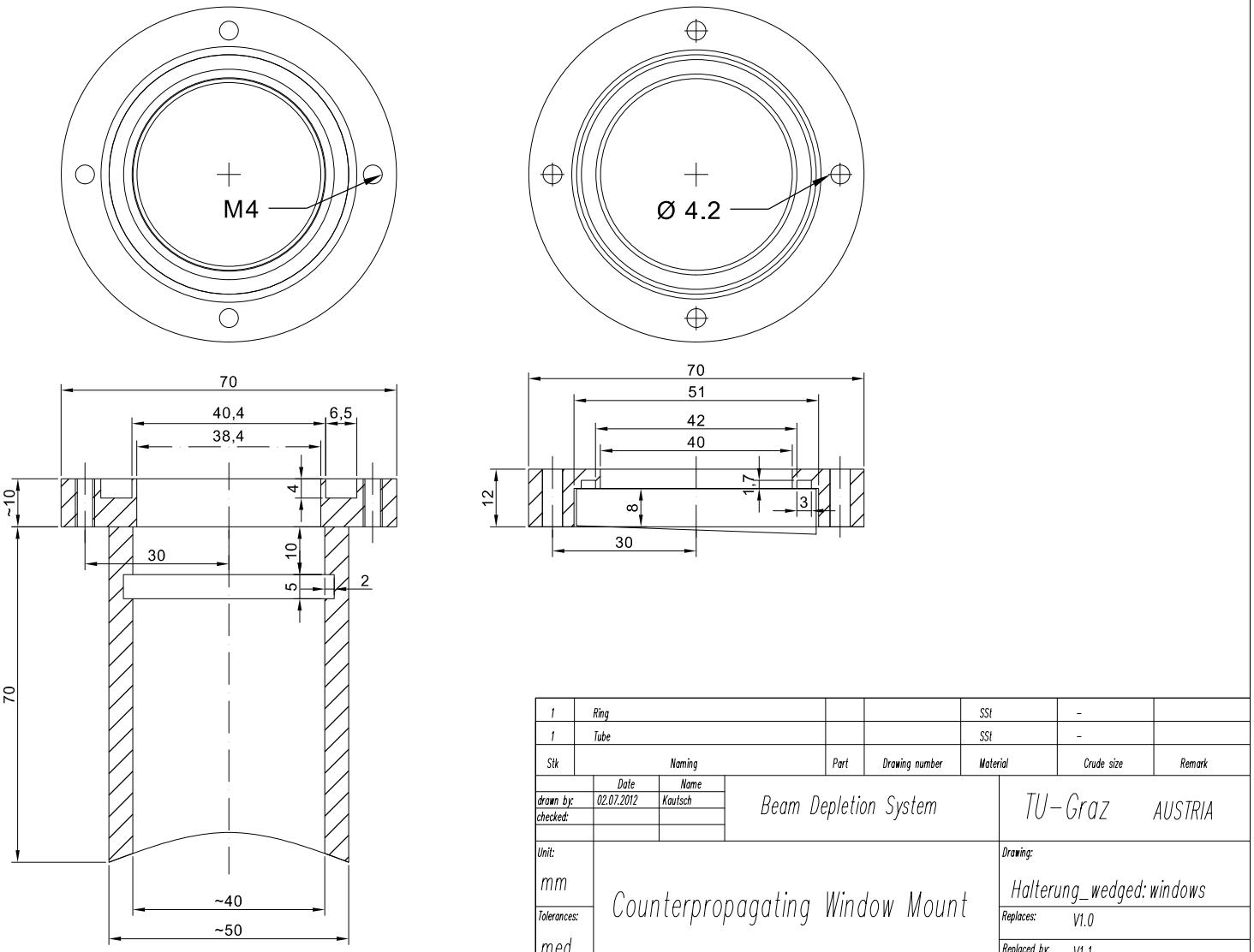

1	Ring			SSt	-	
1	Tube			SSt	-	
Stk	Naming	Part	Drawing number	Material	Crude size	Remark

	Date	Name		
drawn by:	02.07.2012	Kautsch	Beam Depletion System	TU-Graz AUSTRIA
checked:				

Unit: mm	Counterpropagating Window Mount	Drawing: Halterung_wedged:windows
Tolerances: med		Replaces: V1.0
		Replaced by: V1.1

B.2 High Temperature Evaporation Sources

From an experimentalist's view, high temperature crossed beam evaporation sources are more difficult to handle than low temperature cells. Hence, some improvements and useful tricks shall be listed here:

- A constant problem arises with the coating of electrically insulating ceramic parts with evaporated metal. The metal coating creates an electric shortcut that requires the replacement of these parts. This is especially relevant for the ceramic tubes of the Cr high voltage evaporation source, which hold and electrically insulate the crucible from the ground but are not well separated from the region of higher vapor pressure. Additionally, they are very sensitive to metallic coating due to the high voltage applied. Therefore, the ends of these rods were covered with ceramic rods of larger diameter (see Fig. 2.3), preventing the end faces of the inner rods, where the fixation screws are applied, from being coated with metal.
- For both evaporation sources, the slitted lid was machined out of a thicker molybdenum plate (Fig. 2.3) instead of the thin tantalum sheet [65]. The thick molybdenum plate keeps its shape even after high heat treatment which ensures a many cycle reuse. Furthermore, molybdenum is cheaper than tantalum (but harder to machine).
- Concerning the high voltage Cr evaporation source, the wire which connects the voltage supply to the tantalum crucible through the vacuum chamber was insulated by a glass tube from the ground. The advantage is the good insulation over a long distance, the ability to easily guide the wire along a desired path, and the high stability of the glass preventing the tantalum wire from breaking when brittle after the first heat up of the source. For fabrication, the wire is introduced into a glass tube (d $\approx$ 5 mm) of equal length and locally heated with a Bunsen burner. It is on the one hand shaped to be easily fixed with clamps on the evaporation source base plate and on the other hand guides the contact from the vacuum feed-through to the gap between cooling shield and crucible. Afterwards, the ends of the glass rod are cut off to expose the ends of the wire for the electric connection.
- Cr deposition on the inside of the cooling shield leads to the buildup of a thick Cr layer that can detach from the surface, fall off, and connect the crucible with the ground causing an electric shortcut between the crucible and the ground. The probability of this to occur can be reduced when the cool down rate is kept at a low level. In contrast, the heat up rate has no effect. Although this increases the maintenance interval, the cooling shield has to be removed periodically. To enable an easy detachment of the cooling shield from the source without the removal of the stiff water tubes, an alternative layout was developed (see Fig. B.1). A

water cooled copper block is connected to the cooling shield with a thick copper strand, providing the flexibility to remove the cooling shield without detaching the water tubes. In contrast to the design described in Ref. [169], the heat flow is reduced which increases the temperature in the PC. For a combination with low temperature alkali metal pick-up cells, this setup is less suitable because it would heat the neighboring cell.

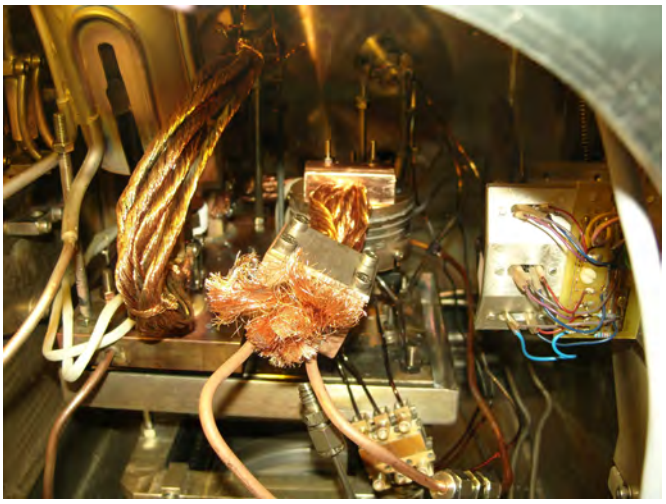

(a)

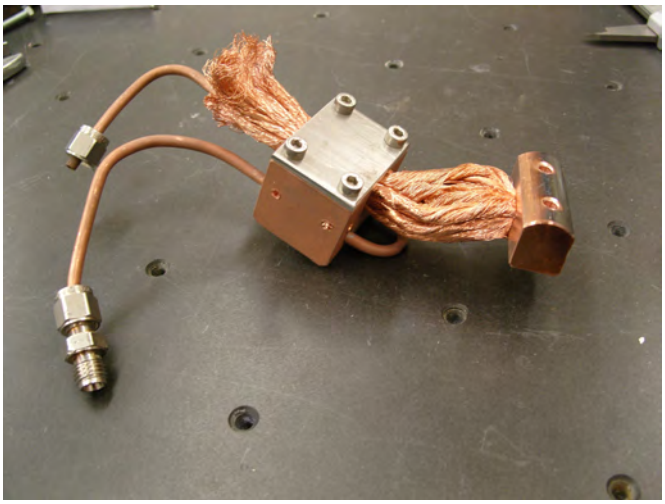

(b)

Figure B.1: Alternative construction to provide a water-cooling for the Cr HT-source cooling shield as well as an easy detachment of the shield for maintenance.

B.3 DVD Content

Files included are:

- Technical drawings for LIF system ('LIFsystem_drawing.dwg', AutoCAD®)
- Technical drawings for BD window mount ('BD_window_mount_drawing.dwg', AutoCAD®)
- LIF detector lens systems
  - for PMT ('LS_Monochromator.SPD', WinLens3D Basic)
  - for monochromator ('LS_PMT.SPD', WinLens3D Basic)
- Program for Fano profile fits ('Fano_Fit.m', MATLAB®)
- Comparing the Cr and Cr_2 vapor pressure ('Cr_Cr2_vaporPressure.m', MATLAB®)
- Main data acquisition program
  - Main Program ('Measurement_main.vi', LabVIEW)
  - Additional subprograms
- Laser remote Program
  - Main Program ('FL3002_LaserControl.m', MATLAB®)
  - FL3002 grating orders ('GratingOrders.fig', MATLAB®)
  - Additional subprograms
- Instructions to set-up the frequency doubling stage ('Frequency_doubling.pdf')
- Cluster Laboratory II maintenance plan ('Maintenance_CLII.docx', MS Word)
- Screen video recorded during a Cr REMPI measurement ('Measurement_Video.avi', Windows Media Player)

The recommended programs to open the files are:

- AutoCAD® 2013
- Free DWG Viewer (Freeware)
- MATLAB® 7.11.0 (R2010b)
- LabVIEW 2013
- WinLens3D Basic (Freeware)